New measurement of oxygen-15 alpha capture through indirect alpha transfer reaction for explosive nucleosynthesis in neutron stars

Jennifer Sanchez Rojo

Doctor of Philosophy

University of York
Physics
December 2021

Abstract

X-ray bursts are a product of thermonuclear runaways taking place on the surface of neutron stars in binary systems. In this scenario, the neutron star is accreting matter from its companion. The accreted matter that falls onto the neutron star surface heats and compresses the environment leading to the ignition of the hot-CNO cycle. This process burns hydrogen into helium releasing energy and heating the plasma. In these cases a break out from the hot-CNO cycle takes place releasing huge amounts of energy, and leading to explosive nucleosynthesis via the rp-process. The ^{15}O + α capture reaction is believed to be the dominant breakout path from the hot-CNO cycle for temperatures up to 1 GK. Here, resonant states in ^{19}Ne are populated. Nuclear properties from this reaction have been studied for over 30 years, however there are still uncertainties and missing information. To understand their production mechanism and nucleosynthesis properties, models need nuclear physics inputs. Determining an accurate cross section for the relevant resonant states is critical for a better understanding of the X-ray burst energy production and light-curves, as well as other novel binary stellar systems involving neutron stars and their potential impact on nucleosynthesis.

To study this reaction an indirect ^{7}Li(^{15}O,t)^{19}Ne alpha transfer reaction in inverse kinematics was performed. The experiment took place at GANIL taking advantage of the post-accelerated ^{15}O Radioactive Ion Beam, and the state-of-the art detection system VAMOS + AGATA + MUGAST coupled together for the first time. This setup provided an unrivalled selectivity for detecting triple coincidences in this reaction. The relevant states in ^{19}Ne were populated.

The experimental set-up and analysis of the data are presented in this work. New results for the strongest populated resonances in ^{19}Ne at $E_x = 4140$ keV and $E_x = 4197$ keV are given, as well as for the excited state at $E_x = 4033$ keV with reduced errors, which is believed to be the strongest contribution to the reaction rate. The main result obtained from this work is the alpha partial width for the 4033 keV state $\Gamma_{\alpha,4033} = 3.0^{+4.0}_{-2.2} \pm 1.4$ μeV at the 1σ C.L. Partial widths for the two other resonance levels were calculated to be $\Gamma_{\alpha,4140} = 0.28 \pm 0.04 \pm 0.13$ μeV and $\Gamma_{\alpha,4197} = 3.0 \pm 0.3 \pm 1.4$ μeV. Finally, the contributions to the ^{15}O(α, γ)^{19}Ne reaction rate from several states in ^{19}Ne at different stellar temperatures are discussed.

Contents

List of Figures

List of Tables

Acknowledgements

I am extremely grateful for having worked during my PhD with many fantastic researchers. My supervisor Christian has always provided me with support and answers. I learned a lot from him and I always felt I could put forward my own ideas and discuss the physics with him. My analysis has been painful at times but our hours of discussion passed by quickly. I cannot mention the analysis without giving special thanks to Nicolas, with whom I have also spent countless hours discussing (and many of them in Spanish, which I really appreciated when I was too tired for/of English). I want to thank him for all the support and for being a great unofficial second supervisor.

I would also like to thank Alison for the exciting discussions, for having always answers for me about nuclear astrophysics (and sometimes about bureaucracy), and for reminding me that I am a good researcher, no matter what my impostor syndrome makes me believe.

I had also the pleasure of been guided by Diego in a big chunk of this project while working on the calibrations and particle identification. I am also specially grateful to him for guiding me both during the experimental campaign and afterwards by zoom meetings.

During the experimental campaigns I had the pleasure to meet many awesome people and I thank each one of them for the discussions, the things I learned from them, the coffee breaks and the fantastic dinners out when the experiments let us have a break. For this, I would like to thank the whole collaboration, without whom this experiment would not have been possible. A special mention to those who chose to spend the second half of July in the control room instead of enjoying the summer holidays. Thanks to Franco for joking around with me, for helping me out so much during the preparation of the experiment and for all the night shifts that he had to do with me (or even for me). Thanks to Kseniia for the company during the night shifts and guidance with AGATA. And many others who I had the pleasure to meet in GANIL.

I would also like to acknowledge the input from the different collaborators to this project, in particular thanks to Emmanuel for providing the AGATA efficiency curves, and thanks to Chen for performing the AGATA Compton background simulations.

I think it is also important to acknowledge the times we are living, where a pandemic has taken the world hostage and, for a little while, the whole world stopped. I was lucky enough to have had my experiment in 2019. The first lockdown took place in march 2020 and, since then, I haven't done anything other than work in my thesis. And for this reason (and more than anything else) I want to thank the people and the things that kept me sane.

Thanks to Murias, for being the best friend I could ask for. He has always been a phone call away any time I needed. Of course, thanks to the Neutron Team, for all the video-calls that helped me so much during lockdown.

Thanks to Charo, for the unconditional love and friendship since we were in high-school, no matter where we are, and for believing in me.

Thanks to Laura (my Lily), for being always there, no matter if it is a seven hour flight or a forty-five minutes drive. Thank you for listening to me and for giving me all your support.

During my analysis, any time I had doubts and questions, Suso has always tried to help me as much as possible, so I would also like to give him a big thanks for all the help and for his friendship (and chocolate!) over the past few years. To the many other people I met during my time in York, and with whom I spent many coffee breaks and climbing sessions with, I would also like to thank for all the good times and memories I shared with them.

Thanks to Matt for helping me so much, for cooking me tasty food and for making me take breaks and go for walks, especially in the last few months when I barely left my desk. I could not have finished this thesis without your support.

A special thanks to my family for having always supporting my crazy idea of becoming a nuclear physicist, and specially to my mum, who keeps encouraging me to follow my dreams no matter what they are, even if I keep moving farther and farther away from home.

And finally, a weird acknowledgment to the ways I escaped from reality: the art that kept me working. Thanks so much to Radiohead, Arctic Monkeys, Sigur Ros, Wolf Alice, Queens of the Stone Age (and so many other bands), thanks to The Office and Friends for giving me laughter over and over no matter how many times I watch them. Thanks to Hermione for showing me since I was little that girls can be smart and bad-ass all at once. Thanks to the Lady Jessica for teaching me the strength of the mind. Thanks to art for the reminder that we live for the beauty of this world.

Author's declaration

This thesis is a presentation of original work and I am the sole author. The contents of this thesis are original and have not been submitted in whole or in part for consideration for any other degree, award or qualification in this, or any other university. I hereby declare that the contents of this dissertation have been written by me and that they are based on my own work, except where specific references and contributions are acknowledged. All sources are acknowledged as references.

Jennifer Sanchez Rojo

"*Fear is the mind-killer.*"
–Dune

Chapter 1

Motivation and previous measurements

1.1 Astrophysical Motivation

Stars are some of the the biggest objects known in the universe and yet they are sustained by the interaction of some of the smallest particles known by human-kind. Nuclear reactions play a key role in the energy production of stars and it is only by studying the properties of the nuclei involved that we understand many of the stars' properties. As a nuclear physicist, I am fascinated by the study of nuclear reactions in astrophysical environments, given that the universe is our biggest laboratory. As we are constrained to Earth, our only hope is to reproduce the nuclear reactions in our own laboratories and then link our results with theoretical models and observations.

Stars have been our companions since the early days of humanity and our ancestors were able to study them with little technology. Astronomy was an ally for explorers of all kinds, especially for navigation campaigns where one had nothing but the sky to be guided by. It is not surprising that scientists wanted to understand what these objects were and how did they get their energy. It is not until the 20th century that modern physics was developed and the stellar nucleosynthesis theory took shape motivated in particular by the studies of Fred Hoyle [Hoy46].

There have been all kinds of studies since then to constrain our models and understanding of the evolution and nucleosynthesis of stars, as well as to understand the production of elements heavier than iron and predict abundances in the Universe. Even though our comprehension of stellar nucleosynthesis has grown significantly in the last 50 years, there are still many uncertainties that must be addressed. Hence, we need to determine the nuclear properties of the most important reactions that take place in different scenarios from core burning to core-collapse supernovae and other interesting astrophysical sites.

In this dissertation I will explain the work carried out to study the $^{15}O(\alpha, \gamma)^{19}Ne$ nuclear reaction and why it plays a key role in the understanding of the mechanism of X-ray bursts.

1.1.1 A brief introduction to stellar evolution

Stars are massive objects constrained by two main forces: gravitational and pressure. They are formed from molecular gas clouds, mainly composed of hydrogen and helium, that start collapsing due to gravitational forces. A very simplified view of stellar formation is given as follows, aiming to have a general understanding of the process.

The initial gas cloud experiences gravitational forces from the interaction between its particles in hydrostatic equilibrium. The total energy of the system E is given as the sum of its potential energy U plus its internal kinetic energy K. To describe a system in equilibrium we can use the virial theorem, that establishes the relation between the kinetic energy K and potential energy U as

$$K = -\frac{U}{2} \quad , \tag{1.1}$$

and whose demonstration is found in many textbooks [Cla68; Rol88; CO13]. The potential energy $U < 0$, and it is increasingly negative as the cloud shrinks. In this system the total energy $E = U + K$ must be conserved. Applying the virial theorem to the total energy of the cloud, we obtain an expression for E that only depends on the potential energy as $E = \frac{1}{2}U$. In consequence, as the cloud shrinks one half of the total energy is used as thermal motion and the other half is radiated.

In order for the collapse to take place the gravitational force must dominate the gas pressure. Hence, the absolute value of potential energy must exceed twice the kinetic energy of the cloud. Following this theorem, sir James Jeans extracted a condition on the minimum mass a gas cloud needs in order to collapse [JD02]. This critical mass is called the Jeans Mass and is deduced from the virial theorem giving a lower limit

$$M_c > M_{\text{Jeans}} \simeq \left(\frac{5kT}{\mu G m_H}\right)^{3/2} \left(\frac{3}{4\pi\rho_0}\right)^{1/2} \tag{1.2}$$

where k is the Boltzmann constant, T the effective temperature of the gas, μ is the average particle mass, G the gravitational constant, m_H the hydrogen atomic mass and ρ_0 the density of the cloud. Therefore, clouds of low temperature and high density will need smaller masses to start the collapse. For the calculation above other effects such as rotation, turbulence and magnetic fields are neglected.

When a molecular cloud exceeds M_{Jeans}, it starts collapsing. In the first stage of this gravi-

tational collapse, it does it homogeneously and in free fall. While the cloud shrinks the density increases quickly in the central region. Through this phase the temperature remains effectively constant [CO13] because of the radiation of the excess thermal energy from gravitational contraction, and every part of the cloud falls at the same velocity. However, when the opacity of the cloud increases due to ionisation and density increase, the temperature increases quickly because the radiation cannot escape [Rol88]. This leads to a rise in pressure that makes the collapse stop. At this point the cloud, or protostar, is composed of a central core in hydrostatic equilibrium and an external region collapsing due to its lower density and temperature. The protostar keeps contracting and heating up ionising the hydrogen atoms until the temperature in the core is enough for the ignition of the hydrogen burning (approximately 1-2·10^7 K). When hydrogen burning is ignited we will say that the star is born. However, there is a minimum mass a protostar must have to allow the ignition of the H-burning, which is $0.08\mathrm{M}_\odot$ [Cla68], where $\mathrm{M}_\odot$ is the mass of the Sun. Protostars below this mass limit will never reach the temperature needed for hydrogen fusion, and they will only be stable against collapse because of gas pressure, ending up as *brown dwarf* stars.

Stars can be classified according to their luminosity, which is related to their radius R and effective temperature T_s by the Stefan law:

$$L = 4\pi R^2 \sigma T_s^4, \tag{1.3}$$

where σ is the Stefan-Boltzmann constant [Rol88].

In 1913 the astronomers E. Hertzsprung and H.N. Russell performed separate studies of the stellar luminosity and effective temperature, reaching the same conclusions. They found a correlation between these two observable properties by plotting the luminosity of stars against its effective temperature. They obtained a graph equivalent to that of figure 1.1 where stars were grouped in specific regions, instead of being uniformly distributed. It was given the name of *Hertzsprung-Russell* diagram (or H-R diagram), and in this diagram four main regions are distinguished: the Main Sequence, the Giants, the Supergiants and the White Dwarfs. During its lifetime, a star will vary its luminosity and effective temperature moving through the H-R diagram, and the followed path depends on the initial mass of the star. Figure 1.1 also shows three examples of the specific path followed by stars whose initial mass is 1, 5 and 10 $M_\odot$. Every star begins its life on the Main Sequence and evolves following different stages depending on its initial mass.

Most of the known stars are distributed along the Main Sequence, which forms a line from the bottom-right to the upper-left corner of the diagram. Before reaching the Main Sequence

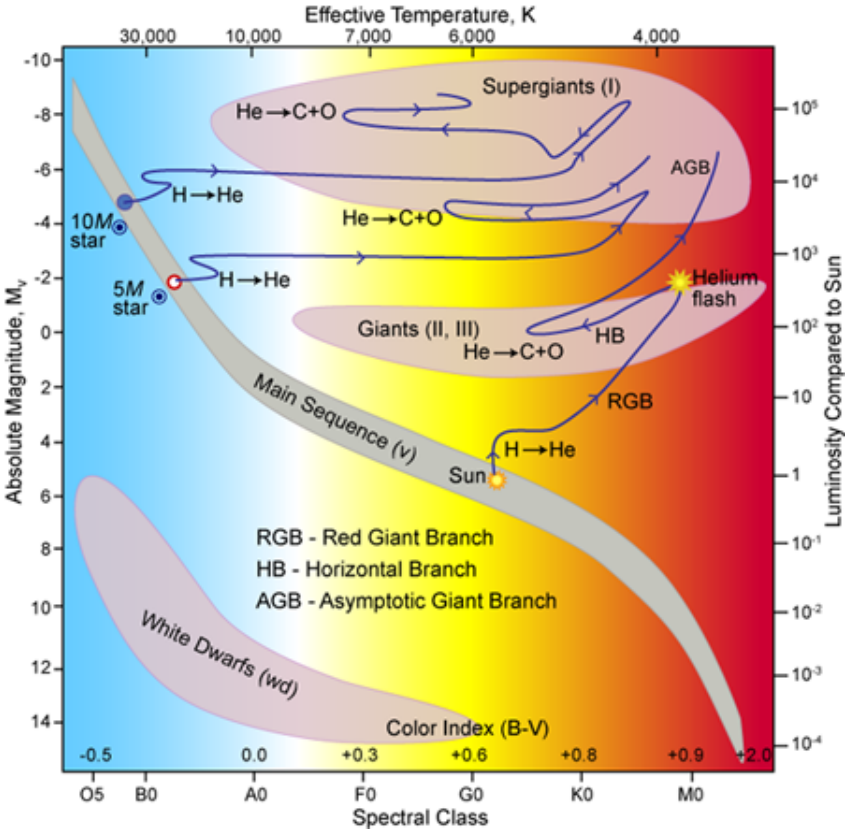

Figure 1.1: Hertzsprung–Russell diagram. Relation of luminosity versus temperature of stars. It also shows the different paths that stars follow depending on their initial mass. Image by R. Hollow, Commonwealth Science and Industrial Research Organisation (CSIRO), Australia, adapted by Carin Cain.

the protostar heats up due to the gravitational collapse, and its radius and luminosity decrease, moving therefore down and to the left in the H-R diagram, approaching the main sequence from the right. This decrease in luminosity is explained using the Stefan law in equation 1.3 and the fact that the gas is very opaque; the heat in the center takes a long time to reach the surface therefore T_s changing very little, and the radius decreases due to the collapse; thus the luminosity of the protostar also decreases. The protostar keeps collapsing becoming hotter and smaller, and moving to the left on the H-R diagram until eventually hydrogen burning in the core is ignited. At this point the protostar reaches the Main Sequence and it begins its journey as a newborn star. It spends a long time on the hydrogen burning stage, and it barely changes in size, temperature or luminosity until hydrogen is exhausted in the core [Rau20]. Figure 1.1 shows that the more massive stars are many orders of magnitude more luminous than the less massive stars. The mechanism of energy production must be more powerful to compensate for the energy production difference, thus the more massive stars burn hydrogen into helium faster than the sun. This fact also means that the more massive stars have a shorter life span as they

exhaust their fuel quicker than the less massive stars.

When the hydrogen in the core is almost exhausted, the core will be mainly composed of helium. The whole star will quickly contract until the temperature and density increase enough to ignite hydrogen burning in a shell surrounding the core. The energy produced at this point is more than the energy that can be radiated away. As a consequence, the outer layers of the star will expand and cool. The star begins to move upwards and to the right in the HR diagram; it becomes brighter and cooler while moving towards the red giant region. At this point, the temperature in the central region of the star is high enough to ignite the helium in its core.

As stated in the preceding, the path of a star from the main sequence is determined by its initial mass and metallicity. The different phases a star experiences are summarised in figure 1.2. For a sun-like star, the density in the helium core is so high that the electrons are

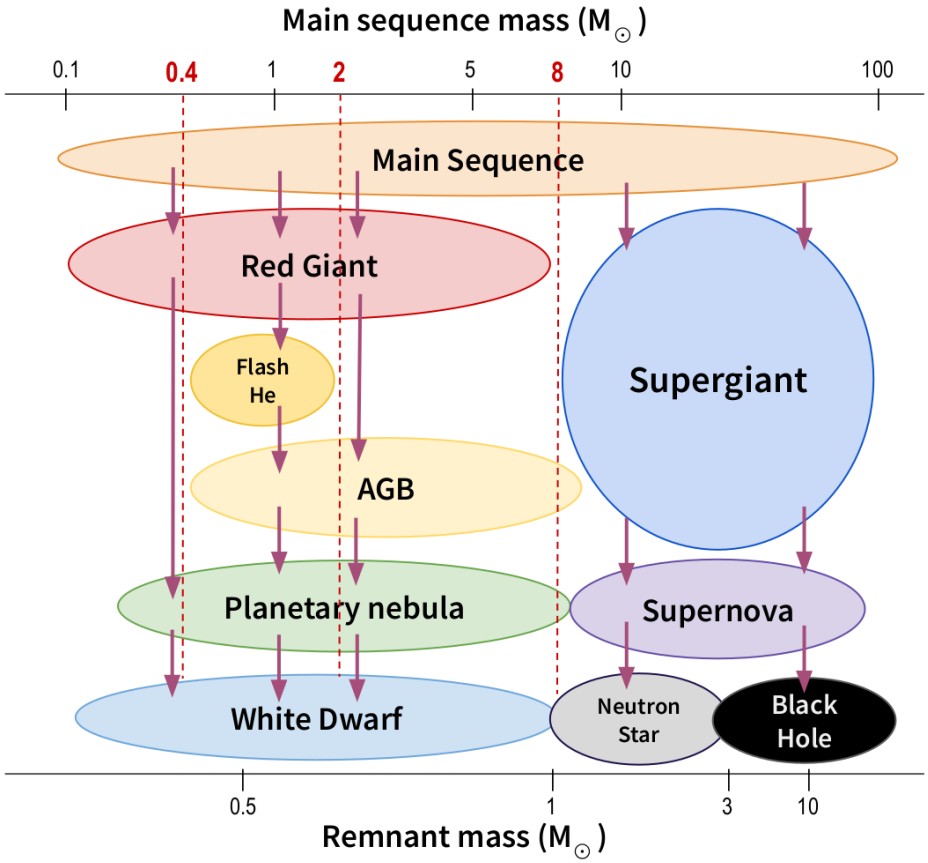

Figure 1.2: Scheme showing the different phases a star follows depending on its initial mass. The mass of the remnant is also shown. For a sun-like star, once the hydrogen is exhausted in the core, it will leave the main sequence evolving to a red giant star, following by some instability phases produced by the helium flashes and finally entering the asymptotic giant branch. From this point, it will lose the envelope creating a planetary nebula surrounding the white dwarf remnant.

degenerate, forcing the temperature and the density to be decoupled. In these circumstances the expansion cooling mechanism is not effective. The environment becomes highly unstable and energy is released through explosions known as helium flashes, which are episodes of rapid helium burning in the core that produce an increase of temperature followed by an expansion and cool down. These episodes will repeat a few times until helium is exhausted. These helium flashes in the degenerate environment are equivalent to the hydrogen burning flashes described later in section 1.1.3 for X-ray bursters. Once there is almost no fuel in the core, the energy production is not enough to stop the contraction of the star. It will move now down and to the left on the HR diagram, entering the horizontal branch. At this point the star will have 2 burning shells surrounding the inert core. They will experience many phases of instabilities producing fast winds that will make the star eject its envelope while it goes up the asymptotic giant branch in the HR diagram. The ejected envelope ends up forming what is called as planetary nebula surrounding the inert core, which forms a carbon and oxygen (CO) white dwarf. Stars with masses lower than 0.4 $M_\odot$ have basically the same path except that their mass is not sufficient to achieve the higher temperatures required to fuse helium nuclei, therefore they do not experience the helium flashes, and they end up forming a He white dwarf surrounded by a planetary nebula [Ili08].

For stars with intermediate masses from 2 to 8 $M_\odot$, the evolution is similar. When they enter the Red Giant phase they also experience instabilities that lead to extreme solar winds expelling their envelopes, however their core material is not degenerate and thus, helium flashes do not take place. In the end the ejected envelope also forms a planetary nebula. The remaining star composed of the inert core forms a white dwarf star.

A star in its Red Giant phase is one of the objects composing the binary systems studied in this project. These stars have an envelope mainly composed of Hydrogen and this fresh hydrogen will play an important role in the binary system. This is described with more details in section 1.1.3.

The most massive stars have the shortest life and the most impressive fates. Due to their mass and the nature of their energy production, they burn the fuel in their core in phases, until nuclear fusion is not allowed anymore. In each burning phase, the core is burning at a higher temperature and pressure, and each time a new layer will form surrounding the core, forming an onion-like structure. Each stage will generate less energy than the former stage, and there will be energy loss from neutrino driven winds in the advanced stages. Once the silicon burning into iron is exhausted in the core, nuclear fusion is not energetically feasible anymore and the star does not have an efficient way of producing energy. As the core stops producing energy, the gravitational force becomes dominant and the star quickly collapses. The temperature

rises extremely quickly, releasing high-energy γ-rays. These photons start a process called photodisintegration, where a series high-energy photons are absorbed by an iron nucleus which splits up releasing many α particles and neutrons through the reaction $\gamma + {}^{56}Fe \longrightarrow 13\,{}^{4}He + 4n$. In this process the released helium particles similarly capture energetic photons splitting it into protons and neutrons through the reaction $\gamma + {}^{4}He \longrightarrow 2p + 2n$. At this point the density is high enough in the core to be electron degenerated and protons start capturing electrons releasing neutrons and neutrinos ($p + e^{-} \longrightarrow n + \nu_e$). The escaping neutrinos result in a huge energy loss cooling down the core, while at the same time removing the electron pressure. This leads to an extremely rapid gravitational collapse until the core reaches a density comparable to that of a nucleus. The gravitational contraction slows down and a shock wave is produced, accelerating the envelope material outwards. Some of the neutrinos created in the electron capture process cannot escape because the in-fall material is increasingly dense. The energy of these neutrinos increases the pressure and temperature of the material producing a huge outburst of energy in the form of a supernova of type II, also known as core-collapse Supernova. In this process a whole new wave of nucleosynthesis takes place and in these explosive conditions nucleosynthesis of very exotic and heavy elements occurs. The shock wave expels the envelope of the star into the interstellar medium and the remnant consists of a very dense core in the form of a neutron star or a black hole. The second component of the binary system studied in this project is such a neutron star left behind after a core-collapse supernova event (see section 1.1.3).

1.1.2 Stellar nucleosynthesis

The evolution of the chemical composition of the universe is explained by the theory of nucleosynthesis, where it is stated that the different nuclei are created by nuclear reactions at different phases of stellar evolution [Bur57; Cla68]. These nuclear reactions are the source of energy in stars, and stellar evolution is directly linked to it. The nuclear reactions triggered in a given star depend on its initial mass and composition, as indicated in the preceding.

A nuclear reaction can only take place if the particles involved are sufficiently close to interact through the strong interaction. However, charged particles are also affected by the Coulomb force, making two particles with the same charge repel each other [TN09]. At stellar temperatures hydrogen cannot classically overcome this Coulomb barrier, but it can penetrate the Coulomb barrier through quantum tunnelling to induce fusion [Rol88] (this is detailed in chapter 2.1). There may also be nuclear reactions involving other heavier elements present in the plasma, producing new elements and releasing energy. However, they do not initially contribute significantly to the energy production in stars, as stars are mostly composed of

hydrogen and helium. The concept of four protons interacting together to form one helium nucleus is extremely unlikely to happen due to the tiny probability of 4 particles interacting together at the same time. Reactions are therefore more likely to happen as a chain of 2-body interactions. The main energy production mechanism in stars is hydrogen burning, and every main sequence star ignites hydrogen to produce helium. The second main energy production mechanism is helium burning, experienced by stars with masses $M > 0.4M_{\odot}$ after leaving the main sequence. There are other reaction mechanisms important for the production of heavier elements. In this section the most important nuclear processes necessary to understand the X-ray burst mechanisms are briefly explained. X-ray bursts occur when the surface of the neutron star is fed fresh hydrogen and helium from the companion star.

Hydrogen burning

There are different ways of burning hydrogen into helium. The main processes of helium creation in stars are the proton-proton chains (or pp-chains) described in equationa 1.4 and the CNO cycles shown in figure 1.3. Depending on its composition, mass and core temperature, a star will burn hydrogen activating one (or several) of these processes.

PP-I	PP-II	PP-III
$p + p \rightarrow d + e^{+} + \nu_e$	$p + p \rightarrow d + e^{+} + \nu_e$	$p + p \rightarrow d + e^{+} + \nu_e$
$d + p \rightarrow {}^{3}He + \gamma$	$d + p \rightarrow {}^{3}He + +\gamma$	$d + p \rightarrow {}^{3}He + \gamma$
${}^{3}He + {}^{3}He \rightarrow {}^{4}He + 2p + \gamma$	${}^{3}He + {}^{4}He \rightarrow {}^{7}Be + \gamma$	${}^{3}He + {}^{4}He \rightarrow {}^{7}Be + \gamma$
	${}^{7}Be + e^{-} \rightarrow {}^{7}Li + \nu_e$	${}^{7}Be + p \rightarrow {}^{8}B + \gamma$
	${}^{7}Li + p \rightarrow {}^{4}He + {}^{4}He$	${}^{8}B \rightarrow {}^{8}Be + e^{+} + \nu_e$
		${}^{8}Be \rightarrow {}^{4}He + {}^{4}He$

(1.4)

For lighter masses the pp-chains dominate the core burning, and they are the main source of energy. Within the p-p chains, the pp-I is the one that occurs most often, taking place about the 86% of the time [TN09] and being the most efficient one. For more massive stars containing carbon and oxygen seeds, the core density is higher, translating also to a higher core temperature, enough to ignite hydrogen burning via the CNO cycles. In this process, carbon, nitrogen and oxygen present in the star act as catalytic material effectively burning four protons into one helium nucleus. As described in figure 1.3 there are four cycles interconnected with each other that will produce alpha particles.

In explosive conditions where the temperature is higher than 0.1 GK proton captures are more likely to take place than β-decays and the so-called hot-CNO cycle (HCNO) is activated. For example the HCNO cycle differs from the normal (or *cold*) CNO cycle in that the proton

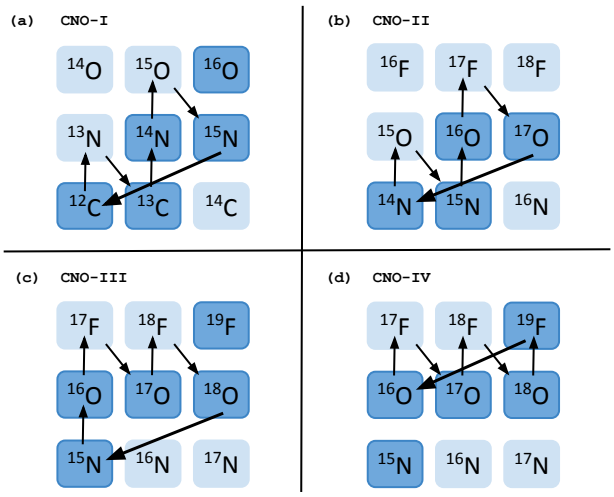

Figure 1.3: The four different CNO cycles. There is a competition between proton captures and β^+ decays. Completing one whole cycle burns four protons into a helium nucleus.

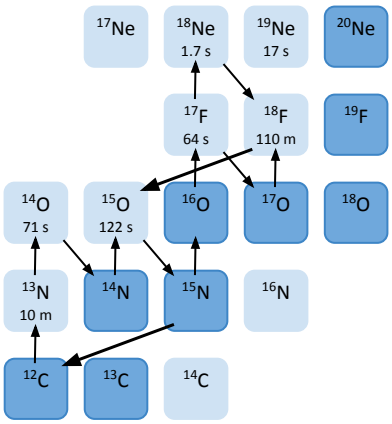

Figure 1.4: Hot CNO cycles. There are 3 different cycles that burn four protons into one helium nucleus. In this context, the proton capture is faster than the beta decay. This makes the HCNO process beta limited, conditioned by the half life of each radioactive isotope participating in the process.

capture on ^{13}N is more likely than its beta-decay, as ^{13}N has a half life of about 10 minutes and the higher temperatures lead to faster proton captures on ^{13}N than beta decays. In this case ^{14}O is created, but ^{14}O is not able to capture a further proton, as ^{15}F is proton unbound (it decays immediately to ^{14}O + p). The same applies to ^{15}O, as ^{16}F is also proton unbound. This cycle is therefore limited by the beta decay of ^{14}O and ^{15}O. The half-lives of ^{14}O and ^{15}O are on the order of 100 of seconds as shown in figure 1.4.

Helium burning

The triple-α process burns helium into carbon. This also happens on the surface of the neutron star, providing seeds for the subsequent proton and alpha captures that lead to the X-ray burst production. The key point is a narrow resonance at around 7.6 MeV that enhances the triple alpha fusion reaction [TN09]. This was predicted by Hoyle in the 1950s [Hoy53; Hoy54]. This prediction was also explicitly referenced in [Dun53]. The triple-α is a two step process where two α particles interact close enough to populate ^{8}Be in its ground state. This beryllium isotope is known to be unstable, having a lifetime on the order of 10^{-16} s which is three orders of magnitude longer than if the two alpha particles scattered in a non resonant way [Cla68]. This leads to a small concentration of unstable ^{8}Be building up in the plasma until it reaches equilibrium. The concentration of ^{8}Be in equilibrium is high enough [Rol88] for an additional alpha capture to happen creating ^{12}C.

$$\begin{aligned} \alpha + \alpha &\rightleftharpoons {}^{8}\mathrm{Be} \\ \alpha + {}^{8}\mathrm{Be} &\rightleftharpoons {}^{12}\mathrm{C}^{*} \end{aligned}$$

This second stage of alpha capture needs to populate the resonant state at 7.654 MeV in ^{12}C which has a big probability to break up again into the ^{8}Be + α. However, there is a small probability of about 0.04% where the ^{12}C resonance decays emitting γ-rays [Eri20].

Some ^{12}C nuclei will also capture an alpha particle, creating ^{16}O, but further alpha captures do not happen in stellar helium burning due to the higher Coulomb barriers and the fact that the alpha capture on ^{16}O is a non resonant reaction, and its cross section is in the range of nanobarns. The cross section for higher resonant levels start to be significant for temperatures from 0.3 GK, corresponding to very massive stars and to explosive scenarios.

αp-process

This process takes place in explosive scenarios where helium seeds are abundant. Explosive scenarios are necessary for the temperature to be high enough to overcome the coulomb barrier. Here, (α,p) reactions are taking place in competition with β^{+}-decays producing heavier elements in the range of mass 20-40. This process is found to connect the breakout from the HCNO

cycle with the rp-process. In this case there is a dependency with temperature, determining the timescale of the reaction flow up to A=36 [FST07]. Within this process there are a few waiting points that may be of importance for the X-ray bursts.

rp-process

Lastly, the rp-process is found in explosive scenarios with a high hydrogen content. When hydrogen rich material reaches high temperatures a series of rapid proton captures and (α, p) reactions are activated leading to the synthesis of heavy elements (up to A = 100). This process involves a competition between proton captures and beta decays. The proton dripline is relatively close to stability, and proton captures are subject to Coulomb barriers. It also depends on the peak temperature of the plasma. There are waiting points at the drip line where photodisintegration and proton unbound isotopes beyond the dripline act as a barrier for further proton captures [Rau20] as also found in the case of ^{14}O and ^{15}O in the HCNO cycle.

1.1.3 Binary systems and X-ray bursts

Looking back at stellar formation, when a massive cloud contracts, thousands of stars will be formed from it. The reason lies on the Jeans criterion (eq. 1.2) and the conditions of the molecular gas. As the cloud contracts and the density increases, many parts of the cloud will fulfil the Jeans criterion. These regions can fragment into individual collapsing clouds if they experience any anisotropies. From this event many stars born at a similar time will be close enough to interact with each other, forming binary systems.

Only a small percentage of the binaries are close enough to experience an interaction. In these close binary systems composed of two stars of different mass, a equipotential surface called the Roche surface (or Roche lobe) is defined shaped as a figure of 8 around the two stars. Any particle on that surface is equally attracted by both stars and it could go to either star. When one of the stars begins to expand reaching its red giant phase, it might expand beyond the Roche lobe and part of its envelope will be transferred to the second star. There are different scenarios of evolution of these binary systems that will depend on their composition.

A particular binary system, formed by a neutron star from the remnant of a dead star and a sun-like star in its red giant phase, such as the example given in figure 1.5, is the object of study in this dissertation. Neutron stars are highly dense objects that create very powerful gravitational fields. The neutron star will absorb matter from its companion's envelope forming an accretion disk from the gas spiraling onto its surface. This material is mainly composed of fresh hydrogen and helium, and it is accelerated to extremely high velocities.

The fresh hydrogen and helium fall onto the neutron star's atmosphere, which starts com-

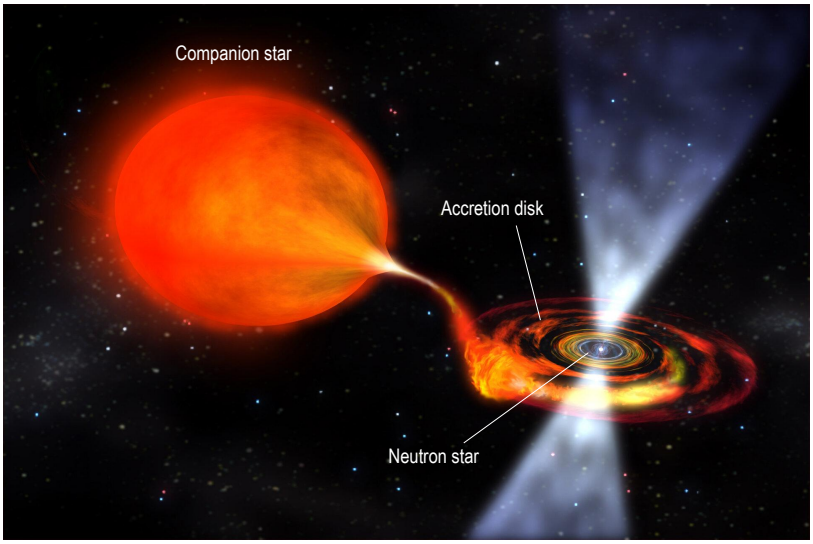

Figure 1.5: Artistic view of a neutron star and a giant star in a binary system. The neutron star is accreting material from its companion and an accretion disk is formed. Image credit: ESA.

pressing and heating up. When the temperature and density conditions are high enough, the triple-α process is activated burning He into C and producing seeds for the CNO cycles. The freshly accreted hydrogen burns via the HCNO cycle at a constant rate. These reactions heat even more the neutron star atmosphere increasing further the fusion rates. After some time the material starts to pile-up in the ^{14}O and ^{15}O waiting points, a consequence of their long lifetimes of about two minutes and the fact that the ^{15}F and ^{16}F are proton unbound isotopes. This means that as soon as ^{14}O or ^{15}O capture a proton, they decay immediately, and ^{15}F and ^{16}F cannot be formed. As the HCNO cycle is heating the atmosphere, the conditions reach the point where α particles have been produced or accreted enough and the pressure and temperature conditions produce the ignition of a thermonuclear runaway through the α capture reactions on ^{15}O and ^{18}Ne. These two are considered the main breakout points. Prior to the present work, it is believed that the ^{15}O$(\alpha,\ \gamma)^{19}$Ne is the dominant reaction for temperatures up to 0.6 GK and that for higher temperatures the ^{18}Ne$(\alpha,\ p)^{21}$Na dominates the breakout. In this dissertation the focus is on the α capture on ^{15}O. Under these explosive conditions of temperature and pressure, ^{19}Ne will mostly capture a proton, against its beta decay. This fact leaves the ^{15}O + α reaction rate to be the bottleneck between the HCNO cycle and the rp-process [Fis06].

Bursts of X-rays are emitted periodically during this thermonuclear runaway, with periods from a few seconds to days [Rol88; Cyb16]. Light curves from the emitted X-rays are the main direct observable of the bursts, and they were first observed in 1976 [Gri76].

As stated before in section 1.1.2, many nuclear processes are involved in the production of the bursts: the triple-α process, the αp-process and the rp-process; involving isotopes from stable nuclei to exotic species close to the proton drip line. Hence, understanding and constraining the reaction mechanisms involving this breakout should be complemented by other studies of the many nuclear reactions taking place. Models predicting light curves for the X-ray bursts need reliable nuclear physics results to constrain parameters such as composition or accretion rate, so that models can be compared with the observed light curves. The present work is focused on measurement of the most important reaction in this context: ^{15}O(α, γ)^{19}Ne.

1.2 Previous work and relevant results

Since the discovery of X-ray bursts more than 40 years ago, there have been many different studies trying to determine the astrophysical sites where these events occur as well as the ignition mechanism that could explain the frequency and luminosity of the bursts.

As explained in section 1.1.3, X-ray bursts are thermonuclear explosions that take place on the surface of a neutron star in a binary system. The ^{15}O(α, γ)^{19}Ne reaction is believed to be the main breakout route from the HCNO cycle leading to the creation of heavier elements by the ignition of the rapid-proton capture process. It regulates the flow between the HCNO cycle and the rp-process. For this reason, this reaction has been the focus of great interest.

1.2.1 Sensitivity studies

For the study of the X-ray burst mechanism a number of models predicting different bursting behaviours have been proposed [CN05; CN07; MMM19; Par13]. As the material created in the bursts is gravitationally bound to the NS, the only observable available is the light curves produced. The models also include the accretion rate of the material from the companion star to the NS and the composition of the accreted matter. The experimental study of reaction rates is very important because of their implementation in these models. It is especially important to constrain the uncertainties of these measurements [Dav11].

To assess the significance of these uncertainties, there have been many sensitivity studies [Cyb16; Par13; PJS14] determining which reactions have a strong impact on the X-ray bursts light curves. Rates of most of the nuclear reactions involved in this process haven't been fully determined experimentally, and the rates of some specific reactions are directly related to the intensity of the light curve. Therefore their uncertainties need to be reduced to implement them in the models. In this, the ^{15}O(α, γ)^{19}Ne reaction has been identified as the most important

Rank	Reaction	Variation	Sensitivity ($\times 10^{38}$ erg)
1	^{15}O(α, γ)^{19}Ne	10 (Dn)	16
2	^{56}Ni(α, p)^{59}Cu	100 (Up)	6.4
3	^{15}O(α, γ)^{19}Ne	100 (Dn)	5.1

Table 1.1: Reactions that impact the burst light curve in the Multi-zone X-ray burst model performed by Cyburt *et al.* This table shows the sensitivity and variation (up or down) parameters taken from tables 2 and 3 in [Cyb16]. The sensitivity defined by Cyburt *et al.* as $M_{LC}^{(i)}$ is calculated as the area between the varied curve and the baseline model.

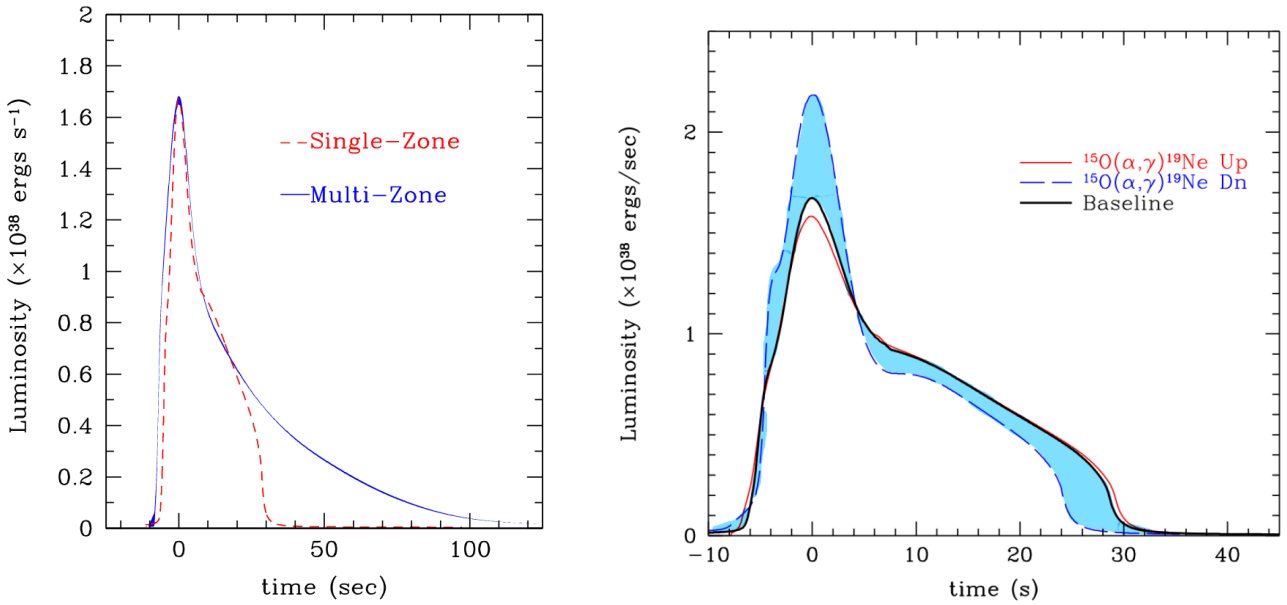

(a) (b)

Figure 1.6: (a) Comparison between the light curves obtained from the single-zone and the multi-zone models used by Cyburt *et al.* [Cyb16]. (b) Light curve obtained using the single-zone model. Modifying the ^{15}O + α reaction rate up or down has a strong impact on the luminosity of the X-ray burst, especially if the rate is lower than previously assumed (adapted from [Cyb16]).

reaction.

Table 1.1 shows the three most important reactions identified by Cyburt *et al.* [Cyb16], where they used a single-zone and a multi-zone X-ray burst model to determine the sensitivity. They defined this sensitivity as $M_{LC}^{(i)} = \int |< L_i(t) > - < L_0(t) >| \, dt$, where $L_i(t)$ is the light curve for each variation and $L_0(t)$ is the luminosity from a baseline model. In figure 1.6a Cyburt *et al.* [Cyb16] show a comparison between the baseline curves obtained from the single-zone (dashed red line) and the multi-zone (solid blue line) models. Figure 1.6b shows how the variation of the ^{15}O + α reaction rate affects the light curve of the bursts for the single-zone model. It also shows the sensitivity for the reaction rate decreased by a factor of 10, determined by the total area enclosed between the varied curve (dashed blue line) and the baseline curve (solid black line), which corresponds to the coloured area in figure 1.6b. The ^{15}O + α capture reaction has a sensitivity 2.5 times higher than the second most important reaction, ^{56}Ni(α, p)^{59}Cu.

1.2.2 Experimental studies of ^{15}O(α, γ)^{19}Ne

The ^{15}O(α, γ)^{19}Ne reaction rate is dominated by the contribution of the ^{19}Ne $\frac{3}{2}^+$ excited state at 4.033 MeV corresponding to a p-wave, with the second most important resonance being the $\frac{7}{2}^+$ state at 4.379 MeV corresponding to an f-wave [WGS99]. The different contributions of the states to the reaction rate are shown in figure 1.7, where the most recent results from Tan *et al.* are shown at the top half. The 4.033 MeV state dominates up to $T_9 = 0.6$ K, where T_9 is the temperature expressed in units of GK. This temperature corresponds to explosive scenarios. For higher temperatures other resonances are dominant, as well as the second main breakout point from the HCNO cycle ^{18}Ne(α, p)^{21}Na.

Several experimental studies have been performed to determine the properties of the ^{19}Ne unbound states to extract the reaction rate and to determine the α width of the states that contribute the most to the reaction rate. In particular, the reaction rate of the 4.033 MeV ^{19}Ne excited state has been very challenging to measure. The different results obtained so far have provided upper limits and results with very big uncertainties. A summary of the different studies of the ^{15}O + α reaction is given in this section.

The experimental studies were focused on determining the α partial width Γ_α, or the branching ratio $B_\alpha = \frac{\Gamma_\alpha}{\Gamma_t}$, where $\Gamma_t = \frac{\hbar}{\tau}$ is the total width of the level and τ is its mean life. The alpha branching ratio measures the percentage of decays emitting an α particle. This alpha partial width is the key astrophysical property, as the reaction rate is calculated using the Γ_α of the populated resonances. More details on its calculation are given in chapter 2.5.

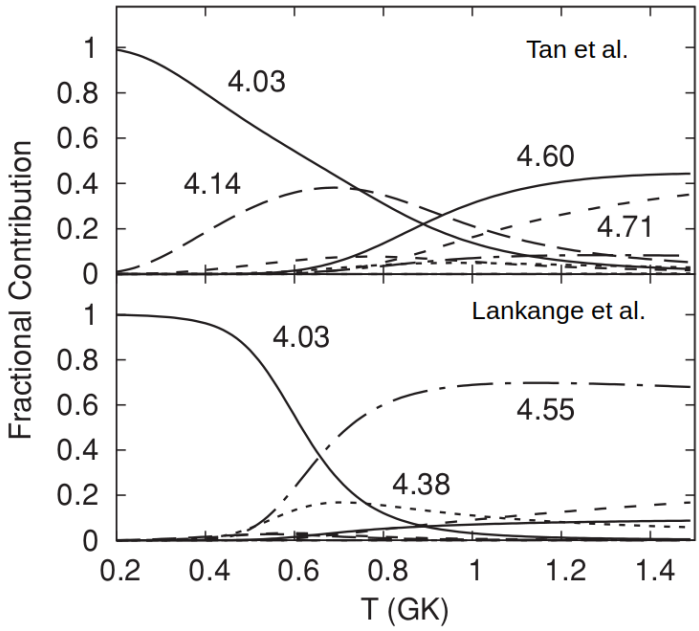

Figure 1.7: Relative contribution to the reaction rate for relevant states obtained by Tan *et al.* [Tan09] (top) and by Lankange *et al.* [Lan86]. The most recent results are the ones obtained by Tan *et al.* This plot has been taken from [Tan09].

This breakout route was first studied by Lankange *et al.* [Lan86] where they estimated the $^{15}O(\alpha, \gamma)^{19}Ne$ and the $^{19}Ne(p, \gamma)^{20}Na$ reaction rates. They also pointed out that the $^{19}Ne + p$ reaction is quicker than the previous $^{15}O + \alpha$ capture reaction, the $^{15}O + \alpha$ reaction therefore being the determining reaction of the overall breakout probability.

Magnus *et al.* studied the $^{19}F(^{3}He, t)^{19}Ne$ reaction, populating the ^{19}Ne resonant states above the α threshold, and determining their B_α [Mag90]. However, this experiment was not sensitive enough to detect the α decay of the 4.033 MeV excited state.

An upper limit on the branching ratio B_α for this state was extracted by Laird *et al.* [Lai02] using a $d(^{18}Ne, ^{19}Ne)p$ reaction, followed by a second upper limit done by Davids *et al.* [Dav03] using the $^{21}Ne(p, t)^{19}Ne$ reaction. Rehm *et al.* [Reh03] were also able to provide an upper limit populating the 4.03 MeV state, in this case using the $^{3}He(^{20}Ne, \alpha)^{19}Ne$ reaction. However, none of these experiments were sensitive enough to measure the branching ratio of this state, expected to be $\sim 10^{-4}$.

A few years later, Tan *et al.* [Tan09] performed a new measurement of the $^{19}F(^{3}He, t)^{19}Ne$ reaction populating the α unbound states. They measured the 4033 keV state branching ratio to be $B_\alpha = (2.9 \pm 2.1) \cdot 10^{-4}$ at 1σ statistical confidence level. The confidence level (C.L.) represents the probability of having a result that lies within the confidence region defined

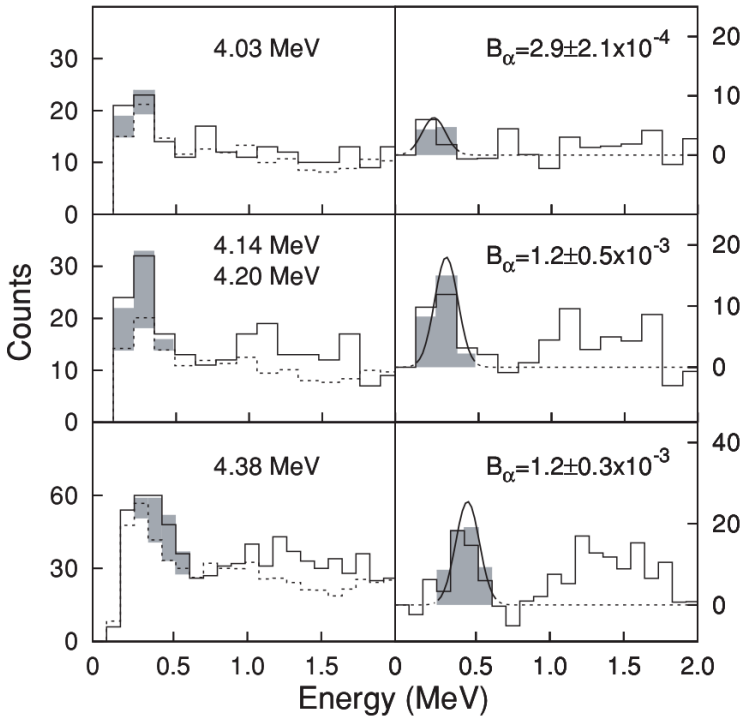

Figure 1.8: Coincident α energy spectra results from Tan *et al.* [Tan09]. The left side shows total number of counts (solid line) and total background estimation (dashed line). The right side shows number of events after background deduction.

around a certain mean value μ and standard deviation σ. In the case of 1σ C.L. the result will be within a region defined as $(\mu - \sigma, \mu + \sigma)$, with 68% probability. In figure 1.8 we can see their number of counts before (left) and after (right) background suppression. They obtained for the 4.033 MeV state 8 counts above their background (dashed line) of $N_{bck} = 36$ counts. The assumption they made was that their background prediction in their spectrum is exact, not taking into account the systematic uncertainty in determining the 36 count background level, and only assuming statistical fluctuations and $N_{back} = 36$. Considering their data, they obtained $\sigma_{bck} = 6$ and 8 events. The number of counts is therefore 1.3σ above the background. Therefore, their result places zero counts within a 90% single-sided C.L. This is consistent with their result of $(2.9 \pm 2.1) \cdot 10^{-4}$, which is consistent with zero at 1.4σ C.L. A summary of the B_α results from the different experiments discussed above is given in table 1.2.

Other important properties of the ^{19}Ne unbound states have been studied as well. Of great importance for this work is the extraction of the lifetime of the 4.033 MeV excited state. Some experiments using the Doppler shift attenuation method have been performed in the past [Tan05; Kan06; Myt08] where this lifetime was measured. A Monte Carlo method was used in [Gla19] to simulate the Doppler broadening of ^{19}Ne γ-rays and compare to the experimental

	B_α			
Ex (keV)	[Lai02]	[Dav03]	[Reh03]	[Tan09]
4033	< 0.01	$< 4.3 \cdot 10^{-4}$	$< 6 \cdot 10^{-4}$	$(2.9 \pm 2.1) \cdot 10^{-4}$
4140	< 0.01			$(1.2 \pm 0.5) \cdot 10^{-3}$ [a]
4197	< 0.01			$(1.2 \pm 0.5) \cdot 10^{-3}$ [a]
4379		$< 3.9 \cdot 10^{-3}$	0.016 ± 0.005	$(1.2 \pm 0.3) \cdot 10^{-3}$

[a] Combined B_α using 4.14 and 4.2 MeV levels

Table 1.2: α branching ratios for the ^{19}Ne levels above the α threshold from the most recent experiments.

data, obtaining also results for the lifetime of the bound excited state at 1507 keV, however no new results were obtained for the 4033 keV excited state or any other α unbound state. A summary of the past lifetime measurements is shown in table 1.3. It is worth noting, however, that for the 1507 keV state there is a 2σ discrepancy between [Tan05] and [Gla19].

The lifetime of the 4033 keV state has been recently calculated [Tan05], [Kan06] but with the result of Mythili *et al.* [Myt08] it is not longer a dominant uncertainty for Γ_α. A result of the partial width equal to $\Gamma_\alpha = 24 \pm 18$ μeV [FLS10] was obtained combining the effort of the previous work [Tan05; Kan06; Tan07; Myt08; Tan09]. However, this result has a big uncertainty and the measurements were consistent with zero at 90% C.L. Based on the current available data the factor of 10 (Dn) variation used in the sensitivity studies [Cyb16] is consistent with the current experimental uncertainties. The main limitation that has delayed the improvement of this data is the selectivity of the events and the background suppression due to the low count rates. In the present project, the background suppression was excellent and the setup performance achieved an outstanding selectivity.

After considering these first attempts to measure the 4.033 MeV state it is clear that more precise measurements of the branching ratios - or more directly of Γ_α - are necessary to determine the importance of this reaction in X-ray Bursts.

		τ_m (fs)			
Ex (keV)	Eγ (keV)	[Tan05]	[Kan06]	[Myt08]	[Gla19]
275.1	275.1				
1507.5	1232.5	1.7±0.3 ps			$4.3^{+1.3}_{-1.1}$ ps
1536	1297.7	16 ±4		19.1±1.1	
4033	4033	13^{+9}_{-6}	11^{+4}_{-3}	7.1±1.9	
4140	2632	18^{+2}_{-3}		$14^{+4.2}_{-4.0}$	
4197	2689.5	43^{+12}_{-9}		38^{+20}_{-10}	
4379	4140	5^{+3}_{-2}		$\leq$5.4	

Table 1.3: Lifetimes for different levels of ^{19}Ne from most recent experiments, and the energy of most intense transition for each state.

Chapter 2

Nuclear theory

In this chapter the theoretical ingredients necessary to understand the present work are given. This work studies a nuclear transfer reaction, which is a direct process where the nuclear properties play an important role. A brief introduction of the nuclear shell model, direct reactions and the method used to extract the spectroscopic factors and calculate the partial widths of the unbound states under study is given below.

2.1 Nuclear shell model

One of the most common models used to explain the nuclear properties is the shell model. It is similar to the atomic shell model in the way that the nucleons are located in energy shells following Pauli's principle, which says that two fermions cannot have the same quantum numbers. It was observed experimentally that for certain numbers of protons or neutrons, there was an increase of the energy necessary to separate a nucleon from the core. Also, it was observed that some configurations presented nucleons less strongly bound in the nucleus compared with the nucleons located in lower energy levels [Hey94]. This separation energy (S_p, S_n) was maximum at the so-called *magic numbers* where strongly bound configurations were found. These configurations could not be explained by the more simple liquid drop model [Kra88].

The nucleons in the nucleus can be described as independent particles moving in single particle orbits. The shell model assumes that nucleons are affected by a central potential where they feel a central force that comes from the interaction with the rest of the nucleons [RS80]. This model is described using a Woods-Saxon central potential:

$$V_{WS}(r) = \frac{-V_0}{1 + \exp[(r - R)/a]}, \tag{2.1}$$

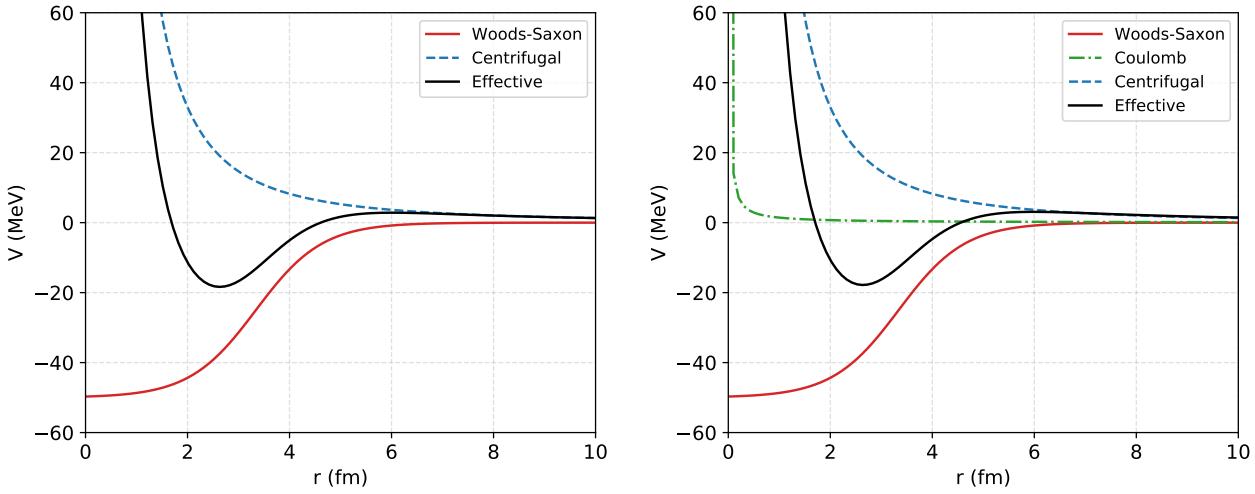

(a) Neutron

(b) Proton

Figure 2.1: Representation of the effective potential V_{nuc}, its Woods-Saxon contribution V_{WS} (red) describing the nuclear charge density distribution, and its centrifugal contribution $\frac{l(l+1)\hbar^2}{2\mu r^2}$ (blue). (a) For the unpaired neutron in ^{19}Ne assuming it to be in the $d_{3/2}$ orbital. (b) If the particle is a proton, the Coulomb interaction needs to be included. The Woods-Saxon contribution has been calculated using the standard parameters $V_0 = 50$ MeV, $r_0 = 1.25$ fm and $a_0 = 0.65$ fm.

where R is the nuclear radius normally describing the nucleus as a sphere with constant density $R = r_0 A^{1/2}$, a is the diffuseness parameter and V_0 is the depth of the potential well. This potential represents the charge density distribution in the nucleus, and its shape is shown in figure 2.1.

The Coulomb potential also plays a role in the description of the nucleus, because each proton creates a Coulomb force that is felt by the rest of the protons. This interaction can be described as the potential field created by a homogeneous charged sphere $V_C(r) = \frac{Ze^2}{r}$, and it introduces a Coulomb barrier of energy $E_C = 1.44\frac{Z_1 Z_2 e^2}{r}$ MeV, where Z_1, Z_2 are the atomic numbers of the nucleus and the nucleon involved. Due to the interaction between protons, the Coulomb potential adds a shift in the proton energy levels towards higher values with respect to the neutron energy levels. In order to completely describe the observed nuclear properties and the *magic numbers*, it was also necessary to introduce the spin-orbit interaction, that accounts for the coupling of the orbital angular momentum and the spin. This term is a result of the spin–orbit dependence of the strong nuclear force and leads to a reordering of energy states especially for larger orbital angular momentum, l [Rau20]. The spin-orbit term effectively introduces the total angular momentum (j) as a result of the coupling and described by $|l - s| \leq j \leq l + s$, splitting the energy levels. Any nucleon has by definition a spin $s = 1/2$,

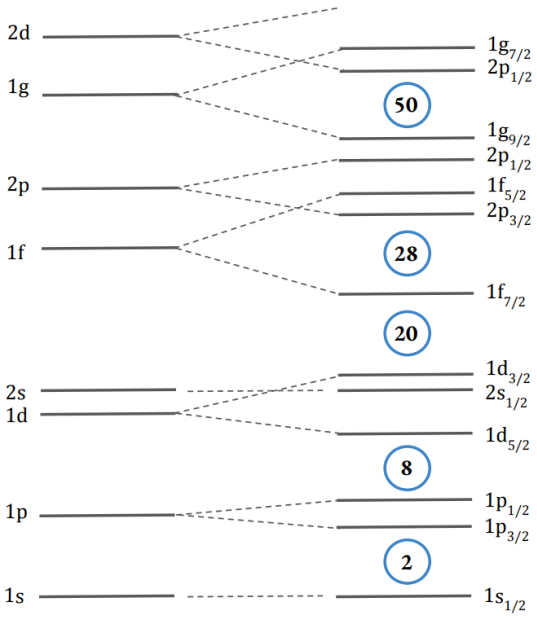

Figure 2.2: Shell model scheme showing the split of the energy levels from the spin-orbit term. Experimental evidence indicates that the ground state is a $J^{\pi} = \frac{1}{2}^{+}$. This places the unpaired neutron on the $2s_{1/2}$ level, instead of in the $1d_{5/2}$.

therefore the spin-orbit term will split the energy levels into two, defined by a total angular momentum $j = l \pm \frac{1}{2}$, and as can be seen in figure 2.2. Thus the nuclear shell model can be described by an effective potential composed of three different components:

$$V_{nuc}(r) = V_{WS}(r) + V_{l\cdot s}(r) + V_C(r), \tag{2.2}$$

where V_{WS} is the Woods-Saxon central potential, $V_{l\cdot s}$ is the spin-orbit term and V_C is the Coulomb interaction. Another important effect to include in the description of the nucleus is the centrifugal barrier, which describes the interaction of the relative angular momentum of the nucleon and the nucleus itself. This centrifugal effect depends on the orbital angular momentum l and it can be calculated as a function of the distance r following $\frac{l(l+1)\hbar^2}{2\mu r^2}$. Figure 2.1 shows the different contributions to the effective potential V_{nuc} for a nucleon in the $d_{3/2}$ orbital. The spin-orbit term is not represented because its effect is very small in comparison to the other terms. In the neutron case (a) the effective potential includes V_{WS} and the centrifugal term. In the proton case (b) the Coulomb term is also included. Using this effective potential to solve the Schrödinger equation gives a result that matches the experimental data and places larger energy gaps between the nuclear shells at the positions required to reproduce the magic numbers of nucleons as can be seen in figure 2.2.

The shell model also explains other nuclear properties besides the nuclear structure, such as the spin-parity of the ground state for even and odd nuclei, the excited states and predictions of the energy levels especially for light nuclei and nuclei close to the valley of stability. However, this model is not perfect and other nuclear properties cannot be explained by it, for example the nuclear deformation needs a more powerful formalism. Yet this model is a very good approximation to understand the work done in this dissertation.

2.1.1 Nuclear structure of neon-19

Studying the population of the excited states of ^{19}Ne allows the determination of structural properties such as the total and partial widths of the levels. A shell model scheme of ^{19}Ne in its ground state is shown in figure 2.3. It has a pair of protons in the *sd* shell and a single neutron also in the *sd* shell. The experimental evidence suggests that the neutron is located in the orbital $s_{1/2}$, and that the $d_{5/2}$ is at a higher energy corresponding to the first excited state.

This project aims to determine the missing properties of the states above the α energy threshold. The α separation energy corresponds to $S_\alpha = 3529$ keV. The excited states above this energy are unbound states or resonant states. They will decay either through α emission or γ decay. The proton and neutron separation thresholds are at higher energies, so proton and neutron emission is not energetically allowed. Figure 2.4 shows the energy levels in ^{19}Ne (right), both α bound and α unbound states of interest are represented. The spin-parities, excitation energies and lifetimes are in some cases known. However, there are still important properties that have not been measured. Information about the most recently measured properties is given in section 1.2.

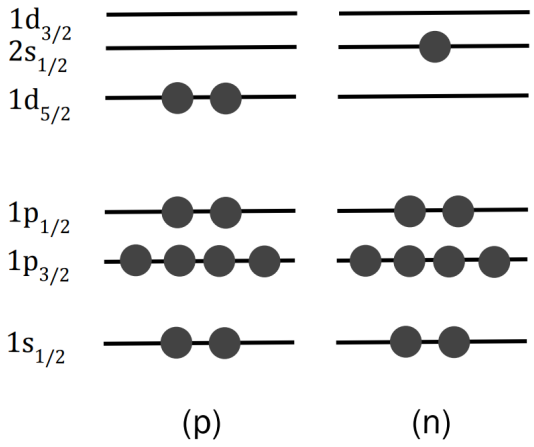

Figure 2.3: Shell model configuration of ^{19}Ne in its ground state.

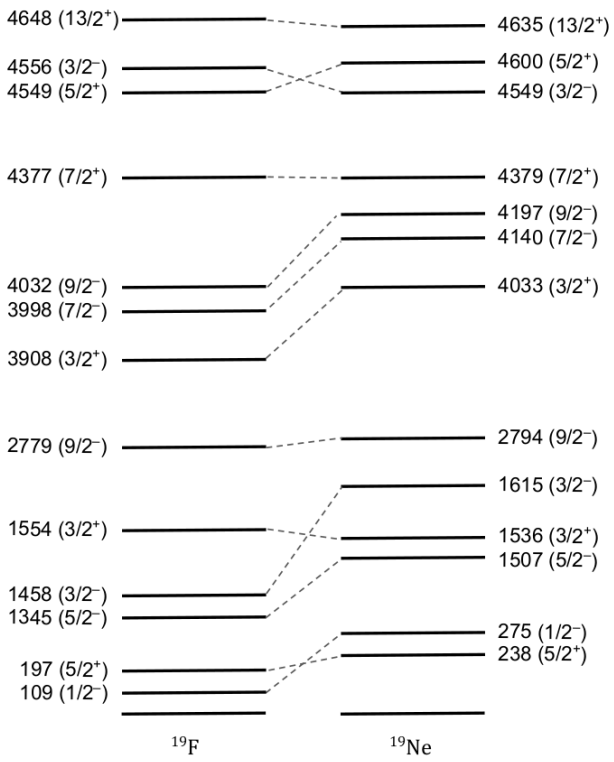

Figure 2.4: Scheme showing a comparison of the level structure of ^{19}F (left) and ^{19}Ne (right). The energies are given in keV. The mirror states are connected by the dashed lines.

The main level to study in this work is the excited state at $E_x = 4033$ keV, which is believed to be the main contributor to the α capture reaction rate. The other levels just above will be also investigated, in particular the ^{19}Ne excited states at $E_x = 4140$ keV and $E_x = 4197$ keV.

2.1.2 Comparison with the mirror nucleus, fluorine-19

Mirror nuclei of low mass are found to have a symmetric structure showing analog states. This fact is advantageous when the properties of a given nucleus are not completely known. This is the case of ^{19}F and ^{19}Ne. Both present similar properties in their states, with the advantage of ^{19}F being stable and well known [Oli97]. The analog states in the mirror nucleus are an indication of the expected properties for the states studied in the present. From the mirror investigations some constrains to the expected results can be made. The corresponding mirror states are also shown in figure 2.4 (left). It is also useful to compare the differential cross sections obtained for the mirror states as it is directly linked to the angular momentum in our direct reaction measurement (see section 2.3). It is furthermore a good benchmark for the theoretical calculations which will be necessary to obtain the spectroscopic factors.

2.2 Reaction cross section and reaction rate

In the stellar environment nuclear reactions take place with a probability that is given by different factors. The particles in the plasma are moving according to the Maxwell-Boltzmann distribution that depends on its average thermal energy $k_B T$. The shape of this distribution is shown in figure 2.5. Nuclear reactions are taking place in this environment with a probability that is given by the reaction cross section and the kinetic energy of the particles involved. At these temperatures the reactions are called thermonuclear reactions. The cross section determines how often a given reaction happens and it is given by

$$\sigma = \frac{N_{int}}{Y_T \cdot N_{tar}}, \tag{2.3}$$

where N_{int} is the total number of interactions, $Y_T = I \cdot t$ is the total number of projectiles coming at an intensity I in a given time t, and N_{tar} is the number of target particles per unit of area.

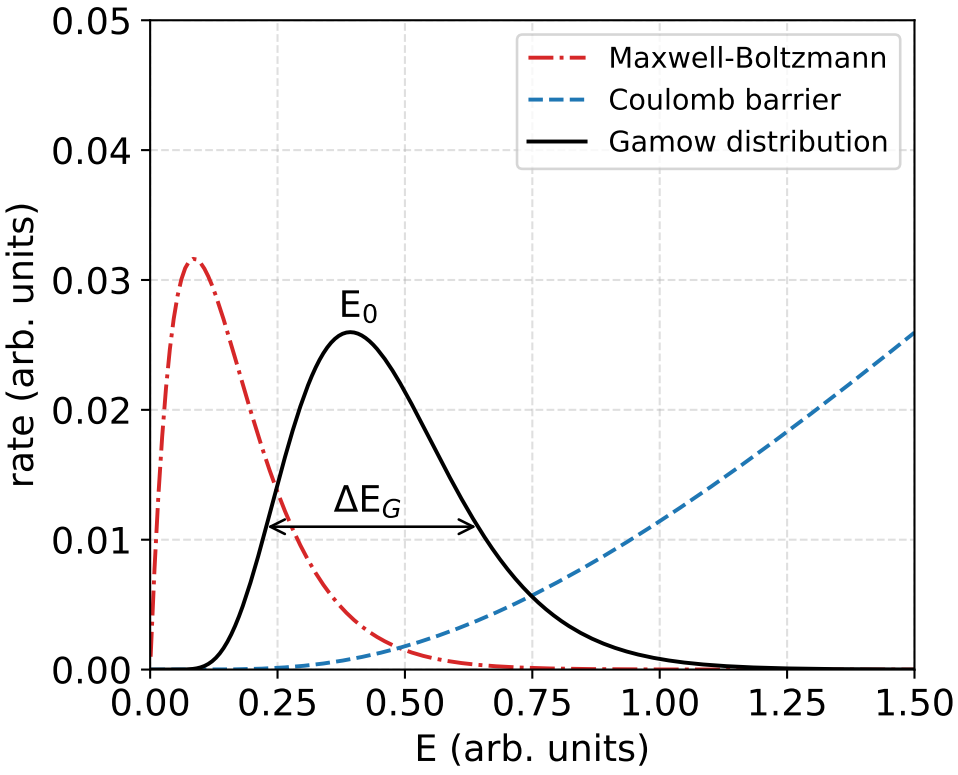

Figure 2.5: Maxwell-Boltzmann, Coulomb penetrability and Gamow distributions. The Gamow distribution has a peak energy given by E_0 and a width given by ΔE_G.

The excited states are given by the solution of the Schrödinger equation for the binding potentials, and these solutions are discrete, meaning that there is a defined number of bound states. When the binding potentials are too weak to bind a particle to the core or when the nucleus is highly excited, the populated states become unbound. There is a continuum dominated by scattering above this separation energy threshold. In this continuum there are certain energy values where the interaction between two particles is stronger and a nuclear reaction is particularly favoured, populating states known as resonant states. These states are nearly-bound because the interacting particles are trapped together inside a potential barrier for some time given by the lifetime of the state (τ). A resonance is described by its spin and parity J^π, its energy E_r and its width $\Gamma = \frac{\hbar}{\tau}$. For a radiative α capture reaction, below the proton and neutron thresholds, there are two contributions to the total width $\Gamma_{tot} = \Gamma_\alpha + \Gamma_\gamma$ where Γ_α, Γ_γ are the partial contributions from the α emission and from the γ decay respectively. Details on how to determine the partial width will be given in section 2.5.

For the case of an α particle interacting with a ^{15}O nucleus, the α particle will feel the central potential V_{WS} created by the oxygen nucleus, the centrifugal force, according to the angular momentum of the α particle, and the Coulomb barrier. As opposed to the nucleon shell model, there is no spin-orbit term in the α potential, as the α particle has a spin of zero. In figure 2.6 the different contributions to the effective potentials are shown, along with the resonance energy at 504 keV above the α threshold. The effective potential includes a barrier that the α particle needs to penetrate. The probability of tunneling thought this barrier is given by the penetrability $P_l(r,\ E_r)$, and it is included in the calculation of Γ_α (see section 2.5).

When a resonance does not overlap with any other close resonances it is considered to be isolated. If its partial width is approximately constant over the total resonance width, or if Γ less than a few keV, a resonance is called narrow [Ili08]. The cross section for narrow resonances is given by the Breit-Wigner expression:

$$\sigma(E) = \frac{\lambda^2}{4\pi}\frac{2J_r+1}{(2J_1+1)(2J_2+1)}\frac{\Gamma_\alpha\Gamma_\gamma}{(E_r-E)^2+\left(\frac{\Gamma(E)}{2}\right)^2}, \tag{2.4}$$

where λ is the de Broglie wavelength of the resonance, J_r is its total angular momentum, J_1, J_2 are the total angular momenta of the target and projectile involved in the reaction, Γ_α and Γ_γ are the partial widths of the different decays, E_r is the resonance energy and E is the energy of the particle [Ili08]. It shows a peak at $E \sim E_r$ as expected, with a full width at half maximum given by Γ.

Depending on the stellar conditions, the reaction rate varies. A given nuclear reaction will

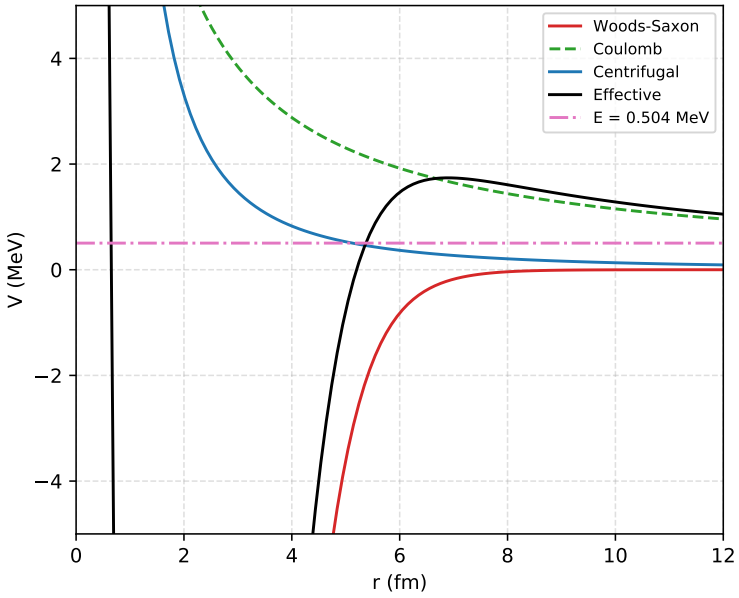

Figure 2.6: Potentials of the $^{15}O + \alpha$ system. Here, the α particle will feel the effective potential (solid black line). The contributions to the effective potential are the Woods-Saxon potential (solid red line), the Coulomb potential (dashed green line) and the centrifugal barrier (solid blue line) which will depend on the orbital angular momentum (l). The horizontal dashed pink line corresponds to the resonance energy at $E_r = 0.504$ MeV.

be more probable for certain energies and therefore temperatures. There is an effective burning energy given by the product of the thermal distribution and the probability for penetration through the Coulomb barrier. This distribution shows a peak $E_0 = 1.22 \cdot (Z_1^2 Z_2^2 \mu T_6^2)^{1/3}$ known as the Gamow peak and a width $\Delta E_G = 0.749 \cdot (Z_1^2 Z_2^2 \mu T_6^5)^{1/6}$, both given in MeV, and where Z_1, Z_2 are the atomic numbers of the reacting particles, μ is the reduced mass and T_6 is the plasma temperature given in MK. It defines a region of energies in which nuclear reactions are more probable to occur for a given temperature. This region is know as *Gamow window* and it is defined by $E = E_0 \pm \frac{\Delta E_G}{2}$ [Rau20]. The Gamow window will also determine the range of resonances most likely to be populated. The three different distributions are plotted in figure 2.5, where the Gamow energy and the Gamow window are also shown.

This Gamow peak arises directly from the reaction rate, since it comes from the product between the Maxwell-Boltzmann term $\left(E \exp\left(\frac{-E_r}{k_b T}\right)\right)$ in equation 2.5 and the penetrability, which is included in the Γ_α term of $\sigma(E)$, defined in equation 2.4. The reaction rate $N_A \langle \sigma v \rangle$ determines how strong a particular reaction is for a given plasma temperature, and it varies

with the temperature. The reaction rate can be calculated from the cross section using

$$N_A \langle \sigma v \rangle = \left(\frac{8}{\mu \pi} \right)^{1/2} \frac{1}{(k_b T)^{3/2}} \int_0^\infty \sigma(E) E e^{\frac{-E_r}{k_b T}} dE, \tag{2.5}$$

where μ is the reduced mass, k_b is the Boltzmann constant, T is the temperature, $\hbar$ is the reduced Planck constant $\frac{h}{2\pi}$, $\sigma(E)$ is the cross section given by equation 2.4 and E_r is the resonance energy. The reduced mass is calculated following

$$\mu = \frac{m_1 m_2}{m_1 + m_2}, \tag{2.6}$$

where m_1, m_2 are the atomic masses of the particles involved in the reaction. When the reaction is dominated by narrow resonances, the total reaction rate will have a contribution for each individual resonance. The contribution to the reaction rate from the individual resonances will be given by

$$N_A \langle \sigma v \rangle = N_A \left(\frac{2\pi}{\mu k_b T} \right)^{3/2} \hbar^2 (\omega\gamma) e^{\frac{-E_r}{k_b T}}, \tag{2.7}$$

where $\omega\gamma$ is the resonance strength.

The resonance strength of a level is given by the widths of the different decay channels that the level presents. To determine the reaction rates it is therefore necessary to know the angular momentum and the partial widths of each resonance. The resonance strength $\omega\gamma$ is given by the spin factor and the reduced widths:

$$\omega\gamma = \frac{2J_r + 1}{(2J_1 + 1)(2J_2 + 1)} \frac{\Gamma_\alpha \Gamma_\gamma}{\Gamma_\alpha + \Gamma_\gamma}, \tag{2.8}$$

where J_r is the angular momentum of the populated resonance, J_1 is the angular momentum of the projectile, J_2 is the angular momentum of the target, Γ_α is the partial width corresponding to the α emission and Γ_γ is the partial width of the γ emission. Resonances are defined as narrow either when $\Gamma_\alpha << \Gamma_\gamma$, or when $\Gamma_\alpha < \Gamma_\gamma$ and $\Gamma_\gamma <<$keV. In the case of narrow resonances deep below the Coulomb barrier $\Gamma_\alpha << \Gamma_\gamma$. Here, the contribution to the total width from Γ_α can be neglected, and the total width can be expressed as $\Gamma_{tot} = \Gamma_\alpha + \Gamma_\gamma \simeq \Gamma_\gamma$. The resonance strength for our narrow resonances of interest can be expressed as:

$$\omega\gamma = \frac{2J_r + 1}{(2J_1 + 1)(2J_2 + 1)} \Gamma_\alpha. \tag{2.9}$$

2.3 Direct reactions

Nuclear reactions can be classified depending on their timescale. When the reaction is slow, on the scale of $10^{-16} - 10^{-18}$ seconds, and the projectile and target interact creating an excited compound nucleus, the process is called a compound reaction. When the reaction is fast, of order 10^{-22} s, and it involves few nucleons on the nuclear surface taking place in a single step, the interaction is called a direct reaction [TN09].

Direct reactions can be described as a one-step transition from the initial state to the final state, presenting a peripheral interaction. They show angular distributions that are forward focused in the center of mass frame. This is because the initial direction of the projectile transfers its momentum to the final configuration, and they will have large cross sections at small θ_{cm}, whereas in a compound process the nucleus rearranges before decaying, and its decay is largely isotropic. For high incident energies the reaction is typically finished more quickly and fewer internal collisions are possible. Therefore, at higher energies the suppression of compound reactions is higher than the suppression of direct reactions.

There are different types of direct reactions. Elastic and inelastic scattering are direct reactions in which a change of direction and transfer of energy may occur, however no nucleons are interchanged. Break-up reactions include fragmentation of the projectile after its interaction with the target. Knock-out reactions are similar, but only one or a few nucleons are removed from the projectile. And finally, transfer reactions are direct processes where one or more nucleons are transferred from the projectile to the target, or vice-versa.

In this project a transfer reaction has been used. In a transfer reaction of type $A + a \longrightarrow B + b$, one or a few nucleons from the projectile are transferred to the target as is shown in figure 2.7. The projectile a is composed of the transferred particle and the ejectile $a = x + b$.

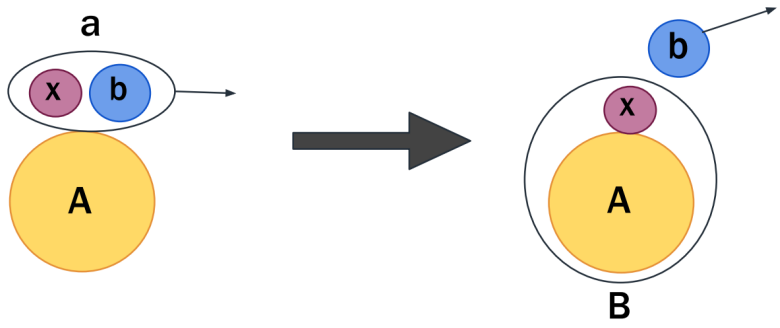

Figure 2.7: Schematic view of the transfer reaction components. Here, a light ion (a) transfers one or a few nucleons (x) to the nucleus A.

The produced recoil will be composed of the target and the transferred particle $B = A + x$. These reactions present two-body kinematics, and by measuring the energy and angle of the ejected particle one can determine the energy of the recoil (and thus its excitation energy) and the differential cross section for each excited state.

Transfer reactions are a great tool to extract information. They are very sensitive to the transferred angular momentum. By studying the shape of the detected angular distribution one can determine the angular momentum and parity of the populated states. From the extracted angular distributions one can also determine the normalisation factor between the experimental and the single-particle differential cross sections [HS21]. This normalisation factor states how well a given excited state in B is described as an A core and an x particle forming a two-body structure, and it is know as spectroscopic factor C^2S_x. Often this is done with a single nucleon as x rather than a cluster, but in the present, x is an α cluster. More details on the spectroscopic factor determination are given later in section 2.5, and cluster structures are explained below.

2.3.1 Clusters

Cluster models are useful to treat the nucleus as a two- or few- body problem. These models divides the nucleus into groups of nucleons or clusters. A cluster may be composed of one or many nucleons. The relative cluster motions are described by internal wave functions. Treating transfer reactions with cluster models simplifies the problem by treating the cluster as one particle with effective quantum numbers given by the individual quantum numbers of the nucleons in the cluster.

There are different types of cluster structures, such as single-particle + core models, multi-particle + core models, triton-core models or alpha-cluster models. In many light nuclei there is evidence of the formation of cluster structures. Clusters are believed to occur as a response to correlations from nucleon-nucleon interactions, especially the pairing interaction. Nuclei with even, and equal, number of protons and neutrons have been found to be particularly stable and they normally present very clear cluster structures, as the alpha particle is exceptionally bound. The arrange of the geometric position of the cluster is normally driven by symmetries, with some configurations more energetically favorable than others [SP14]. Examples of super deformed cluster states where the clusters are easily spotted are ^{8}Be (α + α), ^{16}O (^{12}C + α) and ^{20}Ne (^{16}Ne + α). All of these examples are cases of astrophysical interest, because they take place during the core burning stages. Some of these have already been mentioned in the nucleosynthesis section of chapter 1, section 1.1.2.

The ^{8}Be nucleus is unbound in its ground state by 92 keV, decaying emmiting two α

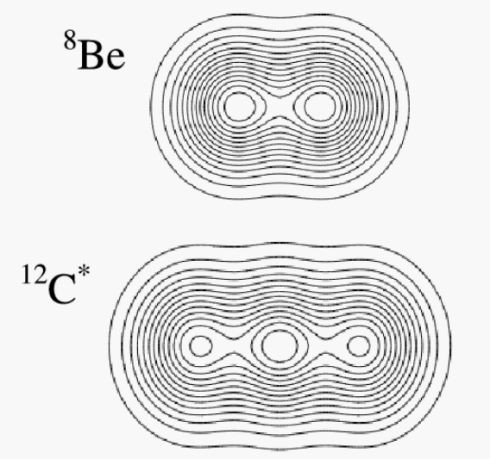

Figure 2.8: Nuclear density profiles for ^{8}Be and the Hoyle state of ^{12}C (at 7.65 MeV) in the linear configuration. Figure extracted from [SP14].

particles, and its lifetime is $\sim 10^{-16}$s [SP14]. Its nuclear density distribution defines two well-separated centers corresponding to two touching α particles. In the ^{12}C case, the famous resonant state at 7.65 MeV known as the Hoyle state also has a cluster structure (α+α+α). An example of the density distribution of these two cases are shown in figure 2.8. Note, however, that recent calculations have shown the Hoyle state to be better described as a triangular cluster [Epe12].

Other interesting cluster systems are the so-called borromean nuclei. They present three bound components that are unbound if one of them is removed. An example of borromean nucleus is ^{6}He ($\alpha + n + n$), where if one neutron is removed this gives the unbound ^{5}He, and if the α particle is removed it gives the unbound two-neutron system. There are other examples, such as ^{9}Be ($\alpha + \alpha + n$) or ^{11}Li ($^{7}Li + n + n$).

However, not all the systems present a well-defined cluster structure. Other nuclei can have energy levels that show a certain amount of clustering. This proportion can be studied by extracting the spectroscopic factor C^2S of a given state with respect to its clustered components. As previously mentioned, C^2S indicates how the wave function $\psi(r)$ of a nucleus can be described as a core + particle configuration. This project studies the α-transfer reaction given by ^{7}Li(^{15}O, t)^{19}Ne. The ^{19}Ne nucleus studied can be partially described as ^{15}O + α. Figure 2.9 shows the shell model configuration for ^{19}Ne in its ground state, where the black nucleons represent the ^{15}O core and the blue nucleons would represent the α cluster. This is a very clear shell model state, and we can see from the configuration of the blue nucleons that this is not a particularly clustered system. These blue nucleons are located filling the lowest energy states available, and in this case the two protons are paired in orbital $1d_{5/2}$, one of the neutrons fills the available gap in orbital $1p_{1/2}$ forming a pair and closing shell, and the last neutron is located

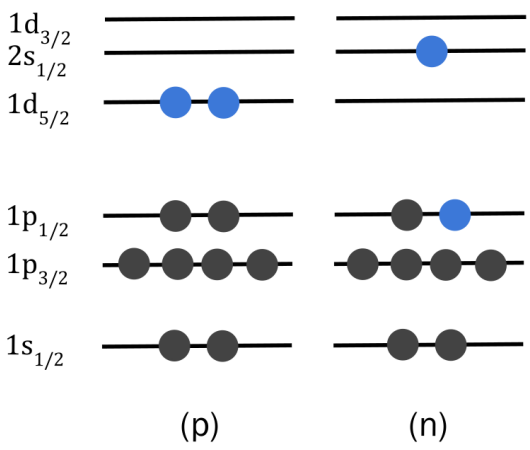

Figure 2.9: Shell model configuration of ^{19}Ne g.s. for the core + cluster structure of the ^{15}O + α system. The core ^{15}O is represented in black and the α cluster is represented in blue.

unpaired in the quantum state $2s_{1/2}$. This configuration is well described as a single-particle state, and not as a cluster state, because neutrons have broken up. Therefore C^2S for the α cluster will be small. The ^{7}Li nucleus presents a cluster structure ($\alpha + {}^3H$) that has been studied in different experiments (e.g. [Yos98]). ^{7}Li is predominantly a cluster configuration, and its $C^2S \simeq 1.0$, whereas the ^{19}Ne is predominantly a shell model configuration. In the present case, the α cluster in ^{7}Li is transferred to the ^{15}O nucleus.

There are some limitations on the application of cluster models. The number of channels included in the wave function reduces the validity of the model at low energies, and when dealing with large nuclear level densities the wave function requires the inclusion of many channels [Rau20]. Thus cluster models can also only be applied to light nuclei such as the ones studied in this work.

2.4 The Distorted Wave Born Approximation

This model is the most commonly used in the description of direct transfer reactions [HS21]. It solves the time-independent Schrödinger equation given by $\left[-\frac{\hbar^2}{2\mu}\frac{d^2}{dr^2} + V(r)\right]\psi(r) = E\psi(r)$, using optical potentials in the entrance (A+a) and exit (B+b) channels. To use it, a number of assumptions are made:

- Both the entrance and exit channels are described by elastic scatterings on a Coulomb field, where the wave functions describing the entrance and exit channels are perturbed by the Coulomb potential (distorted wave).

- The transfer process needs to be weak enough to be treated as a first order perturbation (Born approximation). This means that the incident energy must be much higher than the interaction between the incident particle and the elastic scattering. In this approximation the wave functions can be described as plane waves: $\psi(r) \propto e^{ikr}$, or in the distorted wave approximation as Coulomb-distorted plane waves $F_l(kr)$ and $G_l(kr)$ (regular and irregular, respectively).

- The reaction takes place directly from the initial to the final state, and the transferred particle is directly deposited in the final state, so no nucleon rearrangement takes place.

The main ingredients to describe this model are the distorted wave functions, that describe the elastic scattering in the entrance and exit channels, and the matrix elements, that describe the angular momentum of the particles involved, the nuclear structure information concerning the overlap between the initial and final state and the coupling between the core particle and the transferred particle. Five potentials are needed to describe the transfer process: the two potentials describing the elastic scattering in the entrance and exit channels, the binding potential of the transferred particle with the core in the initial configuration ($a = x + b$), the binding potential of the transferred particle with the core in the final configuration ($B = x+A$), and the residual interaction between the two cores involved in the transfer ($A + b$). For the entrance and exit channels the potentials have a volume, surface and spin-orbit components. The interaction of the transferred nucleons with the core in the initial and final configurations are described by the binding potentials where the depth of the potential is adjusted to match the binding energy of the populated bound state.

Even though the DWBA model describes well the transfer reaction mechanisms, there are uncertainties associated with the chosen optical potentials. These uncertainties come from many factors, such as the lack of elastic scattering measurements or the geometry of the binding potentials. These uncertainties are normally about 30% in relative scale [HS21], and they can be assessed by performing calculations with different sets of potentials.

With this method a single-particle wave function can be computed, in our case with this single particle as an alpha-particle cluster. The single-particle approach basically describes the wave function of B as the wave function of A plus the wave function of the transferred particle x. This calculation is done in this work using the FRESCO code [Tho88] whose parameters will be described later in section 5.1.2.

2.5 Differential cross section and partial width determination

In transfer reactions the cross section strongly depends on the angle of emission. For this work the focus is on α transfer, thus the formalism will be adopted for such reactions. One way to determine the cross section is to measure the angular distribution of a reaction and to extract the differential cross section $\frac{d\sigma}{d\Omega}$, which is the cross section per solid angle. The shape of the differential cross section depends on the angular distribution of the populated state and, thus, on the transferred angular momentum. The differential cross section is also used to extract the spectroscopic factors C^2S_α of the populated excited states. To extract them, the experimental differential cross section $\left(\frac{d\sigma}{d\Omega}\right)_{exp}$ is compared with the theoretical differential cross section $\left(\frac{d\sigma}{d\Omega}\right)_{dwba}$ by using the expression

$$\left(\frac{d\sigma}{d\Omega}\right)_{exp} = C^2S_\alpha \left(\frac{d\sigma}{d\Omega}\right)_{dwba}. \tag{2.10}$$

As explained before in section 2.3, the spectroscopic factor quantifies of how much a state can be described as a pure core + single particle structure. In this context, if an α unbound excited state with a partial width Γ_α can be described as two perfect core + α clusters, then its partial width can be defined as the single particle width Γ^{sp}_α. This Γ^{sp}_α corresponds to the maximum value of the Γ_α. In general, the partial width of an unbound level can then be described as the spectroscopic factor times the single particle partial width:

$$\Gamma_\alpha = C^2S_\alpha\Gamma^{sp}_\alpha. \tag{2.11}$$

The Γ^{sp}_α is defined as

$$\Gamma^{sp}_\alpha = 2P_l(r, E_r)\frac{\hbar^2 r}{2\mu}\left|\psi(r)\right|^2, \tag{2.12}$$

where $P_l(r, E_r)$ is the penetrability for a transferred angular momentum l, μ is the reduced mass and $\psi(r)$ is the radial part of the wave function. Thus, combining equations 2.11 and 2.12 the partial width is

$$\Gamma_\alpha = 2P_l(r, E)\frac{\hbar^2 r}{2\mu}C^2S_\alpha\left|\psi(r)\right|^2. \tag{2.13}$$

This states that the partial width determination is given by the probability of the transferred particle to penetrate the Coulomb and centrifugal barrier, as was shown in figure 2.6, and is given by the penetrability $P_l(r, E_r)$. This penetrability is the same Coulomb barrier penetrabil-

ity discussed for the astrophysical reaction rate and Gamow window in section 2.2. The partial width is also determined by the probability of a single particle to be at the nuclear surface, which is given by the square of the radial wave function $|\psi(r)|^2$.

The penetrability $P_l(r, E_r)$ is

$$P_l(r, E_r) = \frac{kr}{F_l(kr)^2 + G_l(kr)^2}, \tag{2.14}$$

where k is the wave number, r is the radius of interaction and F_l and G_l are the regular e irregular Coulomb (distorted) wave functions, respectively. The Coulomb functions are the solutions to the Coulomb wave equation, and they also depend on the resonance energy E_r [TN09]. The regular function $F_l(kr) = 0$ at $kr = 0$, whereas the irregular function $G_l(kr) \neq 0$ at $kr = 0$. Any solution to the Coulomb wave function can be expressed as $\chi_l = bF_l + cG_l$. These functions are tabulated and can be found in libraries at many different repositories, for example the GNU scientific library [Gou09], where the function *gsl_sf_coulomb_wave_FG_e*() in *gsl_sf_coulomb.h* is used to compute the F_l and G_l functions.

Chapter 3

Experimental setup

The experiment took place at the GANIL[1] facility in France. The setup was comprised of MUGAST, AGATA and VAMOS, which were coupled together to detect the products of the reaction ^{15}O(^{7}Li, t)^{19}Ne, which are tritons, γ-rays and ^{19}Ne recoils. In this chapter the experimental details will be described. A brief summary of the beam and target production will be given, as well as an explanation of the setup, focusing on the technical details, calibrations and detector performances. The performance of this setup has been recently published [Ass21] giving the overall performance of the 2019 and 2020 campaigns.

3.1 Beam production

The production of the radioactive ion beam (RIB) used the Isotopic Separation On Line (ISOL) technique and was performed at the GANIL SPIRAL1 facility. To produce the radioactive ^{15}O, an ^{16}O primary beam is sent into a primary carbon target at an energy of 95 MeV/u. Here, the beam reacts and stops producing a wide range of radioactive isotopes [TN09] that diffuse out of the target into an ERC[2] multi-charge ion source, where they are ionised. The ^{16}O beam is optimal for production of ^{15}O, because it is produced as a simple-neutron knockout, the simplest possible fragmentation of the beam. Here, electrons in the ECR plasma are heated by micro waves, and the ions are confined in this chamber so that multiple ionisations can occur. The confinement time required to ionise ^{15}O is much shorter than its lifetime, therefore there is no substantial decay loss during the ionisation. After ionisation, the ^{15}O ions are selected and post-accelerated using the CIME[3] cyclotron [Hor05] until they reach an energy of

[1] Grand Accélérateur National d'Ions Lourds. Caen, France.
[2] Electron Cyclotron Resonance
[3] Cyclotron pour Ions de Moyenne Energie

4.7 MeV/u. The produced beam has a high purity that comes from the high mass resolution of the CIME cyclotron, where $\Delta m/m \simeq 10^{-4}$. This resolution is much better than the relative mass difference between ^{15}N and ^{15}O, which corresponds to $\Delta A = 2.96 \times 10^{-3}$ u. There is therefore a ^{15}N suppression of $\sim 2\sigma$.

For this experiment a beam intensity of 10^7 pps was required in order to obtain sufficient beam particles on target (N_{beam}), to compensate for the low cross section of the transfer reaction being studied. At these intensities, the beam tracking detector CATS[4], placed before the target chamber, could not be used to monitor the beam position and intensity. This is because as a gas detector, CATS is limited to a beam intensity of 10^5 pps. An alternative measurement of these parameters was done using a beam gas profiler which was located before the target chamber. However, this measurement was not sufficiently accurate for absolute normalisation and was only used as a guideline, and to monitor the beam performance. Therefore, N_{beam} had to be obtained by a different method. The method used is detailed in chapter 4, section 4.6 and further in appendix C.

3.2 Target

The targets were made of enriched (>99%) ^{7}LiF at Argonne National Laboratory (USA). A thin carbon foil was used as backing. The thickness was 1.25 mg/cm^2 ^{7}LiF on a 40 μg/cm^2 carbon foil. The target thicknesses were measured by collaborators using the Rutherford Back Scattering technique at IJCLab (Orsay, France) to confirm the thicknesses. They were mounted on a target holder that could include up to 6 different targets. In this target frame there were also a few other targets in order to perform background and performance tests, as well as an empty position to tune the beam. Information about the different targets included is given in table 3.1. While running the experiment no degradation of targets were observed.

To calculate the experimental cross section, the number of lithium nuclei per cm^2 (N_{Li}) is required. To calculate the number of ^{7}LiF molecules comprising the target, we use its molar mass M(^{7}LiF)=26 g/mol and the target thickness:

$$N_{^7LiF} = 1.25 \cdot 10^{-3} \frac{g}{cm^2} \frac{N_A}{26 g/\text{mol}} = 2.9 \cdot 10^{19} \ ^7\text{LiF molecules}/cm^2, \tag{3.1}$$

where N_A is Avogadro's constant.

The number of lithium atoms in a LiF molecule is in a 1:1 proportion to the molecular content, thus the total number of ^{7}Li nuclei per cm^2 is also $N_{^7Li} = 2.9 \cdot 10^{19}$ atoms/cm^2.

[4]Chambre A Trajectoires de Saclay

Position	Target	Thickness	Diameter (mm)
1	Empty	—	—
2	C (nat)	40μg/cm^2	20
3	^{7}LiF	200μg/cm^2	20
4	^{7}LiF	1.25mg/cm^2	20
5	^{7}LiF	1.25mg/cm^2	20
6	Hole	—	7

Table 3.1: The targets located on the six positions of the MUGAST target frame. The first position was left empty and, along with the tuning frame with smaller hole (6), this was used for the beam tuning. The ^{7}LiF in position 5 was used for the main runs. A backup target (4) was also included in case the main target broke. The carbon target (2) and thin ^{7}LiF (3) were used for background tests and VAMOS tuning.

3.3 MUGAST

MUGAST[5] is a silicon detector array designed to detect charged particles produced in nuclear reactions. It is an intermediate state of the GRIT[6] silicon array [Col], which is under development. The MUGAST configuration consists of 5 trapezoidal detectors and 1 annular detector in the backward direction, 2 square detectors at 90 degrees, as shown in figure 3.1a, and coupled with the 4 MUST2 detectors at forward angles (see figure 3.1b). This configuration provides a large angular coverage that allows the study of stripping reactions and their angular distributions. All of the detectors are read by the MUST2 electronics. A scheme of the electronic used is given in appendix E. The detectors were located in a vacuum chamber and surrounding the target.

The aim of MUGAST in this project is to detect the ejectiles (tritons) of the reaction. For this experiment, only the backwards - trapezoidal and annular - detectors were used. The trapezoidal detectors were 500 μm double-sided silicon strip detectors (DSSSD) with 128 strips per side. The annular detector was also a 500 μm DSSSD detector, with 64 circular strips on one side and 16 radial strips on the other side. The square detectors at 90 deg were not working properly, and the MUST2 detectors at forwards angles were mostly shielded, as shown in the 3D representation in 3.1b, due to possible damage from the high intensity elastic scattering produced by the beam on the target.

[5]MUst2-GASpard-Trace
[6]Granularity, Resolution, Identification, Transparency.

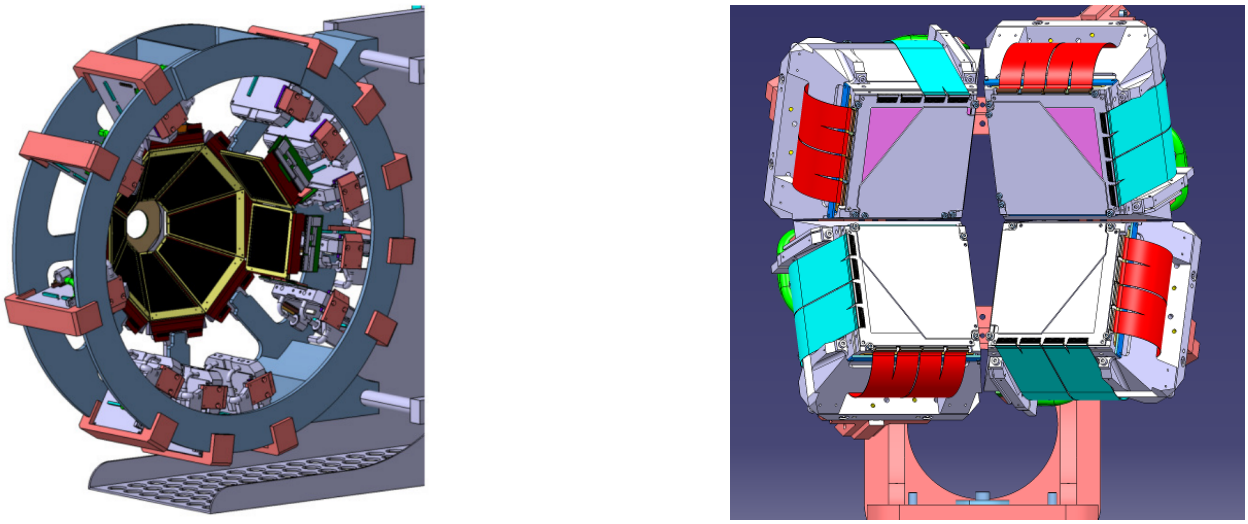

(a) MUGAST (b) MUST2

Figure 3.1: 3D representation of (a) the MUGAST detectors surrounded by the frame holding the electronic cards and (b) the MUST2 detectors partially masked for this experiment. The beam access the chamber from the left, through the space left in the middle of the annular detector, and the recoils produced in the reactions exit the chamber to the right, through the space left between the MUST2 detectors. For this project, MUGAST was in the first stage of development, and it only had 5 trapezoidal detectors. Images provided by M. Assié and the GRIT collaboration [Ass21].

All the detectors were tested using a triple alpha source (^{239}Pu, ^{241}Am and ^{244}Cm) during the preparation of the campaign. In the following sections a detailed study of the detection calibration is presented. Further technical details about necessary adjustments that were made are given in appendix A.1.1.

3.3.1 Calibration

Time and energy calibrations are necessary for each detector. Calibration runs were performed before and after the experiment by the MUGAST collaboration. An automatic calibration routine was performed before the experiment and the calibration parameters were applied to extract *online* spectra. However, a thorough, offline calibration is necessary to correct for possible bad strips not detected in the automatic routine, and to improve the calibration. This offline calibration was carried out as part of the present analysis. One important fact about the MUGAST calibration is that the electronic number of each strip does not correspond to its geometrical position. This means that a "MUGAST map" is needed to translate the raw strip number into the calibrated strip number. The raw plots shown in this section are plots before calibration and, therefore, the strips are not shown in their geometrical positions. For

this reason, the strips in raw plots and in calibrated plots do not match. A summary of the steps in each calibration is given in this section.

3.3.1.1 Time calibration

For each detector side, a time calibration run was performed at the beginning and at the end of the experiment. An electronic pulser was used, sending 32 signals with a frequency of 20 ns. The pulser produces an electronic pulse every 20 ns, which is detected in each strip. The calibration is done for each strip individually, identifying the pulses as shown in figure 3.2a, extracting their channel and doing a polynomial fit (shown in figure 3.2b) to extract the calibration parameters, following the equation:

$$\text{Time} = p0 + p1 \cdot x + p2 \cdot x^2, \tag{3.2}$$

where p0, p1 and p2 are the parameters obtained from the calibration and x is the channel number. This calibration was done in order to align all the strips so that the particle identity can be correctly identified from its time of flight.

Applying the calibration parameters for each strip, the time signal is aligned. An example of time calibration plots can be found in figure 3.3, where a comparison between raw signals before calibration (a) and signals after calibration (b) is shown for the front side (X) of the trapezoid detector MG1. The rest of the detectors behave similarly.

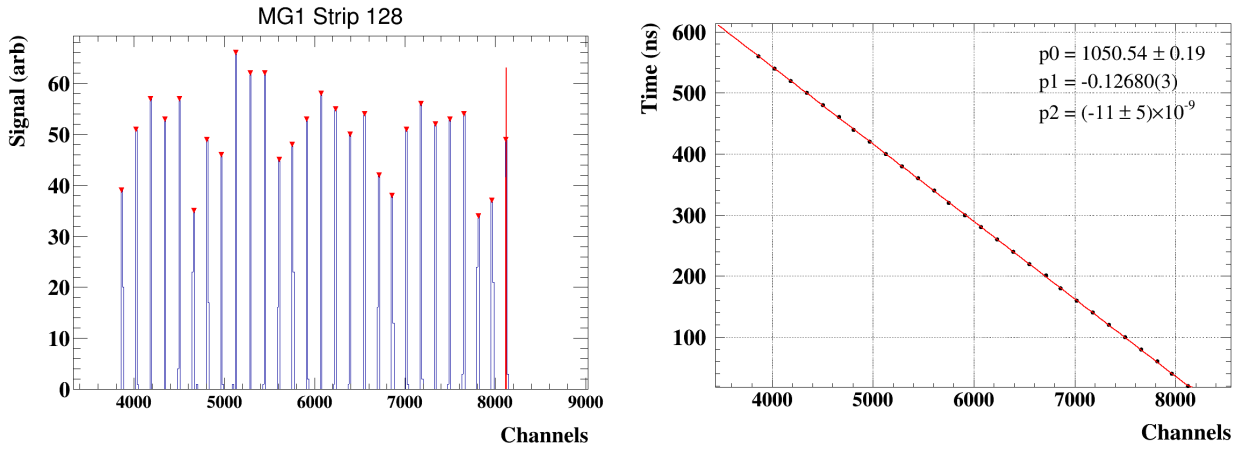

(a) (b)

Figure 3.2: Example of time calibration procedure for MUGAST detector MG1 side X (front) and strip 128. (a) Peak finder and Gaussian fit to identify the channel for each pulse. (b) Polynomial fit to determine the calibration coefficients.

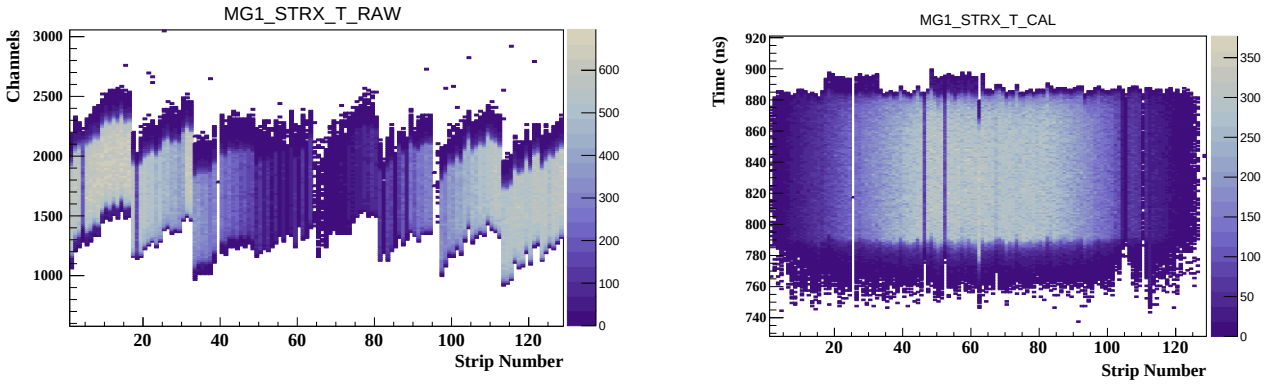

(a) (b)

Figure 3.3: Comparison between a raw histogram and a calibrated histogram for the time calibration. Example done for detector MG1 side X. The colour represents the number of counts. (a) Raw time signal as a function of the strip number. (b) Calibrated time as a function of the strip number.

3.3.1.2 Energy calibration

The energy calibration of the DSSSD detectors was performed using a triple-alpha source. The source was composed of ^{239}Pu, ^{241}Am and ^{244}Cm isotopes that decay emitting alpha particles at well determined energies, and whose information can be found in appendix D, table D.1. The different MUGAST detectors have a side X (front) and a side Y (back). The name of the sides comes from the internal (x,y) coordinate system for each detector. Each side has 128 strips. For every strip the energy peaks are identified and fitted to extract their corresponding channel, as shown in figure 3.4a. Each of the peaks corresponds to an isotope, and there is a broadening to the left of each peak, that corresponds to unresolved sub-peaks. This feature is given by the α decay from excited states of each isotope, and their energies can also be found in appendix D.

The alpha particles reach the detector at an energy E_α. However, there are energy losses ΔE in the detector surface before the charge produced by the particle is collected. Therefore, the detected energy (E_{det}) will be lower than the emitted energy E_α. This energy loss (ΔE) needs to be accounted for, following $E_\alpha = E_{det} + \Delta E$. This happens because the detector surface is covered by a thin layer of aluminium material commonly known as the *dead layer*. For each alpha energy a calculation of the energy loss on the aluminium layer is performed using the SRIM[7] libraries [ZZB10], for an average layer thickness of $\Delta x = 0.35\mu$m, taking into account the impact angle of the α particle. Further details about the dead layer calculation are given in section 3.3.3. After incorporating ΔE into the detected energy, a zero extrapolation

[7]Stopping and Range of Ions in Matter

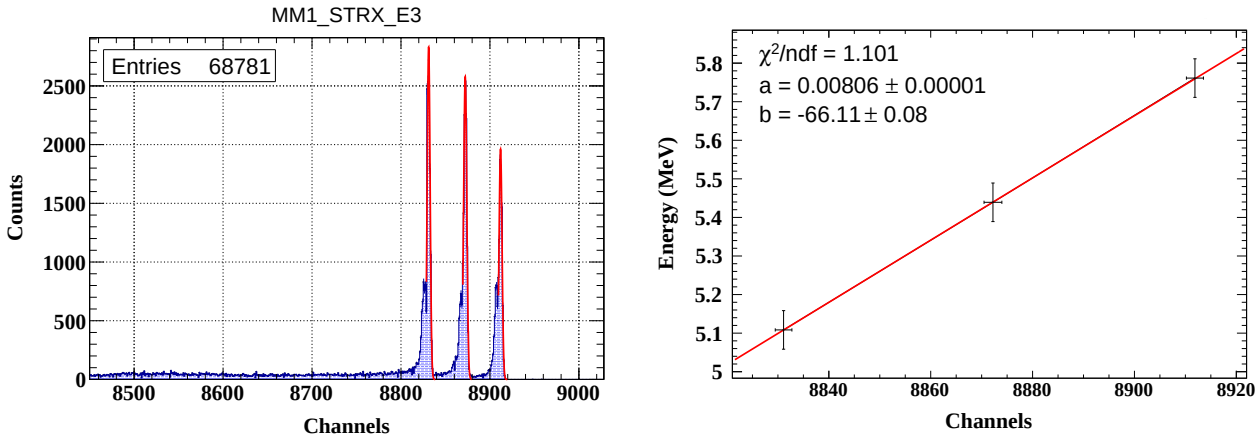

(a) (b)

Figure 3.4: Example of calibration procedure for MUGAST detector MG1 side X (front) and strip 3. (a) A peak finder routine is used to identify each pulse, and a Gaussian fit is done to identify the channel for each peak. (b) Linear fit to determine the energy-channel relationship. Error bars shown are 100 times larger than the actual errors so that they are visible in the graph.

method is carried out to find the energy-channel relationship. This method uses a linear fit between the three points using a function:

$$\text{Energy} = a \cdot \text{Channel} + b, \tag{3.3}$$

where a and b are the parameters of the fit, a given in MeV/channel and b given in MeV. This fit is shown in figure 3.4b for strip 3 of MG1 side X. The vertical errors are fixed to the theoretical errors of the energy peaks, and assumed to be known within 0.5 keV; and the horizontal errors are taken from the uncertainty in the mean of the Gaussian fit, which follows $\sigma/\sqrt{N}$, where σ is the peak width and N is the number of counts in the peak. The error bars shown in the figure have been enhanced ($\times 100$) for clarity. An example of a detector calibration is shown in figure 3.5 where we see detector MG1 side X (front) before and after calibration. Strip number varies between raw and calibrated files, based on the MUGAST strip mapping.

3.3.2 Energy resolution

The calibration using the alpha source can be also used to study the combined resolution of the MUGAST detectors. The peak resolution can be extracted doing a Gaussian fit and calculating the full width at half maximum using the expression $\text{FWHM} = 2\sqrt{2\ln 2} \cdot \sigma$, where

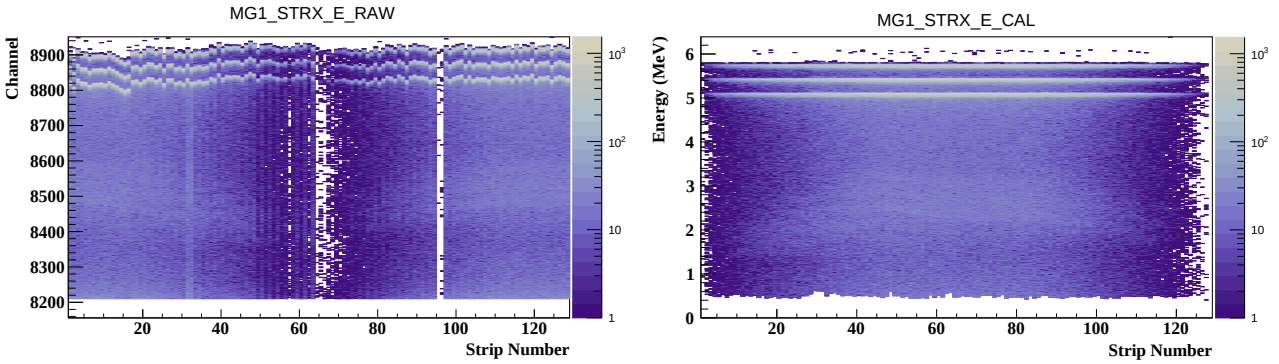

(a) (b)

Figure 3.5: Example of raw and calibrated histograms for detector MG1 side X. The strip number varies between raw and calibrated files. The colour represents the number of counts. (a) Raw alpha particle signal as a function of strip number. (b) Calibrated alpha particle energy as a function of strip number.

σ is the standard deviation. The energy resolution is then defined as:

$$R(\%) = \frac{\text{FWHM}}{E_{peak}}, \tag{3.4}$$

where E_{peak} is the centroid energy of the peak. Table 3.2 gives the combined resolution of the MUGAST detectors obtained for each α peak.

	Peak 1	Peak 2	Peak 3
Mean (MeV)	5.10	5.43	5.75
σ (MeV)	0.022	0.022	0.025
FWHM (keV)	52.65	50.92	58.58
R (%)	1.0	0.94	1.0

Table 3.2: Results of the combined detector resolution for MUGAST. Using the α source runs, a fit of each α peak is performed. Information of the fit is summarised here.

3.3.3 Dead layer

Each detector has an aluminium layer (*dead layer*) that collects the charge produced by the interaction of particles with the detector. This layer is located on the surface of the detector and it has a thickness of about 0.4 μm for the trapezoids and 0.7 μm for the annular detector. As already introduced in the energy calibration section 3.3.1.2, this dead layer lowers the energy

of any detected particle, introducing a systematic error in the calibrations. The energy that the particles loses in the dead layers must be taken into account in order to calculate the real energy of the event.

A charged particle interacting with matter loses energy following the Bethe-Bloch formula, given by

$$-\frac{dE}{dx} = \frac{4\pi e^4 z^2}{m_0 v^2} NZ \left(\ln \frac{2m_0 v^2}{I} - \ln \frac{c^2 - v^2}{c^2} - \frac{v^2}{c^2} \right), \tag{3.5}$$

where v, z are the velocity and charge of the incident particle, N, Z are the density and atomic number of the stopping material, m_0 is the electron mass, e is the electron charge and I is the average excitation and ionisation potential of the absorbing material. Figure 3.6 shows the energy loss of α particles in aluminium. The energy loss is, therefore, proportional to z^2 of the ion moving in the material. An α particle at 1 MeV loses ~300 keV/μm, and an α particle at 5.5 MeV loses ~150 keV/μm.

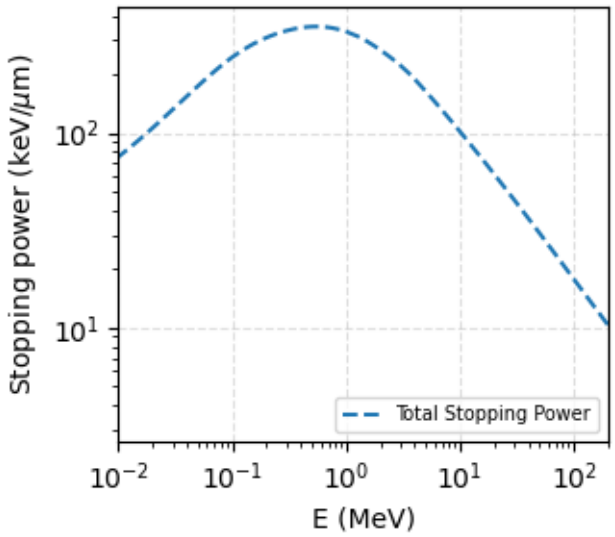

Figure 3.6: Stopping power of α particles in aluminium. Data obtained from the ASTAR database [Ber17].

To characterise the dead layer for each detector, a zero extrapolation method is used on the alpha calibration runs. This method parts from an assumed dead layer thickness and it performs an iterative process where the alpha calibration is done changing the dead layer in small steps. For each iteration, a linear fit is done $E_{cal} = a \cdot E_{ch} + b$ and dispersion $\delta = \mathrm{P} + b/a$ is extracted for each strip, where P is the pedestal signal of the channel. The next step is extracting the mean value of the dispersion obtained for the strips. This mean value is calculated using an iterative process for different dead layer thicknesses and plotted together. An example of this process

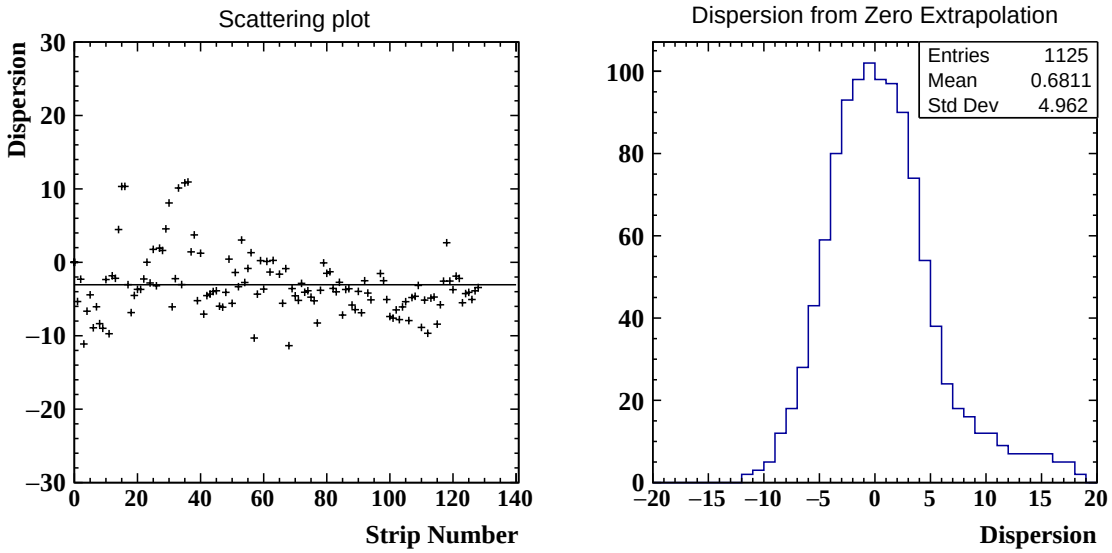

Figure 3.7: Example of the dispersion calculated for 0.34 μm aluminium thickness on the iterative process for detector MG1. For each strip the dispersion is calculated (right plot) and stored in a histogram (left plot). From this histogram, the mean of the dispersion is extracted and used as the mean dispersion of this aluminium thickness.

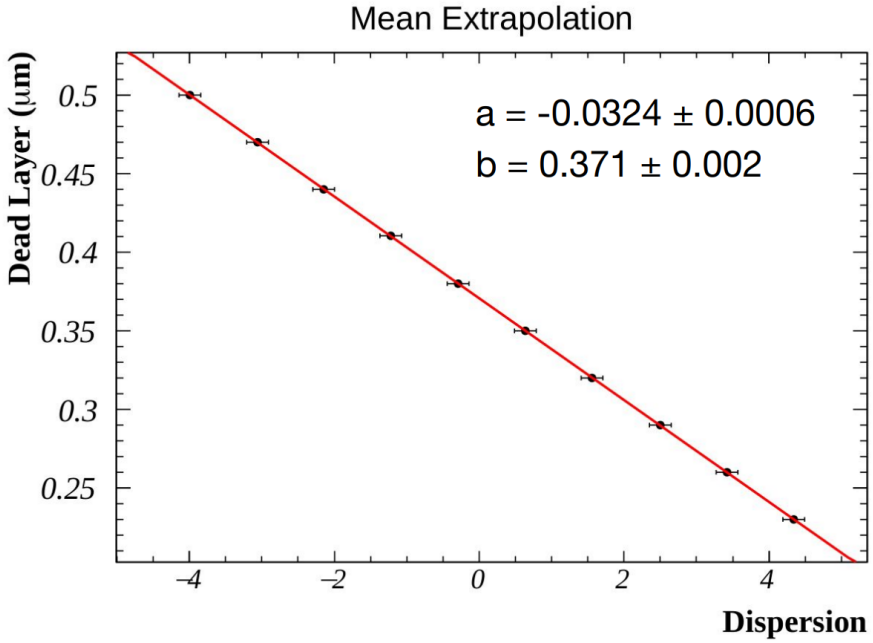

Figure 3.8: Mean values of the dispersion for the different aluminium thicknesses in detector MG1. The dead layer is extracted interpolating to the value where the dispersion is zero, or the parameter b. In this case, the dead layer is 0.371 ± 0.002 μm.

is given in figure 3.7 for one iteration on detector MG1. Finally a linear regression is applied, where the deduced dead layer of the detector is the one corresponding to zero dispersion in the linear fit, as shown in figure 3.8.

The extracted dead layer thickness for each detector is added to the analysis code. This dead layer contribution is also necessary in the simulations so that a full study of the expected resolution is achieved. The addition of dead layers to the simulation code was also performed for the present analysis and it is shown in appendix A.1.1.

3.3.4 Efficiency

The MUGAST efficiency has two components: the intrinsic efficiency ε_{int} and the geometrical efficiency ε_{geo}. The total efficiency is calculated as the product of the two efficiencies as:

$$\varepsilon_{MG} = \varepsilon_{int} \times \varepsilon_{geo}. \tag{3.6}$$

In this section a calculation of these components is given.

3.3.4.1 Intrinsic efficiency

Any charged particle that interacts with the silicon detecting material will generate electron-hole pairs and produce a readable signal. However, these DSSSD type detectors have interstrip material where the detection is not possible. There are some events that hit the detector between two strips, and only a portion of the energy is collected. This feature is known as interstrip events. Even though this surface is made as small as possible, many particles will impact between strips, thus we lose these events. Electronic cross-talk can also happen, which is signal leaking to a neighbouring channel, either because one particular channel is off or because of proximity of two signal lines. In these cross-talk events the detector records a lower energy signal. All these features are filtered out by applying a front-back energy gate.

To understand the detector response, the energy of the events detected in the front side (X) is plotted against the energy of the events detected in the back side (Y) as shown in figure 3.9. The selection of real particles is done by applying an energy window to match the energy of a particle in the front side with its energy in the back side. This energy window considers that the particle energy has to be the same in X and Y, within 300 keV. The rest of the particles detected are discarded. The intrinsic efficiency assesses how many of these events are lost overall and it needs to be taken into account when calculating the differential cross sections. It can be calculated for each detector by dividing the number of interstrip events by the total number of events registered. The annular detector has fewer strips than the trapezoids,

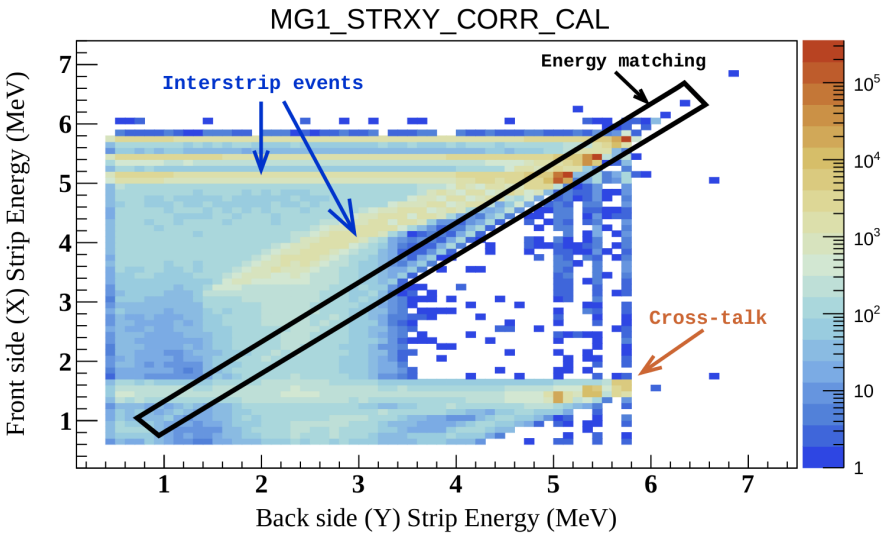

Figure 3.9: Front side against back side plot for detector MG1 obtained from a calibration run to characterise the detector response. The observable features are the alpha particle hits with the same energy (points in diagonal), the events hitting between strips (horizontal lines) and the cross-talk events between strips that show an alpha signal with a much lower energy (bottom-right points).

hence less interstrip material. This translates into a higher intrinsic efficiency for the annular detector. The results of interstrip events were of 6.5% for the annular detector and of 20% for the trapezoids.

The annular detector detects more events than each of the trapezoids, because the reaction is boosted forwards in the center of mass (corresponding to near 180 degrees for the tritons). To do a good estimation of the averaged intrinsic efficiency the percentage of events going to each detector must be included as follows:

$$\varepsilon_{int,T} = \varepsilon_{int,Annular} \cdot \frac{N_{Annular}}{N_T} + \varepsilon_{int,Trapez} \cdot \frac{N_{Trapez}}{N_T} \tag{3.7}$$

Following these calculations using an α calibration run, the intrinsic efficiency of the MUGAST detector is $\varepsilon = 0.845$. An average of 15.5% of events are therefore lost as interstrip events.

3.3.4.2 Geometric efficiency

MUGAST covers a certain solid angle. However, it does not cover the whole space. This implies that there are angles where the particle detection is not possible, and not all the angles are covered equally. Therefore, a study of the geometrical efficiency as a function of angle is needed. This geometrical efficiency is $\varepsilon_{geo} = \frac{d\Omega_{det}}{4\pi}$, where $d\Omega_{det}$ is the solid angle covered by the detector, and we will therefore add a correction factor as a function of angle.

This efficiency can be calculated using a simulation of an isotropic alpha source, launching a minimum of 10^6 particles, in order to have good statistics. The solid angle covered by the detector can be extracted as a function of angle following

$$d\Omega_{det} = \frac{N_{det}(\theta)}{N_{tot}} \cdot 4\pi, \tag{3.8}$$

where $N_{det}(\theta)$ is the number of events detected per angle and N_{tot} is the total number of events launched. The covered solid angle is shown in figure 3.10a, and the total efficiency per angle is shown in 3.10b. The angular range of 160-170 deg in the lab frame has a higher efficiency because this range is covered by the annular detector almost completely. The angular range from 110 to 155 is covered by the 5 trapezoids, which do not cover the full solid angle, as was already shown in figure 3.1a.

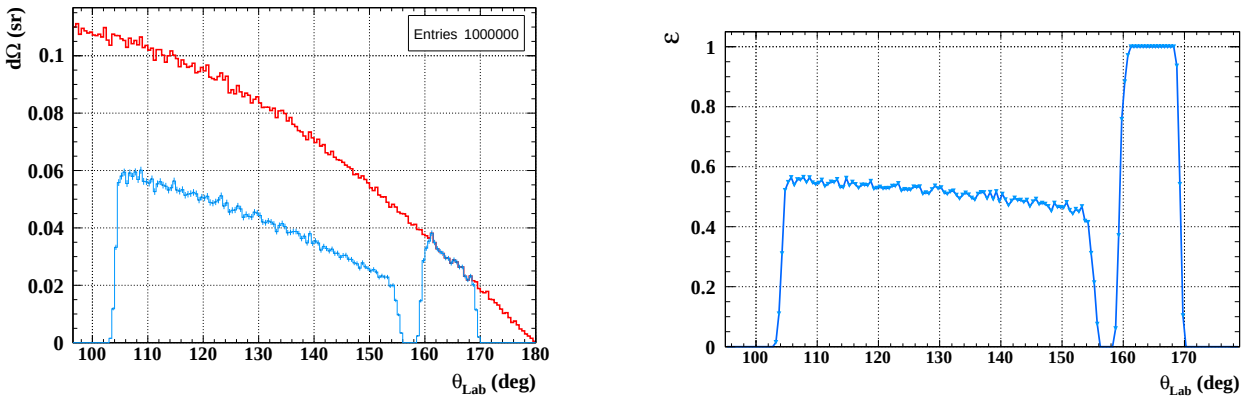

(a) (b)

Figure 3.10: Simulation of an alpha source to study the solid angle coverage and efficiency. (a) Shows the solid angle covered by the detector (in blue) and the total solid angle (in red) as a function of θ_{Lab}. (b) Shows the geometrical efficiency as a function of angle θ_{Lab}.

3.4 VAMOS

VAMOS [Rej11] is a VAriable Mode Operator Spectrometer which uses a ray-tracing and the measured properties in the focal plane to identify the particles. It is used to detect the heavy ions and to identify mass, atomic charge and velocity. Due to its large acceptance at forward angles of ±6 degrees, it is particularly useful for deep inelastic and transfer reactions. Figure 3.11 shows a scheme of the optical components of the spectrometer: two large aperture magnetic quadrupoles, a Wien filter to select velocities $v = \frac{E}{B}$ [Wie98], one dipole and the detection

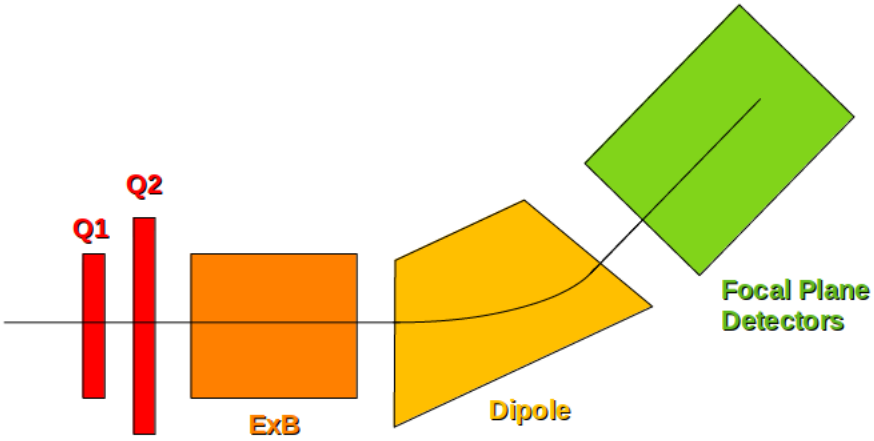

Figure 3.11: Scheme showing VAMOS spectrometer components. From left to right: two magnetic quadrupoles, a velocity filter, one magnetic dipole and the focal plane detector module.

system at the focal plane. VAMOS can be used in two different modes: as a recoil separator and as a dispersive spectrometer, using the dipole to either focus or disperse the recoils.

The optical components allow the ion magnetic reconstruction and the ray-tracing of the trajectory from the target position to the focal plane event by event. The reconstruction of the path is done by the calculation of the magnetic rigidity ($B\rho$). This magnetic rigidity determines the way a given ion is curved with a radius of curvature ρ in a magnetic field B, which depends on its properties of mass A, charge q and velocity v. This different curvature makes each ion hit the focal plane at a different position. The magnetic rigidity, in units of Tm, follows the equation:

$$B\rho = 3.105\frac{A}{q}\beta\gamma, \tag{3.9}$$

where the relativistic velocity β is defined as:

$$\beta = \frac{v}{c}, \tag{3.10}$$

where c is the speed of light in vacuum, and where γ is the Lorentz factor for relativistic velocities defined by

$$\gamma = \frac{1}{\sqrt{1-\beta^2}}. \tag{3.11}$$

Thus, the magnetic rigidity gives the distribution of the different nuclei on the focal plane.

To have an optimal ion identification we need measurements of energy loss, total incident energy, focal plane interaction position, incident angle and time of flight. These observables are measured using the focal plane set of detectors. These detectors are built using modules, sepa-

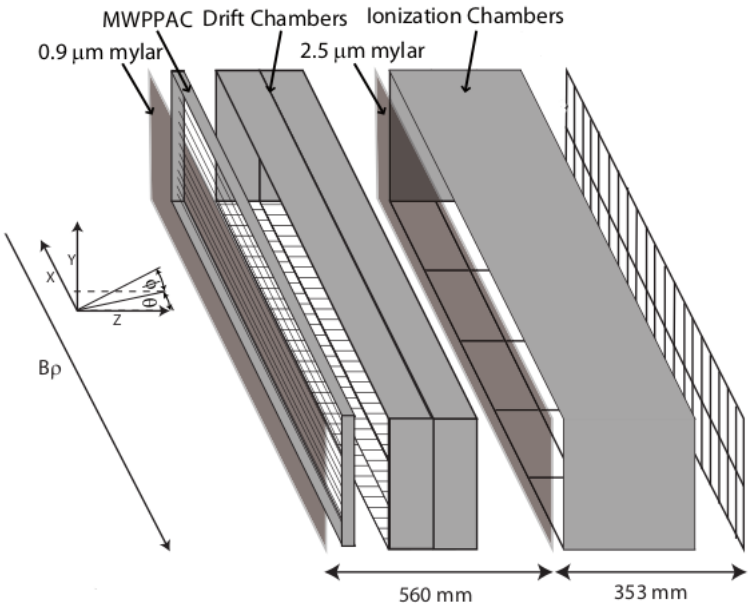

Figure 3.12: Scheme of the different detectors composing the VAMOS focal plane [Rej11]. The Bρ increases to negative values of x on the given coordinated system.

rated by Mylar windows and allowing the isolation of the different types of gas and pressures. The focal plane is composed of a Multi-Wire Parallel Plate Avalanche Counter (MWPPAC), two Drift Chambers (DC) and a Segmented Ionization Chamber (IC) as shown in figure 3.12.

3.4.1 Focal plane components

The MWPPAC is used as the stop signal of the time of flight (ToF) measurement whereas the two DCs measure the X and Y positions at the focal plane as well as the angles necessary to reconstruct the trajectories. The IC measures the energy loss of the particles. These components are gas detectors, they are filled with gas that is ionised when an ion passes throught it, producing an electric signal. Both the DC and the MWPPAC use isobutane at a pressure of 6 mbar. The IC uses a CF_4 gas whose pressure has to be determined depending of the energy loss calculation for the nuclei of interest. This calculation needs the particle incident energy, as well as its energy loss in each section of the focal plane. It was performed using the LISE++ software [TB04] obtaining a required pressure of 45 mbar.

Multi-Wire Parallel Plate Avalanche Counter (MWPPAC)

The MWPPAC is located at the beginning of the focal plane and it is used for timing. It produces a very good time resolution, better than 500 ps [Rej11], and high count rate capabilities. It is composed of two anodes and one cathode between them. The cathode

plane has vertical wires polarised at -500V and the anode planes have grounded horizontal wires. When an ion goes through the detector, the gas is ionised producing electrons that are accelerated towards the anodes, producing an electron avalanche. The corresponding ions are accelerated towards the cathode, which is segmented into 20 sections to reduce the capacitance, ensuring a large amplitude and a fast rise time of the signal. Fast voltage amplifiers process the time signals produced by the ions.

Drift Chambers (DC)

The focal plane includes two drift chambers used to reconstruct the trajectory of each particle including position and angle. Each drift chamber includes a drift gap of 150 mm and an amplification gap of 20 mm separated by a Frisch grid which is grounded. These grids have a double purpose in ionisation chambers, which are the removal of angular dependencies from the induced signal on the anode and to obtain the emission angle of the ionising particle [Al-12]. In order to process the signals, there are amplification wires located 15 mm below the Frisch grid. The amplification wires are positively polarised and the drift electrode is negatively polarised. The cathode plane consists of two rows of pads, each row with 160 pads. In order to improve the measurement of the position between pads, the rows are offset by half a strip. Pads are grounded through the front-end cards. Signals from the pads are read by Gassiplex chips [San94] for readout of gaseous detectors, plugged on the cathode outside the vacuum chamber. The drift region includes six polarised metallic wires placed at the entrance and at the exit of the drift chambers, and producing a homogeneous electric field that will collect the ionisation electrons created in the region. this helps to reduce the uncertainty in the measurement of the drift time.

To determine the X position of the particle the induced charge on the pads is used, applying an algorithm to obtain the centroid of the charge distribution. When the particle enters the Drift Chamber, it ionises the gas nearby, inducing charge in the pads the particle went through. The charge deposition follows a Gaussian distribution. The signal of the charge deposition from the pads is used to reconstruct the charge distribution. The X position of the particle corresponds to the maximum (centroid) of this distribution. Furthermore, if one pad produces a signal but the adjacent pads don't show any signal, this response is discarded since real events will have a broader distribution; at least 3 pads with induced charge are needed to reconstruct the X position. In order to determine the Y position, the drift time between the MWPPAC and the DC wires is measured using the e^- drift velocity (54 cm/μs) [Rej11].

Ionisation Chamber (IC)

Once the particle goes through the drift chambers, it arrives into the ionisation chamber, where its energy loss is detected through each IC segment. The IC is segmented in 7 sections (from IC0 to IC6) with different lengths, which are 60+60+120+120+120+100+20 mm. Each section is composed of a drift cathode, followed by a drift region, a Frisch grid and the anode pads, placed at 20 mm from the Frisch grid. An acceleration grid is placed at a distance of 10 mm from the anode and a grid pitch is placed at the entrance and at the exit of the IC and between the drift cathode and the Frisch grid, to ensure a good field homogeneity in the drift gap. The entrance Mylar window is supported by 32 vertical nylon wires to avoid deformations due to the difference of pressure for the DC and IC. A pad located at the entrance of the chamber collects the ionisation electrons created in the first layer, to have cleaner background. In order to choose the pressure of the CF_4 gas, a LISE++ simulation was performed, obtaining a pressure of 45 mbar, as mentioned. This simulation investigates the energy loss of the beam and the neon recoils at different pressures. The optimal chosen pressure is such that the neon recoils lose energy through the first four chambers, stopping in the fifth section of the ionisation chamber. This choice is based on the study of heavy charged particles (ions) interacting with matter by transferring energy to the material. The interaction of light charged particles (electrons and positrons) with matter is different and will not be considered in the present. As explained before, ions lose energy following equation 3.5. This energy loss can be plotted against the distance travelled defining the Bragg curve. In this curve the energy loss is constant for most of the path, until it suddenly peaks up just before the particle comes to rest. This peak is known as the *Bragg peak*, and it corresponds to the point where the particle deposits the maximum amount of energy [Kno10]. The energy loss is largely proportional to the distance travelled until it reaches the Bragg peak. The optimal position of the Bragg peak in the IC is one that allows a few sections to detect the linear behaviour before reaching the Bragg peak. For this reason the pressure was chosen so that the Bragg peak for the ^{19}Ne ions lies in the middle of the IC. It is also important to have a good detection of the Bragg peak for the later energy calibration of the IC.

3.4.2 Reconstruction

By ray-tracing event by event we can reconstruct the trajectory of every ion. To do this, the position and angles are measured at the focal plane, and they are traced back to the ion's original target position. Using VAMOS we can therefore determine the mass and charge state for the different nuclei detected, identifying the reaction products. In order to relate the parameters

at the target position with the ones at the VAMOS focal plane, a polynomial function is used in the trajectory reconstruction. Measurements of the position and angle at the focal plane, the time of flight and the energy loss from the detectors at the focal plane are also used to identify the recoils. The trajectory reconstruction of the nuclei in the VAMOS optics is done by the VAMOS libraries, and it was performed by the VAMOS group before the experiment. This process is very time consuming and will affect the next corrections and calibrations.

To do the reconstruction a simulation is performed, including 2000 different trajectories as a function of the relative magnetic rigidity:

$$\delta = \frac{B\rho}{B\rho_0}, \tag{3.12}$$

where $B\rho_0$ is the reference magnetic rigidity. The reconstruction depends on the magnetic rigidity of the ion and the incident angle. The simulation provides a relationship between each initial position at target location X_0 and θ_0 and the final parameters at the focal plane X_f and θ_f. After the simulation a polynomial interpolation method is used to find the correct $B\rho$ reconstruction.

The particle reconstruction is done using the position information extracted from the drift chambers. Therefore, a calibration of the wires is needed. This calibration is done before the experiment and is directly applied on the calibration file. For the DC X-position we use the induced charge, Q, on the wire. Q is fitted randomised across the bins through:

$$Q = Q_{Raw} + rnd \tag{3.13}$$

where Q is the induced charge in the wires, Q_{Raw} is the raw value obtained and rnd is a random number between 0 and 1. This random number is required in order to do a randomisation across each channel in Q_{raw}, to avoid systematic fluctuations from re-binning. This same procedure is also done routinely for silicon detectors. Here, the interest is focused on aligning the charge signals by performing a polynomial fit to extract the coefficients (a_0, a_1, a_2) that are included in the calibration files. The DC Y-position calibration similarly needs the performance of a drift time calibration to align the time signals of the wires. Once the X and Y positions are properly determined, the reconstruction of the magnetic rigidity is performed.

The beam was blocked just before the entrance of the focal plane by using a movable lead wall and a diamond detector. However, this wall could not be extended to cover the full beam because it would have overlapped with the position of ^{19}Ne entering the focal plane detectors. Therefore, there was a small percentage (<1%) of beam particles leaking into the focal plane.

Nuclei	E state [MeV]	q	Bρ [Tm]	ΔBρ (%)
^{15}O	0.000	8+	0.564	8.34
^{15}O	5.185	8+	0.540	3.67
^{19}Ne	0.000	10+	0.481	-7.71
^{19}Ne	4.033	10+	0.469	-10.00
^{19}Ne	0.000	9+	0.530	1.80
^{19}Ne	4.033	9+	0.521	0.00
^{19}F	0.000	9+	0.543	4.21

Table 3.3: Calculations of the total and relative Bρ for the main different recoils we will detect on the VAMOS focal plane. For these calculations equations 3.9 and 3.14 were used, taking into account the different charge states and excitation energies.

This was not an issue, as the selectivity of the detectors could separate the beam particles and other possible contaminants from the ^{19}Ne recoils, as will be detailed in the analysis chapter, section 4.2.

The magnetic rigidity and angle at the target position of the reaction products are determined on an event by event basis using the reconstruction procedure. Values of $B\rho$ are calculated in table 3.3 for the most relevant isotopes. Using the magnetic rigidity, the mass-over-charge calculation is straightforward as shown in equation 3.9. The mass is independently reconstructed using combination of the measured velocity and the total energy. The VAMOS resolution has been demonstrated to be $\Delta Z/Z \simeq 1/66$ for the Z resolution, and $\Delta M/M \simeq 1/220$ for the mass resolution [Rej11]. The count rate in the detector system is mainly restricted by the rate of the drift chamber. Typical values of dead time for the acquisition system are ~ 150 μs. Bρ acceptance is limited to a range around $-6\% < \Delta B\rho < 5\%$, with a relatively sharp cut-off at the lower rigidity [Rej11]. Table 3.3 shows the calculation of the relative magnetic rigidity defined as

$$\Delta B\rho(\%) = \left(\frac{B\rho}{B\rho_0} - 1\right) \cdot 100, \tag{3.14}$$

which determines how the different isotopes are located in the focal plane, positioning the 4.033 MeV excited state of ^{19}Ne 9^+ at the center of the focal plane. In figure 3.13 the distribution of the most relevant ^{19}Ne states and the beam in the focal plane are shown. These calculations were necessary to determine the central magnetic rigidity of the spectrometer (Bρ_0), which defines the magnetic rigidity that an ion must have to follow the central trajectory through the spectrometer, ending up at the center of the focal plane.

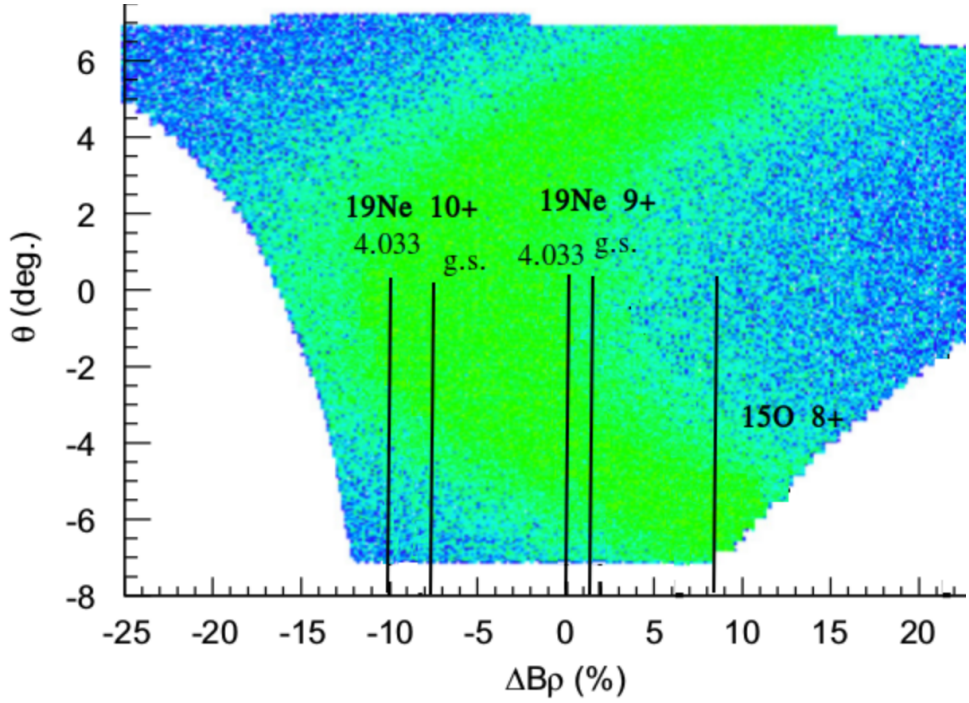

Figure 3.13: Angle as a function of the relative magnetic rigidity of the particles detected in the reaction plane. Both the $B\rho$ acceptance and the θ acceptance are limited as is shown in the image. Image adapted from [Rej11]. The position of the main recoils of interest is shown, relative to centering the 4.033 MeV excited state of ^{19}Ne 9^+ charge state.

The features of the RIB and the target thickness can add angular and energy straggling to the detected particles. It is also important to study how this straggling can affect the signal, as this can broaden the peaks, lowering the resolution. A simulation of the ^{15}O beam and the ^{19}Ne recoil was done and the position and energy straggling were measured and shown in table 3.4. The beam energy is 4.7 MeV/u and the energy straggling is 0.0042 MeV/u, therefore the effect of the energy straggling can be neglected. The angular acceptance of VAMOS is $\Theta \sim 5$ deg ~ 90 mrad, and the obtained angular straggling is 4.37 mrad for the ^{19}Ne recoils. This angular straggling will not significantly alter the VAMOS acceptance. The beam spot has a radius of ~ 2 cm, and the lateral straggling is σ(x)= 0.002 μm, which can also be neglected. Another consideration from the performed LISE++ simulation is the calculation of the recoil charge state, q_{eq}. In this case the result for ^{19}Ne is q_{eq}=9.41, which corresponds to a percentage of Q(9^+)=60% and Q(10^+)=40%. This percentage is taken into account as a correction factor when obtaining the differential cross sections.

	^{15}O	^{19}Ne
σ(E) [MeV/u]	0.0042	0.0040
$\sigma(\Theta)$ [mrad]	3.26	4.38
σ(x) [μm]	0.0016	0.0021
q_{eq}	7.84	9.41

Table 3.4: LISE++ calculations of the energy (σ(E)), angular ($\sigma(\Theta)$) and lateral (σ(x)) straggling of the ^{15}O beam and the ^{19}Ne recoils on their way through the 1.25 mg/cm2 LiF target. Included also a calculation of the charge state equilibrium q_{eq} of beam and recoils after going through the target.

3.4.3 Signal Calibration

There are a series of calibrations to do on the VAMOS detection system, as this is composed of several parts. The focal plane detectors were calibrated just before the experiment by the VAMOS group, and a more detailed calibration was done in the present work for the offline analysis.

3.4.3.1 MWPPAC calibration

In order to calibrate the signal collected by the MWPPAC we measure the time of flight recorded between the MWPPAC and the radio-frequency pulse (RF) of the cyclotron, using VAMOS as trigger. The RF signal has a repetition time of 79.3 ns. When a particle triggers the signal in VAMOS, a time-window (FAG) bigger than 100 ns is opened. During that time-window a RF signal is recorded and used to validate our signal and to determine the ToF. While the acquisition is busy no more signals are being taken, it is only taken when the FAG is free. Furthermore, two time validations are done to make sure the right time is being selected. Finally, the channels are converted to nanoseconds. To calibrate the TAC[8] signal, a time calibrator is used to do the conversion from channels to ns. The signal used comes in pulses every 160 ns. To calculate the offset of the signal for each channel, the magnetic rigidity of the recoils from an experimental run is used.

3.4.3.2 Drift Chamber X position calibration

The reconstruction of the path travelled by each particle needs the position of interaction within the drift chambers. The induced charge is used in order to determine this position. The drift chamber pads must therefore be properly aligned to have an optimal reconstruction of the position in X, along the DC. Before the experiment began, a calibration run was performed

[8]Time to Amplitude Converter

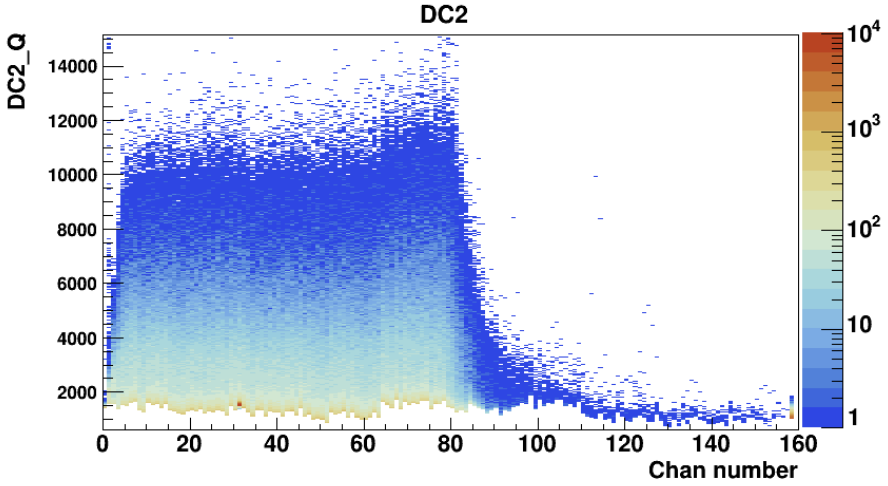

Figure 3.14: Raw spectra of collected charge (Q) for Drift Chamber 2 (DC2), showing the 160 pads 2 from a calibration run. The right hand side of focal plane is blocked by the movable lead panel.

using an alpha source in the focal plane position, to do an electronic alignment of the wires. The raw spectra in figure 3.14 shows the pads of the four sections of the drift chamber, explained in section 3.4.1. For each DC, a pedestal determination, a Q_{max} calculation and a gain matching must be done in order to find a good calibration of the pads. The electronic response is calibrated beforehand using a pulsed signal in order to align the pads.

Pedestal determination

Once the wires are calibrated, the pedestal must be determined for each pad in order to set the thresholds at 0. The pedestal is visible in figure 3.14, around a value of $1000 - 2000$ in collected charge. The pedestal position is determined using a script that runs a loop through all the pads, subtracting the pedestal value for each wire and extracting the alignment parameters. With this pedestal correction we get the alignment of the pads seen in figure 3.15.

Q max calculation

There is a charge distribution for each particle across several pads that will allow us to calculate its maximum value for each pad. The position is determined from the pad where the charge is maximum for each event. A Gaussian fit is performed to find the pad that corresponds to the centroid of the distribution, and the peak height determines the Q_{max} of the pad. This Q_{max} distribution of the pads is shown in figure 3.15.

Gain matching

Using the calibration run, each pad is aligned by applying a scaling factor: $Q_{\text{new}} = A \cdot Q_{\text{old}}$ which aligns Q_{max}. The gain factors will affect the pad distributions and, therefore, the

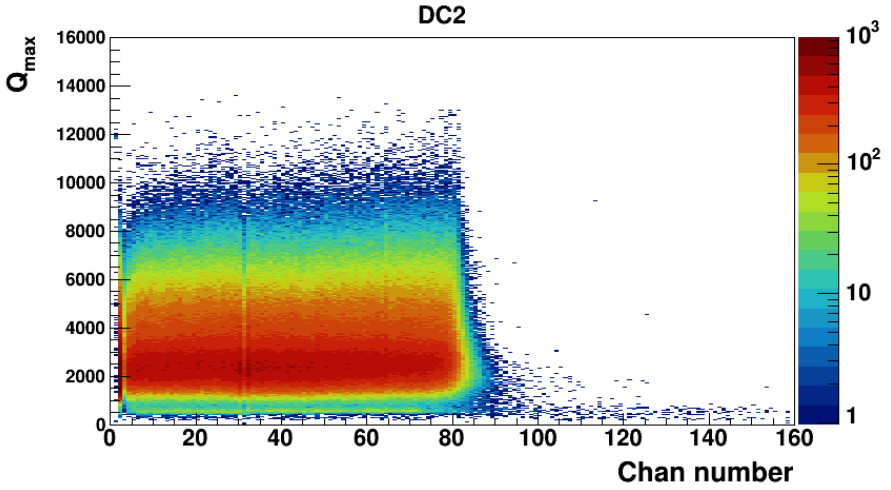

Figure 3.15: Maximum induced charge registered event by event for each pad of DC2. The calculation is done for each particle doing a Gaussian fit, finding its maximum and selecting the corresponding pad only.

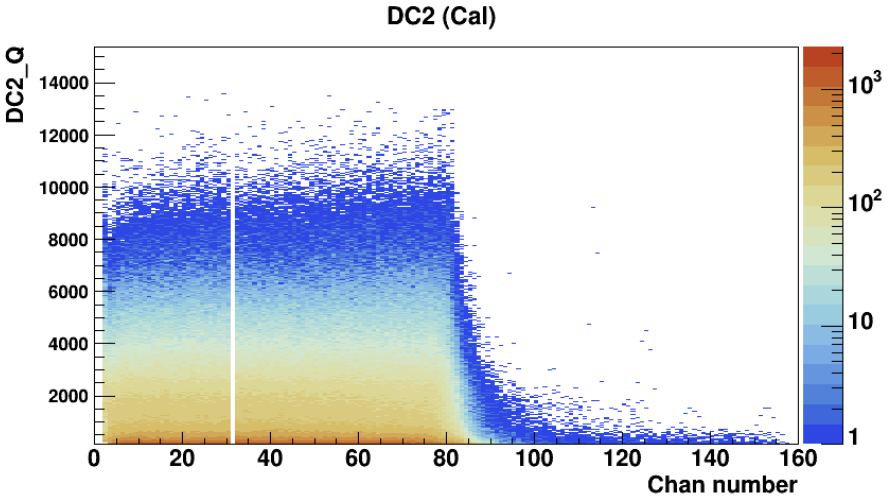

Figure 3.16: Final calibration for drift chamber DC2 after removing problematic pads, such as the ones at the edges of the electronic systems. It is important to remove any pad that might give a false signal, not to bias the position determination by these pads.

maximum charge determination. The pads presenting problems such as electronic background must be disabled. These problematic pads are normally located at the edges of the connections, where no recoils are detected. Figure 3.16 shows the final alignment once the gain matching has been applied and the problematic pads have been removed.

3.4.3.3 Drift Chamber Y position calibration

The Y-position is calculated using the drift time. The time of flight of the recoils from the MWPPAC to the DC is very small (ns) compared to the drift time of the electrons in the DC (μs). This allows the selection of the time recorded on the MWPPAC as the start of the signal on the drift chamber. With this time the Y position is calibrated by aligning the time channels to match the signals from the MWPPAC. Using this time as the start of the signal and the known electron drift velocity (54 cm/μs), the Y position is determined.

3.4.3.4 Ionisation Chamber calibration

The ionisation chamber calibration is important in order to have a good definition of the energy loss and the total energy that will be used to determine the isotope, specifically their mass (A) and nuclear charge (z). Each ^{19}Ne recoil going inside the ionisation chamber will lose its energy until it stops, under the given conditions of pressure and recoil energy. The individual particles follow the same trend when they lose energy. The energy loss is proportional to z^2, meaning the different elements lose more energy the higher z they have, following equation 3.5.

As already explained in section 3.4.1, the maximum amount of energy loss of an ion in a material is produced at the Bragg peak position, and it is characteristic of each element. When one section of the ionisation chamber is plotted against the following IC section, the Bragg peak can be easily identified. Therefore, the calibration can be done identifying this point for each pair of ionisation chambers and comparing to the theoretical value, obtaining a scaling factor for each section following:

$$\mathrm{SF} = \left.\frac{\Delta E_{th}}{\Delta E_{exp}}\right|_{Bragg}, \tag{3.15}$$

as the ratio of experimental (ΔE_{exp}) and theoretical (ΔE_{th}) values. Theoretical data was calculated using a LISE++ simulation, plotting IC[1] - IC[0] (2D plot shown in figure 3.17) and obtaining the scale factor comparing to experimental data. The scaling factor was firstly extracted from a beam control run where the unreacted ^{15}O beam was used.

When the first calculation of the scaling factors was done, a second round was performed using a experiment run where the scaling factors were extracted using the other detected chemical elements, particularly neon and fluorine. Figure 3.18 shows the energy loss of the different chambers for the control beam run and figure 3.19 shows it for an experimental run. This

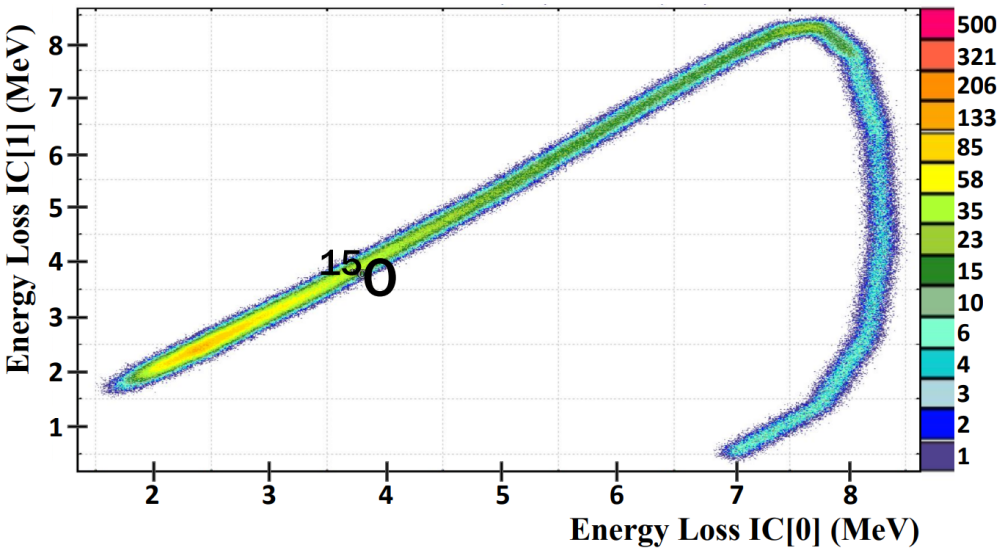

Figure 3.17: LISE++ simulation of ΔE - ΔE spectrum for ^{15}O. This plot shows energy loss detected in IC[1] against energy loss detected in IC[0]. The point of curvature is the Bragg Peak; point with the maximum energy deposition before the particle stops. This energy value is the chosen one to calibrate each ionisation chamber segment.

experimental run must be in agreement with the first round. However, as most of the products stop before IC5, the experimental run is only useful as a cross-check and to refine the first 5 IC sections as it is appreciated in figure 3.19. The final calculation for the scaling factor of each section is done including all the values extracted from the different Bragg peak comparisons, as an average of the scaling factors deduced form the different chemical elements observed:

$$\mathrm{SF}_i = \frac{\sum_j^N \mathrm{SF}_j}{N}, \tag{3.16}$$

where i refers to the different sections, j is the different elements and N is the number of elements used to calculate the scaling factors. Finally, the calculated factors were included in the calibration files of the ionisation chambers.

3.4.3.5 Time calibration

The TAC was calibrated using a time calibrator before the experiment by the VAMOS collaboration. In this calibration the relationship between channels and time was determined and added to the calibration files.

The calculation of the velocity, the mass, and the mass over charge of each particle relies on its time of flight. Therefore, having a well calibrated time signal is critical for a clear identification of the isotopes. The MWPPAC readout is divided in 21 individual signals along the horizontal axis (X). As part of the focal plane was covered by a shield stopping the unreacted

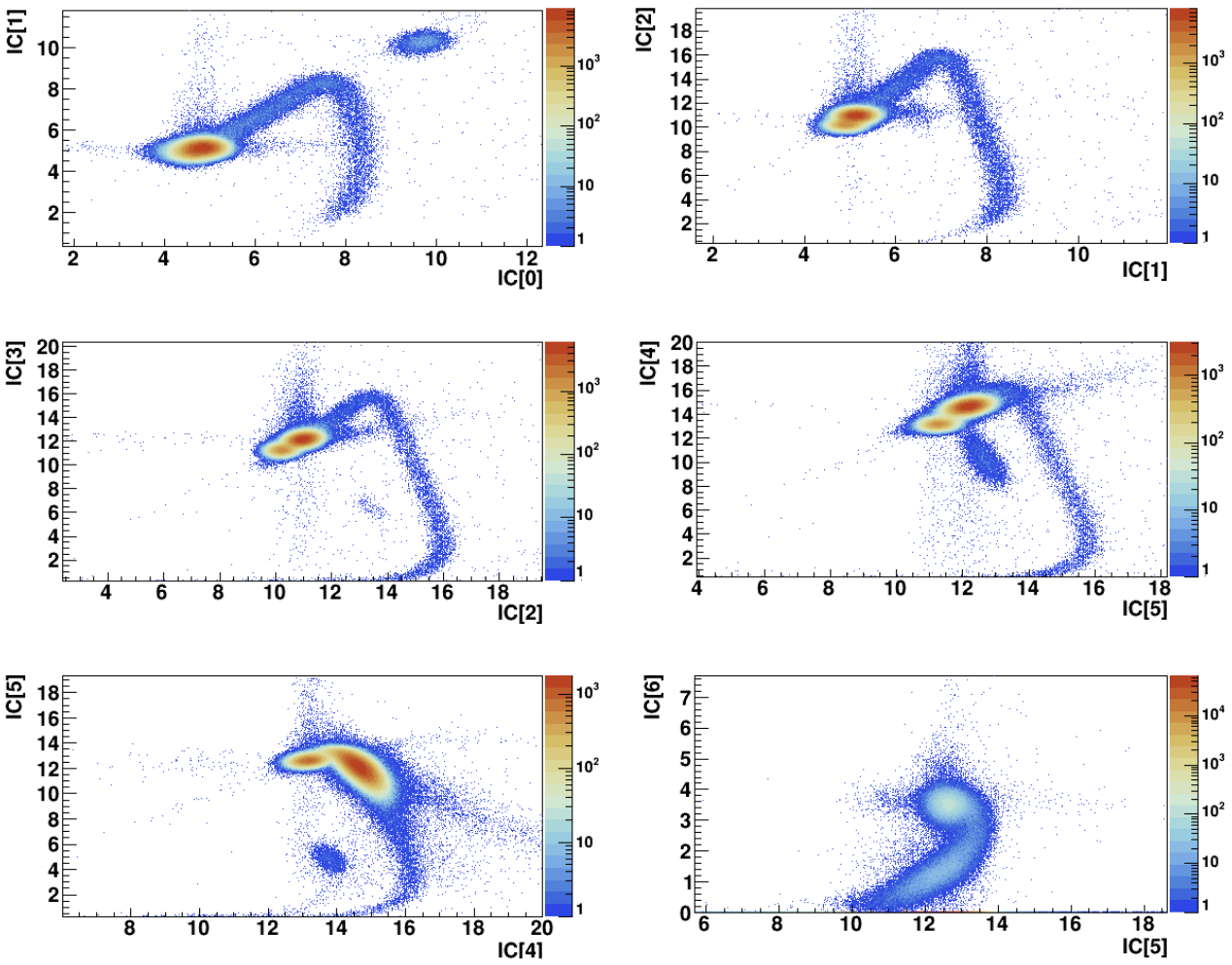

Figure 3.18: ΔE - ΔE plots for different pairs of IC segments, for beam control run (without target). This plot has been done to study the energy loss of ^{15}O in the IC, and extract the scaling factor from the comparison with the simulations.

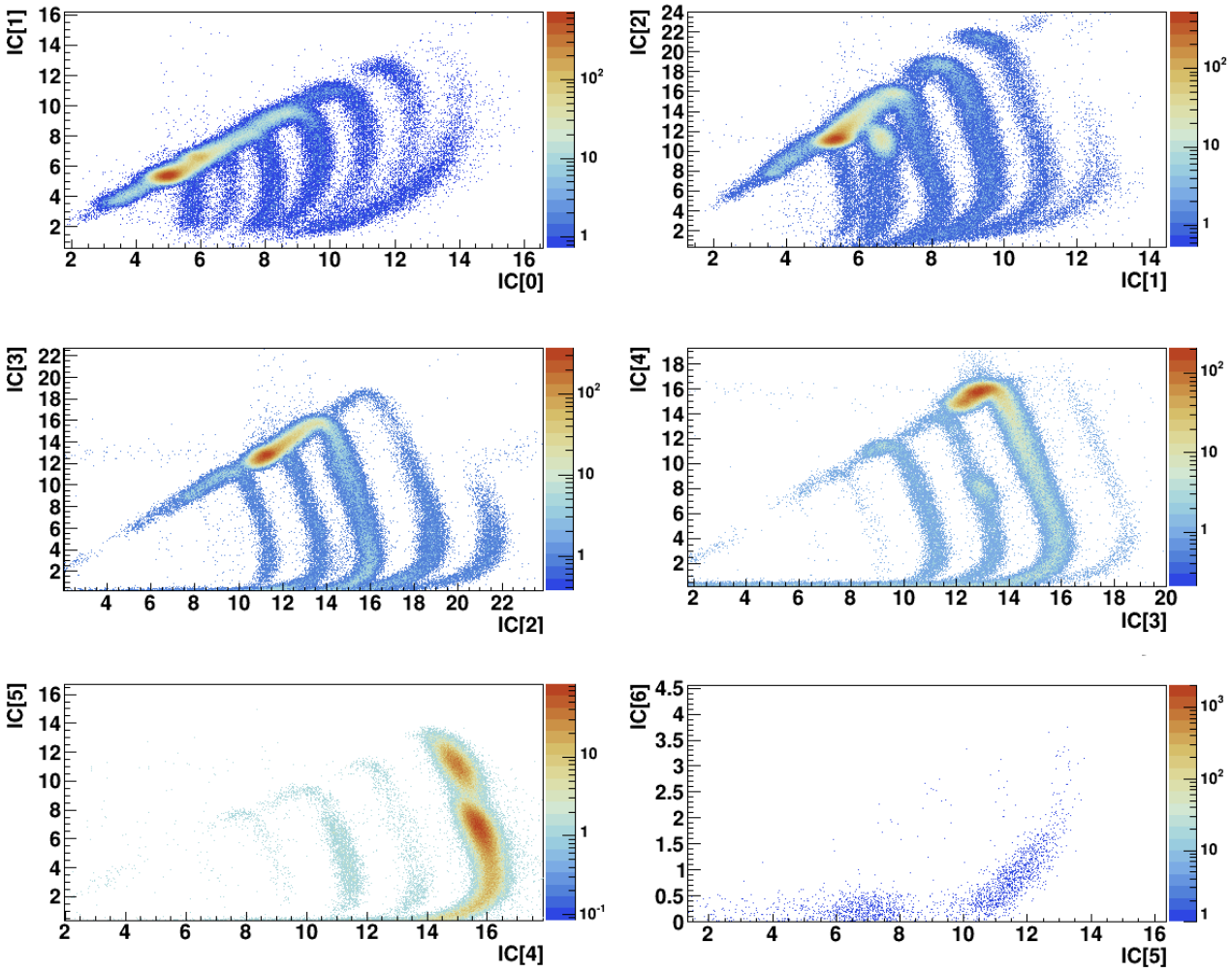

Figure 3.19: Calibrated ΔE - ΔE plots for different pairs of IC segments, for run with target, showing the reaction products as well as the beam. Calibration has been done comparing each curvature with the simulated one, a scaling factor for each IC segment can be extracted. Details are given in the text.

Isotope	Energy (MeV)	Velocity ($\cdot 10^7$ m/s)	ToF (ns)
^{15}O	70.50	3.01	273
^{15}O	65.19	2.89	284
^{19}Ne g.s	65.39	2.48	331
^{19}Ne*	57.81	2.42	339

Table 3.5: Time of flight calculation. ^{15}O time of flight without target and with target. ^{19}Ne calculation for ground state and for 4.033 MeV excited state, with reaction taking place at mid-target position.

beam, we only see signals in the first half of the channels. The first step in the time calibration is the alignment of these channels. As explained before, every particle produces a time signal in the MWPPAC that is processed and converted to a time of flight. The wires must be aligned to make sure the isotopes have the right time of flight. The procedure to align the wires is similar to what is done to extract the scaling factors for the ionisation chambers, using first a beam control run to identify the ^{15}O position for each wire, and then align the wires. We then check the time of flight with a normal experiment run, and align this for the rest of the reaction products. The theoretical time of flight of the more relevant isotopes are calculated and shown in table 3.5. The time of flight calculations between the target and the focal plane have been done using the incident energy of the particles and it is a reference to align the Multi-Wires. The time of flight is measured backwards, meaning that the particle produces a signal in the MWPPAC and, from that signal, the time reconstruction is done for the target position. To get the real time of flight a time offset must be introduced by adjusting the mass over charge calculation. This part will be detailed in the analysis chapter (see section 4).

3.4.4 Energy calibration

The total energy of the particles must be determined for the later mass and charge calculation. Once the particle enters the focal plane, it loses energy on its way through the detectors and windows. However, the energy loss is only registered in the ionisation chamber and the sum of the energy loss of each section of the IC does not give the total energy of the particle at the target position. The real value of the total energy for each particle is the sum of the energy not measured and the energy measured in the IC

$$E_T = E_{nm} + E_{IC}, \tag{3.17}$$

where E_{nm} is the energy not measured and E_{IC} is the energy measured in the ionisation chamber. For a given chemical element, the energy lost inside a material is constant until the Bragg peak is reached, where the particle deposits the maximum energy. After that point, the average energy deposition decreases fast, as they deposit their remaining energy. For a particle entering the focal plane detectors, the energy lost before the ionisation chamber is therefore proportional to the energy lost in the first section of the ionisation chamber (IC[0]). Thus, the energy not measured (E_{nm}) is proportional to the energy registered in IC[0]

$$E_{nm} = f \cdot E_{IC0}, \tag{3.18}$$

where f is the proportionality factor and E_{IC0} is the energy registered in the first section of the IC. Adding this definition to equation 3.17, the total energy of the recoil is given by

$$E_T = f \cdot E_{IC0} + E_{IC}. \tag{3.19}$$

Thus, the total energy can be calculated as a function of the energy measured by the ionisation chamber if f is determined. In order to obtain a good value of f, it is simulated using the signal of different chemical elements. The calculations shown in table 3.6 have been done using LISE++ simulations to obtain the energy loss in the different parts of the focal plane. The final factor is obtained from the mean of simulated proportionality factors, as this is largely independent of the chemical element:

$$f = \frac{\sum_i^N f_i}{N} = 3.015, \tag{3.20}$$

where N is the total number of chemical elements for which the simulation is carried out, in this case three.

Isotope	$\mathbf{E}_{nm}$ **(MeV)**	$\mathbf{E}_{IC0}$ **(MeV)**	**f**
^{15}O	9.813	4.754	3.064
^{19}F	17.99	9.021	2.994
^{19}Ne	18.53	9.331	2.986

Table 3.6: Factor calculation using LISE++ simulation of the energy loss for ^{15}O, ^{19}F and ^{19}Ne in the materials composing the different parts of the VAMOS focal plane detectors before the IC.

3.4.5 VAMOS acceptance

There are many factors playing a role in the acceptance of the recoils from the reaction chamber to the focal plane [Ram16]. It depends on the $B\rho$ and the charge state of the recoil. To calculate this efficiency, a simulation was performed including the VAMOS acceptance map provided by the VAMOS collaboration and discarding any events that go outside this region. This acceptance is included in the $d\Omega_{det}$ histogram obtained combining both the MUGAST and VAMOS geometric efficiencies, already explained in 3.3.4.2.

3.4.6 VAMOS focal plane intrinsic efficiency

The efficiency of detection (or intrinsic efficiency of the focal plane detectors) is a way to determine how well a device detects all the real incident particles. Due to electronic pile-up and background, not all of the signals collected are going to be real events (e.g. ^{19}Ne recoils). A device is more efficient the more particles it is able to detect in relation to the real number of particles entering the detector. However, the total number of particles arriving into the detector is not known. In order to study how efficient the detector is, a study of the number of particles detected in the different sections must be carried out. The VAMOS total efficiency of detection is determined by the product of the individual efficiencies of each of its components

$$\mathcal{E}_{fp} = \mathcal{E}_{IC} \cdot \mathcal{E}_{DC} \cdot \mathcal{E}_{rec}, \tag{3.21}$$

where $\mathcal{E}_{IC}$ is the ionisation chamber efficiency, $\mathcal{E}_{DC}$ is the drift chamber efficiency and $\mathcal{E}_{rec}$ is the efficiency of the event reconstruction. Besides the focal plane intrinsic efficiency, the geometric efficiency is calculated in combination with the MUGAST geometric efficiency, as already detailed in section 3.4.5. In addition to this, VAMOS separates the recoils depending on their charge state. This selection is also detailed in the analysis chapter, section 4.2.1.

3.4.6.1 Ionisation Chamber

As mentioned in section 3.4.3.4, the ionisation chamber is divided in 7 parts or sections. The efficiency of one section in relation to the following section is studied in the following. For the last section it is not possible to perform a calibration as discussed below. However, only a small percentage of beam particles will reach that far. The ^{19}Ne recoils will lose their energy and will be detected within the first 5 sections. Therefore, it is particularly important to determine the efficiency of detection for these first 5 chamber where the recoils will be detected.

The Ionisation Chamber detection efficiency is calculated using the expression:

$$\mathcal{E}_{IC} = \prod_i \mathcal{E}_{IC(i)}, \tag{3.22}$$

where the total ionisation chamber efficiency is the product of the individual efficiencies for each section. A more detailed explanation of the calculations is given below. For a given section of the ionisation chamber, the number of particles detected is defined as:

$$N_{IC(i)} = N_t \cdot \mathcal{E}_{IC(i)}, \tag{3.23}$$

where IC(i) detects $N_{IC(i)}$ particles, which is the total number of particles that come into IC[i], multiplied by its efficiency of detection $\mathcal{E}_{IC(i)}$. The same logic is applied for the following chamber IC($i+1$):

$$N_{IC(i+1)} = N_t \cdot \mathcal{E}_{IC(i+1)}. \tag{3.24}$$

Furthermore, the number of particles that have been detected firstly in section i and secondly in section $i+1$ can be obtained imposing a condition to include only counts detected in both IC(i) and IC($i+1$) simultaneously, and can be expressed as:

$$N_{IC(i)\&IC(i+1)} = N_t \cdot \mathcal{E}_{IC(i)} \cdot \mathcal{E}_{IC(i+1)}, \tag{3.25}$$

which is the total number of particles multiplied by the efficiency of each section. Finally, the efficiency $\mathcal{E}_{IC(i)}$ is determined by dividing equation 3.25 by equation 3.24:

$$\mathcal{E}_{IC(i)} = \frac{N_{IC(i)\&IC(i+1)}}{N_t \cdot \mathcal{E}_{IC(i+1)}} = \frac{N_{IC(i)\&IC(i+1)}}{N_{IC(i+1)}}. \tag{3.26}$$

This means that the efficiency of section (i) is determined using also the number of particles detected in section ($i+1$), and therefore we cannot efficiency calibrate the last section.

The individual efficiencies are calculated using a run with good statistics and applying equation 3.26. In table 3.7 the individual efficiencies calculated can be found. The total efficiency of the ionisation chamber is calculated using equation 3.22 and we obtain:

$$\mathcal{E}_{IC} = 0.67. \tag{3.27}$$

	IC0	IC1	IC2	IC3	IC4	IC5
$\mathcal{E}$	0.9647	0.9855	0.8560	0.9244	0.9159	0.9655

Table 3.7: Efficiencies for each section of the ionisation chamber calculated using equation 3.26.

3.4.6.2 Drift Chamber

The individual particle position is calculated using the drift chambers, as explained in section 3.4.3.3. For each particle passing through the drift chamber, a position calculation is done. The number of counts registered in the position calculation (X_f) is the number of particles detected by the drift chamber. Therefore, following the same principle as done for the ionisation chamber, the efficiency is calculated following expression:

$$\mathcal{E}_{DC} = \frac{N_{IC0\&X_f}}{N_{IC0}}, \tag{3.28}$$

where the number of events registered at the same time in X_f and in the first section of the ionisation chamber (IC0) are compared with the number of particles arriving in IC0. In order to cut possible electronic noise, a condition of $X_f > -200$ mm is set to select the X position of the focal plane in which the recoils are expected, and a condition in the minimum energy loss of the recoils entering the IC is set to be IC0 > 0.1 MeV. With these conditions applied, the efficiency of the drift chamber is:

$$\mathcal{E}_{DC} = 0.93. \tag{3.29}$$

3.4.6.3 Reconstruction

The efficiency of reconstruction gives the percentage of the number of events that have the right Bρ. During the reconstruction, some events registered in X_f will be false signals such as electronic noise. Thus, it is important to determine this efficiency in order to have an evaluation of the number of events lost in the reconstruction. This can be calculated following the same logic as before, following:

$$\mathcal{E}_{rec} = \frac{N_{(B\rho>0.4)}}{N_{(X_f>-200)}}, \tag{3.30}$$

where the number of particles obtained for a $B\rho > 0.4$ Tm divided by the number of particles detected in the drift chamber $N_{(X_f>-200)}$ is given. Here, a condition on the expected $B\rho$ of the recoils is similarly set to avoid including electronic background. The efficiency of reconstruction is:

$$\mathcal{E}_{rec} = 0.97. \tag{3.31}$$

VAMOS total intrinsic efficiency

After calculating the different components that contribute to the intrinsic efficiency of detection in the focal plane, using equation 3.21, the final result is:

$$\mathcal{E}_{fp} = 0.61. \tag{3.32}$$

3.5 AGATA: Advanced GAmma Tracking Array

Energy resolution and position determination for the first interaction are key factors in the study of gamma spectroscopy in transfer reactions involving radioactive ion beams. Determining reaction rates for resonant states with small cross sections has been challenging due to the lack of powerful enough devices. Developing new technologies for radioactive ion beam studies have allowed experimental nuclear physics to enter a new range or possible reactions to study where, in combination with the state-of-the-art detection systems, the access to these relevant states is achieved. Developing high resolution γ-ray germanium detector arrays has been key to the progress achieved in the field. In this experiment the Advanced GAmma Tracking Array (AGATA) [Akk12] has been used. Figure 3.20 shows the initial configuration built for the LNL-Legnaro campaign (Italy, 2010), comprising 15 detectors. For the present campaign AGATA utilised 42 HPGe segmented detectors.

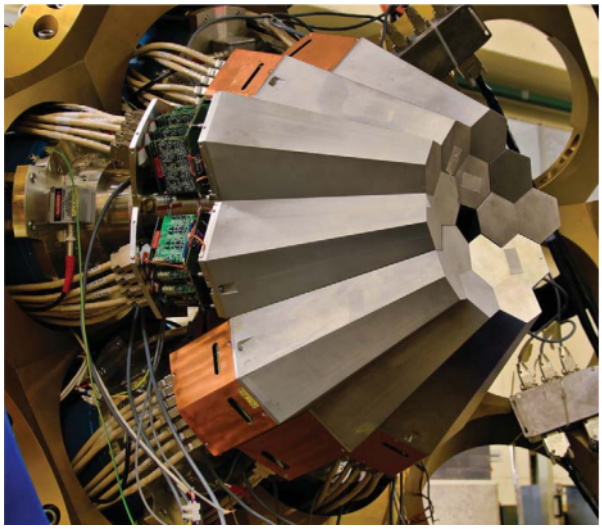

Figure 3.20: Five clusters composed of 3 detectors each in the AGATA array are shown, in the initial configuration built for the LNL-Legnaro campaign. AGATA currently utilises 14 clusters of 42 crystals in total. Image obtained from [Akk12].

3.5.1 Tracking

This array is based on the γ-ray tracking technique using the electrically segmented HPGe crystals, enabling the accurate determination of the points of interaction for each event. This also allows the determination of the energy deposited within the crystal with great precision. Due to the experimental conditions of reactions such as ^{7}Li(^{15}O, t)^{19}Ne where the beam and recoil energies are considered relativistic ($\beta > 0.05$), the relativistic Doppler effect has to be accounted for, necessitating the high position resolution. In this effect, the energy observed (E_{obs}) is different from the energy emitted (E_{em}), and it depends on the angle of emission θ, following $E_{em} = E_{obs} \cdot \gamma\,(1 - \beta \cdot \cos\theta)$. Therefore, if the Doppler effect is not corrected, the γ-rays detected will not correspond to the real decay energies. AGATA uses the *tracking* technique, which takes the position and energy information of each interaction into account, identifying the first interaction point and determining the energy and the direction of emission of the original γ-ray with high precision. Thus, a reconstruction of the full interaction path is achieved leading to an optimal Doppler energy correction, which will be key to a good energy resolution in cases such as γ-rays emitted from a fast moving nucleus.

During the design of this array, its performance was studied using Monte Carlo simulations in order to maximise the covered solid angle to achieve the best detection efficiency while minimising the production costs. The possible configurations were studied in [Far10], where a selection was made in terms of the energy resolution. The aim of the AGATA collaboration is to achieve a 4π solid angle coverage, as shown in figure 3.21a. For the experimental campaign GANIL-2019 AGATA was composed of 14 clusters with a total number of 42 crystals. For this particular experiment 40 out of the 42 crystals were performing well and were therefore used.

As mentioned before, the crystals are grouped in clusters assembled into a single cryostat. These clusters are composed of 3 crystals and they are named Agata Triple Clusters (ATP). The function of the cryostat is cooling the system in order to optimise the noise performance. Each crystal is electrically segmented into 36 readout sections plus a central common core where the total energy is collected. Segmenting the crystals allows us to have a better determination of the interaction points. Figure 3.21b shows a scheme of the segmentation for one crystal. The crystals are composed of n-type high-purity germanium (HPGe) and they are encapsulated to protect their surface. The signals are collected by preamplifiers located near the crystals and operating at cold temperatures, and thus, reducing noise signals considerably.

Pulse-shape analysis (PSA) is used in order to process the signals detected. This technique allows the identification with high precision of the individual interaction points within a segment and, with it, the gamma-ray path can be tracked. When a photon interacts with the material of

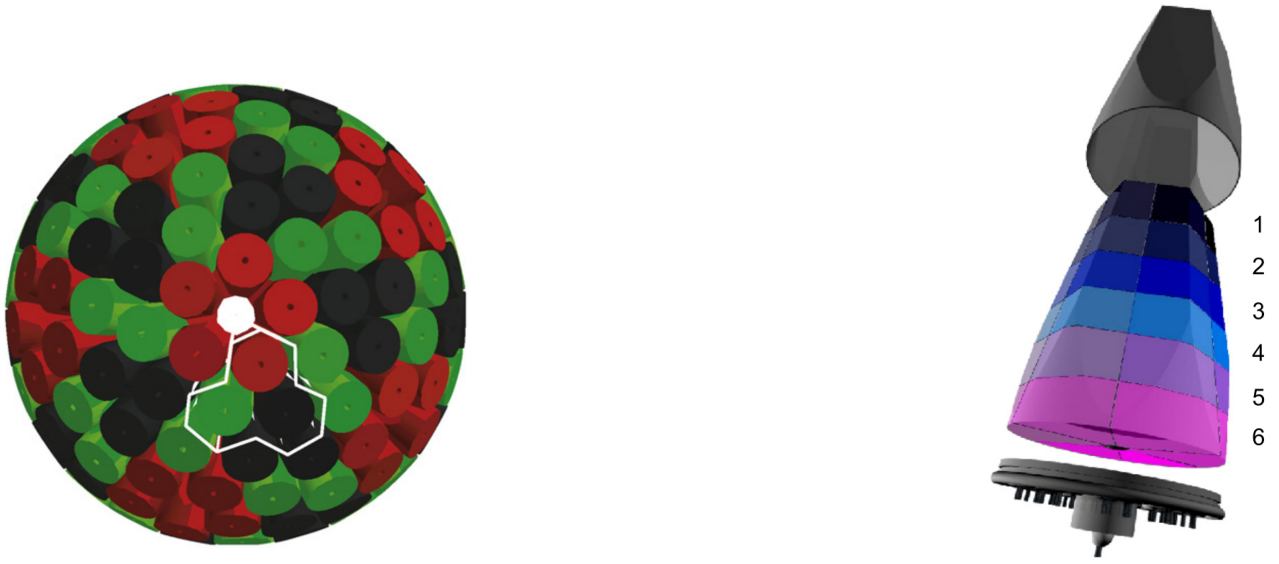

(a) (b)

Figure 3.21: (a) Scheme of the final configuration intended for AGATA with one cluster highlighted [Far10]. (b) Segmentation scheme for a crystal showing how the readout of each crystal is segmented in 36 sections and encapsulated [Akk12].

the crystal electron-hole pairs are produced and the electrodes of the nearest segments collect the net charge created. These collected signals will have a different shape depending on the position of interaction. Studying the different shapes for the different sectors and individual crystals allows the determination with high precision of the interaction position, and these wave-forms are also used to calculate the energy deposited in that point. From these signals a mapping of each individual segment of each crystal was created and it is used as a reference signal to compare with the experimental PSA signals.

The main purpose of the PSA technique is tracking the trajectory followed by a gamma ray. When a photon interacts with the detector, it can interact through Rayleigh scattering, Compton scattering, photoelectric effect and pair production. In the Rayleigh (or *elastic*) scattering the photon changes its direction, but very little energy is transferred from the photon to the material. This effect is more probable for γ-rays with low energy ($E_\gamma < 100$ keV). In the photoelectric absorption, a bound electron from an atom composing the material absorbs a photon, and it is ejected from the atom with an energy $E_{e^-} = h\nu - E_b$, where $h\nu$ is the energy of the photon and E_b is the binding energy of the electron. The photoelectric effect is predominant for photon energies $E_\gamma < 100keV$, and for materials of high Z, due to the higher number of electrons available. The Compton scattering is the dominant effect for γ-rays of energies in the range 0.1 - 10 MeV. In this effect, a photon interacts with the matter by transferring a fraction

of its energy to an electron in the absorbing material. In this transfer of energy, the direction of the photon changes with an angle θ with respect its original direction. Therefore, the energy transferred to the electron varies depending on the deflection angle. The final γ-ray energy can be calculated as:

$$E'_{\gamma} = \frac{E_{\gamma,0}}{1 + \frac{E_{\gamma,0}}{m_0 c^2}(1 - \cos\theta)}, \tag{3.33}$$

where $E_{\gamma,0}$ is the initial γ-ray energy, m_0 is the rest mass of the electron, c is the speed of light and θ is the angle of deflection from the initial direction. The pair-production process is energetically possible when the energy of the γ-ray exceeds 1.022 MeV. In this interaction, a photon creates an electron-positron pair. The excess energy above 1.022 MeV is shared between the electron and the positron. When the positron stops in the material, it is annihilated by interaction with a nearby electron, and two 511 keV photons are produced.

At the energies AGATA will normally operate (150 keV - 10 MeV) the dominant effect is Compton scattering [Akk12]. In this, the photon will undergo several scatterings until it is finally absorbed. The gamma ray will deposit energy in each interaction point and it can be collected within the same segment or it can be scattered to a neighbouring segment or crystal [Söd11]. A schematic view of a chain of interactions is showed in figure 3.22, where the total energy of the gamma ray will be the sum of the energies deposited in each interaction point. Following this principle, AGATA is used in coincidence mode, also known as add-back mode, where the energy detected by the different segments are added in a determined time-window, and operating in neighbouring regime. The add-back mode of detection improves significantly the efficiency.

After applying pulse-shape analysis for each crystal the events are allocated to their timestamps. The tracking algorithm is the applied in order to determine the coincident interaction points that will be used to calculate the total energy, and to reconstruct the scatters back to the emission point and direction of the detected photons. The algorithm also discards the events that are not physically reproduced by a Compton interaction, allowing the application of the background suppression technique. As mentioned before, Compton effect is the dominant process. Therefore, tracking algorithms are based on the properties of this effect. For this experiment the Orsay Forward Tracking (OFT) algorithm [Lop04] is used. It is based on forward tracking technique, where the first step is to group the interaction points into clusters according to their relative angular separation. This algorythm is automatically implemented in the first part of the data processing (given below) and, therefore, this part of the analysis has been processed by the AGATA collaboration.

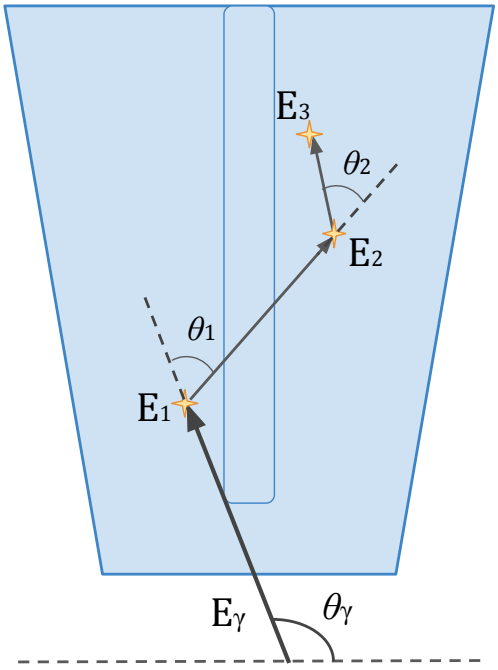

Figure 3.22: Example of a chain of Compton scattering events undergone by the same photon within a crystal. The photon incides with energy E_γ and angle θ_γ. It interacts with the crystal, depositing an energy E_1 and scattering with an angle θ_1. It travels again within the crystal until it interacts a second time depositing an energy E_2 and scattering with an angle θ_2. It finally is absorbed by the crystal depositing an energy E_3. The total energy of the photon is reconstructed adding the energies detected in each interaction using the tracking algorithm. See text for more details.

3.5.2 Data processing

In order to analyse the raw data produced by AGATA, there are 2 different processing levels to operate in. A Local Level Processing (LLP) [Tea19] will be applied before any building of events and a Global Level Processing (GLP) [Tea18] will be in charge of building and merging the events. A simple processing diagram is shown in figure E.1 of appendix E, where the steps to follow are shown and a brief summary of the applied actions for each step is given.

A first Local Level Processing is done before the experiment in order to identify possible dead segments to apply the correct detector topology. The different functions that process the data are called *actors*, and they are chosen at this level and applied on the data flow. This first step is key in order to optimise the data acquisition and peak resolution. There are three different actors within the LLP: preprocessing, PSA and post-PSA; the preprocessing actor is in charge of the calibrations and time alignments for each crystal; the PSA actor will determine the different hits from traces; finally the post-PSA actor applies neutron damage corrections, does recalibrations and finally global time alignments. Once the LLP is defined, it is applied to all the runs of the experiment. This part was done by the AGATA collaboration during the experiment.

The Global Level Processing is applied after the post-PSA corrections. This treats the AGATA data files using different actors in order to build and merge the events, including the data from the ancillaries such as MUGAST and VAMOS. This step is called the data replay and it is done offline using a software called FEMUL [Tea18]. This part was done after applying the VAMOS calibrations and as part of the present project.

Energy calibration

The energy calibration was done using a standard source ^{152}Eu and it was performed before the experiment by the AGATA team. It uses a standard calibration method, where the Eu transitions are assigned a channel and a linear fit is performed, obtaining the relationship between electronic channel and energy. A calibrated spectrum is shown in figure 3.23, where the Eu γ-ray transitions have been identified. This calibration is then extrapolated to the 4 MeV region and cross-checked up to 6 MeV during the experiment using fusion-evaporation channels.

Cross-talk correction

Cross-talk induces energy shifts and decreases the hit location precision as it mixes the signals induced on adjacent electrodes due to the drift of the charge carriers inside the germanium crystal. These effects can be found in any segmented detector, as also found in the

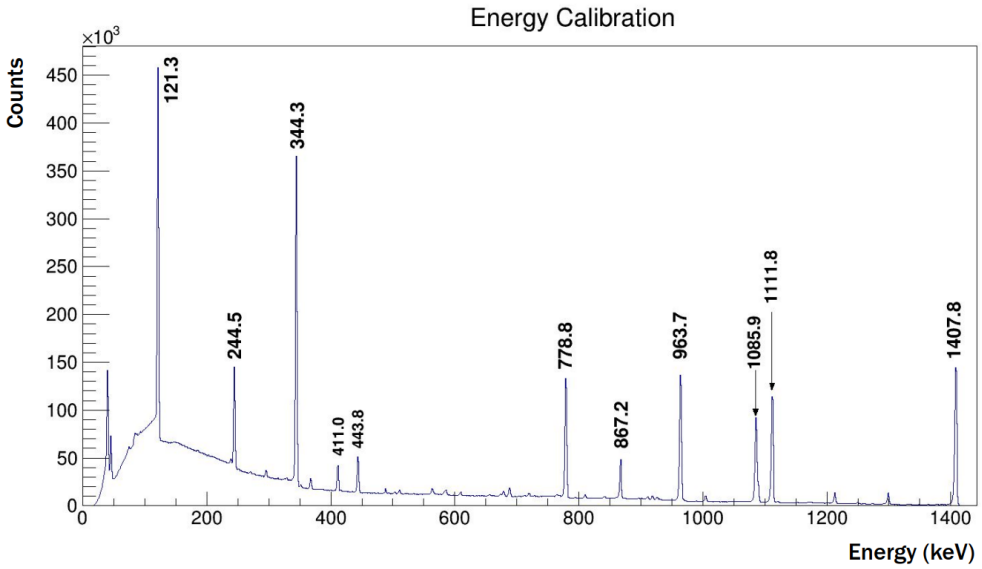

Figure 3.23: AGATA energy calibration is done using a ^{152}Eu source. In the image the gamma rays from the decay are determined and used to calibrate the channels. Y-axis registers the number of counts and X-axis shows energy in keV.

MUGAST detectors in section 3.3.4.1, in particular around missing strips. It is possible to use the AGATA cross-talk correction procedure to recover up to one broken or missing segment per crystal, by using the fact that the sum of the energies of the segments should be equal to the energy detected in the core. This procedure is done at the PSA level, and more details can be found in the AGATA documentation [Tea19].

Neutron damage correction

The interaction between neutrons produced by background reactions in the germanium detectors cause damages to the crystals, and this leads to a decrease of the spectra quality. Neutrons undergoing collisions with the germanium material can produce a displacement in the crystal. This dislocation in the lattice will trap charge carriers and, therefore, the charge collection is incomplete, causing a change in the charge collection properties of the detector. As a consequence, the detected γ-ray peaks present a broaden left tail, and this effect increases with time. Therefore, it is critical to correct this to achieve a good energy resolution. This correction is carried out at the Post-PSA level and it is done in three phases. Firstly, it is necessary to recalibrate the segments. Secondly, an estimation of the neutron damages is done and also a correction of energies. Finally, another recalibration is performed to correct the energies from possible shift induced by the neutron damage correction. An example of neutron damage correction is shown in figure 3.24, where the peaks before correction are shown in red corrected peaks are shown in white, for one of the crystals.

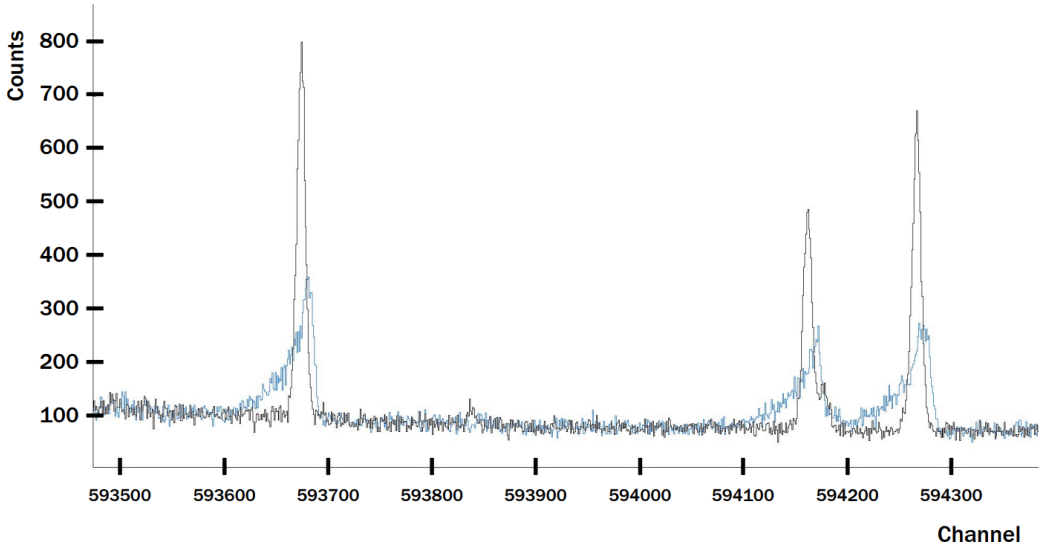

Figure 3.24: Example of neutron damage correction for crystal 10B. The broader line, in blue, is the signal before correction and the peaks after correction are represented in black. X-axis has the channel number for the given core and y-axis has the number of counts. Image adapted from the visualisation done using the TkT software [Tea19], where the individual crystal signals can be checked.

3.5.3 AGATA efficiency

The intrinsic efficiency of a HPGe crystal depends on its shape and the γ-ray energy. For a given detector, the full-energy peak efficiency remains close to 100% for energies lower than 100 keV, assuming that the γ-ray reaches the germanium crystal through its packaging and vacuum chamber. For this region, the photoelectric effect dominates and most of the incident γ-rays are absorbed and detected within a few mm. However, as the energy increases from 100 keV to 1 MeV, γ-rays start experiencing Compton scattering, escaping the detector instead of contributing to the full-energy peak efficiency. For energies higher than 1 MeV γ-rays can pass through the detector without interacting with the material [Kno10]; a significant percentage of events will not be detected and the efficiency quickly drops.

For this experiment, efficiency curves were extracted both from calibration runs and from Monte Carlo simulations. The different curves are shown in figure 3.25, provided by the AGATA collaboration previous to the experiment. The efficiency of detection can be measured using calibrated data at different energies. From this experimental data, an efficiency curve can be extracted to describe the efficiency over a range of energies. This is done by performing a Monte Carlo simulation and scaling it to match the experimental data.

For the present work, experimental data from two different calibration runs have been used.

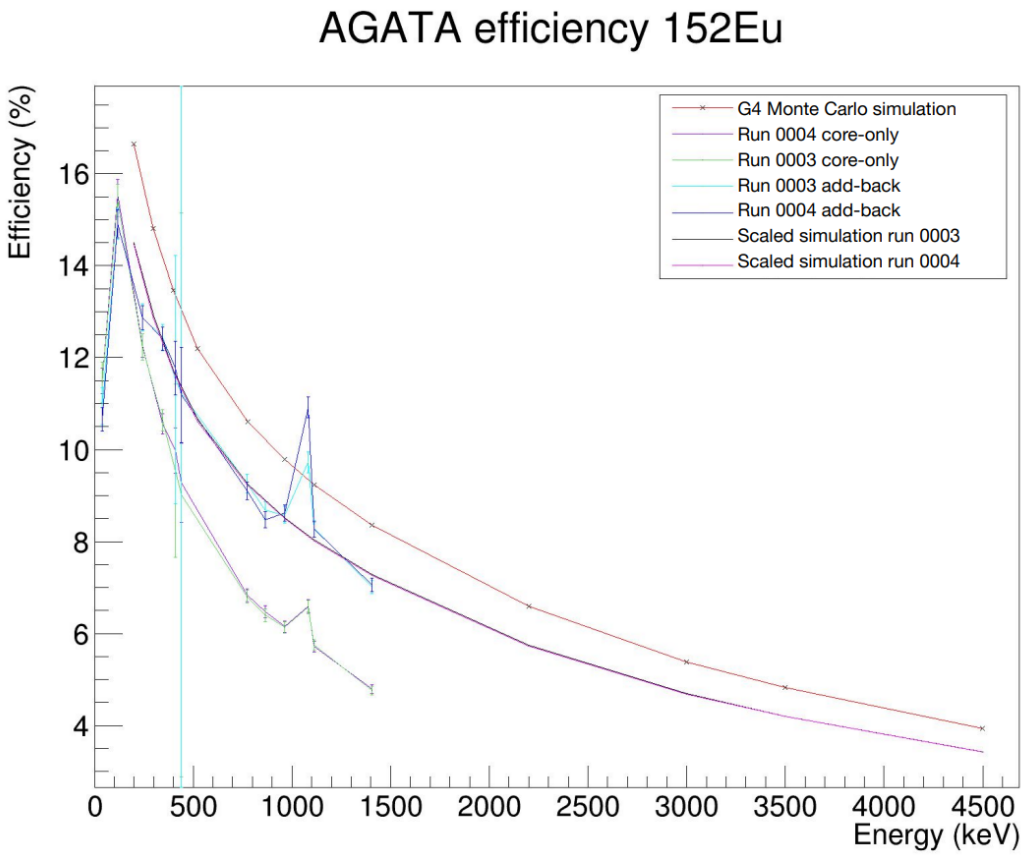

Figure 3.25: Extraction of the AGATA efficiency curve and extrapolation to higher energies, using a ^{152}Eu source (efficiency data from core-only is shown in green and violet, and the full add-back efficiency as used is shown in light and dark blue for runs 0003 and 0004 respectively). The Monte Carlo simulation (shown in red) is scaled (shown in black and pink for scaling to runs 0003 and 0004 respectively) to match the intensity calibrated experimental data. The efficiency curve plot was provided by the AGATA collaboration as part of the 2019 AGATA campaign.

In both cases we used an intensity calibrated ^{152}Eu source, as already detailed in section 3.5.2. In figure 3.25 the data points are shown for the add-back detection mode and for the core-only detection mode. The add-back mode increases the efficiency of AGATA in comparison with the core-only detection, as observed in the figure. The spikes present in the experimental points correspond to γ-rays that do not correspond to any ^{152}Eu transition. The red line with cross points corresponds to the Geant4 Monte Carlo photo-peak efficiency simulation. The black and pink lines, which overlap with each other, correspond to the re-scaled simulated efficiency curve matching the add-back data points from the two separate experimental runs. The re-scaled efficiency curves are consistent with each other, so either one can be used to determine the efficiency at different energies. In the present work, the pink line has been used for this purpose (scaled simulation run 0004).

In this project the γ-rays of interest are at 4 MeV, so it is important to achieve a good efficiency at high energies. This is the reason why AGATA was used in add-back mode as explained in section 3.5.1. The scaled simulation efficiency at 1.2 MeV is 7.6% and at 4 MeV is 3.8%. Because of the low statistics of the experiment, the high efficiency at 4 MeV achieved by AGATA will prove essential in the analysis described in the next chapter and the results following on from there.

Chapter 4

Analysis of the ^{15}O(^{7}Li, t)^{19}Ne reaction

The setup described in chapter 3 was used to perform the α transfer reaction studied in the present dissertation. A schematic representation can be found in figure 4.1, where the post-accelerated ^{15}O beam interacts with the target producing nuclear reactions. The light charged particles produced are detected by MUGAST at backward angles, whereas the recoils enter VAMOS, where they are separated and detected. The prompt γ-rays produced in the de-excitation of the ^{19}Ne recoils are detected by AGATA. A diamond detector was implemented just before the VAMOS focal plane to stop the non-reacted beam and to monitor the beam. This method worked well as an online monitor, however it was too small to cover the whole beam spot and some other performance issues should be addressed to be used as a beam counter alongside as a beam monitor. The work performed with the diamond detector seems promising and a conference proceedings paper was published on this matter: "An implantation Diamond detector as a beam monitor for an intense radioactive ion beam" [Roj20]. Details of this publication are summarised in appendix F.

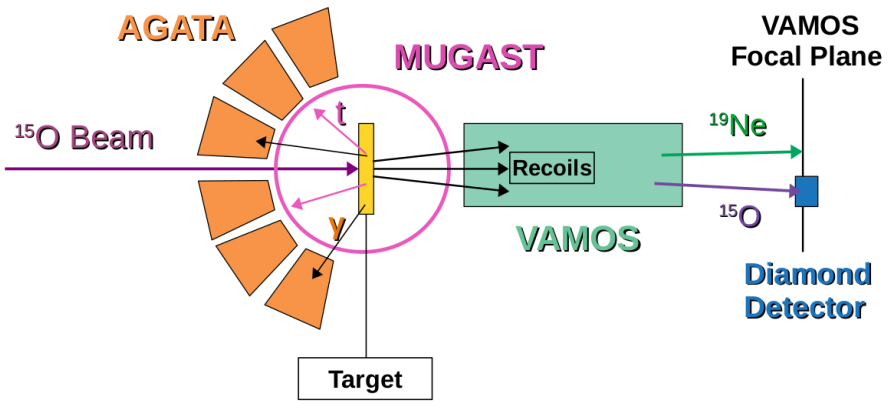

Figure 4.1: Schematic view of the setup.

Performance of an α transfer reaction in inverse kinematics was selected taking advantage of the RIB production at GANIL. The chosen reaction was ^{15}O(^{7}Li, t)^{19}Ne where the excited states of the ^{19}Ne recoils were populated by bombarding a 1.25 mg/cm^2 LiF target using a post-accelerated ^{15}O radioactive ion beam (RIB) at 4.72 MeV/u produced using the SPIRAL1 facility, as already detailed in chapter 3. The setup composed of MUGAST, AGATA and VAMOS was chosen to achieve the triple coincidence between the produced ejectile, recoil and γ-ray from the de-excitation of the recoil.

After calibrating the detectors, a thorough analysis of the experimental data was done. Details of the analysis methods are described in the following sections. This includes heavy-ion identification, triple-particle coincidence, Doppler correction optimisation, excitation energy calculation, analysis of the γ-ray spectra, absolute beam normalisation and extraction of angular distributions and experimental differential cross sections.

4.1 Reaction mechanism

The ^{15}O(^{7}Li, t)^{19}Ne transfer reaction was performed in inverse kinematics. As explained earlier in chapter 2.3, the outgoing kinematics of transfer reactions are constrained by the excitation energy of the populated resonances, and the angular distributions depend on the transferred angular momentum. Extracting the differential cross section for each resonance allows the calculation of spectroscopic factors. Furthermore, by applying energy and momentum conservation rules the angle and energy in the laboratory frame can be linked. For transfer studies it is important to cover the forward angles in the center of mass frame to allow a good description by the DWBA model calculations.

The two experimental possibilities to perform a transfer reaction study are: direct kinematics, where the projectile is lighter than the target; and inverse kinematics, where the projectile is heavier than the target. Depending on the type of kinematic used the angular distributions and energies of the outgoing particles will vary significantly [HS21]. The kinematic lines for direct and inverse kinematics are shown in figure 4.2 for the excited state at 4.033 MeV in ^{19}Ne. Furthermore, forward angles in the center of mass correspond to forward angles in the laboratory frame in case of direct kinematics, and to backward angles in the laboratory frame for inverse kinematics. Also, for direct kinematics the triton energy is of about 25 MeV, while the energy is much smaller ($\sim$2 MeV) in case of inverse kinematics.

Inverse kinematics is advantageous for this project for many reasons. This transfer reaction is not experimentally possible in direct kinematics because an ^{15}O target cannot be synthesised due to the radioactive and short-lived nature of this isotope. However, ^{15}O RIBs are available

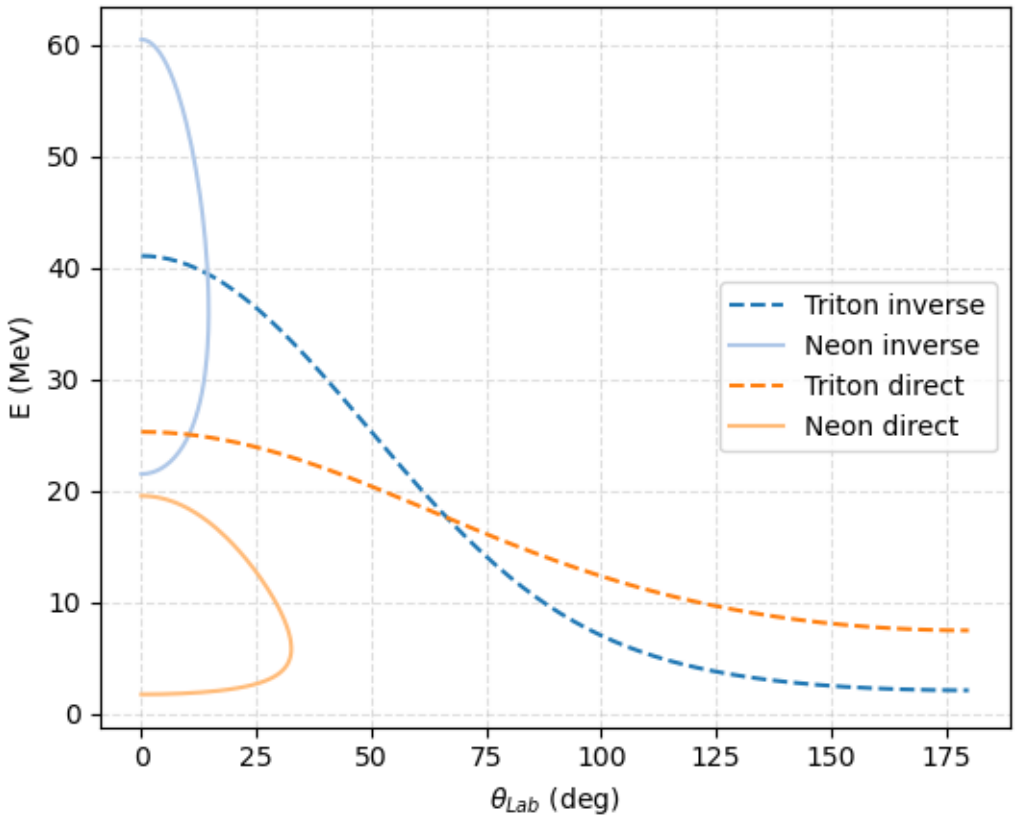

Figure 4.2: Kinematic lines for the outgoing particles in the laboratory frame comparing direct and inverse kinematics.

with a remarkable high intensity at GANIL. In inverse kinematics the recoil angles are constrained to forward angles $\theta_{lab} < 20$ deg, where VAMOS is located covering $\theta_{lab} = \pm 6$ deg. Furthermore, tritons are detected at backward angles $\theta_{lab} > 100$ deg.

4.2 Heavy ion identification

The VAMOS spectrometer and separator was used to detect and select the heavy recoils. This spectrometer has the advantage of achieving a very good recoil selectivity allowing to identify the different isotopes from the reconstruction of each particle's path and velocity, as well as the detection of the energy loss and total recoil energy in the ionisation chamber. It furthermore has a large acceptance, which is important particularly in α-transfer on light beams.

4.2.1 Mass and charge calculation

Having time and energy calibrated, the determination of mass and charge can be easily done defining them from the magnetic rigidity ($B\rho$) reconstruction and the total energy of the recoil. In order to have an optimal identification the calculations are done focusing on the ^{19}Ne 9+ charge state. The steps followed in this section are: element identification, mass over charge reconstruction, mass calculation, charge calculation and, finally, minor corrections to optimise the particle identification.

Z identification

The way a particle loses energy depends on Z. Plotting the energy loss (ΔE) detected in the first two sections of the IC against total energy (E_T) will show patterns that allows the identification of the different chemical elements. Figure 4.3 shows a ΔE - E_T plot where all of the particles lose energy following a linear trend until they reach the Bragg peak at a total energy corresponding to the maximal energy loss in the IC section, and they start losing less energy until they deposit all their remnant energy. This experiment is focused on the creation of neon-19 (Z = 10). Other particles are detected, such as fluorine (Z = 9) and oxygen (Z = 8), products of other reactions taking place and part of the beam coming into the detector. The energy loss was graphically shown in figure 3.17, where simulations were performed using LISE++ to calibrate the ionisation chamber. For the different chemical elements the Bragg

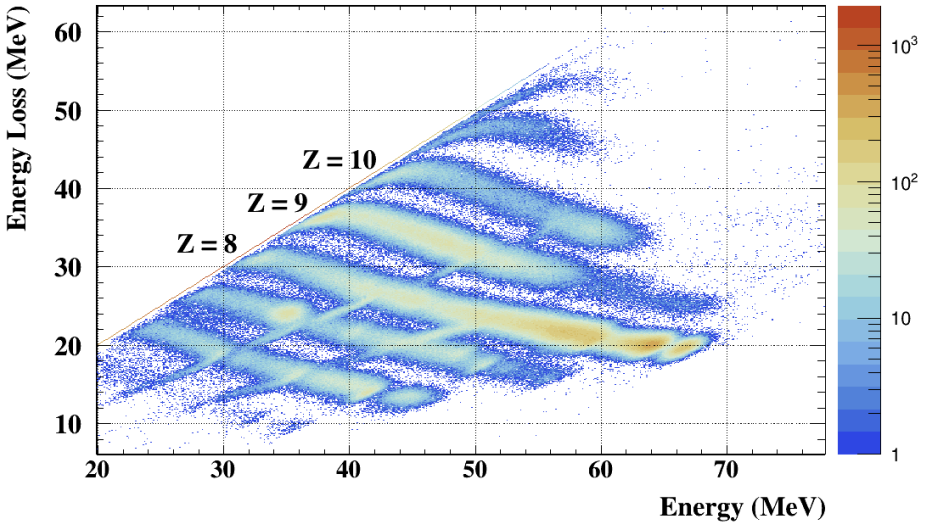

Figure 4.3: ΔE - E plot showing the different chemical elements detected in the IC. ΔE corresponds to the energy loss detected in the first two sections of the IC, and E_T is the total energy detected in the IC.

peak happens at different total energy. Higher Z will have a higher value of energy loss in its Bragg peak, as we can appreciate in figure 4.3, where O, F and Ne are identified. The oxygen particles present three well defined blobs. These blobs correspond to the beam particles that undergo scattering effects when interacting with the target chemical elements (Li and F atoms), entering the spectrometer at different angles and registering a different energy than the unreacted oxygen particles.

Mass over charge reconstruction

Using the reconstruction of the magnetic rigidity ($B\rho$) the determination of the mass over charge (M/q) is given by $B\rho = 3.105\frac{A}{q}\beta\gamma$, where β and γ are the relativistic velocity and the Lorentz factor, defined in 3.10 and 3.11. As we can see, these definitions depend on the velocity of the particles defined as $v = \frac{D}{t}$, where D is the distance from the target to the focal plane and t is the time of flight. In order to have a good definition of mass over charge, the time definition must be as optimal as possible and D must be the specific path for the ion going through VAMOS accounting for the emission angles, as detailed in section 3.4 based on the observed focal plane position and angles. Therefore, the time offset must be optimised to have the right M/q. The way to do it is plotting M/q and gating on the element Neon from the Z identification plot (figure 4.3). Each neon isotope created during the reaction will appear in this plot with a centroid value of M/q close to its real value, shown in table 4.1. The time offset has been optimised for ^{19}Ne (9^+) by aligning the M/q to it.

Isotope	q	M/q [theory]	M/q [centroid]
19-Ne	10+	1.90	1.91
	9+	2.111	2.115
	8+	2.375	2.367
20-Ne	10+	2.00	2.01
	9+	2.222	2.226
	8+	2.50	2.50
21-Ne	10+	2.10	2.12
	9+	2.333	2.31
	8+	2.625	2.623

Table 4.1: Values of mass over charge for the different neon isotopes detected and theoretical values.

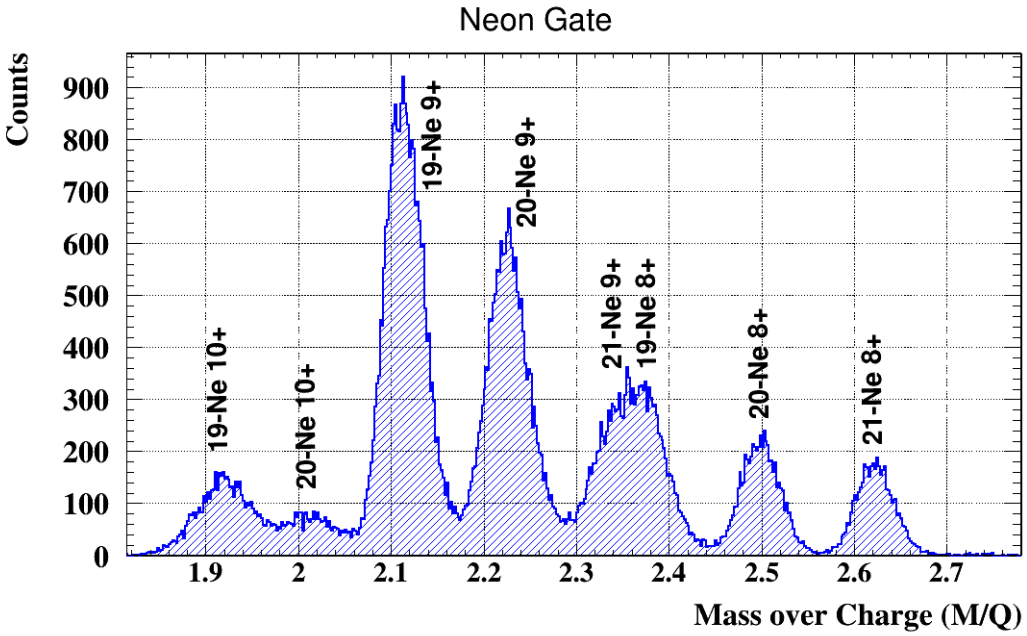

Figure 4.4: Mass over charge plot for the different neon isotopes. A good determination of M/q implies the time calibration is well done. Time calibration optimal for our nucleus of interest ^{19}Ne, with charge state $q = 9^{+}$.

Charge state identification

The last step to have an optimal identification is aligning the charge state. It is calculated from the definitions of mass and mass over charge previously calculated, using

$$q = \frac{M}{M/q} \ . \tag{4.1}$$

The energy loss in the ionisation chamber must be refined by including a scaling factor for each section of the IC and by modifying them until the charge state is aligned. In order to have a better alignment a condition is set (shown in appendix A.6a) to remove the Bragg peak off the calculation, as we can see in appendix A, figure A.6b. This condition removes the particles at lower energies and makes the alignment of the charge states easier. The procedure to align the charge states involves modifying the scaling factors for each ionisation chamber. To check that the alignment is correct, the first two IC sections are modified first, aligning them by plotting charge state versus total energy. When the first two are aligned, the next section is added and the alignment proceeds in the same way. Sections are added subsequently until all of them are aligned and the charge state is flattened. Figure 4.5a shows the charge states before the alignment and figure 4.5b shows the charge state against the total energy after the alignment has been performed. In figure 4.6 mass and charge plots are shown after corrections

have been applied, showing a very good selectivity in the heavy ion determination.

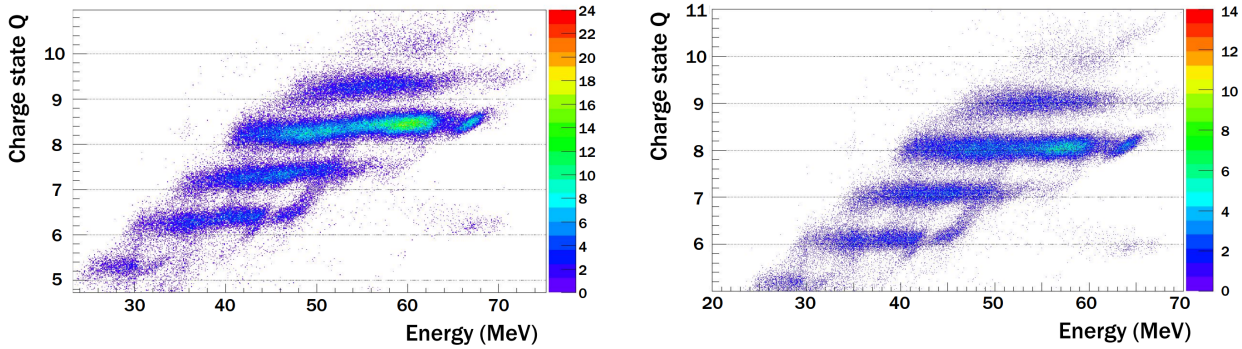

(a) Before alignment.

(b) After alignment.

Figure 4.5: Comparison between charge versus energy plots before and after doing the charge alignment. Alignment done refining the energy loss of each IC segment until it flattened. The colour scheme (z axis) represents the number of events.

Mass reconstruction

In order to determine the mass, the relativistic Einstein equation given by $E = (\gamma - 1)\, Mc^2$ is used, where E is the total energy, γ is the Lorentz factor defined in 3.11, M is the mass of the particle and c is the speed of light. From this expression, the mass can be defined as

$$M = \frac{E}{(\gamma - 1)\, c^2}, \tag{4.2}$$

where γ is the Lorentz factor defined in 3.11, calculated using the velocity of the recoil and, therefore, from the recoil time-of-flight and path.

The total energy is then calculated using the signal detected in the ionisation chamber, and the scaling factor f using equation 3.20. In plot 4.6a the mass value needs to be aligned with the right value for M/q. If the masses are mismatched the scaling factor f can be modified to align them.

4.2.2 Angular deviation

The path done by a particle may vary from one particle to another depending on its incident ϕ angle in the Y axis on the focal plane. In order to include the angular deviation a correction must be performed dividing by $\cos\phi$. The corrected distance is $D_{\text{corrected}} = \frac{D}{\cos\phi}$ as a first order correction. The effect is not very noticeable, as this angle is normally very small with $\phi \simeq 0.01$ radians. However, in order to have the correct distance of the particles every minor detail must be corrected.

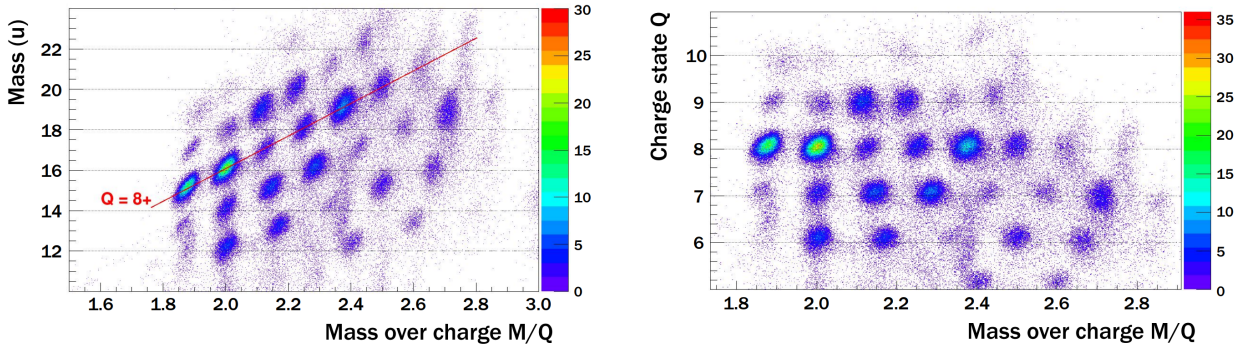

(a) Mass versus M/q

(b) Charge versus M/q.

Figure 4.6: Final plots after applying the calibrations and corrections. The colour scheme (z axis) represents the number of events.

4.3 Triple particle coincidence and Doppler correction

The identification of α transfer reactions is done combining the detection of tritons, heavy ions and γ-rays from the three detector systems. Here, a particle detected in MUGAST triggers a signal starting a time window of coincidence. Within this window, the coincidences are taken from any particle detected in the other two detectors. As shown in figure 4.7 the combination of the triple coincidence achieves a very clean spectrum, removing all of the fusion-evaporation events when the recoil gate is applied. As shown in the heavy ion identification section (4.2), VAMOS is able to isolate the ^{19}Ne recoils in their 9+ charge state.

Using the information of the recoil velocities from VAMOS the Doppler correction for the γ-ray energy is also applied on an event by event basis according to:

$$E_{DC} = E_{det} \cdot \gamma \left(1 - \beta \cdot \cos\theta\right), \tag{4.3}$$

where E_{det} is the energy detected in AGATA, γ is the Lorentz factor, β is the reduced velocity and θ is the angle of detection relative to the direction of the heavy-ion. With this Doppler correction the resolution achieved is 10 keV for a peak at 1 MeV and 40 keV for a peak at 4 MeV, which corresponds to a relative energy resolution of 1%. This is in agreement with the energy resolution $\leq 1.6\%$ simulated by Clement *et al.* for recoil velocities $\beta = 0.1$ [Cle17]. The Doppler correction thereby helps to separate the γ-ray peaks allowing the identification of the different transitions from the ^{19}Ne excited states. This is shown in figure 4.7 where for example the improved separation is particularly clear in the 1.2 MeV region.

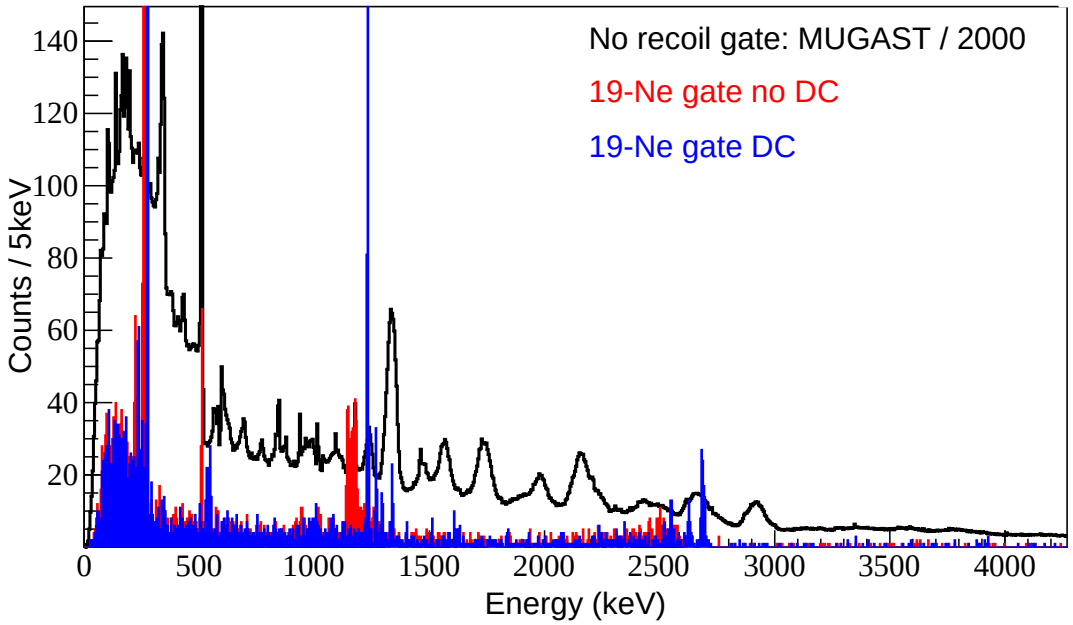

Figure 4.7: γ-ray energy plot comparing the spectrum obtained for different gates. The black line represents the γ-rays in coincidence with any particle detected in MUGAST; this being dominated by the fusion-evaporation reactions, and it has been scaled down to compare with the gated spectra (divided by 2000). The red and blue lines are the spectrum once applied the VAMOS gates, selecting ^{19}Ne 9+ nuclei. The broader, red spectrum corresponds to the detected γ-rays and the blue peaks are the Doppler corrected γ-rays. It is clear that the energy Doppler correction achieved is outstanding, obtaining a very good resolution of $\simeq 1\%$ relative to the energy peak.

4.3.1 Doppler correction optimisation

The Doppler correction depends on the angle of emission of the γ-ray as stated in equation 4.3. If the correction is done assuming the reaction takes place in position (x,y,z)=(0,0,0) the angle might not be the correct one; the Doppler correction will depend on the actual position of the interaction point. To account for this effect, a study of the broadening of the peaks has been carried out by performing a minimisation of the resolution mapping in x and y for the beam position. This is done by reconstructing the Doppler energy for different values of x and y for the beam position on target, fitting the peak, extracting the peak width, σ, and based on this data finding the optimum position where σ is minimal.

The chosen peak for this investigation was the γ-ray at 275 keV, for which the lifetime is long enough to ensure that it decays after the target, thus the resolution not being affected by target effects. With this method it is easy to check whether the interaction position of beam and target deviates with respect to the AGATA detectors as can be seen in figure 4.8. Even

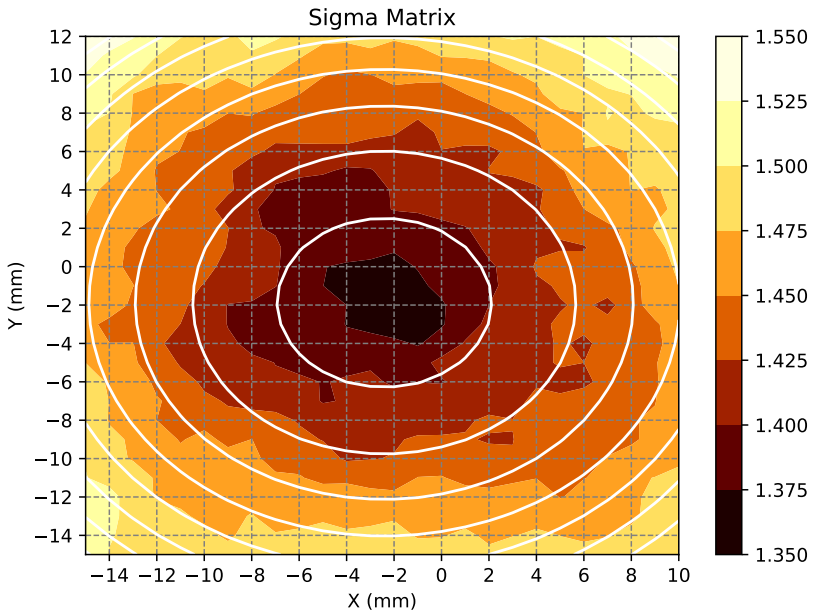

Figure 4.8: Reconstruction of peak resolution for different X and Y coordinates, showing a shift in X and Y.

though this method is good enough to identify the shift, the beam spot size is significant (about 2.5 mm radius) and the position of interaction has a considerable uncertainty.

The same study was also done to correct the z position of the target and the recoil velocity measured in VAMOS. The γ-ray events were separated in two rings defining two different angular regions. For each ring a mapping of z position against $\Delta\beta$ was extracted and a linear fit was done. As β and z have to be consistent for both rings, the shift can be calculated from the intersection of the two lines.

These corrections improve the resolution of the γ-ray energy peaks by 2 keV at 4 MeV. Detailed plots are included in appendix A.4. The target position was calculated using the peak at 1232 keV due to its short lifetime as it decays before leaving the target, obtaining a target position $z_t = 1.33$ mm. An estimation of the lifetime for the 275 keV state can also be done based on target positions. The z, β correction for the 275 keV state indicated that the nucleus decays at position $z_{275} = 2.53$ mm. The distance the recoil travels before decaying is given by the difference between z_{275} and z_t is $d = 1.2$ mm. The lifetime is calculated using

$$d = \tau_m \beta c \ , \tag{4.4}$$

where d is the average distance travelled by the nucleus before decaying, τ_m is the average lifetime, β is the relative recoil velocity and c is the speed of light. A result for $\tau_m = 50 \pm 40$ ps

is found, which is in agreement with the value found in the literature $\tau_m = 61 \pm 30$ ps [Bha70].

4.4 Excitation energy calculations and target effects

The recoil excitation energy E_x can be calculated from the two-body kinematic relationship (see appendix B), where the triton ejected carries information about of the recoil excitation energy. Knowing the energy and the angle in the laboratory frame is sufficient to extract the recoil excitation energy. In this case, the energy in the laboratory frame is detected by the MUGAST detectors, as well as the angle of the triton. From these values, the total triton energy and momentum can be obtained as:

$$e_e = E_{lab} + m_e \tag{4.5}$$

and

$$p_e = \sqrt{p_e^2 - m_e^2} \ , \tag{4.6}$$

in units where $c = 1$ and where e_e is the energy of the triton (ejectile), E_{lab} is the triton kinetic energy measured, m_e is the triton mass given in MeV, and p_e is the the triton momentum. The triton angle θ_{lab} can also be used to reconstruct the momentum components in Cartesian coordinates:

$$\begin{aligned} p_{e,x} &= p_e \cdot \sin\theta_{lab} \\ p_{e,y} &= 0 \\ p_{e,z} &= p_e \cdot \cos\theta_{lab} \end{aligned} \tag{4.7}$$

for an event where the azimutal angle $\phi = 0$, defining the coordinates system such that the x-axis is in the scattering plane.

Using the two-body kinematic equations, the excitation energy, E_x, of the recoil can be calculated by obtaining the recoil energy and subtracting its mass

$$E_x = e_r - m_r \ , \tag{4.8}$$

where e_r is the energy part of the recoil's momentum 4-vector and m_r is the relativistic mass of the recoil in its ground state given in MeV, which can be obtained from

$$m_r = T_p + m_p + m_t - T_e - m_e + T_r \ , \tag{4.9}$$

where T_p, m_p are the projectile kinetic energy and mass , m_t is the target mass, T_e, m_e are the

ejectile kinetic energy and mass, and T_r is the recoil kinetic energy, which can also be deduced from the conservation laws as

$$T_r^2 = T_A^2 + T_b^2 - 2T_A T_b \cos\theta_{Lab} \ . \tag{4.10}$$

Simulation of target effects

NPTool [Mat16] simulations were performed to study the effect of the target thickness on the excitation energy resolution. This is important to include the right gates for each excited state. Simulations were done for the most intense states and for the 4.033 MeV state. The simulated beam used was a *perfect beam* assuming no straggling in energy or angle and different target thicknesses were used to show the dependency on stopping in the target. The target thickness introduces an important effect in the resolution of the peak, adopting a top hat shape as shown in figure 4.9b. From the resolution obtained in the calibration section (see chapter 3.3.2) of about 50 keV the target changes this to 1.5 MeV. This resolution is not enough to resolve the different excited states directly from the triton kinematics. However, gating on the individual γ-rays is sufficient to select the excited events, in combination with a gate for the excited state energy that will prove useful to remove the background events outside the excitation energy region such as indirect feeding of each state from higher-lying states.

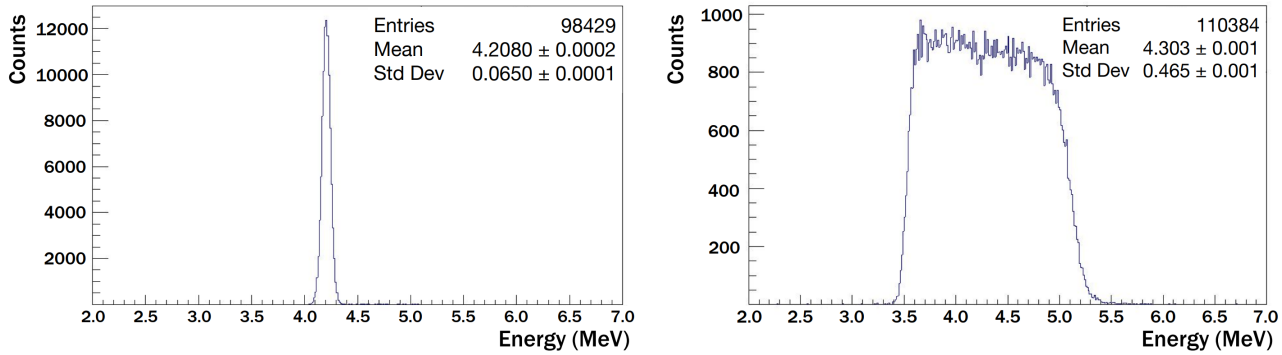

(a) (b)

Figure 4.9: Target effect plots from simulations. (a) shows a simulation of a perfect beam on a very thin target. (b) shows a simulation of a perfect beam on a target of thickness equal to 1.25 mg/cm^2. Using a thick target, therefore, decreases the excitation energy resolution to FWHM= 1.5 MeV.

4.5 Analysis of the gamma ray energy spectrum

Once all the calibrations and optimisations have been applied, the different ranges of energy where gamma rays are expected can be analysed. It is important to do a thorough study of the ^{19}Ne transitions that are populated in order to control the background. Identifying the transitions and the peak resolution at different energies is also important for this work to gate on specific excited states. The total spectra obtained gating on ^{19}Ne 9^+ is shown in figure 4.10, where the spectrum has been divided in three different energy ranges: 0 to 1500 keV (top), 1500 to 3000 keV (middle) and 3000 to 5000 keV (bottom). The identified γ-ray transitions have also been labeled. Table 4.2 shows the excited states and corresponding transitions identified in the plot.

Most of the peaks correspond to well known transitions. However, there are a few new transitions from excited states above the alpha threshold recently identified by Hall *et al.* [Hal19] that are also identified in this work. These are transitions at $E_\gamma = 2527$ keV and at $E_\gamma = 3897$ keV. Studies from Hall *et al.* also suggest a swap of spin-parity of the $E_x = 4140$ keV and $E_x = 4197$ keV excited states. Figure 4.11 shows a simplified decay scheme that includes the new transitions measured by Hall *et al.* (dashed red arrows) and the new transition identified in the present work (solid blue arrow). The events detected in the region below $E_\gamma = 3897$ keV come mostly from the expected Compton background from the peaks above. This background will be assessed in section 4.5.1.

The transition at $E_\gamma = 4197$ keV is not recorded in the previous work or in the new transitions observed by Hall *et al.* The observed peak has 4±2 counts within a energy region equal to approximately 2σ. It has to be a transition to an excited state below 1 MeV, given the excitation energy gates applied. This could correspond to a transition: 4197 $\longrightarrow$ 0 keV, 4435 $\longrightarrow$ 238 keV or 4472 $\longrightarrow$ 275 keV. There is no previous record of experiments indicating a state at $E_x = 4435$ keV or at $E_x = 4472$ keV, therefore these two options are unlikely. This means the detected peak could be a suppressed transition to the ground state with an intensity of about $3 \pm 2\%$, which is below the sensitivity of the previous experiments.

4.5.1 Background assessment

There are two contributions to the background that must be accounted for: Compton background from photo-peaks around the 4 MeV region, and contributions from other isotopes that might leak into the ^{19}Ne gates. As explained before, the neon isotopes are selected by applying a gate in the $\Delta E - E$ plot, shown in figure 4.3. From this selection, the mass of the different

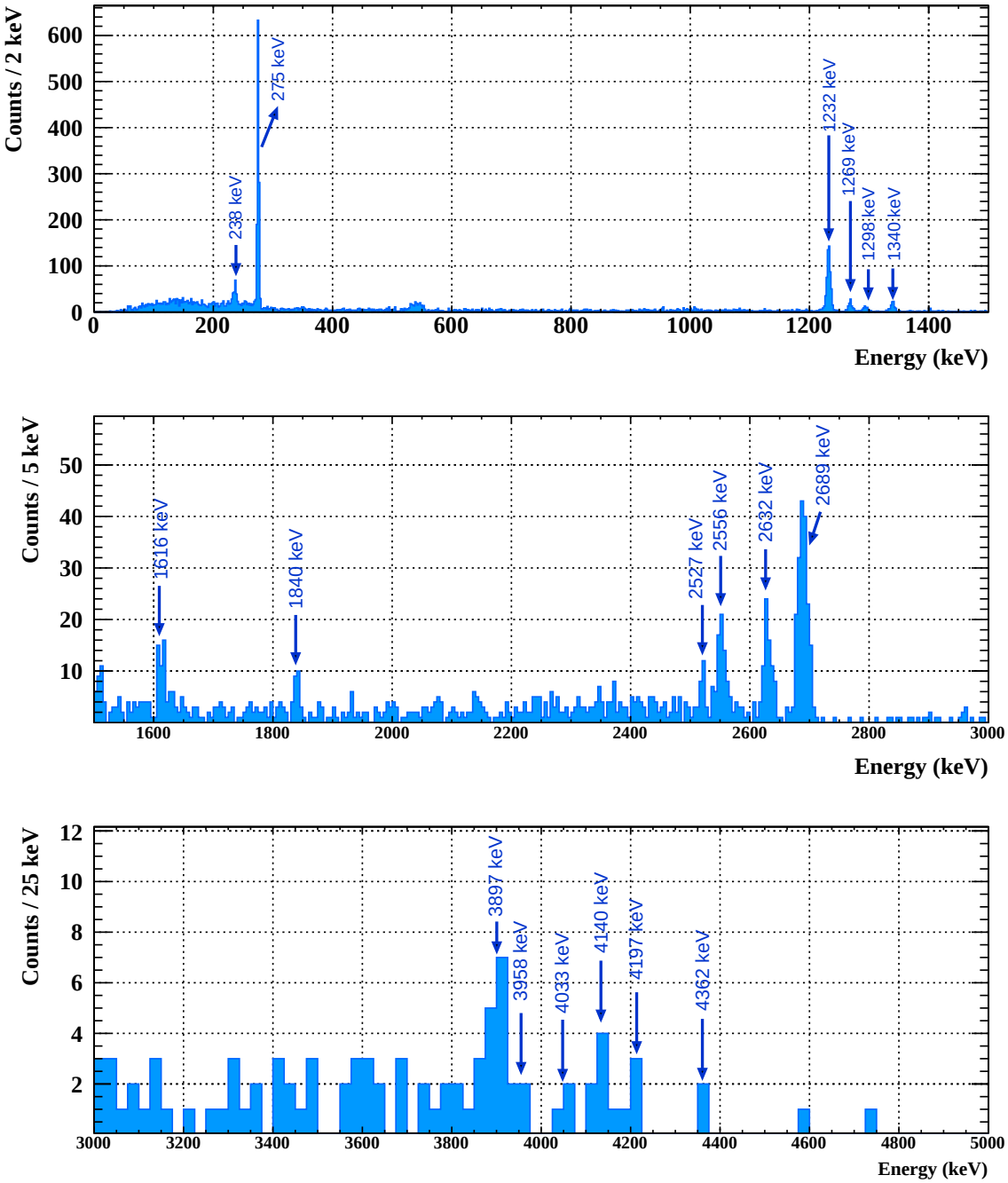

Figure 4.10: Energy spectrum for ^{19}Ne transitions detected in the triple coincidence. The spectrum is divided in three different energy ranges. The main γ-ray transitions are labeled. Different binning has been selected according to the resolution of the energy range.

E_x (keV)	J_i^π	E_f (keV)	J_f^π	E_γ (keV)	N
238.3	$5/2^+$	0.0	$1/2^+$	238.3	222
275.1	$1/2^-$	0.0	$1/2^+$	275.1	1159
1507.6	$5/2^-$	275.1	$1/2^-$	1232.5	548
		238.3	$5/2^+$	1269.3	100
1536.0	$3/2^+$	238.3	$5/2^+$	1297.7	69
1615.6	$3/2^-$	275.1	$1/2^-$	1340.5	95
		0.0	$1/2^+$	1616.0	51
2794.7	$9/2^+$	238.3	$5/2^+$	2556.4	78
4032.9	$3/2^+$	0.0	$1/2^+$	4033.0	3
4140.0	$7/2^-$	1615.6	$3/2^-$	2527.2*	30
		1507.6	$5/2^-$	2635.8	76
		238.3	$5/2^+$	3897.5*	15
4197.1	$9/2^-$	1507.6	$5/2^-$	2689.5	183
		238.3	$5/2^+$	3958.8$^?$	4
		0.0	$1/2^+$	4197.0†	5
4379.1	$7/2^+$	238.3	$5/2^+$	4140.8	6
4600.0	$5/2^+$	238.3	$5/2^+$	4362.0	2
		0.0	$1/2^+$	4602.3*	1
4635.0	$13/2^+$	2794.0	$9/2^+$	1840.0	27

* New transitions observed in [Hal19].

$^?$ Not seen by Hall *et al.* and not distinct in this work.

† New transitions from present work.

Table 4.2: ^{19}Ne excited states with observed transitions listed. Information of spin-parity added for the initial and final states. The total number of counts detected for each transition has been included. Some of the states are fed from above, therefore the direct population has to be evaluated by including excitation energy gates.

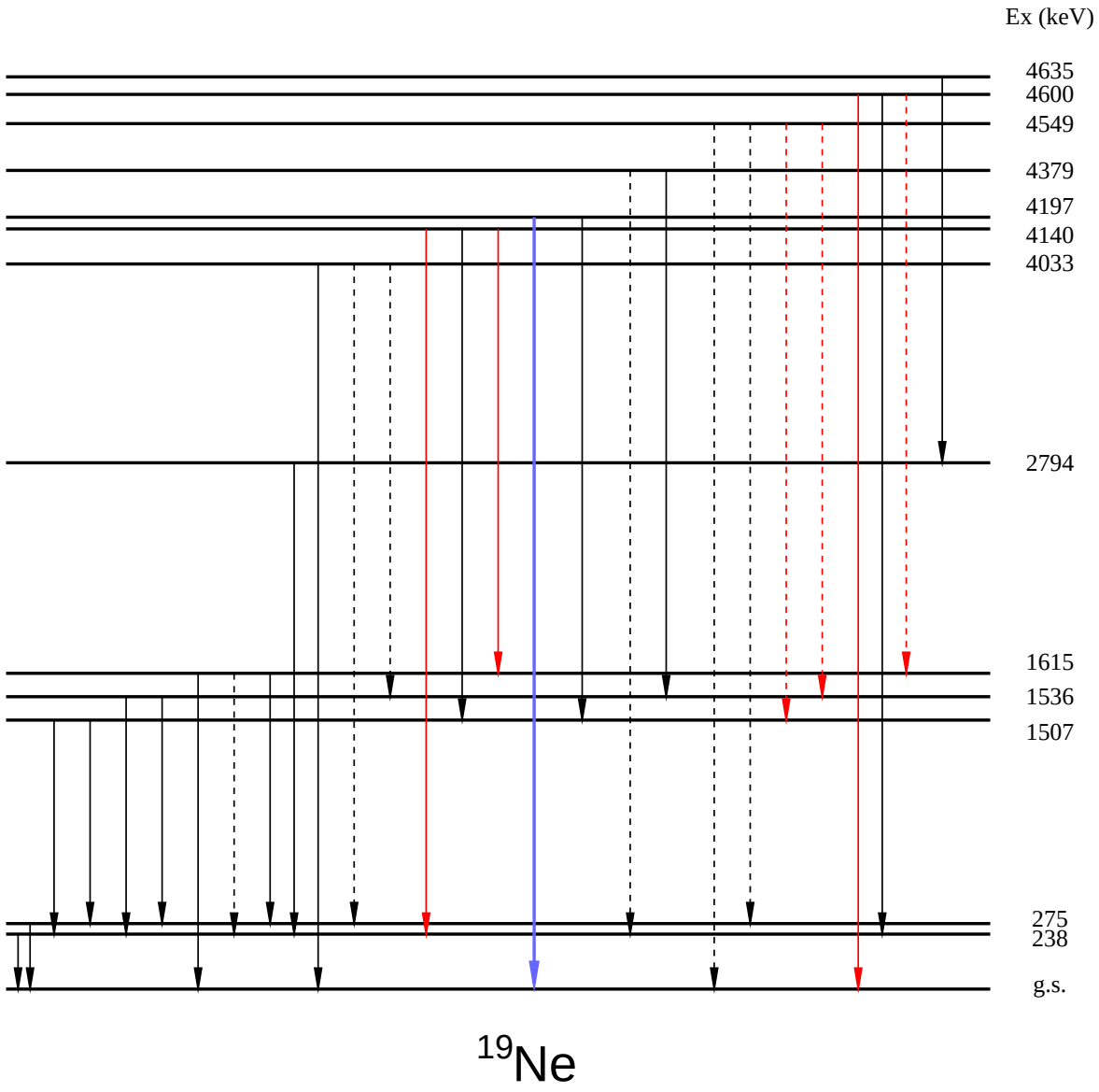

Figure 4.11: ^{19}Ne simplified γ-ray decay scheme. The red arrows indicate the new transitions identified by Hall *et al.* and the black arrows represent the transitions accepted in literature before the Hall measurements. Solid (dashed) lines represent transitions which were observed (not observed) in the present work. The solid blue arrow indicates the tentative new transition detected in the present work.

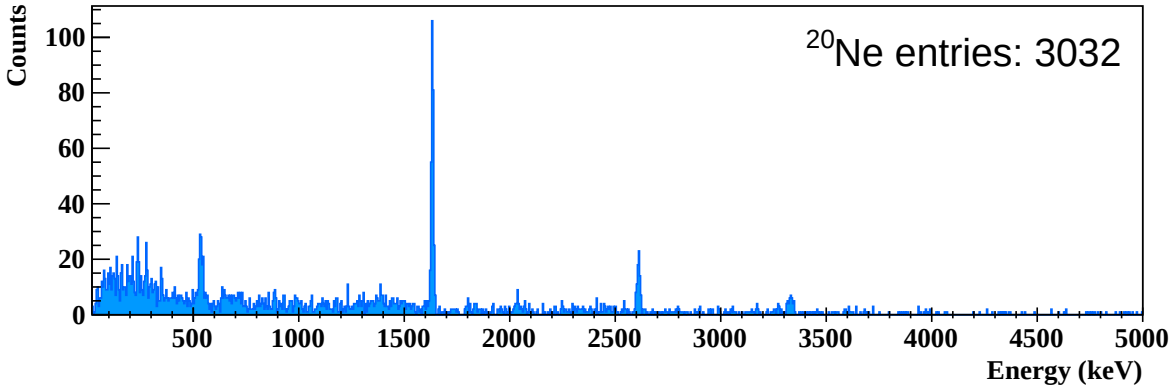

Figure 4.12: γ-ray spectrum obtained for the ^{20}Ne events detected.

neon isotopes can be calculated, as already explained in section 4.2.1. Therefore, a condition can be applied in q and M to select the ^{19}Ne (9^+) events. However, there is a substantial number of ^{20}Ne (9^+) recoils detected, as shown in the γ-ray spectrum in figure 4.12, and the possibility of these events leaking in the imposed ^{19}Ne gate must be studied.

In figure 4.13, the events corresponding to masses $A = 19$ and $A = 20$ are plotted. The gate imposed to select the $A = 19$ is represented by the solid vertical lines, and Gaussian fits have been performed to the two peaks. Here, the left tail of the ^{20}Ne isotope is leaking inside the mass 19 gate. This leakage corresponds to the 2.3% (red filled area) of the ^{20}Ne events detected. It will contribute to the background and it needs to be taken into account especially for the low statistics peaks detected. In figure 4.15 the contribution to the total background by the ^{20}Ne events in the $3200 - 3800$ keV energy region is shown in red.

To study the Compton background expected in our spectrum, Geant4 simulations were performed and provided for each individual state by the AGATA team. The peaks simulated were the expected γ-rays above 3800 keV, shown in figure 4.14. They have been scaled to match the experimental data detected for each photo-peak simulated, by normalising the photo-peak to the area of the observed peaks in the $3800 - 4600$ keV region. The simulations also show the single-escape peaks located at 511 keV to the left of each photo-peak. This gives a good estimation of the expected background. A comparison of the simulated and the observed background is shown in figure 4.15 for the $3200 - 3800$ keV energy region, where the simulated Compton background contribution is shown in blue, and the experimental data obtained is shown in black.

The total contribution from the ^{20}Ne leakage and the Compton background on this region is $N_{back,sim} = 30$, whereas the detected background is $N_{back,det} = 36$. The observed background is therefore approximately 1σ from the value predicted by our experimentally scaled simulations.

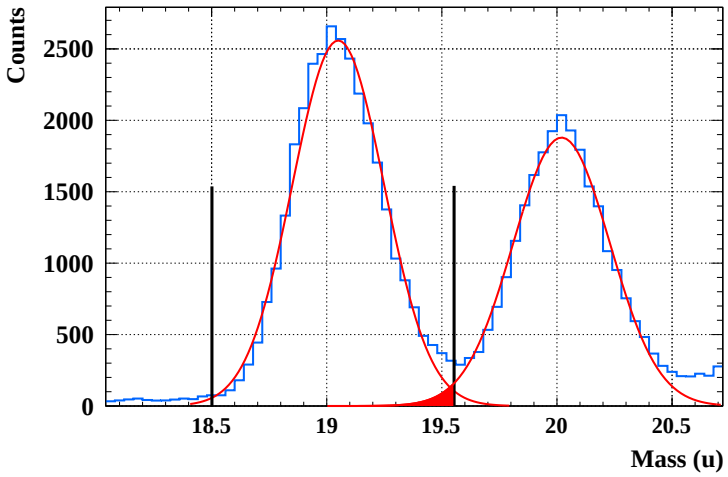

Figure 4.13: Mass plot showing the neon isotopes corresponding to charge state (9^+), and masses $A = 19$ and $A = 20$. The gate imposed to select the ^{19}Ne recoils is represented by the vertical solid lines. Gaussian fits for each isotope are also included.

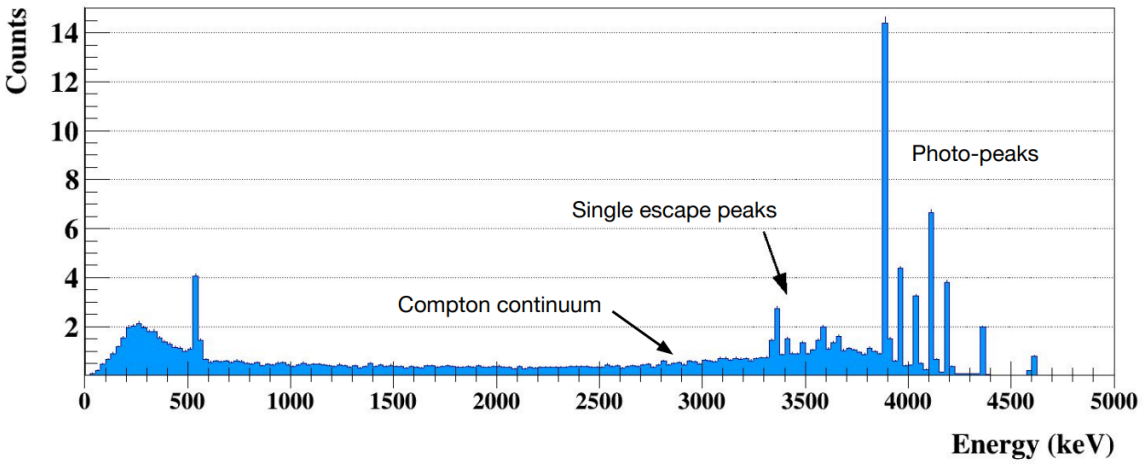

Figure 4.14: Simulated photo-peaks and Compton contribution to the γ-ray spectrum. The simulations were performed by the AGATA team. To extract the expected background, each simulation has been scaled to match the experimental data in the $3800 - 4600$ keV region. This gives a good estimation of the expected background in the $3200 - 3800$ keV energy region. The simulations also show the single-escape peaks located at 511 keV to the left of each photo-peak.

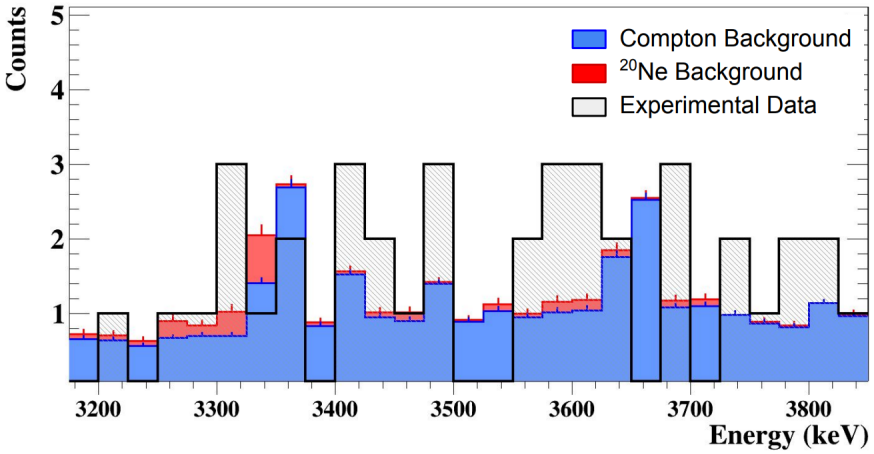

Figure 4.15: Cumulative background plot showing the $3200 - 3800$ keV region. Contributions to the background from the ^{20}Ne leakage (in red) and the simulated Compton background (in blue), are plotted alongside the background events detected (black line histogram).

The experimental background observed is, therefore, consistent with the simulated background across this energy region. The total background (B_{tot}) evaluated in the same way for each state studied in the present dissertation has been included in appendix D, table D.2. A detailed study of the background has been included below for the $E_x = 4.033$ MeV excited state.

4.5.2 Background around the 4.033 MeV region

To include the background on the statistical analysis of the 4.033 MeV region, a study of the background has also been done around this energy region. Figure 4.16a shows the energy region around 4 MeV for the corresponding excitation energy gate of $3.0 - 5.2$ MeV obtained in section 4.4; whereas figure 4.16b shows the same energy region but gated at higher excitation energies ($5.2 - 7.4$ MeV) to find the background contributions. Most of the events can be identified as γ-ray events from the de-excitation of different states in ^{19}Ne in both plots. The event found within the $4 - 5$ MeV region in 4.16b has been identified as the γ-ray transition from the 4.6 MeV excited state, which would be expected to appear in both excitation energy gates.

The contribution of the Compton background is also very small (< 1 count/25 keV) thanks to the AGATA add-back technique, which reconstructs the interactions within the crystal and recovers the total energy of the transition. An assessment of the expected Compton background is done by simulating the expected γ-rays in the 4 MeV region of energy. There are three peaks that could contribute to the background $E_\gamma = 4197$ keV, $E_\gamma = 4362$ keV and $E_\gamma = 4602$ keV. They present a few counts in the spectrum in figure 4.10. For these transitions simulations were provided by the AGATA collaboration and the contribution of the Compton edge was

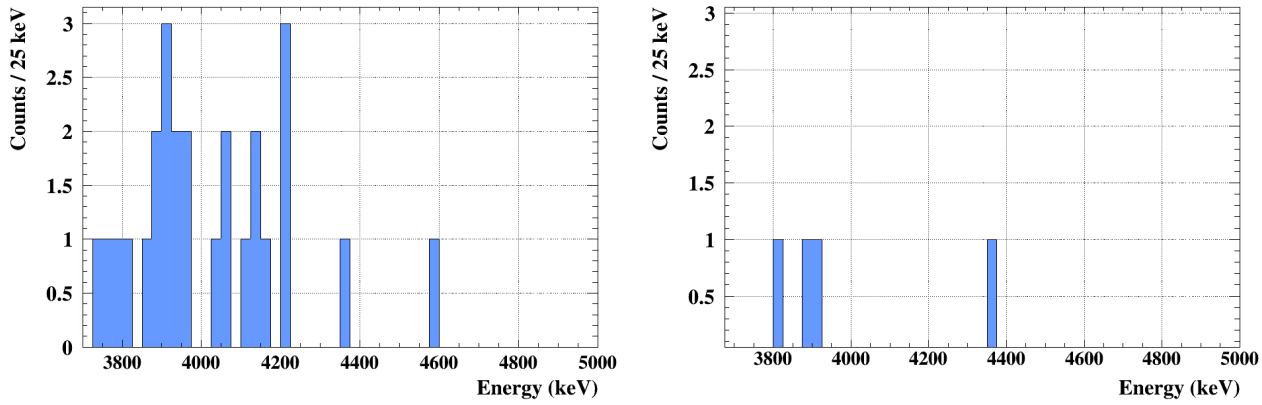

(a) E_x region: 3.0 - 5.2 MeV

(b) E_x region: 5.2 - 7.4 MeV

Figure 4.16: γ-ray transitions detected (a) after applying the selected gates for the 4033 keV state and (b) gating in higher excitation energies. The observed transitions can be explained from expected ^{19}Ne events (see text and table 4.2). The background contribution in the region of 4 to 5 MeV is negligible.

evaluated in the 4033 keV region over a two FWHM energy region (approximately 80 keV). The background to photo-peak ratio was calculated for each transition and the results are given in table 4.3. The total Compton background contribution in the energy region $4000 - 4075$ keV is given by the sum of the individual contributions of the given transitions, i.e. $B_{Comp} = 0.67$. The highest contribution comes from the single escape peak of the very weak 4602 keV γ-ray, which is located in this energy region. The other contribution to the background that must be accounted for is the ^{20}Ne leakage in the $4000 - 4075$ keV region, in line with the small contribution evaluated for the $3200 - 3800$ keV energy region (figure 4.15). This contribution is $B_{leak} = 0.1$ counts over this energy region. Therefore, the total background contribution obtained is $B_{tot} = 0.8$. Including the background contribution the result for the number of counts for 1σ confidence level is

$$N = 2.2^{+2.9}_{-1.6} \ . \tag{4.11}$$

And for the central 90% confidence region the result is

$$N = 2.2^{+3.7}_{-1.9} \ . \tag{4.12}$$

This result is not consistent with zero at 90% central confidence level, unlike the previous work based in lifetime and B_α branching ratio measurements [Tan05; Kan06; Myt08; Tan09].

E_γ (keV)	N^{sim}_{peak}	N^{sim}_{bckg}	B^{sim}_{ratio} (%)	N^{det}_{γ}	B_i
4197	2924	238	8.0	3	0.24
4362	2797	334	12	1	0.12
4602	2705	829	31	1	0.31

Table 4.3: Compton background from the γ-ray transitions found in the 4-5 MeV energy region. N^{sim}_{peak} is the number of events registered in the simulated photo-peak and N^{sim}_{bckg} is the number of events registered in the simulated $4000-4075$ keV region. The evaluated Compton background (B_i) from each peak is then found from the detected γ-rays (N^{det}_{γ}) scaled with the simulated background-to-peak ratio (B^{sim}_{ratio}).

4.6 Absolute beam normalisation

Radioactive Ion Beams are often delivered with varying beam intensity.. Thus they fluctuate within runs and they prove difficult to normalise. For this experiment the normalisation of the beam using the elastic scattering of the beam on target was not possible due to the small angular acceptance of VAMOS and MUGAST, at forward angles, and the incompatible reaction kinematics.

An approximation to the integrated beam over the whole experiment was calculated using the information from a short run with known intensity. The followed methodology can be found in appendix C where a value for the integrated beam on target was found to be $N_{beam} = 5.7 \cdot 10^{12}$ particles. This total yield calculated from these runs has however a big uncertainty that mostly comes from the unreliability of the beam profile detector as a counter. For this reason, an assessment of the obtained results must be done.

A theoretical calculation of the expected number of counts for the bound states at $E_x = 1508$ keV, $E_x = 1536$ keV, $E_x = 1615$ keV and $E_x = 2794$ keV has been done assuming this result and a total running time equal to 169h. This evaluation is done using the DWBA calculations and efficiencies obtained using the methods as presented in sections 5.1 and 5.2 respectively as well as the experimental cross section calculation using the method explained in section 4.7.2. Table 4.4 includes the expected number of counts and the detected number of counts for the four bound states. From these values an average beam intensity is calculated $I = N_{beam}/t = 9.4 \cdot 10^6$ pps. Using the theoretical integrated cross section calculated from the DWBA calculations and the spectroscopic factors from the mirror states in ^{19}F, an estimation of the number of counts expected is done: $N_{estimated} = \varepsilon \cdot N_{beam} \cdot N_{Li} \cdot \sigma_{th}$, where ε is the combined efficiency of detection, N_{beam} is the total number of beam particles on target, N_{Li} is the number of ^{7}Li per unit of area and σ_{th} is the expected cross section from the DWBA calculation scaled with the

E_x (keV)	C^2S mirror	σ_{th}	$N_{expected}$	$N_{detected}$	factor	N_{beam}
1508	0.20	0.2102	472	61	0.14	$8.2 \cdot 10^{11}$
1536	0.21	0.0821	199	18	0.10	$5.9 \cdot 10^{11}$
1615	0.20	0.1353	242	29	0.15	$8.7 \cdot 10^{11}$
2794	0.16	0.1034	176	26	0.14	$7.9 \cdot 10^{11}$

Table 4.4: Calculation of expected counts from the theoretical cross section and the spectroscopic factor taken from the mirror states [Oli95]. Comparison with detected number of counts.

spectroscopic factor from the mirror states and evaluated over the angular range accepted. The expected number of counts is higher than the number of detected particles. This, therefore, demonstrates that the integrated beam calculation based on the beam monitor is not accurate.

From these results one can conclude that the integrated beam calculated is overestimated by a factor of seven to ten. Therefore, a normalisation of this result is needed. A comparison to the mirror states has been done for 4 different observed states using the spectroscopic factors from [Oli95], and the results can be found in table 4.4. From these results a direct average is performed obtaining a value of $N_{beam} = 7.9 \cdot 10^{11}$ beam particles on target. The extracted normalisation factor also points that the total yield was overestimated by almost an order of magnitude. This corresponds to an average beam intensity of $I_B = 1.3 \cdot 10^6$ pps. The beam intensity requested was 10^7 pps over 10 full days, which would have given us $8.64 \cdot 10^{12}$ beam particles on target.

From this result, a calculation of the spectroscopic factors obtained for these four bound states can be found in table 4.5, where a comparison with the spectroscopic factors for the mirror states is also included. There is a very good agreement across all four mirror states.

E_x (keV)	N	C^2S calculated	C^2S mirror
1508	61	0.23	0.20
1536	17	0.18	0.21
1615	29	0.25	0.20
2794	26	0.18	0.16

Table 4.5: Comparison of extracted spectroscopic factor with mirror states, using a beam normalisation based on an average value across the four states. Tha maximal discrepancy for individual states is 20%.

4.7 Angular distributions and differential cross sections

In this section the methodology followed to extract the angular distributions and differential cross sections is explained. An example is given for the bound state at $E_x = 1508$ keV, and the same method is followed for the rest of the analysed excited states in chapter 5.

4.7.1 Solid angle

The solid angle covered by the detector is needed in order to calculate the geometrical efficiency of the reaction. It is also required for our calculation of the angular distribution and differential cross section for each state, as this depends on the accepted angular range. The geometrical efficiency as a function of angle is given in figure 3.10 for an isotropic alpha source simulation.

A Monte Carlo simulation using NPTool has been performed to obtain the solid angle covered for the reaction of interest. Here, the ^{7}Li(^{15}O, t)^{19}Ne* reaction is simulated for the recoil excited state at 4033 keV using an isotropic distribution in the center of mass. Figure 4.17 shows the emitted particles (red line) and the particles detected (blue region) per degree in θ_{cm}. The annular detector covers the lower angles in the center of mass almost completely,

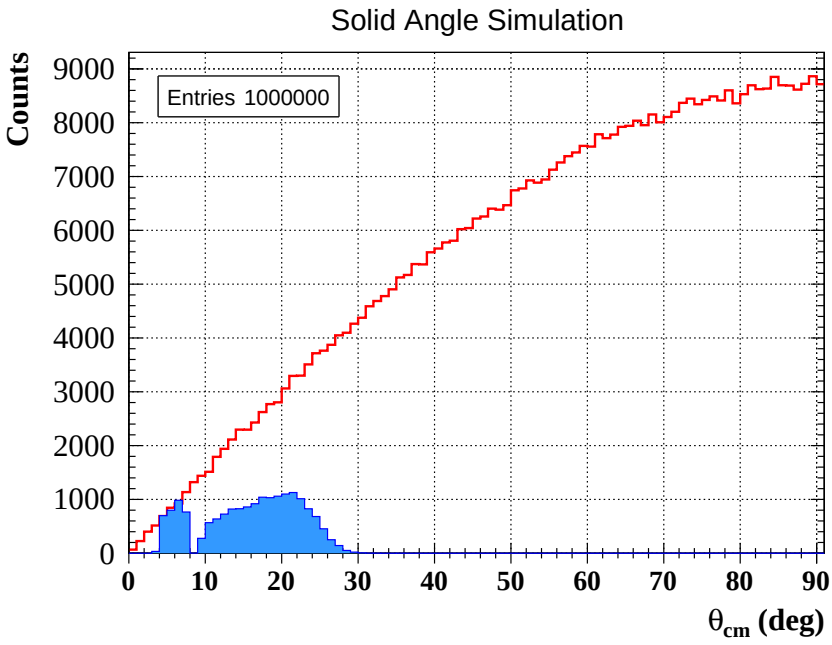

Figure 4.17: Simulation of the solid angle covered by the MUGAST detectors. The simulation was done for a million events and using an isotropic distribution for the ^{7}Li(^{15}O, t)^{19}Ne transfer reaction. The red line represents the emitted particles and the blue region represent the detected particles.

achieving a high geometrical efficiency. The trapezoids cover the $10 - 30$ degree region, and their efficiency is smaller, as only 4 of the 8 detector positions were fully instrumented for the 2019 campaign. The VAMOS acceptance furthermore reduces the detection for angles higher than 20 deg in the center of mass. The cross section for the studied transfer reaction thereby cuts off at around 30 degrees in the center of mass. However, with this, the setup is optimally matched to the differential cross sections detailed in chapter 5.

4.7.2 Experimental calculation of the differential cross section

To extract the experimental angular distributions and calculate the differential cross section for each excited state, a selection of the level must be done by applying the gates on excitation energy and γ-ray energy. The number of counts per angle is then extracted determining the appropriate binning and finally, the angular-dependent efficiency is applied. Following these steps, the observed differential cross section is given by

$$\left(\frac{d\sigma}{d\Omega}\right)_{exp} = \frac{N(\theta_{cm})}{N_{beam} N_{^7Li} \varepsilon_{fp} Q_{9+} \varepsilon_\gamma B_\gamma \varepsilon_{MG,int} \varepsilon_g \Delta\Omega(\theta_{cm})} \ , \tag{4.13}$$

where N_{beam} is the total number of beam particles on target, $N_{^7Li}$ is the number of ^{7}Li nuclei per cm^2, ε_{fp} is the efficiency of detection in the VAMOS focal plane, Q_{9+} is the correction for the population of the detected ion charged state, ε_γ is the AGATA efficiency of detection that depends on the energy of the detected γ-rays, B_γ is the γ-ray branching ratio for the observed transition, $\varepsilon_{MG,int}$ is the intrinsic efficiency of MUGAST and ε_g is the combined geometric efficiency for MUGAST and VAMOS. Most of these factors are the same for each state, however, the γ-ray efficiency and branching ratio depend on the detected transition.

There are two different types of detectors covering an angular range of 0 - 30 deg in the center of mass frame: the annular and the trapezoids from the MUGAST setup. They behave slightly differently, which is why a separate calculation of the differential cross section has been done for each type. In figure 4.18 the angular distribution for the 1508 keV excited state is shown; with the annular detector on the left hand side and the trapezoids on the right hand side. The binning has been chosen so that each bin has sufficient statistics (where possible at least $5 - 10$ events per angular bin).

The experimental cross section for population of a given excited state is calculated as the sum of the differential cross section corrected by the solid angle for each bin:

$$\sigma_{exp} = \sum_i \left.\frac{d\sigma}{d\Omega}\right|_i \cdot \Delta\Omega_i \ , \tag{4.14}$$

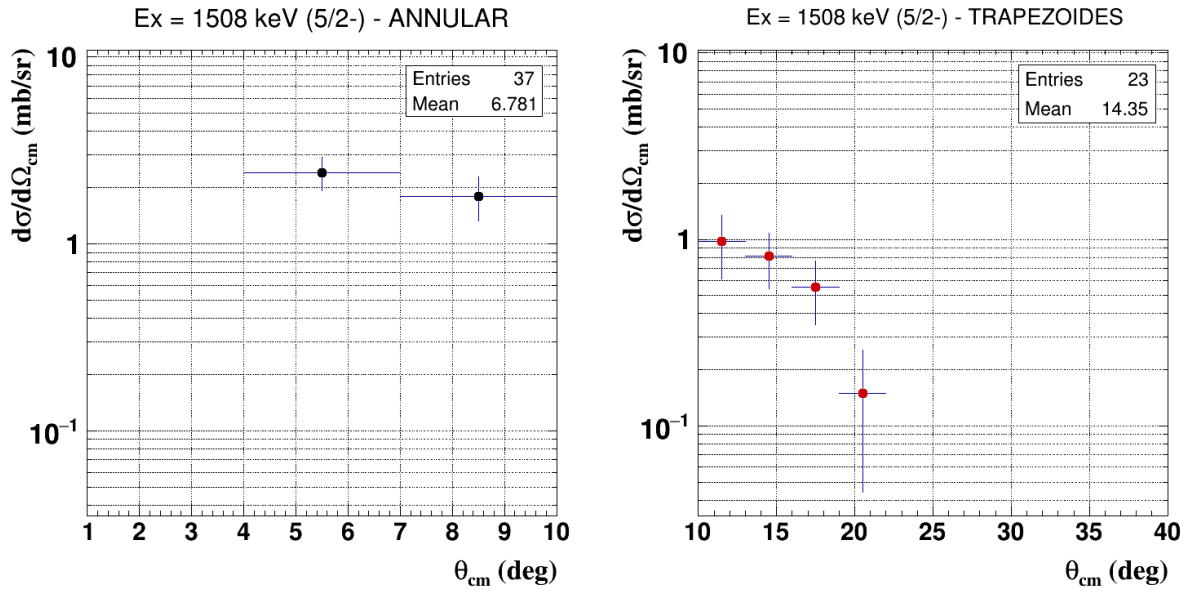

Figure 4.18: Example of the angular distribution for the $E_x = 1508$ keV excited state separated for the two different types of detectors.

where $\frac{d\sigma}{d\Omega}\big|_i$ is the differential cross section corresponding the bin i, and $\Delta\Omega_i$ is the solid angle of bin i that is calculated:

$$\Delta\Omega = \int_{\theta_1}^{\theta_2} 2\pi \sin\theta d\theta = 2\pi \left(\cos\theta_1 - \cos\theta_2\right) \ . \tag{4.15}$$

Using these formulae an integrated cross section can be calculated for each bin. An example of this calculation is given for the $E_x = 1508$ keV state. Results can be found in table 4.6. The integrated experimental cross section obtain in the angular range $\theta_{cm} = 3 - 19$ deg is $\sigma_{exp} = 0.24259$ mb.

Bin (θ_{CM} in deg)	N	ε_g	$\varepsilon_{MG,int}$	$\Delta\Omega$	$\frac{d\sigma}{d\Omega}$ (mb/sr)	σ ($\times 10^{-2}$ mb)
4-7	24	0.91	0.94	0.0315	1.64	5.17
7-9	14	0.72	0.94	0.0305	1.26	3.85
10-13	7	0.31	0.80	0.0656	0.79	5.21
13-16	9	0.37	0.80	0.0824	0.67	5.54
16-19	7	0.36	0.80	0.0989	0.45	4.42

Table 4.6: Integrated cross section corresponding to the different bins for the experimental data points in $E_x = 1508$ keV. The total integrated cross section over the range of interest is the sum of the cross section obtained for each bin.

The calculation of the differential and integrated cross sections have also been performed using this method in chapter 5 for the excited states at 1536, 1615, 2794, 4033, 4140, 4197, 4379 and 4600 keV. These results are subsequently used to extract spectroscopic factors and partial widths.

Chapter 5

Spectroscopic factors and Γ_α in ^{19}Ne

The data analysis discussed in the previous chapter led to the extraction of angular distributions and differential cross sections for the different excited states detected. In this chapter the alpha spectroscopic factors (C^2S_α) are calculated by comparing the experimental cross sections to theoretical calculations.

The following sections are focused on the explanation of the methodology followed by the theoretical DWBA calculations (see section 5.1) and the extraction of the C^2S_α results. Benchmarking these calculations is important to obtain robust results for the unbound states. A benchmark of these calculations is performed using the bound state at $E_x = 1508$ keV in section 5.2. A second benchmark is performed on the $E_x = 1536$ keV state in section 5.3.1, which is particularly important for the comparison to the $E_x = 4033$ keV state. A detailed calculation of the spectroscopic factor is also done for the $E_x = 4033$ keV state in section 5.4, accounting for its unbound nature. Systematic and statistical errors are also discussed for the $E_x = 4033$ keV case and applied subsequently for the rest of results. Other relevant unbound states populated in this work have also been studied in section 5.5. Following the extraction of spectroscopic factors, the alpha widths, Γ_α, are calculated for all the unbound states observed in the present work. The results are discussed and compared with previous data.

5.1 DWBA calculations

Theoretical differential cross section calculations can be performed for transfer reactions using the distorted wave Born approximation explained in chapter 2.4. The ingredients and tools needed to perform DWBA calculations are summarised in this section.

5.1.1 Multi-transfer quantum numbers

For the reaction ^{15}O(^{7}Li, t)^{19}Ne both projectile and residual nucleus have a cluster structure

$$\begin{aligned} {}^{7}Li &= \alpha + t \\ {}^{19}Ne &= \alpha + {}^{15}O \end{aligned}$$

For the DWBA calculations the transferred quantum numbers must be defined for the overlap functions of both projectile and residual nuclei. The total momentum and parity must follow the conservation rules.

In the case of the α+t wave function the transferred orbital momentum L must be extracted,

$$\vec{J}_T^{\pi} = \vec{j}_\alpha^{\pi} + \vec{j}_t^{\pi} + \vec{L} \ , \tag{5.1}$$

where $\vec{J}_T^{\pi}$ is the total angular momentum of the system, $\vec{j}_\alpha^{\pi}$ is the total angular momentum of the transferred alpha particle, $\vec{j}_t^{\pi}$ is the total angular momentum of the triton core and $\vec{L}$ is the orbital angular momentum. Similarly the parity obeys:

$$\Pi_T = \Pi_\alpha + \Pi_t + \Pi_L \ , \tag{5.2}$$

where Π_T is the total parity of the system, Π_α is the parity of the alpha particle, Π_t is the parity of the triton particle and Π_L is the transferred parity.

Here the transferred particle is a helium nucleus from ^{7}Li, arising from the cluster structure mentioned above. Under the shell model approach the nucleons composing the α cluster are located as shown in figure 5.1. Therefore, the transferred angular momentum and parity are

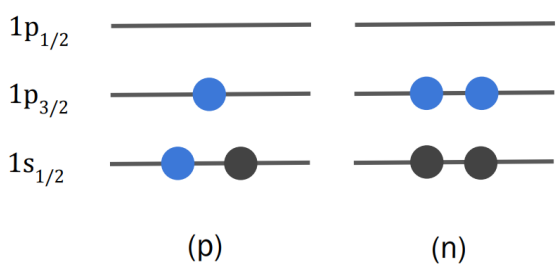

Figure 5.1: Shell model scheme of the two clusters composing the ^{7}Li nucleus in its ground state. The alpha cluster is represented in blue and the triton core is represented in black.

calculated as follows:

$$\frac{3}{2}^{-} = 0^{+} + \frac{1}{2}^{+} + \vec{L}\ , \quad (-) = (+)\cdot(+)\cdot\Pi_L\ .$$

The transferred parity must be $(-)$ and thus the transferred angular momentum is $L = 1$. To deduce the number of nodes the Talmi-Moshinsky relationship can be used

$$Q = 2N + L = \sum_i (2n_i + l_i), \tag{5.3}$$

where n_i and l_i are the quantum numbers of the α cluster in the ^{7}Li configuration. In this case, the oscillator quantum number is $Q = 3$ and the angular momentum $L = 1$, thus the number of nodes to use is $N = 1$.

For the overlap function ^{15}O + α clusters, the same logic applies. Now, the total angular momentum is for the populated excited state in ^{19}Ne. An example is given below for the excited state at $E_x = 1508$ keV, for which $J^{\pi} = 5/2^{-}$. The angular momentum and parity conservation laws must be followed:

$$\vec{J}^{\pi}_{T} = \vec{j}^{\pi}_{\alpha} + \vec{j}^{\pi}_{^{15}O} + \vec{L} \tag{5.4}$$

and

$$\Pi_T = \Pi_\alpha + \Pi_{^{15}O} + \Pi_L\ , \tag{5.5}$$

which in this case have values of

$$\frac{5}{2}^{-} = 0^{+} + \frac{1}{2}^{-} + \vec{L}\ , \quad (-) = (+)\cdot(-)\cdot\Pi_L\ ,$$

deducing a value for the transferred parity of $\Pi = (+)$ and for the transferred orbital angular momentum of $L = 2$.

The deduction of the number of nodes is uncertain, because one cannot be sure of the configuration of the transferred α particle in the ^{19}Ne excited structure. An example of different configurations is given in figure 5.2 where the blue nuclei are the transferred α cluster particles. They will populate the empty higher energy levels. For the 3 represented configurations the number of nodes obtained using equation 5.3 is $N = 3$, however it does not necessarily correspond to the number of nodes that best describes the state. Thus the calculations must be done for different number of nodes and compared with the experimental angular distribution shapes. For this work, previous studies on the oscillator quantum number have been taken into consideration from the ^{19}Ne excited states discuss in [FLS10] and from the studies of the mirror nucleus ^{19}F from [Oli95].

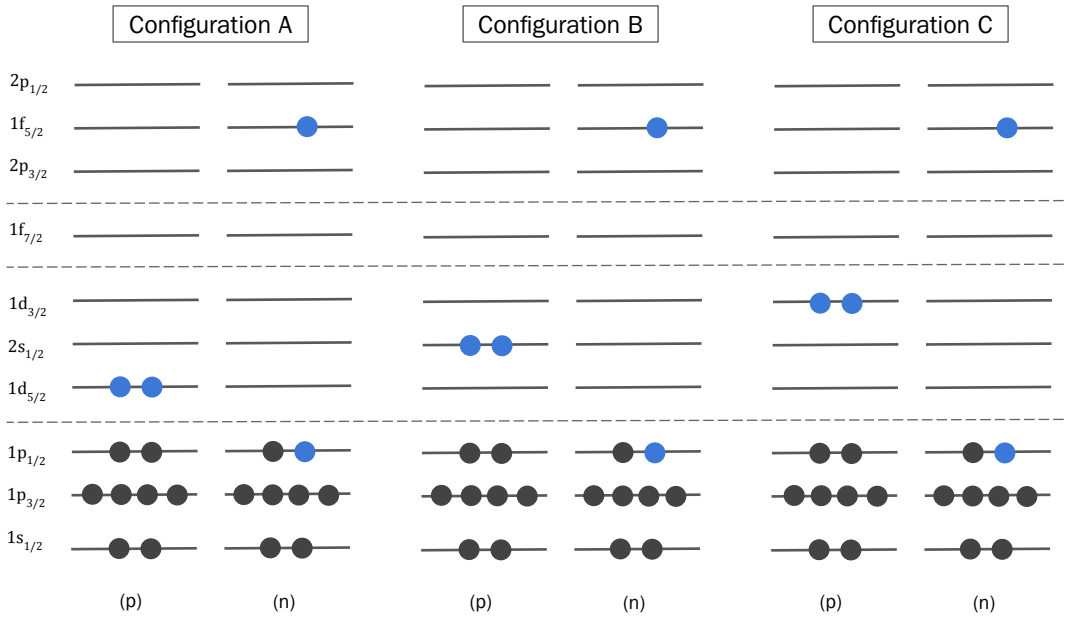

Figure 5.2: Example of different shell model configurations for the ^{19}Ne excited state $E_x = 1508$ keV $(5/2^-)$. This figure is only a representation of the shell model energy levels and it is not to scale. Dashed lines represent major shell gaps for clarity.

E_x (MeV)	J^π	Q	L	E_b (MeV)
1.508	$5/2^-$	8	2	2.021
1.536	$3/2^+$	7	1	1.993
1.615	$3/2^-$	8	2	1.914
2.479	$9/2^+$	7	5	0.735
4.033	$3/2^+$	7	1	-0.504
4.140	$7/2^-$	10	4	-0.611
4.197	$9/2^-$	10	4	-0.668
4.600	$3/2^+$	9	3	-1.071

Table 5.1: Transferred angular momentum, number of nodes and binding energies for the different excited states. These parameters are used on the theoretical calculation of the differential cross section for each state.

The same procedure as before is followed to obtain the transferred quantum numbers for the different excited states of interest. In table 5.1 details of spin-parity, transferred angular momentum and binding energy are given from the excited states studied.

5.1.2 FRESCO

FRESCO [Tho88] is a reaction code created by Ian Thompson. Its purpose is calculating nuclear reactions that can be expressed in a coupled channels form. It also includes a fitting sub-routine called SFRESCO where experimental data can be included while it calls FRESCO to fit the selected parameters. Within the performed calculations, the differential and integrated cross sections are included for different processes of the nuclear reactions, including elastic, inelastic and transfer reactions.

For transfer reactions FRESCO utilises the DWBA method, which allows the treatment of different types of direct reactions (see chapter 2.4). They require a certain number of parameters to define the different interactions:

- The α-cluster wave function within the ^{7}Li nucleus: calculated from a nuclear potential.
- The nuclear potentials used as a perturbation to the Coulomb wave functions.
- Optical potential parameters to describe the scattering of ^{7}Li(^{15}O, ^{15}O)^{7}Li, i.e. the entry channel.
- Optical potential parameters to describe the scattering of ^{19}Ne(t,t)^{19}Ne, i.e. the exit channel.
- The α-cluster wave function within the ^{19}Ne state in question.

There are other important parameters regarding the integration process. These integration parameters must be adjusted on a case by case basis to make sure the calculation is accurate. FRESCO also includes warnings and recommended values for some parameters in the output files. For the calculations performed in this project, the *prior* formalism for the perturbation have been adopted, where the perturbation with respect the entrance channel is considered.

5.1.3 Optical model potentials

The distributions obtained from the calculation using different optical potentials can vary significantly, and the extracted spectroscopic factors might differ by a factor of 3 in some cases [TN09]. Thus it is important to assess the uncertainties of the results by doing the calculations

for different optical potentials. Table 5.2 includes the optical potentials used for the different channels:

- POT A: Entrance channel potentials corresponding to the elastic scattering ^{15}O(^{7}Li,^{7}Li)^{15}O
- POT B: Exit channel potentials corresponding to the elastic scattering ^{19}Ne(t, t)^{19}Ne
- POT C: Binding potentials corresponding to the wave-function of α in ^{19}Ne
- POT D: Binding potentials corresponding to the wave-function of α in ^{7}Li

The residual potential corresponding to the core-core interaction t + ^{15}O is not as accessible as the others. For this reason some approximations must be done for this potential and the exit channel potential (POT B) is used instead, using the same source in both cases.

For the final calculations of this work, potentials A1-B1-C1-D1 were used, with the remainder potentials used for testing the systematic errors.

POT	V_0	r_V	a_V	W	r_W	a_W	r_c	From
A1	284.7	0.84	0.907	8.982	2.416	0.67	1.3	[WBJ82]
A2	246.0	0.90	0.907	7.6	2.42	0.7	1.3	[Oli95]
B1	104.3	1.10	0.77	30.10	1.29	1.06	1.3	[WH91]
B2	241.0	1.15	0.642	23.7	1.434	0.997	1.4	[Ver82]
C1	50.0	1.3	0.70	—	—	—	1.3	[Kub72]
C2	50.0	1.3	0.80	—	—	—	1.3	[Kub72]*
D1	93.7	2.05	0.70	—	—	—	2.05	[Kub72]
D2	43.2	3.49	0.65	—	—	—	3.49	[FK78]

* Same potential modifying parameter a.

Table 5.2: Optical Model potentials. Potentials A and B correspond to the elastic scattering of the entrance (^{15}O+^{7}Li) and exit (^{19}N+t) channels respectively. Potentials C and D correspond to the binding potentials of the α+^{15}O system and the α+t system respectively.

5.2 Benchmarking calculations with the 1508 keV 5/2- excited state

The purpose of this section is to study the angular region for the fit of the experimental data and to optimise the FRESCO integration parameters. The $E_x = 1508$ keV excited state has been chosen for this benchmark of the DWBA calculations because it is a bound state with enough statistics.

5.2.1 Fresco parameters

FRESCO calculations have also been performed as part of the present analysis. It is important to understand how each parameter behaves to achieve a good calculation. The FRESCO manual provides some guidelines to have a good starting point. However, every calculation must be optimised by finding a good set of parameters.

The important integration parameters to modify are *rmatch*, *hcm*, *hnl* and *cutl*. FRESCO computes the wave functions from 0 to a radius *rmatch* at intervals of *hcm*. The parameter *hnl* is the integration step for non-local kernels, and it is required when dealing with transfer reactions. Finally, the *cutl* parameter defines the radial points per angular momentum of lower radial cutoff when integrating the radial equations. More detailed information of the integration parameters can be found in the FRESCO documentation in [Tho88]. Each of these parameters was modified one at a time, leaving the others constant, assessing the convergence of the calculation. In figure 5.3 different values for each parameters are compared.

For the *cutl* parameter -5.5 can be excluded because it is not consistent with the two other options. Values of -3.5 and -4.5 are consistent with each other across the angular range covered in the experiment, and it is only for higher angles where they differ.

The *rmatch* parameter needs to be big enough to cover the integration across the interaction region. However once it reaches an optimum value, the integration does not vary and it only increases the integration time. Thus, the used value is the minimum one that covers the whole interaction.

The *hcm* and *hnl* step parameters need to be small enough to do an accurate integration and they big enough for the integration to be relatively fast. The suggested range of values for them is (0.05 - 0.10).

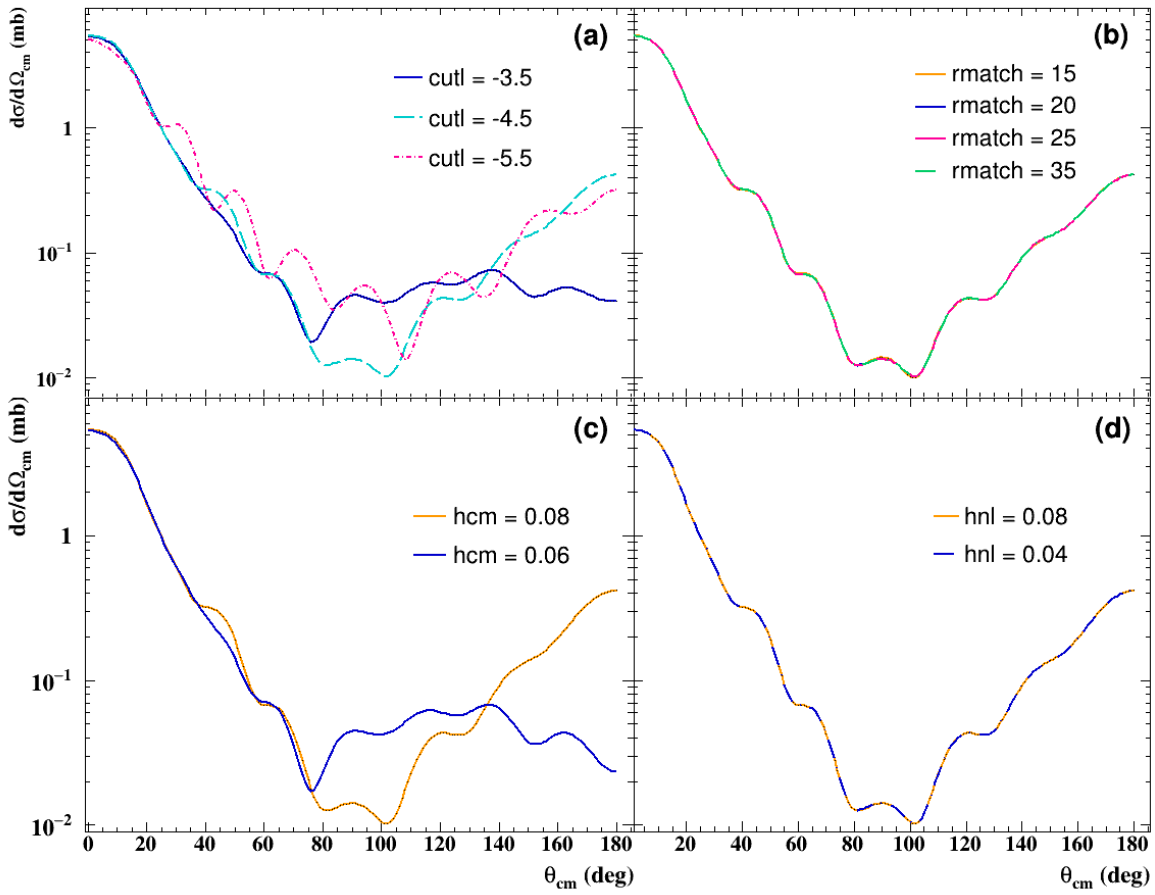

Figure 5.3: Modifying the different FRESCO integration parameters, the calculated cross section may vary. These parameters need to be slightly adjusted for each calculation to obtain an optimal result. The four different plots show a variation of one parameter leaving the rest of them constant. It is clear that the *cutl* parameter shown in plot (a)is the most critical parameter. The integration step *hcm* in plot (c) is also important, especially at higher angles. However, parameters *rmatch* and *hnl* shown in plots (b) and (d) have very limited impact on the differential cross section at these values of *rmatch*.

5.2.2 Radius of interaction

The asymptotic normalisation coefficient (ANC) describes the amplitude of the tail of the radial overlap function at radii beyond the nuclear interaction radius [HS21]. The ANC and the partial width Γ_α must be evaluated at the interaction radius r_c, where the $\alpha + {}^{15}\mathrm{O}$ wave function behaviour stops being dominated by the nuclear contribution and starts being dominated by the asymptotic behaviour. ANCs are important because they determine the direct capture rate at the limit of zero relative energy [TN09]. Outside the nuclear potentials the asymptotic behaviour of the overlap function is proportional to a Whittaker function $W(r)$. This function is the solution to the Coulomb wave function for negative energies, and it follows an exponential decay [Nob04]. This is used because the DWBA calculations are computed using the weakly-bound approximation, and the C^2S is then extrapolated to the positive resonance energy. The radius for which the wave function is well approximated by the Whittaker function is the interaction radius r_c. In figure 5.4 the radial wave function is represented in black, where the contribution of the nuclear potentials is observed for $r < r_c$, and the contribution of the Coulomb potential dominates for $r > r_c$. The asymptotic behaviour of the Coulomb

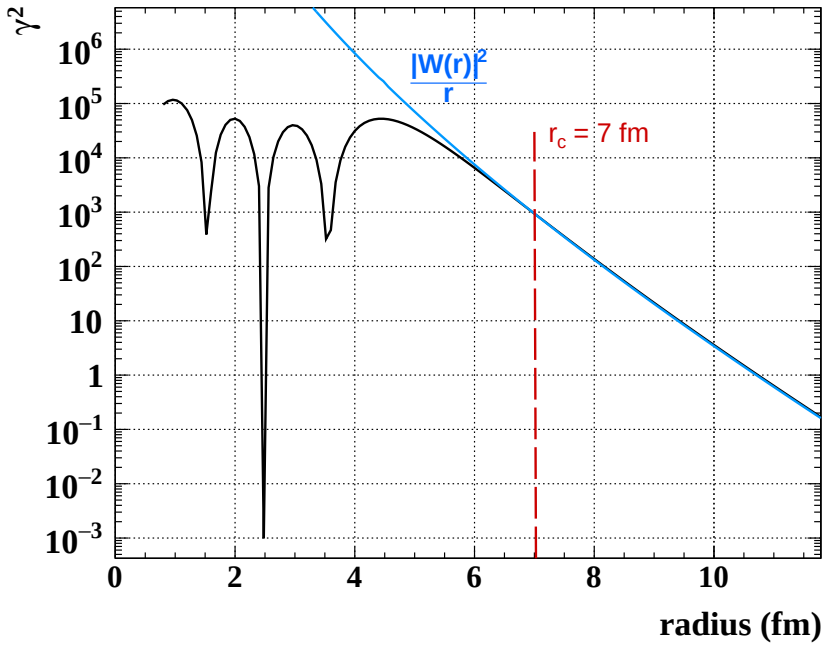

Figure 5.4: Radial wave function (black) showing the asymptotic behaviour following the Whittaker function (blue). The radius of evaluation is extracted where the radial part of the wave function starts its asymptotic behaviour, for $r = r_c$.

interaction follows the Whittaker function represented in blue. The main contribution to the norm of an overlap function comes from the nuclear interior. The ANC is a peripheral quantity, meaning that the interaction occurs on the surface of the nucleus, at $r = r_c$. If spectroscopic factors are extracted from peripheral reactions the uncertainty from the single-particle potential parameters are extremely large, however, the ANC remains constant.

The interaction radius is defined therefore as the point from which both functions have the same asymptotic radius dependence. The radius r_c was determined in the present work by comparing the alpha reduced width with the Whittaker function for different states. A radius of interaction $r_c = 7$ fm was obtained for all of the states and adopted in all of the calculations.

5.2.3 Selection of angular range

The angular distribution obtained in figure 4.18 can be fitted using SFRESCO. This is done by providing in the input files the experimental points obtained. The fit routine adjusts the single-particle differential cross section calculated in FRESCO to match the experimental data-points. The normalisation factor that adjusts the curve to the points corresponds to the spectroscopic factor. To make judgements and decisions about goodness-of-fit the relevant quantity is the integral:

$$\text{Prob}(\chi^2; N) = \int_{\chi^2}^{\infty} P(\chi'^2; N) d\chi'^2 \ , \tag{5.6}$$

which gives the probability of a particular function describing a set of N data points giving a value of χ^2 as large as (or larger than) the obtained value. In the case of fitting data to a certain function the N data points are used in the fit to adjust a number of variables, the probability is calculated as before but now using the degrees of freedom n = N - p, where p is the number of free parameters in the fit. The χ^2 results are shown in table 5.3 for each of the data-points. Using a goodness of fit test: the total χ^2 is 11.84. This corresponds to 5 degrees of freedom (6 number of points minus 1 parameter to fit). The probability of exceeding 11.07 is 5% according to the critical χ^2 values table [Bar89]. This means the obtained value of 11.84 lays outside the 95% confidence level. This confidence level of 95% corresponds to the probability of having a value of χ^2 lower than 9.49. In this case, as the result is outside, and the fit is not good.

How much does this fit improve after excluding the last data point located at 20 deg? Running SFRESCO to obtain a new fit, now removing the last data-point, the total value of χ^2 is 4.35, well within the 95% confidence level. These χ^2 results are also shown in table 5.3. Removing the last experimental data point from the fit corresponds to removing one degree of freedom and gives an improvement of 7.5 in χ^2. This value lies outside the 3σ region for the χ^2 distribution for 1 degree of freedom, where the probability of exceeding a $\chi^2 = 6.63$ is 1%. The

	All data-points				Removing last data-point			
θ_{CM}	value	error	theory	χ^2	value	error	theory	χ^2
5.500	2.4401	0.50074	1.3227	4.9793	2.4401	0.50074	1.6367	2.5744
8.000	1.8179	0.48779	1.2373	1.4167	1.8179	0.48779	1.5310	0.3460
11.500	0.98705	0.37387	1.0295	0.0129	0.98705	0.37387	1.2739	0.5886
14.500	0.82134	0.27427	0.79754	0.0075	0.82134	0.27427	0.98683	0.3641
17.500	0.56175	0.21258	0.57281	0.0027	0.56175	0.21258	0.70876	0.4783
20.500	0.15134	0.10705	0.40060	5.4213	—	—	—	—

Table 5.3: Results of the fits done to the experimental data-points including and excluding the point at 20.5 deg. Details of the statistical analysis can be found in text.

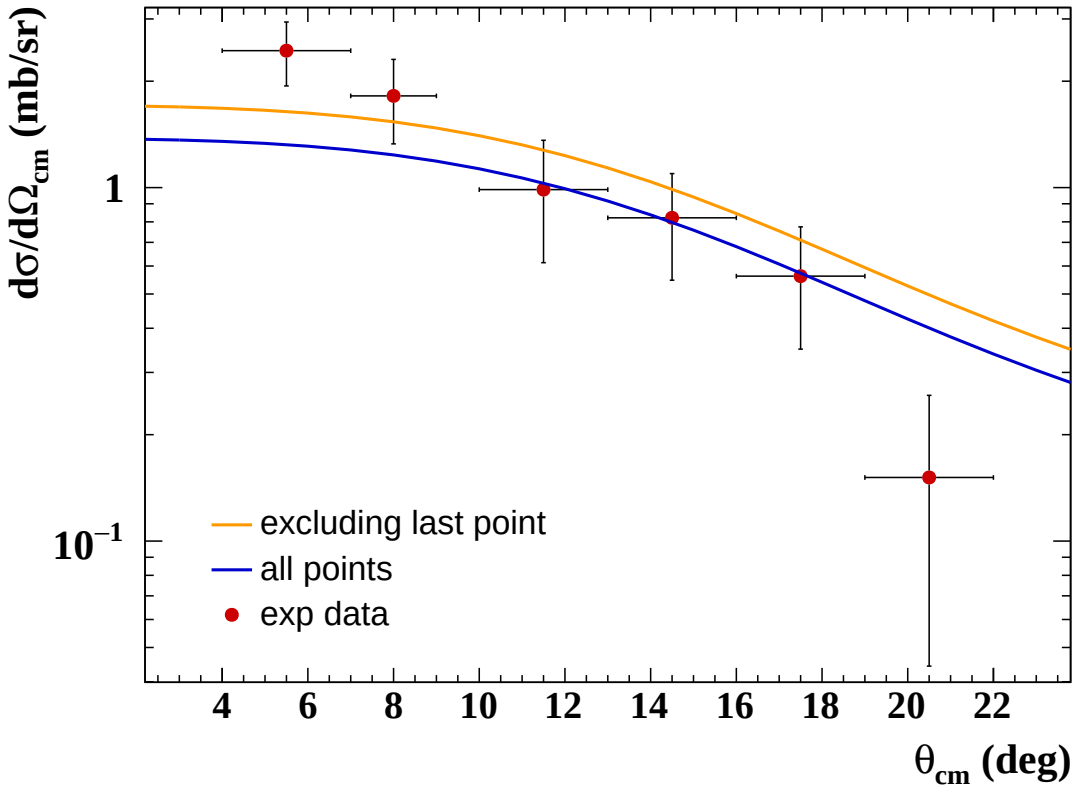

Figure 5.5: SFRESCO calculations of the differential cross section. The experimental data points are used to adjust the theoretical calculations, including (blue line) and excluding (yellow line) the point located at 20 degrees.

experimental differential cross section is represented in figure 5.5 along with the two different fits. This statistical study shows the improvement of the fit by excluding the data point at angles higher than 20 deg. Therefore, there is a robust statistical reason to exclude it.

The larger angles are furthermore questioned in terms of the VAMOS acceptance cuts; recoils of angles higher than 4.6 degrees are not detected by the spectrometer. This corresponds to roughly 20 degrees in the center of mass. A decision is made from this cut and from the statistical study above to limit this angular distribution study to 19 degrees in the center of mass consistently for all of the states.

5.2.4 Comparison to the mirror state

Another cross-check of the theoretical calculation can be done by comparing the spectroscopic factor obtained from the fit to the data with the spectroscopic factor obtained from the mirror state. A FRESCO calculation was done using the same optical potentials, changing the reaction to the mirror reaction ^{15}N(^{7}Li, t)^{19}F and using the spectroscopic factor $C^2S = 0.20$ obtained in [Oli97] for the mirror state which is located in ^{19}F at $E_x = 1346$ keV. The differential cross section obtained from this calculation is shown in figure 5.6 (yellow line).

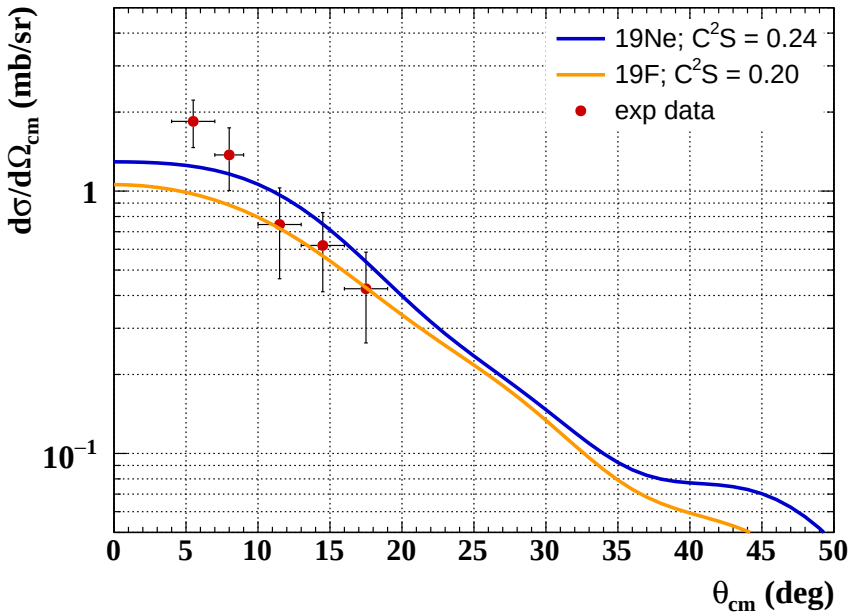

Figure 5.6: Differential cross section plot obtained for the $E_x = 1508$ keV state (data-points). The figure also shows the fit of the theoretical calculation to the data-points (blue line) and the comparison with the differential cross section of the mirror state in ^{19}F. The spectroscopic factors for both cases are in good agreement.

5.2.5 Spectroscopic factor calculation

There are two different methods to extract the spectroscopic factor: the first is fitting the data using SFRESCO, as previously shown. The second is by integrating the differential cross section over the selected angular range and comparing this integration to the theoretical integral over the same angular range.

Using the fitting method the value obtained for the spectroscopic factor was $C^2S_\alpha = 0.24 \pm 0.03$. This fit is shown in figure 5.6.

To calculate it by the integration method, the experimental cross section is calculated as explained in chapter 4.7.2 now compared to the theoretical cross section obtained for the DWBA calculation and integrated[1] over the same angular range

$$\sigma_{th} = 2\pi \int_3^{19} \left.\frac{d\sigma}{d\Omega}\right|_{dwba} \sin\theta d\theta \ . \tag{5.7}$$

Integrating the theoretical differential cross section obtained in the DWBA calculation. The result of this integral is $\sigma_{th} = 1.05092$. From these two results, the spectroscopic factor is obtain

$$C^2S = \frac{\sigma_{exp}}{\sigma_{th}} = 0.23 \pm 0.03 \ . \tag{5.8}$$

This result is consistent with the value obtained with the SFRESCO fit.

5.3 Other bound states

Besides the $E_x = 1508$ keV state, three other bound states were detected and studied in this dissertation for different purposes. These are the $E_x = 1536$ keV $(3/2^+)$, $E_x = 1615$ keV $(3/2^-)$ and $E_x = 2794$ keV $(9/2^+)$ states.

5.3.1 1536 keV state

This state corresponds to $J^\pi = 3/2^+$ and it is important to study it because its angular distribution can be directly compared with the 4033 angular distribution. The reason why they can be compared is because the population of both states is done by transferring an angular momentum of $L = 1$, and the shape is therefore expected to be the same.

[1] Integral performed excluding the $9 - 10$ degree bin, due to the zero detector acceptance over this angular region.

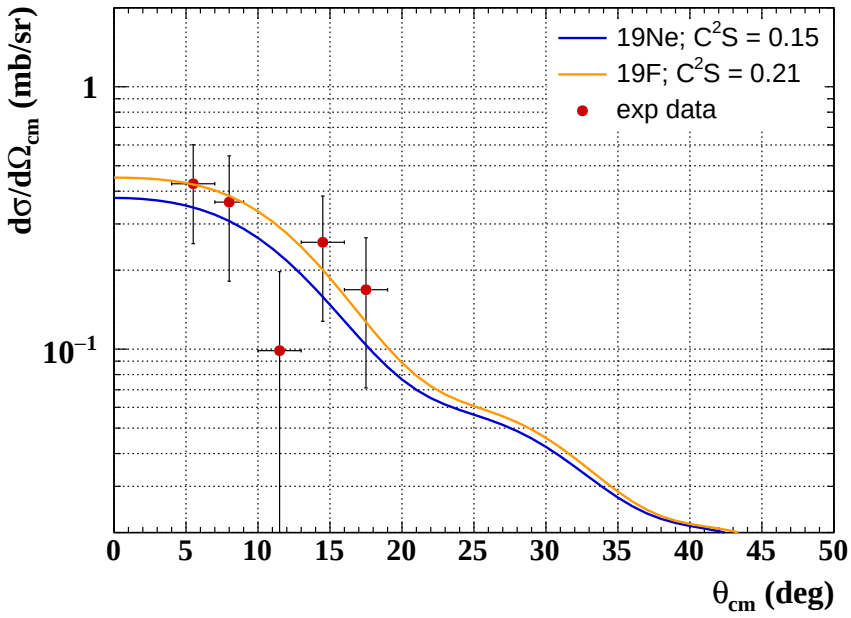

Figure 5.7: Differential cross section plot for $E_x = 1536$ keV showing the experimental data (red points), the SFRESCO fit to the data (blue line) and the comparison to the theoretical distribution obtained for the mirror state. Fitting the data a spectroscopic factor $C^2S = 0.15$ was obtained, which is consistent with the value obtained for the mirror state in ^{19}F measured in [Oli95].

The two different methods discussed in section 5.2 to extract the spectroscopic factors are also used here. Fitting the experimental points using SFRESCO as shown in figure 5.7 gives a result for the spectroscopic factor of $C^2S = 0.15 \pm 0.04$. Using the integration method over the angular range $\theta_{cm} = 3 - 19$ deg gives a value of $C^2S = 0.18 \pm 0.04$. Both results are also consistent with each other, although it is noticeable that the data point at 11 deg lowers the value of the spectroscopic factor obtained from the fit.

The total number of events detected for this state was $N = 18$ in the selected angular range, and not all of the bins have the same number of counts. There are possible biases that might be introduced into the fit by the lack of statistics. These statistical biases come from the fitting routine applied by SFRESCO, where a Neyman χ^2 minimisation is used. Here, the maximum likelihood estimator used in the fit is constructed as:

$$\chi^2_{Neyman} = \sum_i \frac{(\mu_i - N_i)^2}{N_i}, \tag{5.9}$$

where i is the bin, μ_i is the mean value of the bin and N_i is the number of events in the bin [Ji20].

This estimator, however, is biased when N_i is small. To investigate this bias, T. Hauschild and M. Jentschel [HJ01] performed a study of the statistical biases for a flat distribution in counting experiments. This study gives an idea of the possible biases that can be introduced when fitting histograms with low statistics. They found a statistical bias for the fitting using the Neyman's χ^2 that underestimated the number of counts per bin that is especially acute for low number of counts. While in this case the distribution is not flat and the study hasn't been done for this case, the bias can still be important for the determination of the spectroscopic factor by the fitting method, especially when the statistics obtained are low. With the integration method this bias does not apply. Henceforth extracting the spectroscopic factor using the integrated cross sections will provide a more robust result as the remainder of the bound states are all low-statistics data. The results for the unbound states will similarly be calculated using the latter method, which is a more robust routine for low statistics.

5.3.2 1615 keV and 2794 keV states

These two bound states were useful to calculate the absolute beam normalisation performed in chapter 4.6. Following the integration method explained before, the spectroscopic factors for these two states were extracted. Experimental cross section calculations were found to be $\sigma_{exp,1615} = 0.1669$ mb and $\sigma_{exp,2794} = 0.1157$ mb, and the spectroscopic factors are $C^2S_{1615} = 0.25 \pm 0.05$ and $C^2S_{2794} = 0.18 \pm 0.04$. Angular distributions are shown in figures 5.8a and 5.8b

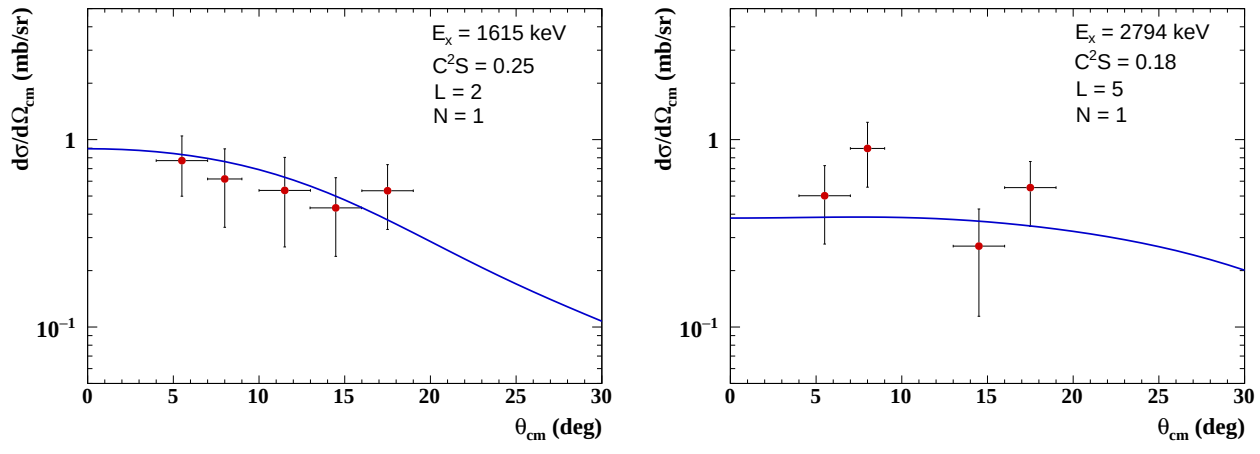

(a) (b)

Figure 5.8: Angular distributions obtained for the excited states at (a) $E_x = 1615$ keV and (b) $E_x = 2794$ keV. Each figure also includes the theoretical differential cross section curve calculated using FRESCO and scaled by the given spectroscopic factor.

respectively. More details on the results of these calculations can be found in table D.2 of the appendix.

5.4 4.033 MeV state

This state is believed to be the main contributor to the reaction rate for the $^{15}O + \alpha$ capture reaction. In this experiment only 3 events corresponding to this state were detected, as it was explained in section 4.5. A detailed study of this state has been performed. Extraction of spectroscopic factor and partial width is carried out in this section along with the determination of systematic uncertainties.

5.4.1 Spectroscopic factor of the 4.033 MeV state

To extract the spectroscopic factors, the experimental cross section must be compared to the theoretical calculations. The experimental cross section has been calculated following the methodology explained in detail in section 4.7.2. This value is given for each bin in table 5.4 and the total value corresponds to $\sigma_{exp} = 0.0176$ mb.

Bin (θ_{CM} in deg)	N	ε_g	$\frac{d\sigma}{d\Omega}$ (mb/sr)	σ (μb)
3-6	1	0.75	0.22	5.8
6-8	2	0.85	0.38	10.2

Table 5.4: Integrated cross section corresponding to the different bins for the experimental data points in $E_x = 4033$ keV. The total integrated cross section over the range of interest is the sum of the cross section obtained for each bin.

There are two ways of calculating the spectroscopic factor for this level. The first, is the integration method used for the bound states, where the experimental cross section is compared to the integrated cross section obtained for the theoretical calculation. The second method is by comparing to the bound $3/2^+$ excited state at $E_x = 1536$ keV. Both methods are discussed below.

In both cases, the theoretical DWBA calculation is needed. To calculate the theoretical cross section there are a few steps to follow. In particular, FRESCO does not calculate the cross sections for unbound states, hence an extrapolation must be performed. The calculations are done for different binding energies close to the separation energy value, at $S_\alpha = 3.529$ MeV. For each calculation a value for the integrated cross section over the angular range $\theta_{cm} = 3 - 19$

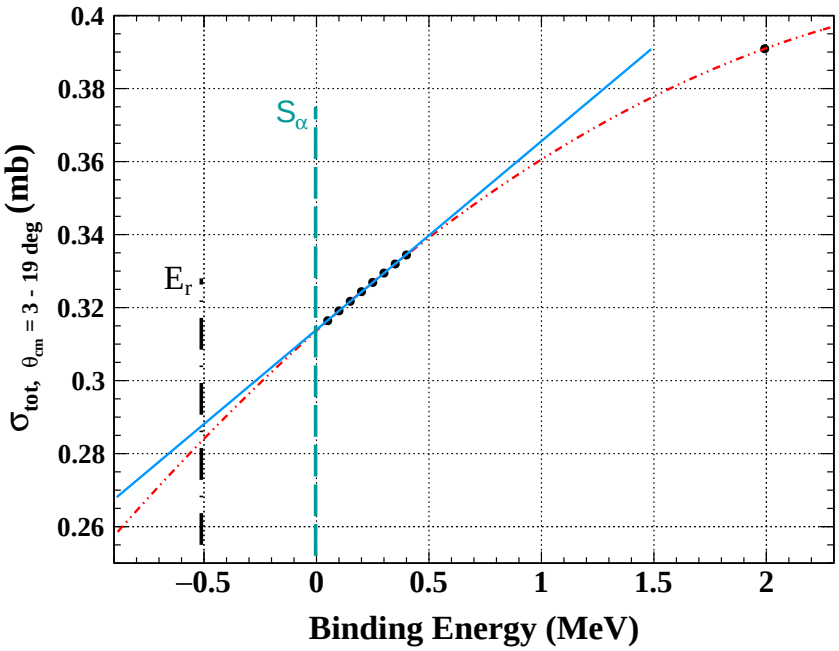

Figure 5.9: Calculation of integrated cross section (mb) for different binding energies (MeV). The integral has been evaluated over an angular range $\theta_{cm} = 3-19$ deg for every case. Negative binding energies correspond to unbound states and positive binding energies correspond to bound states. The integrated cross section has been calculated for the bound state at $E_x = 1536$ keV and for hipotetical binding energies close to the α separation threshold situated at $S_\alpha = 3529$ keV. Two different fits can be performed to extrapolate the cross section for the 4033 keV excited state, that corresponds to a resonance energy $E_r = -504$ keV. The quadratic fit (discontinuous red line) takes into account the higher binding energy of the 1536 state. The linear fit (solid blue line) fit the points for binding energies closer to the separation threshold.

deg is obtained and finally an extrapolation to the resonance energy is done obtaining the integrated cross section for the unbound state. This is graphically explained in figure 5.9, where two different extrapolations are used: a linear fit including the results for binding energies close to the α threshold, and a quadratic fit, including the value for the $E_x = 1536$ keV excited state, with a binding energy $E_b = 1.993$ MeV. Extrapolating using the linear fit gives a very good result for resonance energies close to the separation threshold, only differing by a 3%. Extrapolating to $E_r = -0.504$ MeV the value obtained for the theoretical integrated cross section is $\sigma_{th} = 0.28804$ mb.

Using the integration method C^2S_α is extracted as the scaling factor between the experimental cross section and the theoretical extrapolation at 1σ confidence level:

$$C^2S_{\alpha,4033} = \frac{\sigma_{exp}}{\sigma_{th}} = 0.06^{+0.08}_{-0.04} \ . \tag{5.10}$$

The second method takes into account the small energy dependency and makes use of the DWBA calculation of the 1536 ($3/2^+$) state. After calculating the value of the spectroscopic factor extracted for the angular distribution of the 1536 keV state (see 5.3.1), a comparison with this C^2S_α obtained can be done for the 4033 state. This comparison is possible because both states are $3/2^+$ states and in both cases the transferred angular momentum corresponds to $L = 1$. This means that the shape of each angular distribution are effectively the same and the single particle DWBA calculation only differs by the contribution of the binding energy of the levels. This can be accounted for by integrating the theoretical differential cross sections over the accepted angular range and extracting an scaling factor by comparing the observed and calculated integral cross sections for the $E_x = 1536$ keV and the $E_x = 4033$ keV states.

To obtain the C^2S_α for the 4033 keV state the following relationships are compared:

$$\left(\frac{d\sigma}{d\Omega}\right)_{exp,1536} = C^2S_{\alpha,1536}\left(\frac{d\sigma}{d\Omega}\right)_{dwba,1536} \tag{5.11}$$

and

$$\left(\frac{d\sigma}{d\Omega}\right)_{exp,4033} = C^2S_{\alpha,4033}\left(\frac{d\sigma}{d\Omega}\right)_{dwba,4033} \ . \tag{5.12}$$

In these two equations, the relationship between the experimental and theoretical differential cross sections is given by the spectroscopic factor for each state C^2S_{α,E_x}. The experimental differential cross section is calculated using equation 4.13. Integrating over the MUGAST acceptance ($\theta_{cm} = 3 - 19$ deg):

$$\sigma_{exp,1536} = C^2S_{\alpha,1536}\sigma_{dwba,1536} \tag{5.13}$$

and

$$\sigma_{exp,4033} = C^2S_{\alpha,4033}\sigma_{dwba,4033} \ . \tag{5.14}$$

The integrated cross section for the theoretical calculation at 1536 keV excitation energy is equal to $\sigma_{dwba,1536} = 0.3908$ mb for the angular coverage of $\theta_{cm} = 3 - 19$ deg. With the linear fit done in figure 5.9 the value obtained for the cross section is $\sigma_{dwba,4033} = 0.28804$ mb. From this calculation, the differences in the DWBA model calculation for both states are taken into account by comparing the integrated cross section extracted for each state:

$$\sigma_{4033} = f \cdot \sigma_{1536} \ , \tag{5.15}$$

obtaining a scaling factor equal to $f = 0.737$. The spectroscopic factor $C^2S_{\alpha,4033}$ is therefore obtained by dividing equation 5.14 by equation 5.13:

$$\frac{N_{4033}}{N_{beam}N_{Li}\varepsilon_d\varepsilon_{int}Q_{9+}\varepsilon_g\Delta\Omega(\theta_{cm})\varepsilon_{\gamma,4033}B_{\gamma,4033}}\frac{N_{beam}N_{Li}\varepsilon_d\varepsilon_{int}Q_{9+}\varepsilon_g\Delta\Omega(\theta_{cm})\varepsilon_{\gamma,1536}B_{\gamma,1536}}{N_{1536}} = \frac{1}{f}\frac{C^2S_{\alpha,4033}}{C^2S_{\alpha,1536}}\ , \tag{5.16}$$

where the constant terms cancelled each other in the division. Note that the geometric efficiency given by $\varepsilon_g\Delta\Omega$ cancels out because the evaluation is done over the same angular range. The γ-efficiency ε_γ is extracted from the efficiency curve in figure 3.25, at $\varepsilon_{1536} = 0.076$ and $\varepsilon_{4033} = 0.038$. The B_γ are taken from NNDC as $B_{\gamma,1536} = 0.95$ and $B_{\gamma,4033} = 0.80$. With these ingredients, the spectroscopic factor for the 4033 keV state at 1σ confidence level is found to be

$$C^2S_{\alpha,4033} = 0.07^{+0.09}_{-0.05}\ . \tag{5.17}$$

For this state the angular distribution obtained includes only one experimental point at 5.5 deg. This corresponds to 3 counts detected in the annular detector at $\theta = 3 - 8$ deg. The

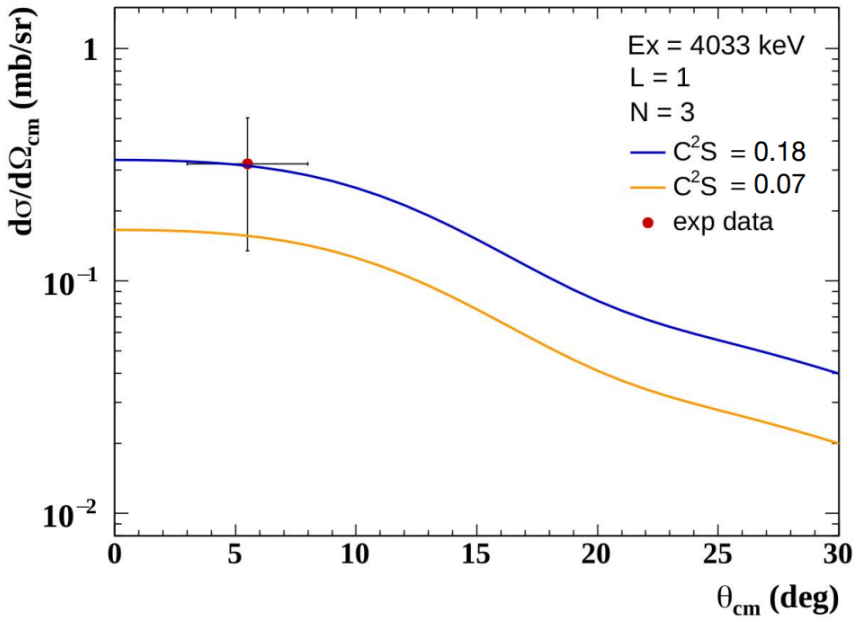

Figure 5.10: Angular distribution for the 4033 state showing the experimental differential cross section corresponding to the 3 detected events within the angular range $\theta_{cm} = 3 - 8$ degrees, binned together to decrease the statistical uncertainty. differential cross section curves are shown for the spectroscopic factor extracted from the FRESCO fit ($C^2S = 0.18$) and compared with the spectroscopic factor obtained from the comparison to the $E_x = 1536$ keV state ($C^2S = 0.07$).

three events have been binned together to reduce the statistical error. A comparison between the spectroscopic factor obtained from fitting to the amplitude of the experimental point and the spectroscopic factor obtained from the comparison to the $E_x = 1536$ keV level is shown in figure 5.10. The fit only takes into account the amplitude of the experimental data at 5.5 degrees. On the other hand, the comparison to the 1536 keV state is done integrating the differential cross section in the range $\theta = 3 - 19$ degrees. The fact that no data is detected in the trapezoids needs to be accounted for in the extraction of C^2S_α, but this is not accounted for by the SFRESCO fit. The fit can also present some biases from the low statistics, as it was discussed for the $E_x = 1536$ keV state in section 5.3.1. Therefore, in conclusion, the integral comparison to the $E_x = 1536$ keV state is overall most robust.

5.4.2 Systematic uncertainties

There are different sources of systematic uncertainties. The main contribution to the systematic error comes from the model dependencies of the theoretical calculation.

The optical potentials have been previously defined in section 5.1.3. The set used in the DWBA calculations is the A1-B1-C1-D1 set and its parameters can be found in table 5.2. However, the models used can vary the results of the spectroscopic factor significantly, and this also affects the partial width calculation. To understand these variations the different potentials are changed one at a time. For each set of potentials a calculation of the integrated cross section in the angular region $\theta_{cm} = 3 - 19$ deg, and the Γ_α in the single-particle approach is performed. This theoretical calculation is done for the $E_x = 4033$ keV state using the weakly bound approximation, where the unbound state is assumed to be bound at an energy very close to the separation threshold. For this calculation a binding energy of $E_b = 50$ keV is used. The results are summarised in table 5.5. Note that these calculations were performed to assess the uncertainties derived from the optical model potentials used, and they are not the final results for the α partial widths. Here the systematic uncertainty is dominated by the wave function from potential C, where a difference of up to 40% is found.

The beam normalisation inherits uncertainties from the mirror symmetry assumptions. However, four different mirror states were used to extract the normalisation factor and the result comes from the average of these 4 values. These calculations can be found in section 4.6. The uncertainty on this calculation is 20%.

The uncertainty on the measurement also contribute to the systematic errors. The uncertainty on the number of ^{7}Li particles per unit of area is approximately 4%. The uncertainty on the charge state distribution is 15%. The branching ratio of the gamma ray transition comes

Set	σ_{th}	$\Gamma_{\alpha,sp}$	C^2S_α	Γ_α
A1-B1-C1-D1	0.31641	43.082	0.0578	2.49
A2-B1-C1-D1	0.36512	43.082	0.0501	2.15
A1-B2-C1-D1	0.36396	43.082	0.0502	2.16
A1-B1-C2-D1	0.34552	66.476	0.0529	3.52
A1-B1-C1-D2	0.43545	43.082	0.0420	1.81

Table 5.5: Spectroscopic factor calculation for different combinations of optical potentials. Potentials A and B correspond to the elastic scattering of the entrance (^{15}O+^{7}Li) and exit (^{19}N+t) channels respectively. Potentials C and D correspond to the binding potentials of the α+^{15}O system and the α+t system respectively.

with an uncertainty of less than 18% over all of the transitions. These uncertainties on the measurement are, however, included when performing the beam normalisation, and they cancel out when calculating the relative spectroscopic factors.

Adopting these conservative values for the evaluation of uncertainties, the total systematic uncertainty obtained from the quadratic combination of the above contributions is approximately 45%.

5.4.3 Partial width calculation

The partial width of the unbound 4033 keV ($3/2^+$) state can be calculated using equation 2.13 evaluated at $r_c = 7$ fm and $E_r = 0.504$ MeV. The radial part of the wave function ($\phi(r)$) is calculated using the weakly bound approximation, where a FRESCO calculation is done at a binding energy close to the separation threshold (in this case a binding energy $E_b = 0.05$ MeV was adopted). The spectroscopic factor used is $C^2S_\alpha = 0.07^{+0.09}_{-0.05}$, calculated from the comparison with the $E_x = 1536$ keV ($3/2^+$) state based on the linear extrapolation to the unbound resonance energy. The resulting alpha width is

$$\Gamma_\alpha = 3.0^{+4.0}_{-2.2} \pm 1.4\ \mu\text{eV}, \tag{5.18}$$

where the statistical errors are given at the 1σ confidence level and the systematic error corresponds to 45%, as previously discussed. This result is based on the $N = 3$ counts obtained with a very low background ($B_{tot} = 0.8$) as detailed in chapter 4.5.1. The previous result for the branching ratio obtained for this state by Tan *et al.* was based on 44 counts with a background of 36 counts. This is why their result had a significant uncertainty and was consistent with

zero at the 90% single-sided confidence level, as detailed in section 1.2, where we summarised the many attempts to constrain the α branching ratio. Some upper limits were published and only one measurement on the branching ration has been reported to be $B_\alpha = 2.9 \pm 2.1 \times 10^{-4}$ [Tan09] at 1σ confidence level. Combining the reported lifetimes from [Tan05; Kan06; Myt08] an averaged lifetime is reached $\tau = 7.9 \pm 1.5$ fs. With this result and the result of the B_α, a partial width $\Gamma_\alpha = 24 \pm 18$ μeV is obtained in [FLS10].

While the statistical 1σ error of this measurement is similar to the 1σ error of Tan *et al.*, the low background of our measurement means that our result of $\Gamma_\alpha = 3.0^{+4.0}_{-2.2} \pm 1.4$ μeV is distinct from zero even at the 95% single-sided confidence level (or 90% central as detailed in section 4.5). With this new value for the partial width the branching ratio would be $B_\alpha = \frac{\Gamma_\alpha}{\Gamma_T} = 3.6 \times 10^{-5}$. Furthermore, our best value is much lower than the earlier measurements but it is in agreement with their lower limits, as shown in section 1.2 (table 1.2), where the previous values reported in literature are compiled.

5.5 Other resonances

In addition to the critical 4033 keV state, there are other resonant states observed in this work. These states are also important because they contribute to the reaction rate at different ranges of temperature. The two main populated states detected in this work are the excited states at $E_x = 4140$ keV $(7/2^-)$ and $E_x = 4197$ keV $(9/2^-)$. The α widths of these two levels have not previously been directly measured.

The spectroscopic factor calculation is done by using the integration method explained earlier, where a comparison between the integration of the differential cross sections obtained from the experimental data and from the single-particle theoretical calculation is done. The experimental cross section calculation is performed following again the steps explained in chapter 4.7.2 for each resonance. Table 5.6 shows the number of counts and the experimental integrated cross section results for each angular bin for the 4140 keV and 4197 keV states. In figure 5.11 the experimental angular distributions for both states are shown.

For the $E_x = 4140$ keV state the experimental integrated cross section over the angular range $\theta = 3 - 19$ deg has a value of $\sigma_{exp} = 0.2796$ mb and the theoretical cross section integrated over the same range is $\sigma_{th} = 2.7678$ mb. This gives a spectroscopic factor value of $C^2S_{\alpha,4140} = 0.10 \pm 0.01 \pm 0.05$. For the $E_x = 4197$ keV state the corresponding values are $\sigma_{exp} = 0.7831$ mb and $\sigma_{th} = 3.5052$ mb, yielding a spectroscopic factor of $C^2S_{\alpha,4197} = 0.23 \pm 0.02 \pm 0.10$. The uncertainties given correspond to the statistical error and the systematic error respectively.

The alpha width, Γ_α, for these levels can also be calculated using equation 2.13, evaluating

		4140 keV		4197 keV	
Bin (θ_{CM} in deg)	ε_g	N	σ ($\times 10^{-2}$ mb)	N	σ (mb)
3-6	0.75	10	3.5	23	0.10
6-8	0.85	11	3.3	21	0.08
10-13	0.37	9	7.3	18	0.18
13-16	0.37	13	10.5	24	0.24
16-19	0.38	5	3.9	20	0.20

Table 5.6: Integrated cross section results for the $E_x = 4140$ keV and $E_x = 4197$ keV states.

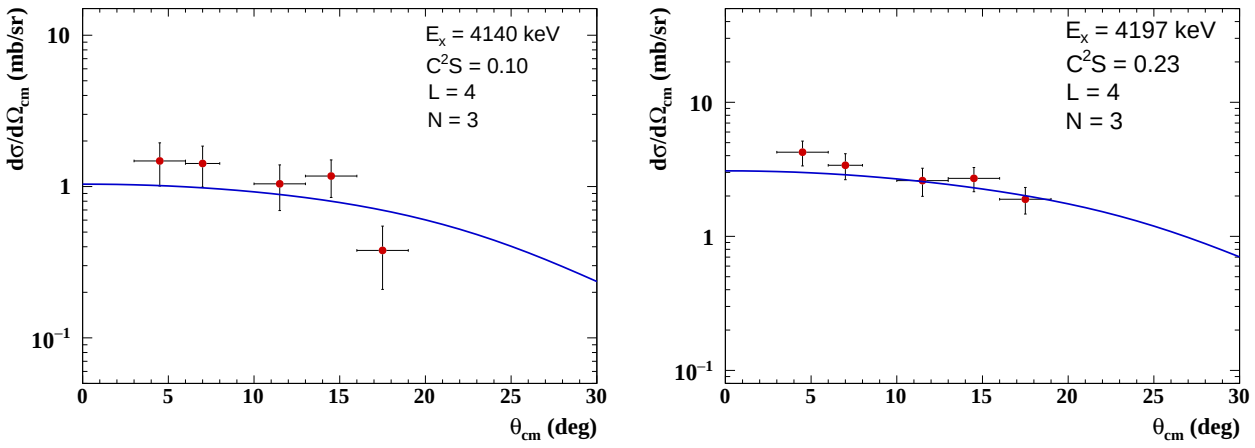

(a) (b)

Figure 5.11: Angular distributions obtained for the excited states at (a) $E_x = 4140$ keV and (b) $E_x = 4197$ keV. Each figure also includes the theoretical differential cross section curve calculated using FRESCO and scaled by the given spectroscopic factor.

it at $r_c = 7$ fm and at $E_r = 0.611$ MeV and $E_r = 0.668$ MeV respectively. The results obtained for the two states are $\Gamma_{\alpha,4140} = 0.28 \pm 0.04 \pm 0.13$ μeV and $\Gamma_{\alpha,4197} = 3.0 \pm 0.3 \pm 1.3$ μeV (statistical and systematic uncertainties respectively).

These two resonances have been studied in the past. However they are very close in energy and the former experiments were not sufficiently sensitive to resolve their signals. In this work the selectivity of detection was based on the exceptional resolution of AGATA, and a separate measurement of each level was achieved. Here, the γ-ray transitions corresponding to each level were identified and resolved with negligible background contribution, as shown in figure 5.12, where the two peaks represent the γ-ray transitions detected for these excited states.

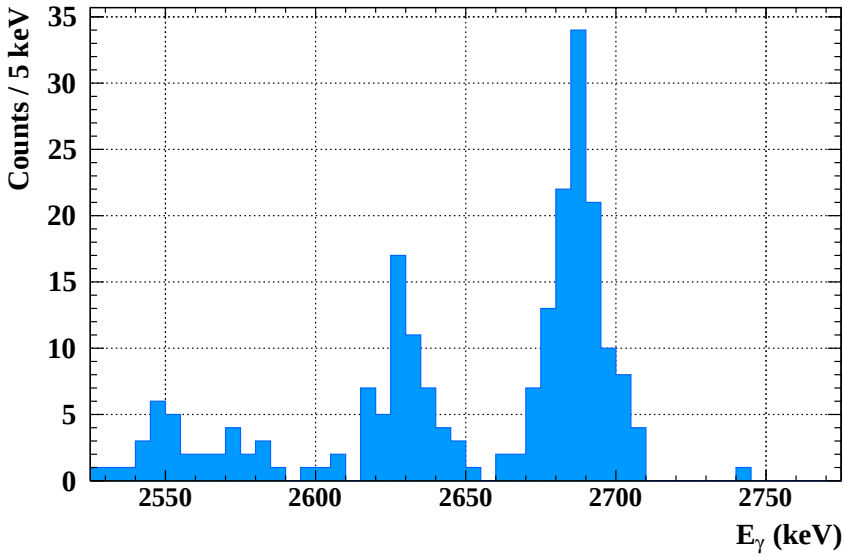

Figure 5.12: γ-ray transitions for $E_x = 4140$ keV at $E_x = 4140$ keV at $E_\gamma = 2632$ keV, and for $E_x = 4197$ keV at $E_\gamma = 2689$ keV. They are resolved and almost no background contribution is observed after applying the excitation energy and VAMOS acceptance gates.

Tan *et al.* gave a combined measurement of the branching ratio for these two levels, and they extracted a separate partial width assuming that the contribution was 100% from one of them for each calculation. In table 5.7 a comparison of the results from this work and their results have been done. Their result is given at 1σ confidence level, and a significant background suppression was done to extract their branching ratio. They also show a higher statistical error than in the present work.

A few counts for two other resonances were also detected at $E_x = 4379$ keV and at $E_x = 4600$ keV. A partial width calculation was performed following the same methodology as followed for the other resonances, and the results were compared with previous data. However, due to

	Γ_α (μeV)		
E_x (keV)	This work	[Tan09]	[FLS10]
4033	$3.0^{+4.0}_{-2.2}$	17 ± 13	24(18)
4140	0.28 ± 0.04	44 ± 20	
4197	3.0 ± 0.3	18 ± 9	
4379	128^{+123}_{-68}	160^{+110}_{-70}	150(6)
4600	$3.4^{+4.4}_{-2.2} \cdot 10^3$	$24^{+33}_{-10} \cdot 10^3$	$96(24) \cdot 10^3$

Table 5.7: Γ_α for the measured states, for this work and for previous measurements. Errors presented are statistical uncertainties at the 1σ confidence level. A conservative systematic error of 45% was extracted in chapter 5.4.2 and it has been included in the results presented in the text.

the lack of statistics for these two states, the extracted Γ_α is only used here as a comparison with previous results. For the reaction rate calculation only our data for the three lower lying resonant states will be used, and the previous results will be adopted for other contributions.

For the $E_x = 4379$ keV $(7/2^+)$ state 3 counts at $\theta_1 = 3 - 6$ deg, $\theta_2 = 13 - 16$ deg and $\theta_3 = 16 - 19$ deg were observed. A value of $\Gamma_\alpha = 128^{+123}_{-68} \pm 58$ μeV was extracted at 1σ confidence level. This result is consistent with the given value obtained by Tan *et al.* in [Tan09], but has a higher uncertainty.

For the $E_x = 4600$ keV $(7/2^+)$ state only 2 counts were observed at $\theta_1 = 3 - 6$ deg and $\theta_2 = 10 - 13$ deg and a $\Gamma_\alpha = 3.4^{+4.4}_{-2.2} \pm 1.5$ meV was extracted also in the 1σ confidence level. In this case the result lays on the edge of the 2σ region reported by Tan *et al.* In addition, the 4600 keV state falls close to the edge of the VAMOS acceptance, which makes out result for this state less reliable than for the lower lying resonances.

These results are also used as a cross-check for the absolute beam normalisation performed in chapter 4.6. Comparing the Γ_α calculated here with previous results (see table 5.7) allows us to check whether there are any inconsistencies in the normalisation. As discussed before, these results are consistent with the previous values.

Details of number of events detected, cross section calculations and extracted spectroscopic factors can be found in appendix D, table D.2, for the different excited states studied in this dissertation.

Chapter 6

Conclusions and perspectives

This project has primarily focused on the detection of the $E_x = 4033$ keV state in ^{19}Ne. There have been many studies in the past suggesting that this particular resonant state was the main contributor to the ^{15}O(α,γ)^{19}Ne reaction rate. This reaction has been thought to be the dominant breakout route from the HCNO cycle in the range of thermonuclear temperatures $T = 0.1 - 1.0$ GK, and an accurate measurement of the properties of the resonant states is key to our understanding of the X-ray burst mechanism on neutron star surfaces.

The cross sections of the populated states are extremely small. The determination of the Γ_α would not have been possible without the combination of the three powerful state-of-the-art detectors MUGAST, AGATA and VAMOS. Each device provided its own advantages on the detection of the triple particle coincidence. The data analysis performed during this project brings out the fantastic selectivity in recoils, the high energy resolution achieved for the γ-rays and also the angular coverage provided by the DSSSD detectors allowing the extraction of the ejectile energy and angle. With this setup the background contribution is almost zero and it was proven to be critical in the identification of the detected α-transfer events.

Further improvements in future α-transfer experiments must be done experimentally in terms of the absolute beam normalisation. The lack of a reliable beam counter for high-intensity radioactive ion beams means that a normalisation based on mirror state assumptions had to be done. Fortunately, there were four bound states detected and the mirror state spectroscopic factors were used to extract a normalisation factor. The average beam intensity extracted from this normalisation is $I_B = 1.3 \cdot 10^6$ pps. This value is our effective average beam intensity across our running time of 7 days.

For the first time a direct α-transfer has been measured with a radioactive ^{15}O ion beam.

On the analysis of the γ-ray spectra, a new transition was observed and identified as a γ-decay from the $E_x = 4197$ keV state to the ground state. Analysis of the data furthermore led to the extraction of spectroscopic factors for several excited states followed by the calculation of their respective alpha widths Γ_α.

The main result obtained in this work was the detection of α-transfer events populating the $E_x = 4033$ keV state. The number of events isolated, after background assessment was $N = 2.2^{+2.9}_{-1.6}$ at the 1σ confidence level. The spectroscopic factor was then extracted by comparing to the single-particle cross section calculation and a result of $C^2S_\alpha = 0.07^{+0.09}_{-0.05} \pm 0.03$ was obtained. With this value, the partial width was calculated to be $\Gamma_\alpha = 3.0^{+4.0}_{-2.2} \pm 1.4$ μeV. The uncertainty band has been reduced with respect to former studies, providing the most accurate result so far.

Another two resonances at $E_x = 4140$ keV and $E_x = 4197$ keV were isolated in the present work for the first time. Furthermore the observed Γ_α is lower than previous measurements indicated. Although their contribution to the reaction rate have been found to be very small, this is a big step forward on the knowledge of the properties of these resonances, as one of the two was thought to contribute significantly. For the $E_x = 4140$ keV state a spectroscopic factor $C^2S_\alpha = 0.10 \pm 0.01 \pm 0.05$ was extracted and a value of $\Gamma_\alpha = 0.28 \pm 0.04 \pm 0.13$ μeV was obtained. For the $E_x = 4197$ keV state the spectroscopic factor calculated was $C^2S_\alpha = 0.23 \pm 0.02 \pm 0.10$ and the partial width obtained had a value of $\Gamma_\alpha = 3.0 \pm 0.3 \pm 1.4$ μeV. These results were compared with previous measurements concluding that this new measurement is both more accurate and far lower than indicated by previous data.

Two other resonances were furthermore measured at higher energies for the $E_x = 4379$ keV and $E_x = 4600$ keV states. Partial widths were extracted for each state: $\Gamma_{\alpha,4379} = 128^{+123}_{-68} \pm 58$ μeV and $\Gamma_{\alpha,4600} = 3.4^{+4.4}_{-2.2} \pm 1.5$ meV. For these last two resonances detected in the present project the lack of statistics prevented a more robust determination of the partial widths than the previous results, and for the latter, an additional systematic error from the vicinity of the VAMOS acceptance should be expected.

The new values of Γ_α with reduced errors are expected to have important astrophysical implications. The partial width calculations lead to the extraction of the resonance strengths ($\omega\gamma$) and reaction rates for temperatures in the range $T = 0.1 - 1.0$ GK. The new reaction rate calculation can be implemented in nucleosynthesis models constraining the uncertainties. The next step to do in this program are studies of the astrophysical implications from these results. The total resonant reaction rate is calculated as the sum of the reaction rate for each resonance. In table 6.1 the ingredients for its calculation are given. The new values of the partial widths are used for the first three resonances at $E_x = 4033$ keV, $E_x = 4140$ keV and $E_x = 4197$ keV.

E_x (keV)	E_r (keV)	J_r^π	Γ_α (μeV)	$\omega\gamma$ (μeV)
4033	504	$3/2^+$	$3.0^{+4.0}_{-2.2}$	$6.0^{+8.0}_{-4.4}$
4140	611	$7/2^-$	0.28 ± 0.04	1.1 ± 0.2
4197	668	$9/2^-$	3.0 ± 0.3	15.0 ± 1.5
4379	850	$7/2^+$	160^{+110}_{-70}	630^{+450}_{-280}
4600	1071	$5/2^+$	$24^{+33}_{-10} \cdot 10^3$	$54^{+72}_{-23} \cdot 10^3$
4712	1183	$5/2^-$	$200 \pm 70 \cdot 10^3$	$101 \pm 210 \cdot 10^3$

Table 6.1: Adopted Γ_α and resonance strengths. The three lower lying levels are taken from this work and the other three resonances are taken from the previous work done by Tan et al. [Tan09]. Errors included are statistical and they are shown at 1σ confidence level.

The other contributions are taken from [Tan09]. The reaction rate is calculated as a function of temperature and in figure 6.1 the different contributions have been plotted along with the total reaction rate. The dashed lines represent the contributions using the Γ_α results from Tan et al. for the three higher lying states.

A comparison between the relative contribution to the reaction rate obtained in this work is done in figure 6.2a, and the results obtained by Tan *et al.* are shown in figure 6.2b. The $E_x = 4033$ keV state is still the main contributor for temperatures $T_9 < 0.7$. For higher temperatures the two main contributors are $E_x = 4712$ keV and $E_x = 4600$ keV excited states. These results differ from the results obtained by Tan et al. at lower temperatures, where they predicted that the contribution from the $E_x = 4140$ keV would be important in the range of temperatures $T_9 = 0.4 - 0.8$ if the B_α measured came purely from the $E_x = 4140$ keV state, as discussed in detail in section 5.5.

The total reaction rate is compared with Tan results in figure 6.3a, where the present results are shown with a 1σ uncertainty band, using the upper 1σ limit and lower 1σ limit respectively for all resonances. The previous results are higher by almost an order of magnitude in the region $0.4 - 0.8$ GK. The ratio to Tan is given in figure 6.3b where it is clear that the present work has a lower reaction rate. In table 6.2 a comparison between these results and previous results are given including our conservative upper and lower limits.

The contribution to the reaction rate is indeed dominated by the state at $E_x = 4033$ keV up to $T_9 = 0.7$. From that temperature onwards, the contribution from higher energy resonances dominate. However, these new partial width results are far lower than the predicted results: the reaction rate is therefore lower than the adopted in Tan et al. [Tan09] by almost an order of magnitude from the central value.

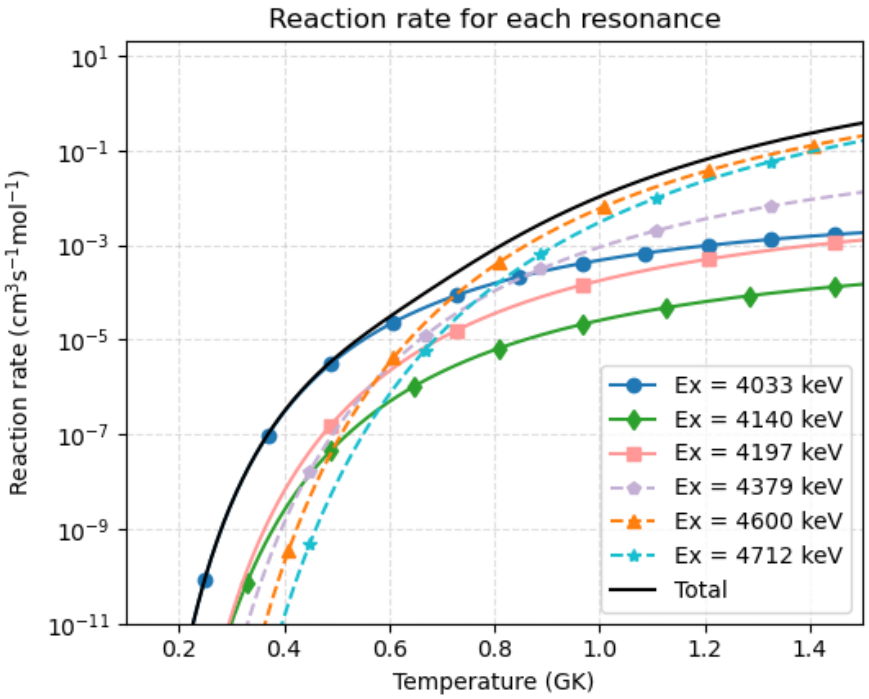

Figure 6.1: Reaction rate contribution from the different excited states. The solid lines represent the contribution of the states calculated in this project, whereas the dashed lines are the contributions from states previously measured in [Tan09].

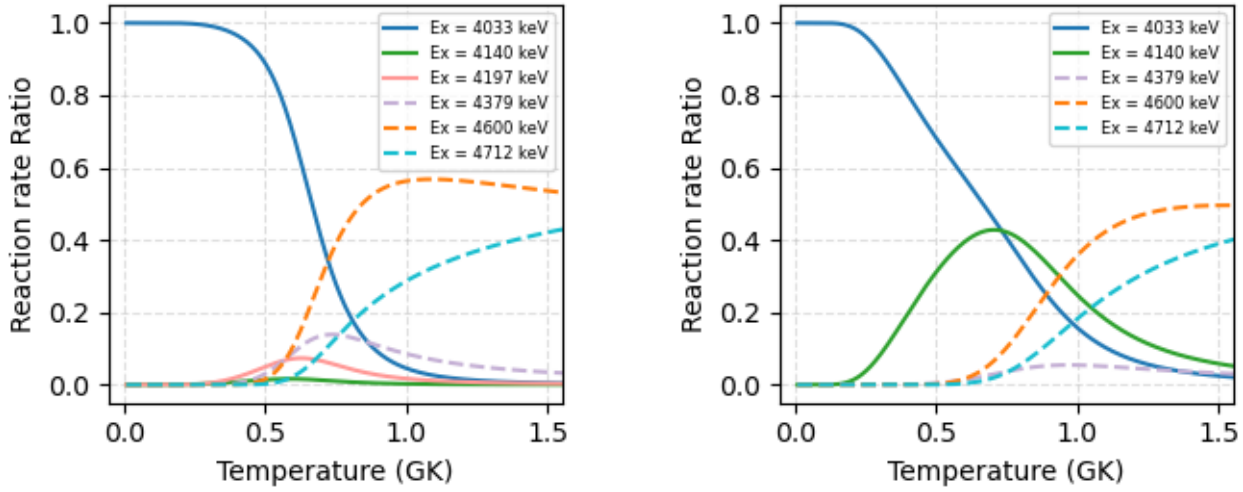

(a) (b)

Figure 6.2: Relative contribution to the reaction rate for (a) this work and (b) Tan et al.[Tan09]

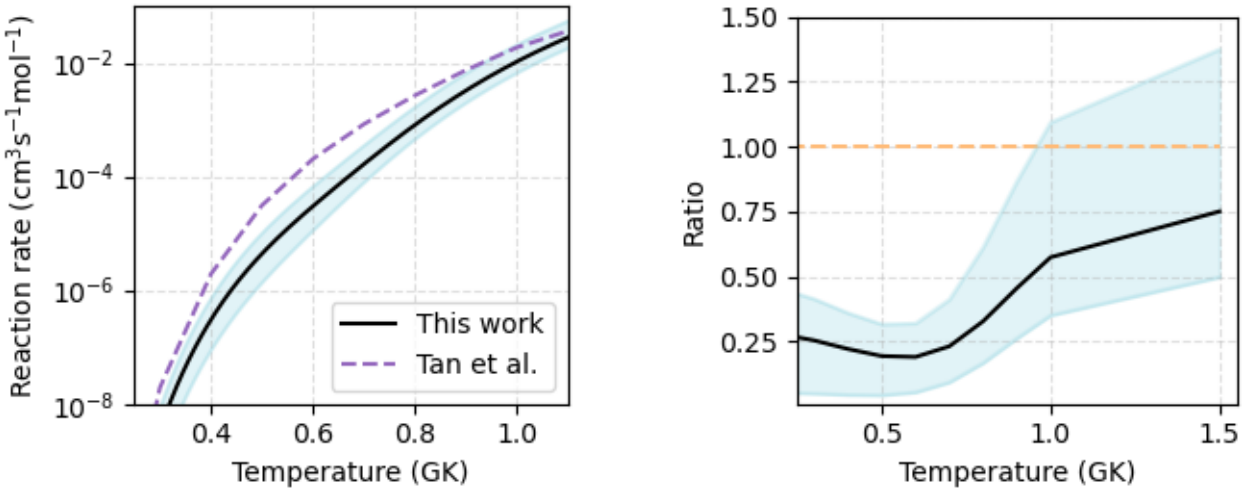

(a) (b)

Figure 6.3: (a) Total reaction rate for this work in comparison with the total reaction rate extracted from the values given in [Tan09] (dashed line). These values can also be found in table 6.2. (b) Similarly the ratio of the present rate is plotted relative to Tan et al. The determination of the upper and lower limits have been done taking the contribution of the 1σ uncertainty for all the resonances.

	This Work			Tan et al.		
T_9	Mean	Lower	Upper	Mean	Lower	Upper
0.1	2.08×10^{-25}	5.68×10^{-26}	4.82×10^{-25}	1.09×10^{-24}	3.20×10^{-25}	1.87×10^{-24}
0.2	3.69×10^{-13}	1.01×10^{-13}	8.56×10^{-13}	1.89×10^{-12}	4.08×10^{-13}	3.38×10^{-12}
0.3	3.47×10^{-9}	9.54×10^{-10}	8.01×10^{-9}	1.94×10^{-8}	4.64×10^{-9}	3.42×10^{-8}
0.4	3.03×10^{-7}	8.54×10^{-8}	6.93×10^{-7}	1.93×10^{-6}	5.44×10^{-7}	3.32×10^{-6}
0.5	4.38×10^{-6}	1.33×10^{-6}	9.83×10^{-6}	3.11×10^{-5}	1.02×10^{-5}	5.21×10^{-5}
0.6	3.01×10^{-5}	1.10×10^{-5}	6.51×10^{-5}	2.04×10^{-4}	7.56×10^{-5}	3.37×10^{-4}
0.7	1.65×10^{-4}	7.72×10^{-5}	3.44×10^{-4}	8.36×10^{-4}	3.46×10^{-4}	1.38×10^{-3}
0.8	8.10×10^{-4}	4.45×10^{-4}	1.63×10^{-3}	2.67×10^{-3}	1.23×10^{-3}	4.47×10^{-3}
0.9	3.26×10^{-3}	1.94×10^{-3}	6.43×10^{-3}	7.43×10^{-3}	3.80×10^{-3}	1.27×10^{-2}
1	1.05×10^{-2}	6.54×10^{-3}	2.04×10^{-2}	1.87×10^{-2}	1.03×10^{-2}	3.27×10^{-2}
1.5	0.379	0.252	0.696	0.507	0.339	0.863

Table 6.2: $N_A \langle \sigma v \rangle$ in units of cm^{3}mol^{-1}s^{-1} for different temperatures and comparison with results given in [Tan09]. The upper and lower values for the present work have been calculated as the contribution of the 1σ uncertainty for all the resonances.

These new results provide a better determination of the total reaction rate with reduced errors. The reaction rate is found to be significantly lower than the previous results estimated. The impact that these results will have on the astrophysical models must be addressed in detail following the present work. Beyond the present project, the next step is the implementation of the new reaction rate measurements in the stellar models to study the astrophysical impact that they have in the rp-process nucleosynthesis and in the production of X-ray bursts.

Further investigations are also needed for the second breakout route, the ^{18}Ne(α, p)^{21}Na, to determine the temperature range in which the two breakout routes are dominant, and to investigate its effect on rp-nucleosynthesis. This is particularly significant as with the reduced reaction rate for the ^{15}O(α, γ)^{19}Ne it is more important to know the ^{18}Ne(α, p)^{21}Na at a similar level of detail.

Appendix A

Technicalities

The analysis part of this work has been affected by several issues concerning the definition of the MUGAST detector for the simulations and analysis codes, and its performance during the experiment. These issues aroused while analysing the data and were consequently dealt with. Furthermore, some corrections were included in the analysis of the data, which concerned the recoils optimal identification and the γ-ray Doppler correction. A brief indication of these issues has been included in this appendix, for the reader to have a nicer reading experience.

A.1 MUGAST adjustments

A.1.1 Dead Layer Simulation

In this work simulations of the ^{15}O(^{7}Li, t)^{19}Ne transfer reaction were necessary to benchmark the results and performance of the detectors. NPTool [Mat16] was used for this matter. However some modifications to the code were needed, in particular, the implementation of the dead layers for the trapezoid detectors and for the annular detector.

NPTool uses Geant4 to perform the simulations. The dead layer was added to the geometry of each MUGAST detector in five steps. Firstly, the vector position with respect to the silicon material was defined. Then, the dimensions of the dead layer were added, defining the dead layer volume. A logic volume that contains the information of the dead layer material was then defined and used to fill the dead layer volume with the selected material, in this case aluminium. This material was located in the dead layer position using the vector defined in the first step. Finally, the dead layer was coloured in red to visualise it in the simulations. The piece of code used for the implementation of the dead layers for the trapezoid detectors is shown in figure A.1.

```
////////  Dead Layer  ////////

//// Define dead layer vector position:
G4ThreeVector  positionDeadLayer = G4ThreeVector(0, 0, -0.5*SiliconThickness-0.5*m_DeadLayer[DetNbr]);

//// Define dead layer dimensions and material:
G4Trap* solidDeadLayer = new G4Trap("solidDeadLayer",
          0.5*m_DeadLayer[DetNbr], 0*deg, 0*deg,
          TrapezoidHeight*0.5,  TrapezoidBaseSmall*0.5,TrapezoidBaseLarge*0.5, 0*deg,
          TrapezoidHeight*0.5,  TrapezoidBaseSmall*0.5,TrapezoidBaseLarge*0.5, 0*deg);

//// Define dead layer volume where the material will be placed:
G4LogicalVolume* logicDeadLayer = new G4LogicalVolume(solidDeadLayer,
        MaterialManager::getInstance()->GetMaterialFromLibrary("Al"),
        "logicDeadLayer",
        0, 0, 0);

//// Define dead layer position in Trapezoid volume:
new G4PVPlacement(0,
      positionDeadLayer,
      logicDeadLayer,
      Name + "_m_DeadLayer",
      logicTrapezoid,
      false,
      0);

//// Visualisation of dead layer:
G4VisAttributes* DeadLayerVisAtt = new G4VisAttributes(G4Colour(1.0, 0.0, 0.0));
logicDeadLayer->SetVisAttributes(DeadLayerVisAtt);
```

Figure A.1: Code used to incorporate the dead layers of the trapezoid detectors into the NPTool simulations. A brief explanation is given in the text.

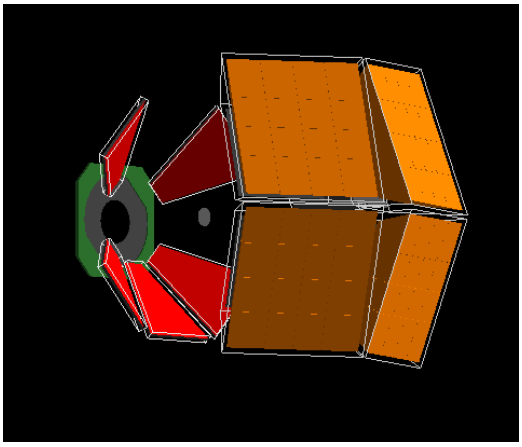

Figure A.2: Dead layer simulation for the trapezoid detectors. The dead layers are shown in red. The dead layer of the annular detector was also implemented, although it is not shown here.

The geometry of the implemented dead layers is shown in figure A.2 , where the dead layers are plotted in red for the trapezoids. The same was done for the annular detector and they were benchmarked by simulating the α transfer reaction assuming a *perfect beam*[1], i.e. a beam with $\sigma_x = \sigma_y = 0$, and no physical target (or very thin target) in order to reproduce the exact excitation energy for the ^{19}Ne simulated excited states.

A.1.2 MUGAST MG3 and MG4 readjustment

While working in the excitation energy plots and comparing the different MUGAST detectors, two of them showed a lower resolution and a shorter, wider Gaussian profile as it is shown in figure A.3a for detector MG4. A mistake in the definition of the geometry of these two detectors was thought to be the most probable reason. Thus, the configuration file was studied for them. The horizontal (X side) strips were found to be defined in the wrong order. The first step was inverting the X strips for detector 3 and doing a simulation to check the resolution. Once the right position was found. In figure A.3b a comparison of the excitation energy is shown for a reference detector, and it is clear that the resolution was recovered once the strip definition was corrected.

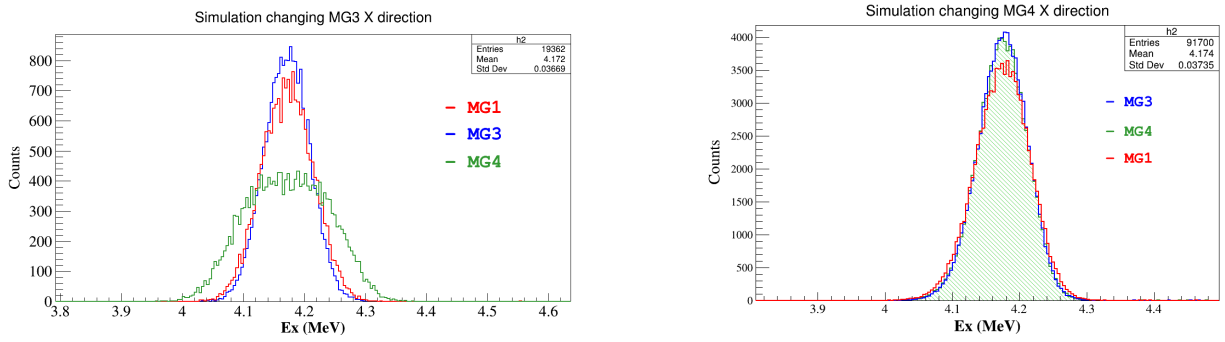

(a) (b)

Figure A.3: Figure showing the comparison between resolutions for a reference detector (MG1) and for MG3 and MG4. In (a) is shown detector MG3 after the redefinition of the X side strips, and MG4 is shown before changing the strip direction. Here the improvement in resolution is clear by comparing with the MG1 detector, whose strips were properly defined. In figure (b) both detectors have been fixed and the resolution is recovered.

[1] A realistic beam was used for the simulations and analysis of the transfer reaction, this perfect beam was only used to benchmark the dead layer implementation in the code.

A.1.3 MUGAST MG11 readjustment

The annular detector (MG11) had also some problems in the definition of the strips. This time the issue was the between the electronic channels and the physical strip number for one of the sides. This problem is very difficult to isolate and was spotted for another set of data from the same experimental campaign. To check that the MUGAST strip reference map was wrong for this experiment, an alpha calibration run was studied plotting the XY impact matrix for MG11 for both configurations (figure A.4, and checking that the strips with lower statistics were located in the outer part of the detector.

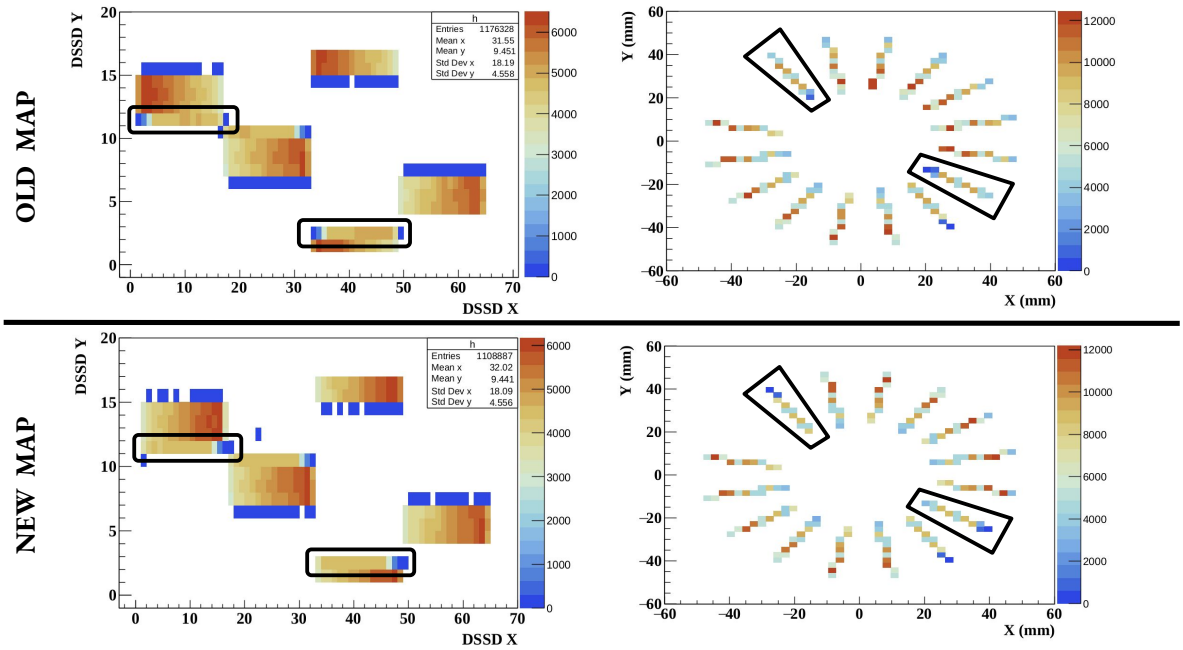

Figure A.4: Comparison of the impact matrix plot before and after changing the MUGAST map for detector MG11. The two plots above represent the old strip configuration, the two plots below represent the new strip configuration. The surrounded sectors are the ones modified. It is clear, comparing the impact matrix plots on the right that with the new configuration the lower statistics is in the outer parts of the detector.

Spotting this problem was especially important for the angular distribution reconstruction because many particles were given the wrong coordinates X and Y, impacting directly in the calculation of the angular coordinated for the events detected within these sectors.

A.1.4 Radio-frequency time adjustment

Earlier in this work has been mentioned the fact that some events experience a jump in radiofrequency, wrong time of flight for some of the detected particles (see chapter 3). These

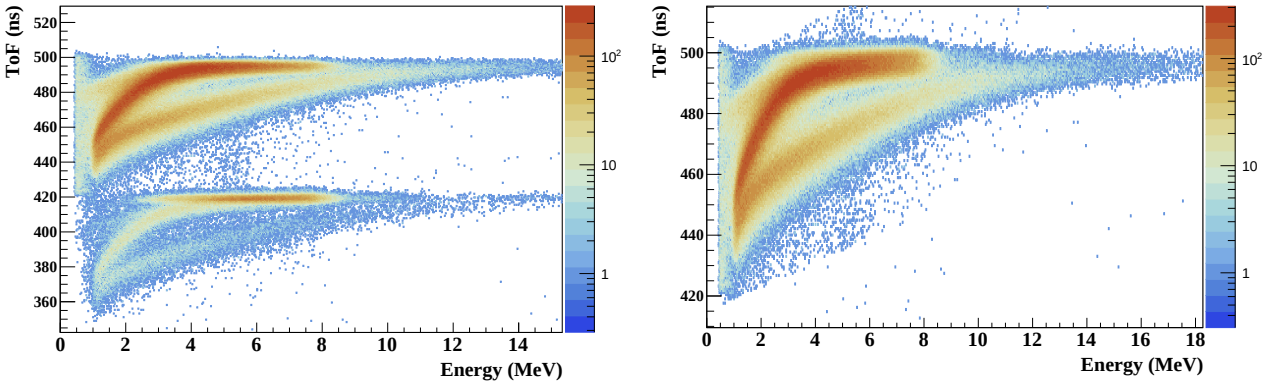

(a) (b)

Figure A.5: Adjustment of the time of flight value for the events that underwent a jump in radiofrequency.

jumps have been easily re-adjusted by adding a jump of 79.1 ns to the events that had the wrong time. The adjustment is shown in figure A.5.

A.2 Bragg peak removal

The charge state alignment is done in chapter 4.2.1 in order to extract a good charge identification. Removing the Bragg peak of the signal creates a cleaner spectra.

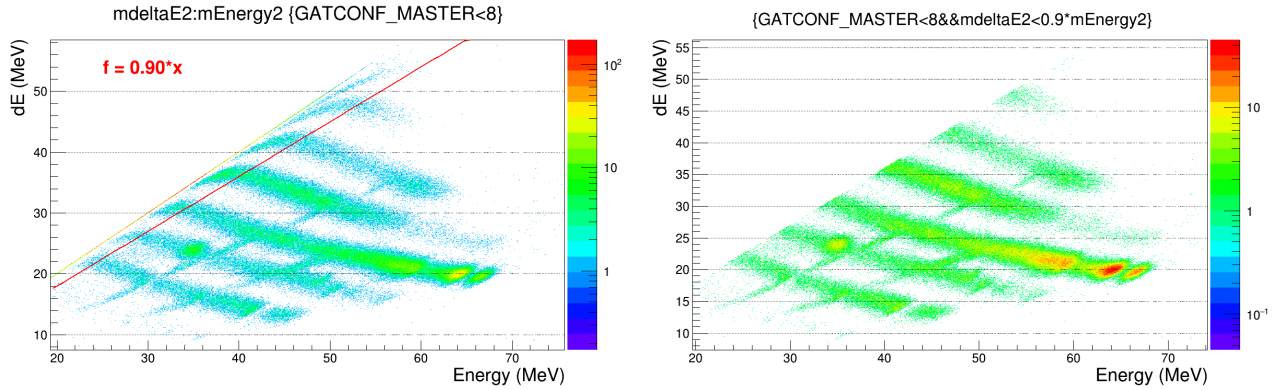

(a) Condition. (b) Condition applied.

Figure A.6: Condition applied to get rid of the Bragg peak. This condition is important in order to have a cleaner spectra and to be able to do an optimal charge alignment.

A.3 Average beam position on target

The beam position before entering in the reaction chamber couldn't be monitored. Thus, an uncertainty in the position interaction on target affects the calculations of the light particle impact angle and the excitation energy. An estimation of the beam X and Y interaction position has been done by performing a minimisation of the Ex resolution. In figure A.7 the beam spot is represented with this method, and it is clear that the beam was not centered. An average beam position was extracted using the whole set of statistics, choosing the minimisation of resolution and difference between the centroide and a reference energy, using the MINUIT algorithm embedded in ROOT. The parameters X,Y,Z (position of interaction) and target thickness T were set as free. The results in table show the expected shifts in X and Y, and also a slight shift in Z. However, the target thickness didn't vary, staying at the expected 4.37 μm also measured by the RBS technique.

X (mm)	-4.75
Y (mm)	-0.10
Z (mm)	+1.0
T (μm)	+4.37

Table A.1: MINUIT results for the position parameters X, Y, Z, and the target thickness parameter T.

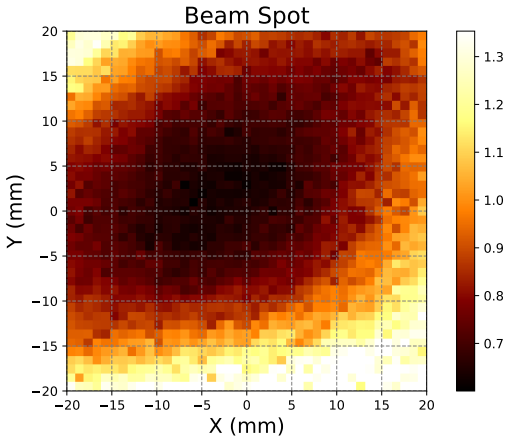

Figure A.7: Beam impact on target position.

A.4 Doppler Correction Optimisation figures

The following plots are useful to visualise the different positions of the peak centroid before and after the Doppler correction optimisation is performed. The plots are separated in four quadrants each representing the position of the peak detected in each Cartesian quadrant in the laboratory frame. All the figures should have their peaks aligned at zero (X vertically and Y horizontally).

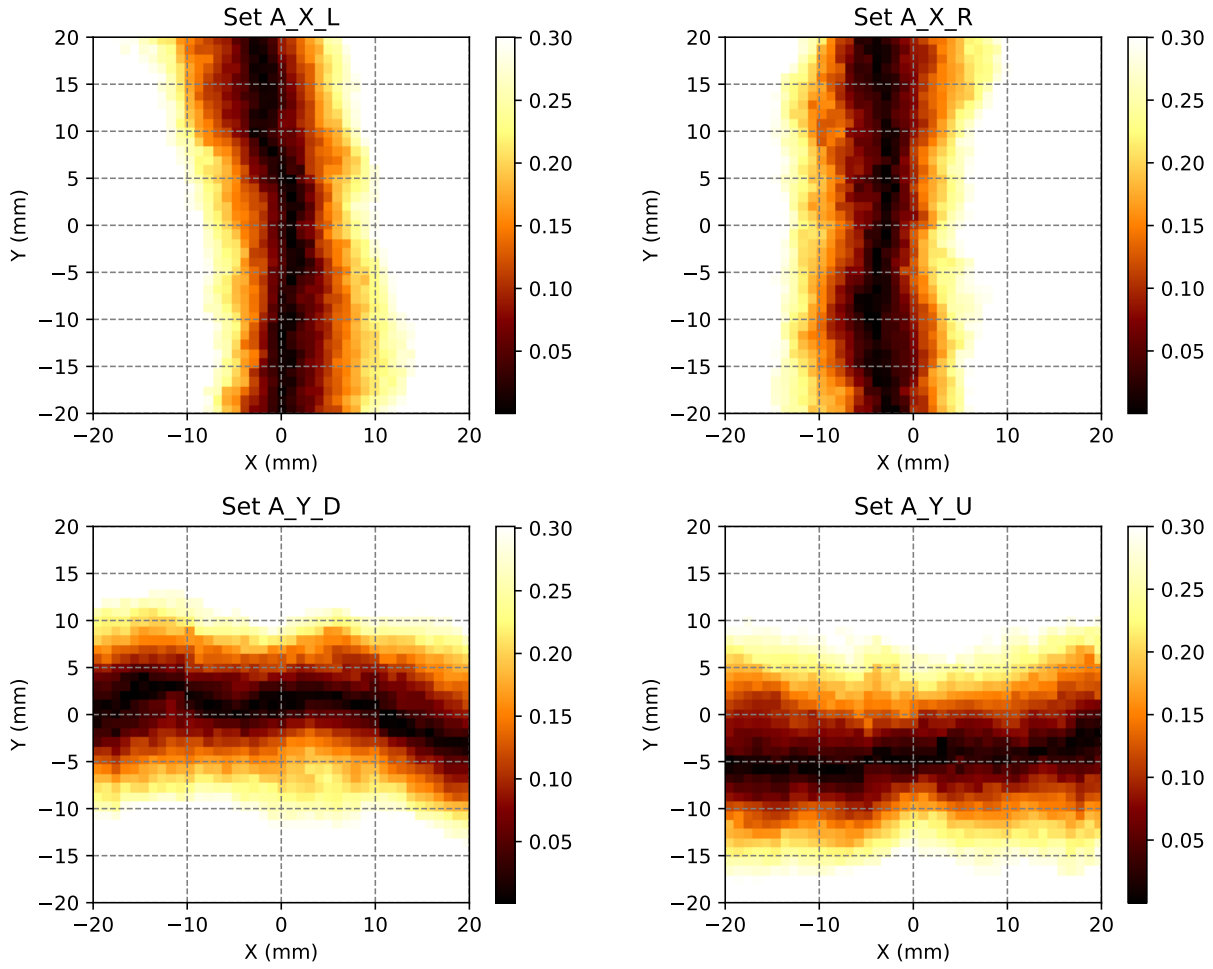

Figure A.8: Position of the peak centroid before optimisation.

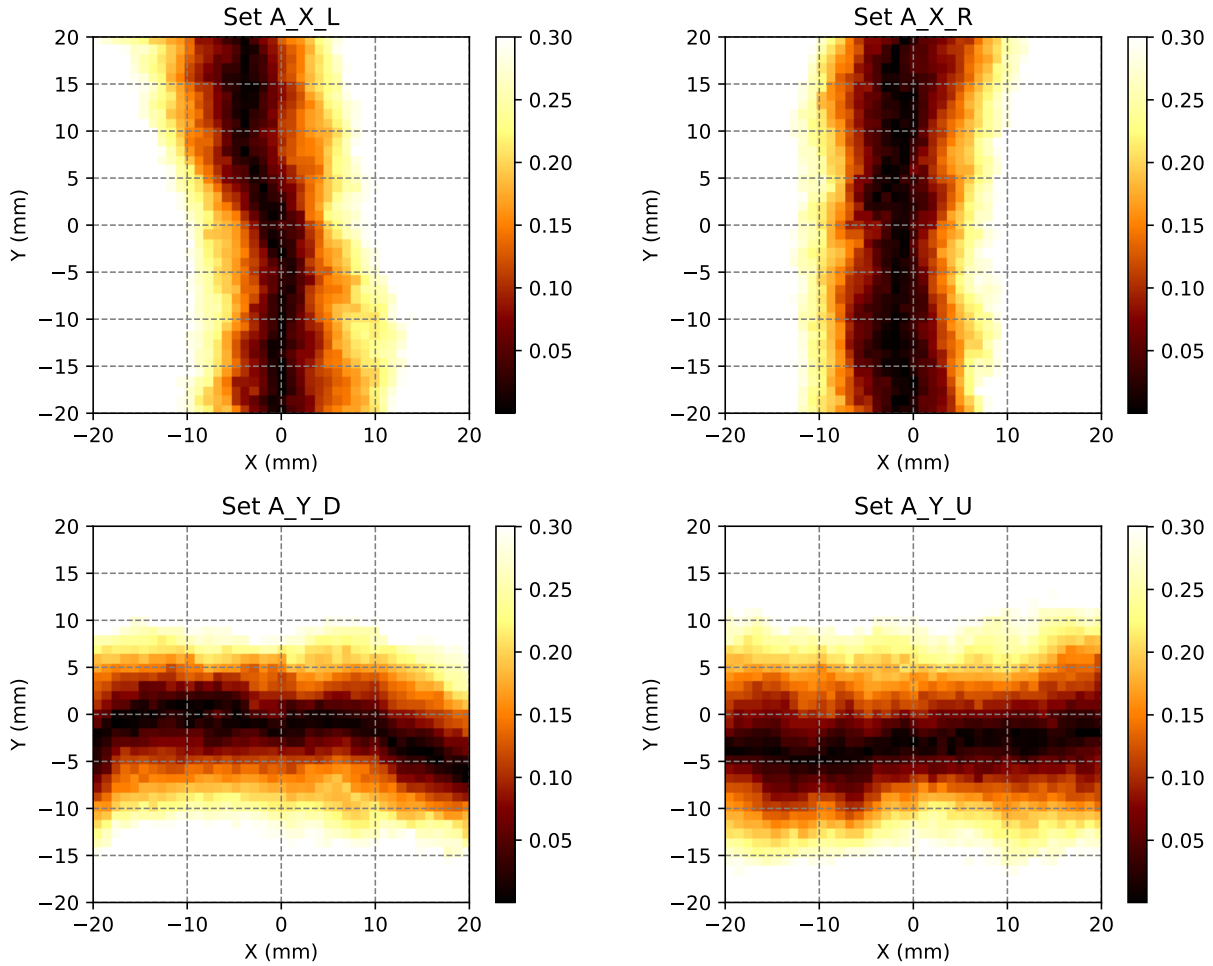

Figure A.9: Position of the peak centroid after optimisation.

Appendix B

Two-body kinematics

Studying the kinematics of a two-body interaction results on the determination of the energy and angle of the involved particles.

In a nuclear reaction, the energy and momentum must be conserved. Considering the reaction

$$A + a \Longrightarrow B + b, \tag{B.1}$$

the energy and momentum conservation laws establish that

$$E_A + E_a = E_B + E_b \tag{B.2}$$

$$\vec{p}_A + \vec{p}_a = \vec{p}_B + \vec{p}_b \tag{B.3}$$

The energy of a moving particle can be defined as $E = T + m$, where T is the kinetic energy and m is the mass in MeV. Also, a relationship between energy and momentum is given by $E^2 = p^2 + m^2$. For a relativistic kinematics, the momentum 4-vector can be defined [TN09] to study the reaction kinematics

$$\vec{P} = m_0\gamma(c, v_x, v_y, v_z) \tag{B.4}$$

where $m_0\gamma$ represents the relativistic mass, c is the speed of light and $\vec{v} = (v_x, v_y, v_z)$ is the vector velocity. Applying the 4-vector to each term of the reaction and using the convection $c = 1$, the momentum 4-vector for each particle in the laboratory frame can be written as

$$
\begin{aligned}
\vec{P}_A &= (T_A + m_A,\ 0,\ 0,\ p_{A,z}) \\
\vec{P}_a &= (m_a,\ 0,\ 0,\ 0) \\
\vec{P}_B &= (T_B + m_B,\ p_{B,x},\ 0,\ p_{B,z}) \\
\vec{P}_b &= (T_b + m_b,\ p_{b,x},\ 0,\ p_{b,z})
\end{aligned}
\tag{B.5}
$$

where the target a is not moving. The momentum of each particle can be referred to its lab frame coordinates as shown in figure B.1. By knowing the properties of the projectile and target, and by measuring the ejectile energy and angle, one can calculate the energy and angle of the recoil using the momentum and energy conservation equations.

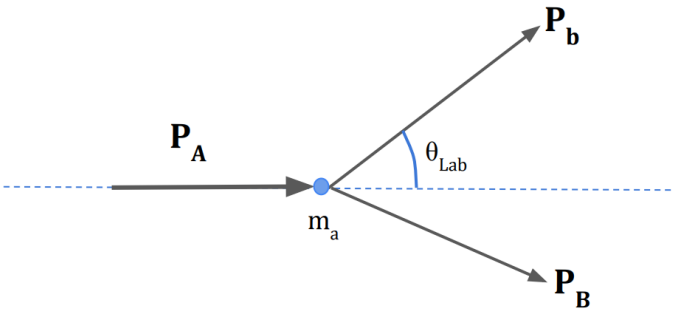

Figure B.1: Schematic view of the two-body kinematics vectors in the lab frame.

Appendix C

Integrated beam on target

In this appendix the calculation of the total number of beam particles on target is performed for the whole data set using the total yield from the relationship:

$$Y_T = Y_{\text{run}} \frac{N_T}{N_{\text{run}}} \tag{C.1}$$

where Y_{run} is the yield on target for a given run, N_T is the total number of particles registered and N_{run} is the number of particles registered during the selected run.

A short, stable run with known intensity is selected to extract the number of beam particles on target (Y_{run}) and the number of ^{19}Ne 9+ events (N_{run}). The total number of ^{19}Ne 9+ events are also extracted from the whole data set using the same gates (N_T). The total number of Ne events detected can be used instead of using only ^{19}Ne events, in case the statistics is low. The number of beam particles on target can be extracted following the equation

$$Y_{\text{run}} = I_{\text{run}} \cdot t \tag{C.2}$$

where I_{run} is the intensity of the run and t is the running time. It is important to use a stable run where the intensity is known and doesn't fluctuate. In order to choose a stable run, or a stable period of time from a particular run, a plot of number of events against running time is produced. An example of this plot is shown in figure C.1 for run 124, where the running time is shown in minutes. Different measurements of the beam intensity were done for each run using a beam monitor that extracted the beam profile. A calibration of this beam monitor was done comparing with the measurement obtained using the CATS detectors, located just before the target chamber. From this calibration a relationship between the real intensity and the measured intensity is extracted to be $I_r = 0.833868 \cdot I_m - 1204.65$ pps.

Profiler	CATS	%
$2.3 \cdot 10^4$	$1.8 \cdot 10^4$	21.7
$1.4 \cdot 10^5$	$1.16 \cdot 10^5$	17.1
$9.0 \cdot 10^3$	$7.3 \cdot 10^3$	18.9
$5.0 \cdot 10^4$	$3.9 \cdot 10^4$	22.0

Table C.1: Calibration of beam monitor using measurements of beam intensity from CATS. The beam profiler overestimates the intensity by about 20% comparing with the intensity measured using CATS.

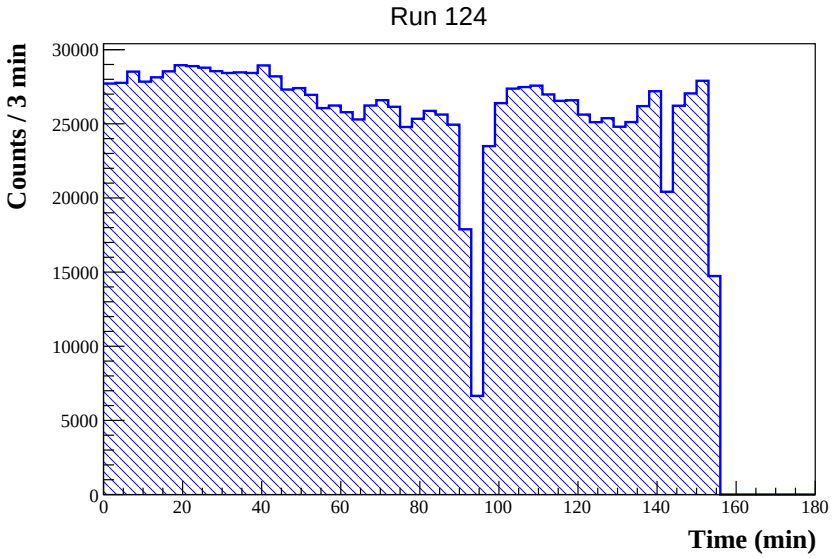

Figure C.1: Time stamp plot for run 124. Stable intensity throughout the whole running time, only disturbed by a measurement of the intensity by the beam monitor halfway through the run.

Two different runs were selected to extract the total yield on target, run 124 and run 152. From each run, different ranges of time were used, where the beam intensity was stable and had been recently measured, as shown in figure C.2.

Table C.2 shows the information used to calculate the yield on target from each selected range of time, as well as the number of neon events and 19Ne events registered using the same conditions. For the whole data set, the total number of particles registered are $N_{T,\mathrm{Ne}}$=20730 and $N_{T,^{19}\mathrm{Ne}}$=4638. Using equation C.1 the total yield on target can be extracted. An average is calculated from each of the measurements to find the final result:

$$Y_T = 5.727 \cdot 10^{12} \text{ part}$$

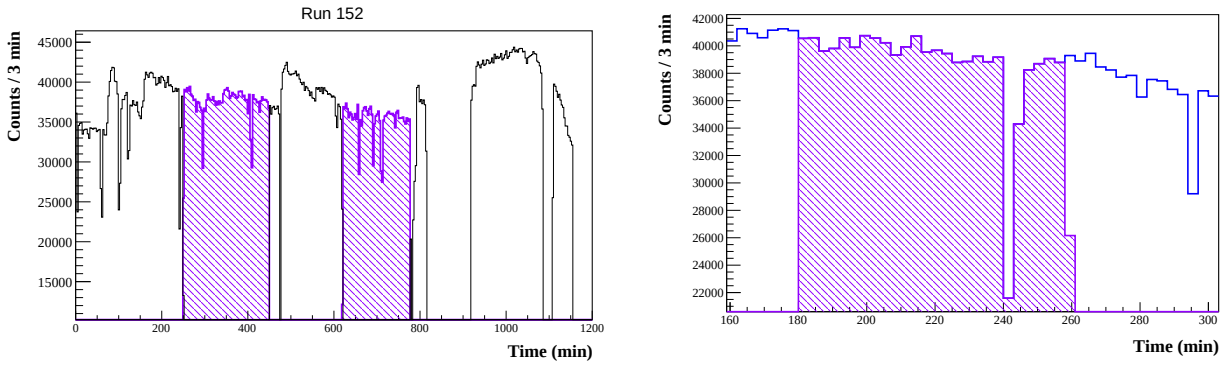

Figure C.2: (left) time stamp plot for run 152 and (right) zoom on range of time between 180 and 260 minutes. The highlighted regions are the chosen ones to extract a total yield on target value.

Run	T Range [min]	t [min]	Y_{run}	N_{Ne}	$N_{\text{19-Ne}}$	$Y_{\text{T,Ne}}$	$Y_{\text{T,19-Ne}}$
124	0 - 46	46.0	$3.45 \cdot 10^{10}$	116	30	$6.165 \cdot 10^{10}$	$5.334 \cdot 10^{10}$
124	46 - 152	106.0	$6.76 \cdot 10^{10}$	211	48	$6.641 \cdot 10^{10}$	$6.532 \cdot 10^{10}$
152	180 - 260	79.0	$6.32 \cdot 10^{10}$	254	45	$5.161 \cdot 10^{10}$	$6.518 \cdot 10^{10}$
152	250 - 450	200.0	$1.60 \cdot 10^{11}$	631	129	$5.260 \cdot 10^{10}$	$5.756 \cdot 10^{11}$
152	620 - 777	157.0	$1.18 \cdot 10^{11}$	537	102	$4.547 \cdot 10^{10}$	$5.356 \cdot 10^{11}$

Table C.2: Selected range of time for runs 124 and 152 including calculation of number of beam particles on target (Y_{run}) and number of detected events. Total yield on target estimated. An average yield from these results is given in text.

Appendix D

Tables

D.1 Alpha source

The MUGAST energy calibration was performed using an α-source composed of ^{239}Pu, ^{241}Am and ^{244}Cm. The α-decay of these isotopes is well known and benckmarked. They emit alpha particles at well determined energies that are summarised in table D.1. This information is used for the energy calibration of the individual detector strips and the methodology followed can be found in section 3.3.1.2.

	Half life (yr)	Energy (MeV)	Intensity (%)
^{239}Pu	$2.4{\cdot}10^4$	5.15659(14)	70.77(14)
		5.11443(8)	17.11(14)
		51055(8)	11.94(14)
^{241}Am	432.2	5.48556(12)	84.8(5)
		5.44280(13)	13.1(3)
		5.38823(13)	1.66(2)
^{244}Cm	18.1	5.80477(5)	76.40(12)
		5.76264(3)	23.60(12)

Table D.1: Components of the triple-alpha source used to do the detector energy calibration. The different isotopes decay emitting an alpha particle at a very well known energy. With the 3 different more intense energies detected we can do a fine calibration of our detectors. Detailed information of the followed procedure is given in the text.

D.2 Cross section and spectroscopic factor calculations

In this appendix a summary of the data used to extract the spectroscopic factors using the integration method explained in chapter 4.7.2 is given. Table D.2 includes information of the number of particles detected for each measured excited state in ^{19}Ne. For each state, a calculation of the experimental cross section integrated over the angular range $\theta_{cm} = 3 - 19$ deg has been done and compared with theoretical DWBA calculations (σ_{th}) to extract the spectroscopic factors.

E_x	N	B_{tot}	σ/N (μb)	σ_{exp} (mb)	σ_{th} (mb)	C^2S_α
1508	61	6.0	2.17	0.24	1.05	0.23
1536	18	1.8	2.01	0.07	0.39	0.18
1615	29	3.6	2.72	0.17	0.68	0.25
2794	26	5.1	2.84	0.12	0.65	0.18
4033	3	0.8	4.77	0.018	0.29	0.06
4140	48	7.0	2.84	0.28	2.77	0.10
4197	106	4.0	3.55	0.78	3.51	0.23
4379	3	0.7	4.61	0.031	2.14	0.014
4600	2	0.2	6.04	0.024	1.59	0.015

Table D.2: Results of experimental cross section integrated over the angular range $\theta_{cm} = 3 - 19$ deg, and spectroscopic factors for ^{19}Ne excited states. The value of σ/N gives an idea of the contribution to the cross section per triton before geometrical efficiencies are applied. The total background B_{tot} found for each state has also been included.

Appendix E

Schemes

This appendix contains the AGATA data processing scheme where the steps followed to read and process the raw data are given. It also includes the electronic schemes used on the experimental setup as a reference point for future experiments.

E.1 AGATA data processing scheme

In this section of the appendix a scheme explaining the steps followed in order to process the AGATA raw data are outlined. This is explained in more detail in chapter 3.5.2. In scheme E.1 two different processing levels are identified: Local Level Processing and Global Level Processing. The collected raw data follows first the steps indicated for the LLP, where energy and time calibrations are applied, pulse-shape analysis is carried out and re-calibrations and corrections are done. This first part was done by the AGATA collaboration during the experiment. The GLP takes the output data from the LLP and merges it with the data from the ancillary detectors, applying time coincidences and tracking algorithms. This part was done by me after the experiment and after the calibration of the ancillary detectors. The GLP includes the event validation applying timestamp windows, application of coincidence windows to merge the AGATA data with MUGAST and VAMOS data, and the event builder actor, where the output root tree is created and stored. More details on the data processing can be found in the AGATA documentation.

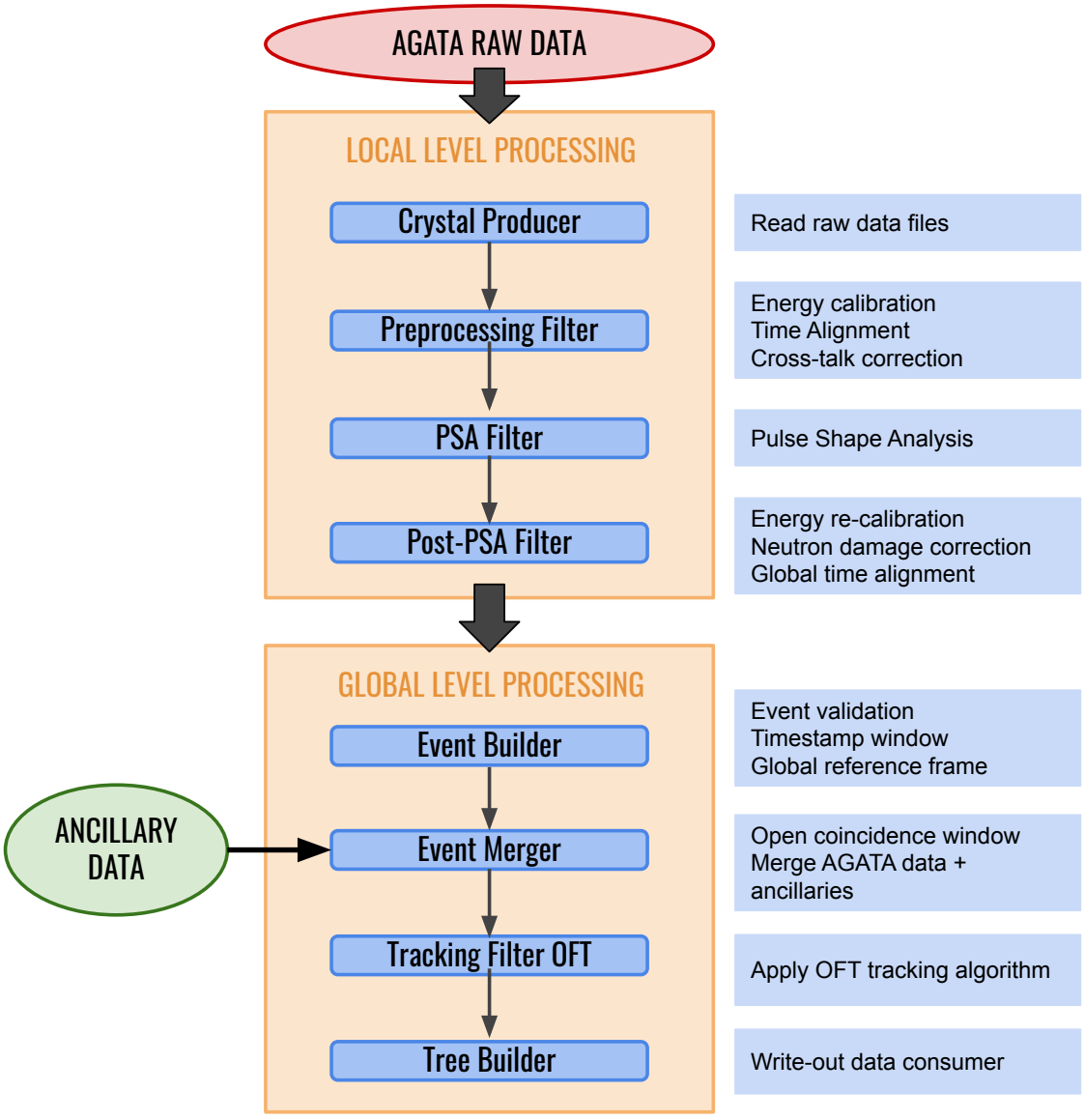

Figure E.1: AGATA scheme explaining the steps followed on the data processing from writing on disk to analysis root files.

E.2 Electronic schemes

In this section of the appendix a schematic view of the electronics used during the experiment are shown. Note that for the present experiment the beam tracking detector (CATS) had to be removed from the setup because the beam intensity used was too high for them to cope with it. The MUVI electronics refers to the MUGAST + MUST2 detectors.

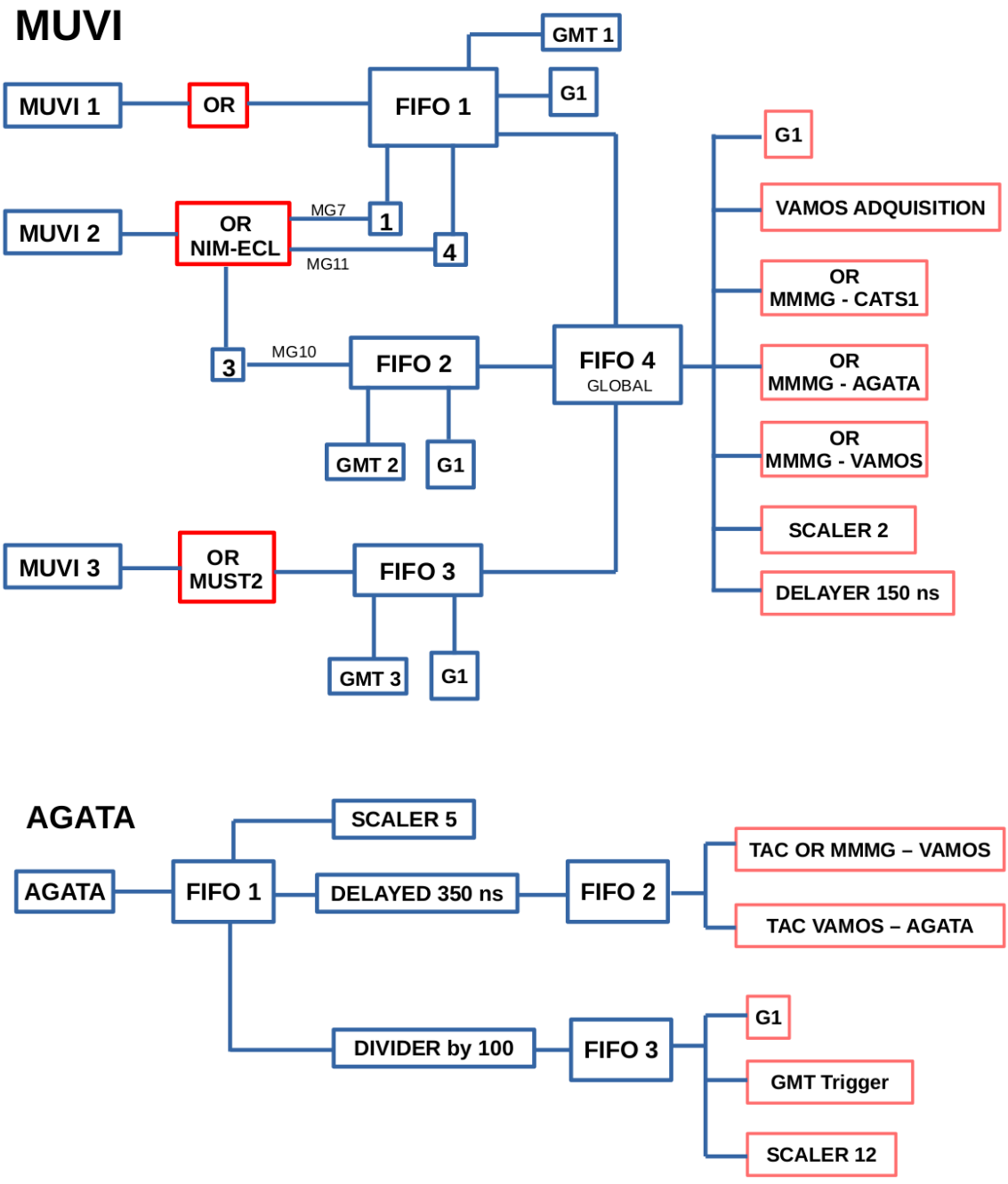

VAMOS trigger (MWPPAC)

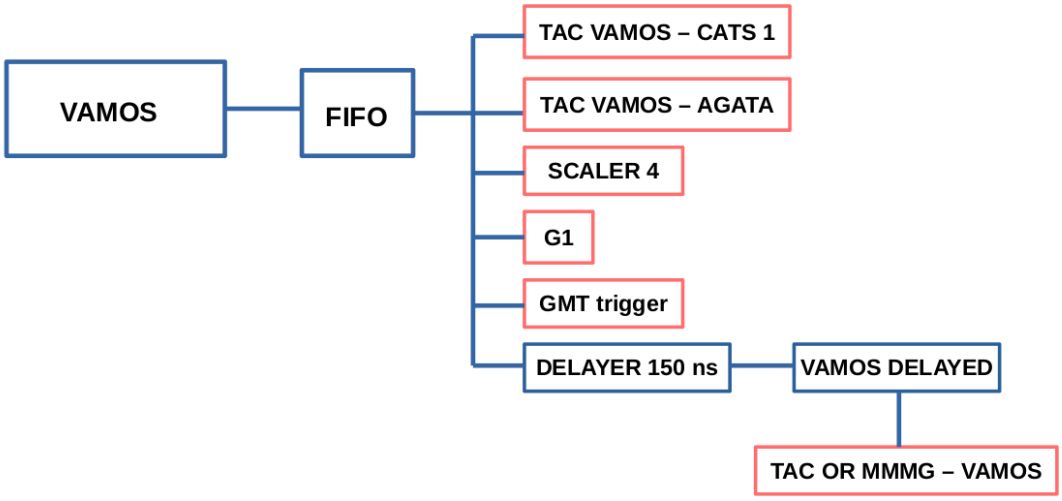

DEAD TIME

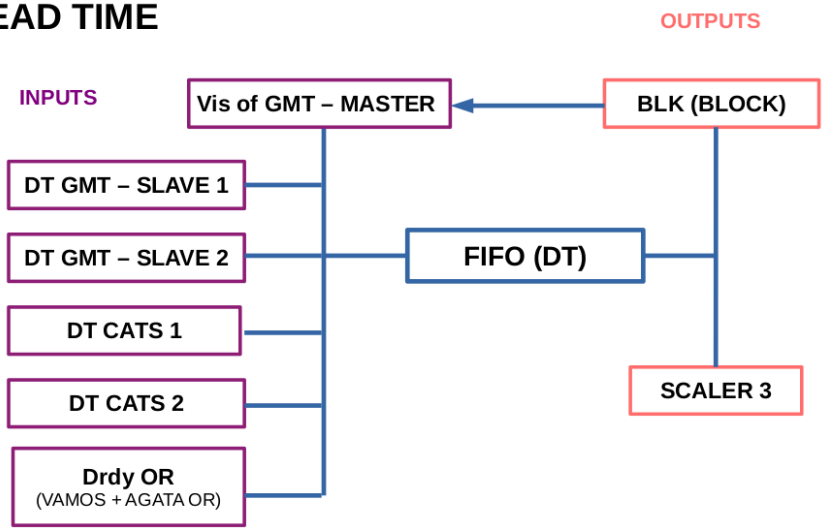

HIGH FREQUENCY

HF of the cyclotron. Signal coming from VAMOS

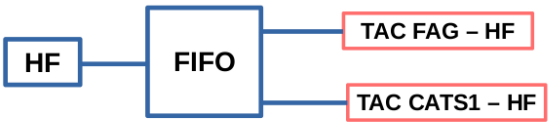

Appendix F

Diamond detector

The present appendix has already been published in the proceedings paper "An Implantation diamond detector as a beam monitor for an intense radioactive ion beam" that can be found in J. Phys.: Conf. Ser. 1643 012040 (2020), also included in reference [Roj20]. I am the sole author of this text. The contents of the paper have been slightly modified to match the style of this dissertation. However the text is mostly presented as published.

Monitoring the beam was a challenge during this particular experiment due to its characteristics. Low intensity beams up to 10^5 pps can be monitored by plastic scintillators or silicon detectors. On the other hand, high intensity beams of about 10^9 pps or more are easily monitored using a current integrated Faraday cup. However, for this experiment a radioactive ^{15}O beam at 10^7 pps was needed, intensity too high to use a plastic or a silicon detector and too low to be able to use a faraday cup. Thus, a new technique for monitoring this particular intensity was applied during the experiment, using a diamond detector as a beam rate monitor with full stopping of high intense radioactive ion beams.

Diamond has the great advantage of being a semiconductor material with a band gap of 5.6 eV [Mor01], big enough to be able to operate in room temperature conditions, and achieving a breakdown field strength of 10^7 V/cm [Sch12]. Diamond is a covalent material: it is composed by atoms instead of being composed for ions. Its chemical composition makes diamond a non electrical conductor. Within its properties can be highlighted its radiation hardness, very robust material with great tolerance to high particle intensities.

The high mobility and charge carrier saturation provide diamond a extremely good time resolution, meaning short, uniform rising times < 100 ps, experiencing high counting rate capability of 10^9 pps. Thus, a resolution of picoseconds is achieved, given by the high mobility

Figure F.1: Diamond detector frame and substrate. The board was mounted on the movable part of the VAMOS focal plane. The total size of the boar is 3.45 x 2.20 cm^2.

of charges (e-h saturation velocity 10^7 cm/s) [Ber]. Timing limitations are given by the resolution of the electronics and the quality of the diamond detector [Due11].

The diamond detector used during the experiment is shown in figure F.1. It has a size of (2x2) cm^2 and 0.5 mm thick. It was located at the focal plane of the VAMOS spectrometer. The electronics used to process the signal was a Diamond Broadband Amplifier [Mor01], fast enough to collect the signal.

Details of the diamond preparation and electronics used can be found in reference [Roj20].

F.0.1 Time performance test

Two different time response tests were done with a triple α source (Am-Cm-Pu) at University of York. The first test was performed in order to make sure that the diamond sample was in working order. The second test was performed after mounting the substrate on the new frame with the new contacts. These tests confirmed that the detector was working fine. For the performance test the detector and the α source were located inside a vacuum chamber. The distance between the source and the detector was 15mm.

Measurements of shaping time and rise time were conducted. In figure F.2 a pulse obtained

during the test is shown. It is noticeable how fast the detector is, having a shaping time of around 2-3ns.

A third test was performed with a Cf-202 source once the diamond detector was properly located on the VAMOS focal plane. This test ensured that the electronics was working and allowed the adjustment of the threshold in order to avoid noise.

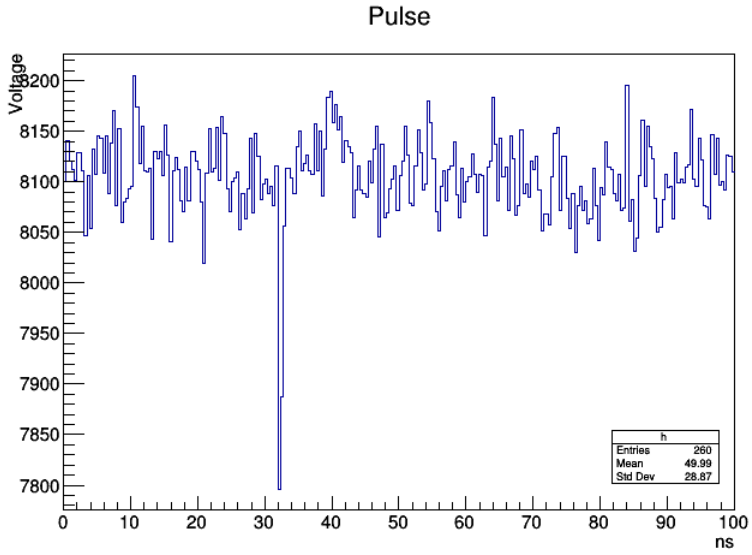

Figure F.2: Time response of the diamond detector. Units of voltage in (mV) and units of time in (ns). A single pulse is shown on the image, corresponding to one single alpha particle signal. The very fast response is noticeable on the spectrum. A shaping time of about 2 ns can be appreciated.

F.0.2 Implementing the diamond counter on the VAMOS focal plane

The diamond detector was mounted on the movable mechanism of the VAMOS spectrometer focal plane. It was located directly to stop the non-reacted beam. Stopping the beam on the detector allowed to monitor it by counting the particles impacting on the diamond detector. While the beam position is fixed, the count rate scales with the beam intensity. If the beam slightly moves, the detector rate is reduced as the beam is no longer centered on the diamond detector. If the beam switches off, the detector rate drops. In figure F.3 an example of the signal of the diamond detector is shown. It is largely constant around 7500 s^{-1} and it drops to zero at around 06:53 where the beam was stopped. This is a very nice way to monitor the beam: by seeing the signal and being able to graphically determine the amount of time where the beam was not available. Instabilities on the beam intensity were also monitored during the experiment.

Unfortunately some limitations were experienced during the experiment. Working with a radioactive beam such as ^{15}O means that the beam production and optimization is not straightforward and is the reason why the beam spot ended up being too big to cover with the current detector. The beam also needed to be moved to the right of the centre of the detector for technical reasons. Only a percentage of the full beam signal was detected. The electronics was the main limitation on the detector performance in terms of time resolution, as it has to process a very fast signal. Diamond Broadband Amplifiers (DBA-IV) [Mor01] signal processors were used.

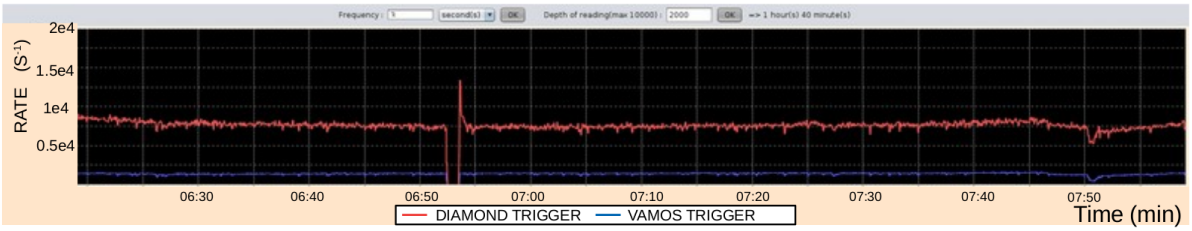

Figure F.3: Online graphic monitor of the diamond detector used during the experiment. Trigger rate (y-axis) units in s^{-1} and time (x-axis) units in minutes. A constant signal is shown, only perturbed by a few minutes' cut. This cut is caused by a beam loss in chamber.

Using a diamond detector as a beam monitor was successful as an online tool. However it was too small to cover the whole beam spot and some other performance issues should be addressed to be used as a beam counter alongside as a beam monitor. Nontheless, the technique looks promising for both monitoring and normalising high intense radioactive ion beams and further studies are encouraged in this direction for experiments using high-intensity radioactive ion beams.

Bibliography

[Akk12] S. Akkoyun et al. "AGATA—Advanced GAmma Tracking Array". In: *Nuclear Instruments and Methods in Physics Research Section A: Accelerators, Spectrometers, Detectors and Associated Equipment* 668 (Mar. 2012), pp. 26–58.

[Al-12] A. Al-Adili et al. "On the Frisch–Grid signal in ionization chambers". In: *Nuclear Instruments and Methods in Physics Research Section A: Accelerators, Spectrometers, Detectors and Associated Equipment* 671 (2012), pp. 103–107.

[Ass21] M. Assié et al. "The MUGAST-AGATA-VAMOS campaign: Set-up and performances". In: *Nuclear Instruments and Methods in Physics Research Section A: Accelerators, Spectrometers, Detectors and Associated Equipment* 1014 (Oct. 2021), p. 165743.

[Bar89] R. J. Barlow. *Statistics: A Guide to the Use of Statistical Methods in the Physical Sciences (Manchester Physics Series)*. Reprint. WileyBlackwell, 1989.

[Ber] E Berdermann et al. "CVD-Diamond Detectors for Spectroscopy and Timing". en. In: (), p. 12.

[Ber17] M.J. Berger et al. *ESTAR, PSTAR, and ASTAR: Computer Programs for Calculating Stopping-Power and Range Tables for Electrons, Protons, and Helium Ions (version 2.0.1)*. National Institute of Standards and Technology, Gaithersburg, MD. 2017. URL: http://physics.nist.gov/Star. (accessed: 10.03.2022).

[Bha70] K. Bharuth-Ram et al. "Nuclear Lifetime of the Ne-19 275-keV Level". In: *Phys. Rev. C* 2 (1970), pp. 1210–1213.

[Bur57] E. Margaret Burbidge et al. "Synthesis of the Elements in Stars". In: *Reviews of Modern Physics* 29.4 (Jan. 1957), pp. 547–650.

[Cla68] Donald D Clayton. *Principles of stellar evolution and nucleosynthesis*. eng. New York: McGraw-Hill, 1968.

[Cle17] E. Clement et al. "Conceptual design of the AGATA 1π array at GANIL". In: *Nuclear Instruments and Methods in Physics Research Section A: Accelerators, Spectrometers, Detectors and Associated Equipment* 855 (2017). Title in WoS: Conceptual design of the AGATA 1 pi array at GANIL, pp. 1–12.

[CN05] Randall L. Cooper and Ramesh Narayan. "Theoretical Models of Superbursts on Accreting Neutron Stars". In: *The Astrophysical Journal* 629.1 (Aug. 2005). arXiv: astro-ph/0410462, pp. 422–437.

[CN07] Randall L. Cooper and Ramesh Narayan. "Hydrogen-Triggered Type I X-ray Bursts in a Two-Zone Model". In: *The Astrophysical Journal* 661.1 (May 2007). arXiv: astro-ph/0702042, pp. 468–476.

[CO13] Bradley W Carroll and Dale A Ostlie. *Introduction to Modern Astrophysics, an.* eng. Pearson custom library. Harlow, United Kingdom: Pearson Education, Limited, 2013.

[Col] The GRIT Collaboration. *GRIT, next generation silicon detector.* URL: http://grit.in2p3.fr/.

[Cyb16] R. H. Cyburt et al. "Dependence of X-ray burst models on nuclear reaction rates". en. In: *ApJ* 830.2 (Oct. 2016), p. 55.

[Dav03] B. Davids et al. "α-decay branching ratios of near-threshold states in ^{19}Ne and the astrophysical rate of ^{15}O$(\alpha,\gamma)^{19}$Ne". In: *Phys. Rev. C* 67 (1 Jan. 2003), p. 012801.

[Dav11] Barry Davids et al. "The influence of uncertainties in the ^{15}O(α, γ)^{19}Ne reaction rate on models of type I X$_r$*ayburs*ts". In: *The Astrophysical Journal* 735.1 (June 2011), p. 40.

[Due11] J.A. Dueñas et al. "Time structure of ns duration bunches with single crystal diamond detector". In: *Nuclear Instruments and Methods in Physics Research Section A: Accelerators, Spectrometers, Detectors and Associated Equipment* 641 (2011), pp. 33–36.

[Dun53] D. N. F. Dunbar et al. "The 7.68-Mev State in C^{12}". In: *Phys. Rev.* 92 (3 Nov. 1953), pp. 649–650.

[Epe12] Evgeny Epelbaum et al. "Structure and rotations of the Hoyle state". In: *Phys. Rev. Lett.* 109 (2012), p. 252501.

[Eri20] T. K. Eriksen et al. "Improved precision on the experimental $E0$ decay branching ratio of the Hoyle state". In: *Phys. Rev. C* 102 (2 Aug. 2020), p. 024320.

[Far10] E. Farnea et al. "Conceptual design and Monte Carlo simulations of the AGATA array". en. In: *Nuclear Instruments and Methods in Physics Research Section A: Accelerators, Spectrometers, Detectors and Associated Equipment* 621.1 (Sept. 2010), pp. 331–343.

[Fis06] Jacob Lund Fisker et al. "The Importance of $^{15}O(\alpha, \gamma)^{19}Ne$ to X-Ray Bursts and Superbursts". en. In: *ApJ* 650.1 (Oct. 2006), p. 332.

[FK78] H. T. Fortune and D. Kurath. "Alpha transfer to ^{18}O with empirical wave functions". In: *Phys. Rev. C* 18 (1 July 1978), pp. 236–238.

[FLS10] H. T. Fortune, A. Lacaze, and R. Sherr. "Update on -particle and nucleon widths in F 19 and Ne 19". en. In: *Physical Review C* 82.3 (Sept. 2010).

[FST07] Jacob Lund Fisker, Hendrik Schatz, and Friedrich-Karl Thielemann. "Explosive hydrogen burning during type I X-ray bursts". In: *arXiv:astro-ph/0703311* (Mar. 2007). arXiv: astro-ph/0703311.

[Gla19] B. E. Glassman et al. "Doppler broadening in $^{20}Mg(\beta p\gamma)^{19}Ne$ decay". In: *Phys. Rev. C* 99 (6 June 2019), p. 065801.

[Gou09] B. Gough. *GNU scientific library reference manual*. Network Theory Ltd., 2009.

[Gri76] J. Grindlay et al. "Discovery of intense X-ray bursts from the globular cluster NGC 6624." In: 205 (May 1976), pp. L127–L130.

[Hal19] M. R. Hall et al. "New γ-ray transitions observed in ^{19}Ne with implications for the $^{15}O(\alpha,\ \gamma)^{19}Ne$ reaction rate". In: *Phys. Rev. C* 99.3 (Mar. 2019). Publisher: American Physical Society, p. 035805.

[Hey94] K Heyde. *Basic ideas and concepts in nuclear physics. An introductory approach*. Dec. 1994.

[HJ01] T. Hauschild and M. Jentschel. "Comparison of maximum likelihood estimation and chi-square statistics applied to counting experiments". In: *Nuclear Instruments and Methods in Physics Research A* 457.1-2 (Jan. 2001), pp. 384–401.

[Hor05] M B Gómez Hornillos et al. "Mass measurements with the CIME cyclotron at GANIL". In: *Journal of Physics G: Nuclear and Particle Physics* 31.10 (Sept. 2005), S1869–S1872.

[Hoy46] F. Hoyle. "The synthesis of the elements from hydrogen". In: 106 (Jan. 1946), p. 343.

[Hoy53] F. Hoyle et al. "A state in C^{12} predicted from astrophysical evidence." In: *Presented at the Minutes of the New Mexico Meeting Held at Alberquerque* 92 (Sept. 1953), p. 1095c.

[Hoy54] Fred Sir Hoyle. "On Nuclear Reactions Occuring in Very Hot STARS.I. the Synthesis of Elements from Carbon to Nickel." In: *Astrophysical Journal Supplement Series* 1 (1954), pp. 121–146.

[HS21] Faïrouz Hammache and Nicolas de Séréville. "Transfer Reactions As a Tool in Nuclear Astrophysics". In: *Frontiers in Physics* 8 (2021), p. 630.

[Ili08] Christian Iliadis. *Nuclear Physics of Stars*. en. Google-Books-ID: rog9FxfGZQoC. John Wiley & Sons, July 2008.

[JD02] James Hopwood Jeans and George Howard Darwin. "I. The stability of a spherical nebula". In: *Philosophical Transactions of the Royal Society of London. Series A, Containing Papers of a Mathematical or Physical Character* 199.312-320 (1902), pp. 1–53. eprint: https://royalsocietypublishing.org/doi/pdf/10.1098/rsta.1902.0012.

[Ji20] Xiangpan Ji et al. "Combined Neyman–Pearson chi-square: An improved approximation to the Poisson-likelihood chi-square". In: *Nuclear Instruments and Methods in Physics Research Section A: Accelerators, Spectrometers, Detectors and Associated Equipment* 961 (May 2020), p. 163677.

[Kan06] R. Kanungo et al. "Lifetime of ^{19}Ne*(4.03 MeV)". In: *Phys. Rev. C* 74 (4 Oct. 2006), p. 045803.

[Kno10] Glenn F. Knoll. *Radiation Detection and Measurement*. John Wiley & Sons, Aug. 2010.

[Kra88] Kenneth S Krane. *Introductory nuclear physics*. New York, NY: Wiley, 1988.

[Kub72] K. -I. Kubo. "Finite-range DWBA analyses of the 16 O(7 Li, t) 20 Ne and 15 n(7 Li, t) 19 F reactions". In: *Nucl. Phys. A* 187 (1972), pp. 205–218.

[Lai02] A. M. Laird et al. "Indirect study of the astrophysically important ^{15}O$(\alpha,\gamma)^{19}$Ne reaction through ^{2}H(^{18}Ne,^{19}Ne)^{1}H". In: *Phys. Rev. C* 66 (4 Oct. 2002), p. 048801.

[Lan86] K. Langanke et al. "A new estimate of the Ne-19(p, gamma) Na-20 and O-15(alpha, gamma) Ne-19 reaction rates at stellar energies". In: 301 (Feb. 1986), pp. 629–633.

[Lop04] A. Lopez-Martens et al. "-ray tracking algorithms: a comparison". en. In: *Nuclear Instruments and Methods in Physics Research Section A: Accelerators, Spectrometers, Detectors and Associated Equipment* 533.3 (Nov. 2004), pp. 454–466.

[Mag90] P. V. Magnus et al. "Measurement of 15O(,)19Ne resonance strengths". en. In: *Nuclear Physics A* 506.2 (Jan. 1990), pp. 332–345.

[Mat16] A Matta et al. "NPTool: a simulation and analysis framework for low-energy nuclear physics experiments". In: *Journal of Physics G: Nuclear and Particle Physics* 43.4 (Mar. 2016), p. 045113.

[MMM19] Zach Meisel, Grant Merz, and Sophia Medvid. "Influence of Nuclear Reaction Rate Uncertainties on Neutron Star Properties Extracted from X-Ray Burst Model-Observation Comparisons". en. In: *ApJ* 872.1 (Feb. 2019). Publisher: American Astronomical Society, p. 84.

[Mor01] P. Moritz et al. "Broadband electronics for CVD-diamond detectors". In: *Diamond and Related Materials*. Proceedings of the 7th International Conference on New Diamond Science and Technology(ICNDST-7) 10.9 (Sept. 2001), pp. 1765–1769.

[Myt08] S. Mythili et al. "Lifetimes of states in Ne19 above the O15+ breakup threshold". In: *Physical Review C* 77 (Mar. 2008), p. 035803.

[Nob04] C.J Noble. "Evaluation of negative energy Coulomb (Whittaker) functions". In: *Computer Physics Communications* 159.1 (2004), pp. 55–62.

[Oli95] F. de Oliveira Santos. "Détermination par réaction de transfert de largeurs alpha dans le fluor 19. Applications à l'astrophysique. Astrophysique stellaire et solaire [astro-ph.SR]". PhD thesis. Université Paris Sud, 1995.

[Oli97] F. de Oliveira et al. "Comparison of low-energy resonances in $^{15}\mathrm{N}(\alpha,\gamma)^{19}\mathrm{F}$ and $^{15}\mathrm{O}(\alpha,\gamma)^{19}\mathrm{Ne}$ and related uncertainties". In: *Phys. Rev. C* 55 (6 June 1997), pp. 3149–3151.

[Par13] A. Parikh et al. "Nucleosynthesis in type I X-ray bursts". en. In: *Progress in Particle and Nuclear Physics* 69 (Mar. 2013), pp. 225–253.

[PJS14] A. Parikh, J. José, and G. Sala. "Classical novae and type I X-ray bursts: Challenges for the 21st century". In: *AIP Advances* 4.4 (Jan. 2014). Publisher: American Institute of Physics, p. 041002.

[Ram16] D. Ramos. "Fragment Distributions of Transfer- and Fusion-Induced Fission from $^{238}\mathrm{U}+\ ^{12}C$ Reactions Measured Through Inverse Kinematics". PhD thesis. Universidad de Santiago de Compostela, 2016.

[Rau20] Thomas Rauscher. *Essentials of Nucleosynthesis and Theoretical Nuclear Astrophysics*. 2514-3433. IOP Publishing, 2020.

[Reh03] K. E. Rehm et al. "Branching ratio $\Gamma_\alpha/\Gamma_\gamma$ of the 4.033 MeV $3/2^+$ state in $^{19}\mathrm{Ne}$". In: *Phys. Rev. C* 67 (6 June 2003), p. 065809.

[Rej11] M. Rejmund et al. "Performance of the improved larger acceptance spectrometer: VAMOS++". en. In: *Nuclear Instruments and Methods in Physics Research Section A: Accelerators, Spectrometers, Detectors and Associated Equipment* 646 (2011), pp. 184–191.

[Roj20] J S Rojo et al. "An implantation Diamond detector as a beam monitor for an intense radioactive ion beam". In: *Journal of Physics: Conference Series* 1643 (Dec. 2020), p. 012040.

[Rol88] Claus E Rolfs. *Cauldrons in the cosmos : nuclear astrophysics*. eng. Theoretical astrophysics. Chicago ; London: University of Chicago Press, 1988.

[RS80] P. Ring and P. Schuck. *The nuclear many-body problem*. New York: Springer-Verlag, 1980.

[San94] Jean-Claude Santiard et al. *Gasplex: a low-noise analog signal processor for readout of gaseous detectors*. Tech. rep. Geneva: CERN, Oct. 1994.

[Sch12] F. Schirru et al. "Development of large area polycrystalline diamond detectors for fast timing application of high-energy heavy-ion beams". en. In: *J. Inst.* 7.05 (May 2012), P05005–P05005.

[Söd11] P. -A. Söderström et al. "Interaction position resolution simulations and in-beam measurements of the AGATA HPGe detectors". en. In: *Nuclear Instruments and Methods in Physics Research Section A: Accelerators, Spectrometers, Detectors and Associated Equipment* 638.1 (May 2011), pp. 96–109.

[SP14] C. Scheidenberger and M. Pfützner. *The Euroschool on Exotic Beams, Vol. IV*. Lecture Notes in Physics. Springer Berlin Heidelberg, 2014.

[Tan05] W. P. Tan et al. "Lifetime of the astrophysically important 4.03-MeV state in ^{19}Ne". In: *Phys. Rev. C* 72 (4 Oct. 2005), p. 041302.

[Tan07] W. P. Tan et al. "15O(alpha,gamma)19Ne breakout reaction and impact on X-ray bursts". eng. In: *Phys. Rev. Lett.* 98.24 (June 2007), p. 242503.

[Tan09] W. P. Tan et al. "Measurement of the decay branching ratios of the α-unbound states in ^{19}Ne and the $^{15}\mathrm{O}(\alpha,\gamma)$ reaction rate". In: *Phys. Rev. C* 79 (5 May 2009), p. 055805.

[TB04] O. B. Tarasov and D. Bazin. "LISE++ : design your own spectrometer". In: *Nuclear Physics A* 746 (2004), pp. 411–414.

[Tea18] AGATA Data Analysis Team. *AGATA Data Analysis User's guide Global Level Processing*. Nov. 2018. URL: https://atrium.in2p3.fr/nuxeo/nxfile/default/addab6d3-ef22-453a-a3b1-629f145376f3/blobholder:0/AGATA_GLP_UsersGuide.pdf. (accessed: 09.2020).

[Tea19] AGATA Data Analysis Team. *AGATA Data Analysis User's guide for Local Level Processing*. Sept. 2019. URL: https://atrium.in2p3.fr/nuxeo/nxfile/default/878272cd-bb33-4b35-aa30-227c1a38e8d1/blobholder:0/AGATA_LLP_UsersGuide.pdf. (accessed: 09.2020).

[Tho88] Ian J. Thompson. *FRESCO documentation*. 1988.

[TN09] Ian J. Thompson and Filomena M. Nunes. *Nuclear Reactions for Astrophysics: Principles, Calculation and Applications of Low-Energy Reactions*. Cambridge: Cambridge University Press, 2009.

[Ver82] J. Vernotte et al. "Optical model analysis of 3He elastic scattering from s-d shell nuclei at 25 MeV". In: *Nuclear Physics A* 390.2 (1982), pp. 285–313.

[WBJ82] C L Woods, B A Brown, and N A Jelley. "A comparison of Woods-Saxon and double-folding potentials for lithium scattering from light target nuclei". In: *Journal of Physics G: Nuclear Physics* 8.12 (Dec. 1982), pp. 1699–1719.

[WGS99] M. Wiescher, J. Görres, and H. Schatz. "Break-out reactions from the CNO cycles". en. In: *J. Phys. G: Nucl. Part. Phys.* 25.6 (Jan. 1999), R133–R161.

[WH91] R P Ward and P R Hayes. "Compilation of triton optical model parameters, 1954-1990". In: *Atomic Data and Nuclear Data Tables; (United States)* (Nov. 1991).

[Wie98] Willy Wien. "Untersuchungen über die electrische Entladung in verdünnten Gasen". In: *Annalen der Physik* 301.6 (Jan. 1898), pp. 440–452.

[Yos98] T. Yoshimura et al. "Alpha spectroscopic factors for 6 Li, 7 Li, 9 Be and 12 C from the (p, pα) reaction at 296 MeV". In: *Nucl. Phys. A* 641 (1998), pp. 3–20.

[ZZB10] James F. Ziegler, M. D. Ziegler, and J. P. Biersack. "SRIM - The stopping and range of ions in matter (2010)". In: *Nuclear Instruments and Methods in Physics Research B* 268.11-12 (June 2010), pp. 1818–1823.